The Dissertation Committee for Xiang Yan
Certifies that this is the approved version of the following dissertation:

Statistical Model of Beam Distortion by Tissue Inhomogeneities in Tissue Harmonic Imaging

Committee:

Mark F. Hamilton, Supervisor

Stanislav Emelianov

Elmer L. Hixson

Yurii A. Ilinskii

Preston S. Wilson

Statistical Model of Beam Distortion by Tissue Inhomogeneities in Tissue Harmonic Imaging

by

Xiang Yan, B.S., M.S.

DISSERTATION
Presented to the Faculty of the Graduate School of
The University of Texas at Austin
in Partial Fulfillment
of the Requirements
for the Degree of

DOCTOR OF PHILOSOPHY

THE UNIVERSITY OF TEXAS AT AUSTIN

December, 2004

To my family

ACKNOWLEDGMENTS

I extended my thanks to Dr Mark F. Hamilton, my supervising professor, for his important guidance and help in every aspect during the course of this work. His suggestions were invaluable to the completion of this work.

Dr Preston S. Wilson is thanked for serving as a member of the dissertation committee and for his help in preparing the dissertation writing. Dr Elmer L. Hixson and Dr Stanislav Emelianov are thanked for reviewing this dissertation and providing important suggestions. Dr Yurii A. Ilinskii is thanked for his help in understanding many concepts in statistics.

I would also like to thank my fellow acoustic students for helpful discussions during course study. Special thanks to Steve Younghouse for his help in running the experiment apparatus and helpful guidance for learning the numerical algorithm.

Finally, my family are thanked for lifetime of love and support.

This work was supported by the Office of Naval Research.

December, 2004

Statistical Model of Beam Distortion by Tissue Inhomogeneities in Tissue Harmonic Imaging

Publication No. _____

Xiang Yan, Ph.D.

The University of Texas at Austin, 2004

Supervisor: Mark F. Hamilton

In tissue harmonic imaging (THI) the images are formed using the second harmonic component that is generated nonlinearly when ultrasound propagates inside the body. THI improves image resolution by reducing effects of phase distortion and reverberation in the body wall layer. A statistical investigation was performed to quantify improvement achieved with THI in the presence of tissue inhomogeneity. The investigation was both theoretical and experimental. In the theoretical model, a thin random phase screen located just in front of the source approximates the effect of inhomogeneity in the body wall layer. The phase variations across the screen are characterized statistically by zero mean, small variance, and Gaussian spatial correlation function. An analytical solution was derived for the expected value of the intensity of the second harmonic for a source that radiates a focused Gaussian beam. Contributions due to the coherent and scattered field components appear as separate terms in the solution. Validity of the statistical solution was established by comparison with ensemble averages of direct numerical simulations. Evolution of the beam profile and variation in energy content of the scattered second harmonic as a function of phase screen statistics are discussed. In comparison with the scattered field at the source frequency, the scattered field at the second-harmonic frequency is shown to be more localized about the beam axis. The results demonstrate clearly and quantitatively how distortions due to phase aberrations near the source are reduced by THI. Numerical simulations were also performed for beams radiated from a focused circular source with uniform amplitude. These results exhibit similar behavior. Dependence of results from the theoretical model on the distance between the source and phase screen was investigated. A transformation based on geometrical acoustics was obtained that approximates the mean scattered field due to a phase screen at a given distance away from the source using the solution obtained when the phase screen is in the source plane. Use of multiple phase screens to approximate thick inhomogeneous layers was also investigated. Experiments performed with a focused circular source and phase screens created with randomly indented plastic plates confirm the general theoretical approach.

Contents

List of Figures

List of Symbols

a	characteristic source radius
$A(\mathbf{R})$	amplitude function
b_1	axial distance from the screen to the source
b_2	axial distance from the screen to the focal plane
B_x, B_y	angular spectrum bandwidth
$c(\mathbf{R})$	sound speed of inhomogeneous medium
$c'(\mathbf{R})$	fluctuation of $c(\mathbf{R})$
c_0	mean value of $c(\mathbf{R})$
c_n	sound speed for nth harmonic
c_w	sound speed in the water
c_p	sound speed for the polyethylene plate
C_2^{sc}	shape factor for the scattered beam profile for second harmonic
$C_{n'}$	correlation function of refractive index fluctuation
C_ϕ	correlation function of phase fluctuation
d	focal distance
D	Jacobian of the transformation from Cartesian to ray coordinates
E_1	exponential integral
E_n^{tot}	total acoustic energy for nth harmonic
E_n^{coh}	energy in the coherent field for nth harmonic
E_n^{sc}	energy in the scattered field for nth harmonic
E_{foc}	focal energy
E_{per}	peripheral energy
$\mathcal{F}$	Fourier transform
G	focal gain
h	thickness of the polyethylene plate
$H(f_x, f_y)$	filter function
$\langle I_n \rangle$	mean intensity of nth harmonic

I_n^{coh}	coherent intensity of nth harmonic
I_n^{sc}	scattered intensity of nth harmonic
I_m	mth order modified Bessel function
I_{2l}	intensity associated with q_{2l}
I_{2n}	intensity associated with q_{2n}
I_{2ln}	intensity associated with $q_{2l}q_{2n}^*$
$j = \sqrt{-1}$	imaginary unit
J_m	mth order Bessel function
k	wavenumber based on fundamental frequency ω_0
k_z	wavenumber in axial direction
k_1	wavenumber in axial direction for fundamental field
k_2	wavenumber in axial direction for second harmonic
k_p	wavenumber in the polyethylene plate
l	inhomogeneity scale (correlation length) of the medium
L	thickness of the body wall layer
$L_{t'}$	absorption and dispersion operator
m_n	nth order moments
$n(\mathbf{R})$	refractive index of the inhomogeneous medium
$n'(\mathbf{R})$	fluctuation of $n(\mathbf{R})$
p	acoustic pressure
p_0	reference acoustic pressure
p_n	acoustic pressure for nth harmonic
q	complex acoustic pressure
q_n	complex acoustic pressure for nth harmonic
$q^{(m)}$	mth order scattered field
$q_n^{(m)}$	mth order scattered field for the nth harmonic
q_{2l}	second-harmonic field generated at $z = b_1$
q_{2n}	second-harmonic field generated from $z = b_1$ to $z = d$
Q	relative focusing quality
Q_n	angular spectrum for the nth harmonic
Q_{10}	angular spectrum of the source pressure

$\mathbf{r} = (x, y)$	coordinates transverse to beam axis
$\mathbf{R} = (x, y, z)$	coordinates in three dimensions
s	diatance along ray path
$t' = t - z/c_0$	retarded time
T	transmission coefficient at water-plate interface
TL	transmission loss of the polyethylene plate
$z_0 = ka^2/2$	Rayleigh distance
z_w	specific acoustic impedance of water
z_p	specific acoustic impedance of polyethylene plate
α_n	absorption coefficient for nth harmonic
β	nonlinearity coefficient of the medium
δ	sound diffusivity
Δx, Δy	spatial sample intervals
ϵ	acoustic Mach number, small parameter
ϕ	phase function
$\Gamma(\mathbf{r})$	eikonal function
$\boldsymbol{\kappa}$	wave vector transverse to beam axis
$\lambda = 2\pi/k$	wavelength
μ	variance of $n'(\mathbf{R})$
$\nu = a/l$	ratio of radius to inhomogeneity length scale
$\rho(\mathbf{r})$	density of inhomogeneous medium
ρ_0	mean density
ρ_p	density of polyethylene plate
ρ_t	transition radius
σ	variance of phase change
$\sigma_{n'}(\mathbf{r})$	projected correlation function
ω_0	fundamental angular frequency
ω_n	nth harmonic angular frequency
ψ	field variable in Rytov's method
$\psi^{(n)}$	nth order scattering field in Rytov's method
$\zeta = z/d$	dimensionless axial distance

Chapter 1

Introduction

The use of ultrasonic waves inside human bodies to detect small objects and interfaces between different media has been exploited in medical diagnostics with great success.[1] In conventional ultrasound imaging, the transducer is placed directly on the surface of the body and transmits a pulse train at center frequency f, typically in the range of 1–10 MHz.[2] The reflected signals at frequency f from different locations inside the body are collected and processed to form a gray scale image. The ultimate resolution of the system is restricted by wavelength, so increasing probe beam frequency will increase scan resolution. However, there are drawbacks to this approach. First of all, tissue absorption increases with frequency, normally according to a frequency power law.[3,4] Therefore a higher frequency beam has shorter penetration depth inside the body. Second, effects of aberrations introduced by the sound speed inhomogeneity of the body wall tissue also increase with frequency.

The body wall usually possesses complex layer-like compositions that include skin, fat, muscle and connective tissue. It has been observed that the amplitude and phase fluctuations of ultrasound waves are associated with the sound speed difference between different compositions and the scattering from septa within subcutaneous fat inside the body wall.[5] Generally speaking, these fluctuations increase with probe frequency. In the pulse-echo method, the wave propagates through the body wall twice before it is received by the transducer, so effects of aberration are introduced during both the transmission and receiving process. The resulting degradation of beam focusing quality is due to the broadening of the main lobe and increase in side lobe energy, causing a reduction of lateral and contrast resolution in the images.[6] So in conventional ultrasound imaging, simply increasing probe frequency does not necessarily improve the image quality.

In addition to the aforementioned effects, there are other effects that cause the reduction in resolution. For example, the ultrasound pulse can reflect repeatedly back and forth between the interfaces inside the body wall, resulting in reverberation noise and haze in the image. Also, scattering of side lobes can introduce many artifacts into the image.[7] All of the above effects are unavoidable in medical ultrasound imaging.

Several limitations of conventional imaging methods can be greatly reduced without changing the system architecture by using imaging techniques based on nonlinearity associated with acoustic propagation. In the 1980s, Carstensen et al.[8] and Starritt et al.[9,10] noticed nonlinear propagation effects produced by diagnostic B-mode scanners during normal clinical use. However, not until the 1990s were these nonlinear effects widely used to advantage for imaging.[2,11–13] Tissue harmonic imaging (THI) is the main nonlinear acoustical imaging technique that is currently in use. It is based on use of the second-harmonic component generated by finite-amplitude propagation inside the body to construct the images.[2,6,11] THI uses various techniques[7,14,15] to eliminate frequency components radiated from the source, and the nonlinearly generated second-harmonic components are used for image formation. THI is a grayscale imaging technique that can greatly improve the image quality. The clinical benefits from THI include reductions in reverberation noise, clutter level and phase aberrations, improved border delineation and increased contrast resolution.[16]

In THI, the harmonics are generated nonlinearly when the transmitted pulse propagates through tissue. The finite amplitude properties of the pulse are the contributors to harmonic generation.[11,16] Since second-harmonic generation is a cumulative effect along the propagation path, its focal point is often observed to be a little deeper than that of the corresponding fundamental field,[17] i.e., the second-harmonic has a slightly greater penetration depth. Another improvement provided by THI is the increase of spatial and contrast resolutions due to the narrower main lobe and lower side lobe levels with the second-harmonic beam. Generally speaking, the second-harmonic amplitude is essentially proportional to the square of the fundamental. Therefore a side lobe that is 20 dB down produces a second harmonic roughly 40 dB below what is generated on axis.

All side lobes in the fundamental beam generate even lower side lobes for the second harmonic. For the same reason, the second-harmonic field has a sharper main lobe compared to the fundamental beam. The narrower main lobe increases spatial resolution and reduces image slice thickness, while lower side lobes can reduce the artifacts and clutter associated with their scattering, which results in improved contrast resolution.[2,12,16]

Aberration introduced by the body wall inhomogeneity can also be greatly reduced by THI. Two main reasons account for this reduction. First, at skin level, the second-harmonic amplitude is virtually zero. In a typical diagnostic environment it is more that 30 dB lower than the fundamental field,[16] and therefore the reverberation and scattering inside the body wall provides almost no contribution to the harmonic field generated beyond the body wall. Second, although the fundamental beam suffers aberration from the body wall, which results in increased side lobe levels and broadening of the main lobe beam width, these distortions are reduced in the nonlinearly generated second-harmonic beam. A qualitative explanation for these phenomena is described as follows. Since the increase in side lobe level and beam width for the fundamental field is a weak effect, the corresponding increase in the levels of the second-harmonic field is even weaker because generation of the second harmonic is proportional to the square of the amplitude of the fundamental wave. A quantitative analysis of this issue is the main objective of this disertation, as we will quantify the distortion in the second harmonic beam caused by the distortion in the fundamental beam.

Over the years, THI has been shown clinically to provide improved visualization of endocardial borders,[18] clearer identifications of lesions in duct stones and liver, and improved diagnosis of renal cell carcinoma and kidney stones that were often undetectable with conventional imaging.[7] These days, many diagnostic ultrasound systems set the THI to be the default diagnostic mode. Presented in Fig. 1.1 are two sets of echocardiograms obtained using both fundamental and harmonic imaging from an Acuson ultrasound system. In the figure, B-mode echocardiograms for two separate diagnoses are represented by the first and second rows. By comparison, the THI images (right column) result in enhancement

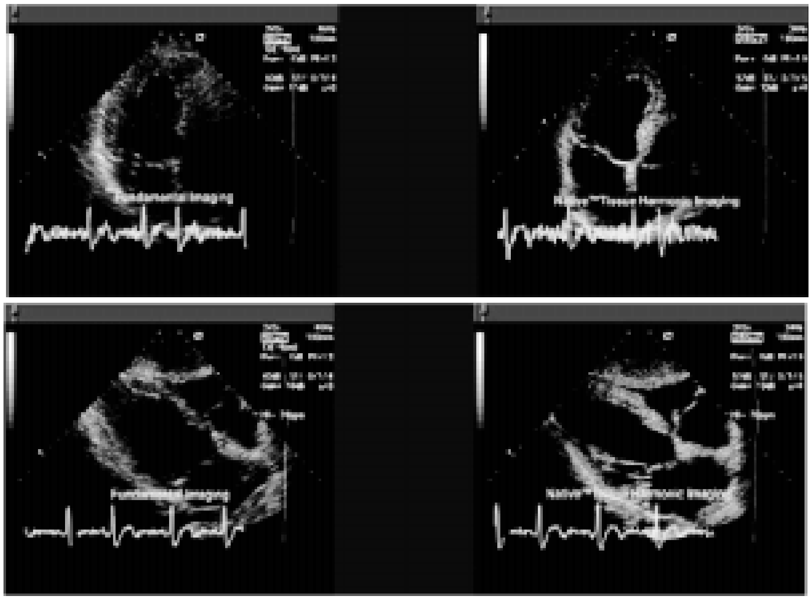

linear imaging

tissue harmonic imaging

Figure 1.1: Echocardiograms obtained from an Acuson ultrasound system. Left column are the images obtained using a conventional linear method with transducer frequency 2.5 MHz. Right column images are obtained using THI, transmit frequency 1.75 MHz, receive frequency 3.5 MHz.

and clearer definition of endocardial boarders, and noise and artifacts are reduced. In contrast, the images obtained from conventional imaging based on linear acoustics (left column) produce boarders that appear very vague, some of which cannot even be seen. For these diagnoses, THI images can provide more valuable information than conventional images.

Although THI is currently available on clinical scanners, the reasons for the improved images obtained with THI are still not well understood, partly because of the complexity of the nonlinear process it involves. Scattering due to tissue inhomogeneity coupled with nonlinear propagation effects make the analysis very difficult, and therefore analyses of THI have been restricted exclusively to numerical[6,16,19,20] and experimental[11,21] investigations. All of these investigations are based on case-by-case realizations of specific inhomogeneous propagation paths. Absent from the available literature is a theoretical investigation of the expected performance of THI based on general statistical properties of the propagation path. The latter approach should provide a broader perspective that may assist in the further improvement of image quality using THI.

The main objective of this dissertation is to develop a statistical model that predicts nonlinear harmonic generation in the presence of tissue inhomogeneity. Biological tissues vary considerably among individuals in terms of inhomogeneity.[22] Tissue is thus treated here as a random medium characterized by its statistical properties.

In Sec. 1.1, we discuss available experimental data on the characterization of tissue inhomogeneity. In Sec. 1.2, the extensively investigated linear propagation in tissue is briefly reviewed. In Sec. 1.3, the investigations by others of imaging techniques based on nonlinear acoustics are discussed, noting the similarities and differences with our model. Finally, in Sec. 1.4, the scope of this dissertation is presented.

1.1 Characterization of tissue inhomogeneity

In a clinical environment, tissue inhomogeneity mainly introduces phase fluctuations in the ultrasound wave fronts that propagate through it. In abdominal wall imaging, the majority of the phase fluctuations occur inside the body wall tissue, as shown in Fig. 1.2. Although inhomogeneity within viscera (internal organs) can also result in phase fluctuation, the magnitude of these fluctuations does not introduce significant phase distortion as compared to the body wall.[23] Moreover, the small transverse extent of the transmitted beam in the viscera far from the transducer makes the phase aberration a local phenomenon, which only affects the image pixels in that small area. In contrast, large sound speed variations in the body wall near the transducer can result in phase distortion affecting every pixel in the image.[23] Hence, phase aberration introduced by viscera is minor compared to that introduced by the body wall. Aberration is considered in the present work to arise solely from the body wall, and the viscera will be treated as homogeneous media.

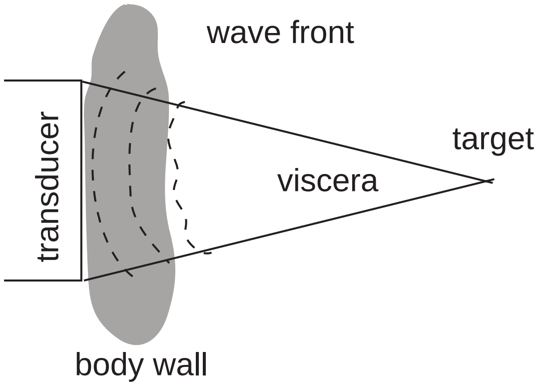

Figure 1.2: Model of phase aberration due to the body wall.

It has long been known in conventional ultrasound imaging that phase aberration can cause degradation of beam patterns, which directly affects image quality. Poor images are always associated with large phase aberrations, while better images are associated with smaller phase aberrations.[24] In an early study, Krammer and Hassler[25] made one-dimensional measurements of the time delay fluctuation caused by human abdominal wall. They found that the level of wave front distortion produced by these samples varies in a very random manner and can be quite different from one sample to the next. Later, Sumino and Waag[26] measured the pulse arrival time fluctuations produced by human abdominal wall specimens at room temperature. The selected abdominal wall sections obtained through autopsy were from in front of the liver, and they were comprised mostly of fat. The fluctuation measurements for each specimen, although different, appear to have statistically similar patterns. The data lead to an estimated correlation length of the tissue inhomogeneity on the order of several millimeters. An extension of these measurements was obtained by Hinkleman et al.[22] In their experiments, 14 human abdominal wall layers were measured at body temperature. Their samples included regions in the liver, gall bladder, pancreas, aorta, and kidney. Each specimen consisted of skin, a layer of fat, a lower layer of muscle, and a peritoneal membrane. The pulse arrival time difference was measured and converted to a time delay map for each sample. The statistics of the time delay variance and its correlation length were calculated based on sample measurements and averaged over these 14 samples. The averaged variance is 43 ns, and the mean correlation length is 7.9 mm. The correlation length was believed to be independent of orientation, as no anisotropy was observed for the specimen. For a given ultrasound frequency, the time delay data are transformed into the corresponding phase variations. These measurements provide valuable data on phase aberrations introduced by human abdominal wall, and they have been used by several authors in their investigations.[6,27]

1.2 Conventional imaging based on linear acoustic propagation

There have been extensive investigations of conventional imaging based on linear acoustic wave propagation through body wall tissue. Most of the work is focused on the phase fluctuation measurements, and schemes for correcting these aberrations. In the earlier work, the phase aberration was approximated by a single phase screen situated between the transmitter and receiver. The terminology “phase screen” typically refers to a hypothetical surface that alters the phase of a wave transmitted through it as a function of position on the surface, but which introduces no transmission loss. Many time-shift compensation algorithms have been developed using this model.[23,27–30] These methods are capable of removing some of the aberrations. The correct choice of model requires better understanding of wave propagation in real tissue. Later on, Mast et al.[5] performed two-dimensional simulations of ultrasonic pulse propagation through anatomically realistic abdominal wall cross sections. The abdominal wall inhomogeneity was represented by two-dimensional matrices of sound speed and density values, which were determined through scanned images of abdominal wall cross sections. Visualization of incident plane wavefronts through the abdominal wall shows the development of time-shift fluctuations due to large-scale tissue inhomogeneities. Although the calculation is restricted by two-dimensional propagation, the results reveal qualitative agreement of the wavefront distortion with the measurements. Their results suggest that a significant amount of time-shift aberration can be explained using a simple phase screen model. However, the amplitude fluctuation and waveform distortions are mainly due to multiple scattering from high-contrast inhomogeneities, such as septa within subcutaneous fat, which could not be modeled as single phase screens. Later, multilayer phase screen models were used by Huang and Tsao.[31] In these models, the continuously varying inhomogeneity of the medium is lumped into a series of discrete, parallel phase screens. Each phase screen is statistically independent, and for every screen the phase change is modeled as an independent distributed normal random variable with zero mean across the aperture. Propagation between adjacent screens was calculated using an angular spectrum method. Their results show that the mean speckle brightness, which is used as an image quality factor, decreases monotonically with the rms phase error of each screen. They also developed a correction method for two-dimensional wavefront compensation based on the multi-screen model.

1.3 Tissue harmonic imaging based on nonlinear acoustic propagation

Nonlinear propagation of an ultrasound beam in tissue has been investigated numerically by several authors.[6,16,19,20,32] In a review paper on THI by Averkiou,[16] nonlinear pulse propagation through a medium with typical tissue properties (sound speed and absorption, etc.) was investigated using the KZK equation.[33,50,52] Both a focused circular piston and a rectangular phased array were used as the source. Although only the rectangular sources are used in medical imaging systems, computations of the two sources reveal the same physics, and both can explain what has been observed in THI. In Averkiou's paper, the nonlinear evolution of the pulse spectrum, the axial field, and the focal beam patterns were discussed. His results clearly illustrate the advantages and limitations provided by THI. In his computations, however, the tissue is assumed to be homogeneous. A simplified model that accounts for inhomogeneity is obtained by considering tissue as a homogeneous layer with different sound speed, density and attenuation factor than the surrounding medium (taken to be distilled water). This method was used by Zhang et al.[19] to calculate the transmitted second harmonic field. In this case scattering occurs at the interface between the tissue and water. Another investigation of pulse propagation through realistic abdominal wall morphology was conducted by Wojcik et al.[20] Computations were made for a two-dimensional focused wave front that propagates through a two-dimensional abdominal wall tissue containing fat, muscle and connective tissue, and then is focused into a liver medium. Scattering in this case occurs inside the abdominal wall. Computations were based on a pseudospectral method that evaluates the spatial derivatives of the model equation using FFTs, while evaluating time derivatives using a finite difference method. This approach accounts for tissue absorption based on multiple relaxation mechanisms. The second-harmonic component was obtained by performing a Fourier transform of the pulse at each observation point. The focal shift and distortion of the second-harmonic field induced by a real inhomogeneous structure are apparent from their calculations.

A three-dimensional analysis of distortion of the second-harmonic beam by abdominal wall inhomogeneity was performed by Christopher.[6] The inhomogeneity is modeled by two random phase screens situated at positions occupied by the body wall layer. The propagation medium is liver and the source is a focused Gaussian transducer. Data for the phase distribution on each screen were obtained from the time-delay measurements of human abdominal wall specimen by Hinkelman et al.[22] One-way (transmission) and two-way (transmission and reception) focal beam patterns were calculated at the fundamental (2 MHz) and second harmonic (4 MHz) frequencies. The linear beam pattern at the 4 MHz frequency was also included for comparison, which was to emphasize the differences in beam patterns between linear propagation and nonlinear generation at the same frequency. The second-harmonic signal is generated during transmission, and its reflection is assumed to be modeled by linear theory. In the one-way calculation, the defocusing effect of the abdominal wall increases the side lobe levels. This effect is found to be more prominent in the two 4 MHz fields than in the 2 MHz field. The higher frequency wave, due to its shorter wavelength, is more affected by the phase screen and therefore subject to greater defocusing effects. The phase screen appears to have very little effect on broadening of any main lobes. In the two-way calculation, the second-harmonic profile has a narrower main lobe beam width and lower side lobe levels than the 2 MHz fundamental beam. It also has a slightly broader main lobe than the 4 MHz fundamental profile. In all cases, the side lobe levels for the second harmonic are lower than for their linear counterparts. Also in this work, comparison of continuous and pulsed waveforms shows that the second harmonic generated in a pulsed beam can be very well described by considering continuous wave propagation, which is very helpful for analysis.

In this dissertation we also use a phase screen model to analyze the second harmonic associated with propagation through random media. The phase screen is random in nature and is characterized by its variance and correlation length. Our approach is novel in this regard. The model does not rely on specific realizations of the random media, i.e., on the precise features of the inhomogeneities. It depends only on statistical properties of the medium. In cases where individual realizations are needed for comparison with statistical solutions, the phase screens are generated artificially with prescribed statistics rather than obtained from measurements. The statistics we use are based on the measurements reported by Hinkelman et al.[22] No analytical results were previously available that relate the scattered beam pattern statistics with the statistics of the phase screen. This is the main objective of the dissertation.

We start with the KZK equation to derive an expression for the ensemble averaged beam intensity for the second harmonic for the case of a single random phase screen aberration. A focused Gaussian source is assumed for the analysis. The contribution due to the scattered field appears as a separate term in the solution for the expected value of the intensity, and it depends on the phase variance and correlation length. Direct numerical simulations of second-harmonic generation due to Gaussian beam propagation through a single realization of a random phase screen agree with the theoretical results. We were unable to derive practical analytical solutions for the expected value of the second-harmonic intensity corresponding to radiation from a circular piston source. This case was investigated with numerical simulations and experiments.

Although numerous clinical images have demonstrated the reduction of aberration in nonlinearly-generated second harmonics, measurements of harmonic beam patterns following propagation through random medium layers have been investigated by only a few authors. Averkiou et al.[11] reported the first measurements of nonlinearly generated harmonic beam patterns due to propagation through real inhomogeneous tissue layers. Beef tissue was used in the experiments. The nonlinearly generated harmonics exhibited narrower main lobes and lower side lobe levels than at the fundamental frequency. Jing and Cleveland[34] also made measurements with tissue mimic phase screens. Both a sinusoidal phase screen and a random phase screen were used. The scattered side lobes for the second harmonic in their experiments were found to be at least 6 dB lower than in the fundamental field. In this dissertation, similar experiments are carried out with a random phase screen placed in front of a focused circular piston transducer. Focal beam patterns are measured and compared with computations in which the exact phase variations can be incorporated into the code. The main lobe beam width and the side lobe levels for the fundamental and second harmonic are compared.

1.4 Scope of this dissertation

This dissertation is both theoretical and experimental in nature. In the theoretical work, the mean intensities for the fundamental and second harmonic fields following distortion by a random phase screen are derived for a focused Gaussian beam. Numerical computations of individual realizations, based on an angular spectrum method, are performed to compare with the theoretical results for expected values of the radiation patterns. Numerical investigations are also performed for beams radiated by a focused circular piston source, for which we lack analytical results. Experiments are reported for a random phase screen, which are compared with the numerical model.

In Chap. 2 we review briefly the classical theories of linear wave propagation through media with random phase variations. The emphasis is on introduction of the phase screen model, which will be used throughout this disseration. In Chap. 3 we discuss the model equations used for analysis and computation. The KZK equation is used for the derivation of the statistical beam patterns. Use of the KZK equation inherently restricts the analysis to cases of weak and forward scattering. Our solutions are therefore subject to these constraints. Also in this chapter, we discuss the numerical scheme used for all computations for individual realizations of phase screens. The numerical algorithm we use to calculate both the fundamental and second-harmonic fields in these cases is based on calculations of angular spectra. For calculations involving a 3D inhomogeneous medium, which are presented in Chap. 5, we use a finite difference algorithm to investigate the KZK equation numerically. All analytical and numerical solutions are based on the assumption that the amplitude of the second harmonic is small compared with that of the fundamental. This approximation is reasonable in practice during THI.

In Chap. 4 the averaged beam intensities are derived for a focused Gaussian beam perturbed by a single random phase screen. The scattered intensity in the solutions is a function of phase variance and correlation length. Several statistical properties of the scattered field can be deduced from the solutions. Numerical simulations of Gaussian beam propagation through random phase screens are in good agreement with the statistical solutions. Effects of phase variance, correlation length, and position of the screen are also discussed in this chapter. A focusing quality factor is introduced to quantify the influence of phase aberration.

In Chap. 5 the beam pattern radiated by a focused circular piston source is investigated numerically. The dependence on phase variance, correlation length, and screen positions is discussed. The results are compared with the predictions for a Gaussian beam. In this chapter we also compare a multi-phase screen model with the single phase screen model to investigate the difference in scattering provided by a volume phase change (multi-phase screen model) and by a lumped phase change (single phase screen model). Follow which is the discussion regarding the validity of using a single screen model to approximate a 3D inhomogeneous medium.

In Chap. 6 experiments are carried out on radiation from a focused piston transducer that undergoes phase changes introduced by insertion of a plastic plate with varying thickness that simulates an ideal phase screen. The plates provide both regular and random phase perturbation patterns. Fundamental and second-harmonic focal beam patterns are measured and compared to numerical computations. The statistics of the scattered field observed in experiments are discussed with reference to the theoretical results.

Finally, conclusions are presented in Chap. 7. The appendices expand on portions of the derivations in Chaps. 3 and 4.

Chapter 2

Review of classical theories

Wave propagation in inhomogeneous or random media has been studied extensively in optics and acoustics. Most of the work is devoted to linear wave propagation. A review by Soczkiewicz and Chivers[36] discusses the most common methods used to study acoustic wave propagation in random media. These methods include geometrical optics (ray theory), the Born approximation (or small perturbation theory), and Rytov's approximation (or smooth perturbation theory). The phase screen method is described by Uscinski.[37] In each of these methods, the sound speed and/or density of the medium fluctuate randomly. The statistical behavior of the wave field, such as the fluctuation of the amplitude and phase, the mean intensity, the correlation function, etc., are often the solutions that are sought. In this chapter, we will briefly review these methods, and also discuss their possibilities for extension to nonlinear propagation.

2.1 Geometrical acoustics (ray theory)

This method is widely used for high frequency or large scale wave propagation.[38] Under the condition $\lambda z \ll l^2$, where λ is the wavelength, z is the observation distance, and l is the length scale of inhomogeneity, ray theory can be applied. Diffraction is not taken into account with this approach. Consider the linear wave equation[39]

$$\nabla^2 p - \frac{1}{c^2(\mathbf{R})}\frac{\partial^2 p}{\partial t^2} - \frac{1}{\rho(\mathbf{R})}\boldsymbol{\nabla}\rho(\mathbf{R})\cdot\boldsymbol{\nabla}p = 0, \tag{2.1}$$

in which $c(\mathbf{R})$ and $\rho(\mathbf{R})$ are the sound speed and density of the medium, p is the acoustic pressure, and $\mathbf{R} = (x, y, z)$ is the 3D coordinate vector. In most literature the density variations are neglected, and the last term is dropped from the equation. The last term does not affect the present discussion, and therefore it is also neglected here.

It is conventional to discuss the solution of Eqn. (2.1) in the frequency domain, and we thus express the acoustic pressure in the form

$$p = \frac{1}{2j} q e^{j\omega t} + \text{c.c.}, \tag{2.2}$$

where ω is the angular frequency, q is a complex pressure, and c.c. denotes the complex conjugate of the preceding terms. Equation. (2.1) thus becomes the inhomogeneous Helmoholtz equation,

$$\nabla^2 q + k^2 n^2(\mathbf{R}) q = 0\,. \tag{2.3}$$

Here, $k = \omega/c_0$ is the wave number, $n(\mathbf{R})$ is the refractive index of the medium defined by

$$n(\mathbf{R}) = \frac{c_0}{c(\mathbf{R})}\,, \tag{2.4}$$

with c_0 the reference sound speed (usually taken to be the mean sound speed of the medium). The complex pressure q is often written in the following form:

$$q = A(\mathbf{R}) e^{-jk\Gamma(\mathbf{R})}, \tag{2.5}$$

where $A(\mathbf{R})$ is the amplitude and $\Gamma(\mathbf{R})$, called the eikonal, describes the wavefront. By neglecting diffraction, ray theory results in an eikonal equation that determines the ray path,

$$\boldsymbol{\nabla}\Gamma \boldsymbol{\cdot} \boldsymbol{\nabla}\Gamma = n^2(\mathbf{R}), \tag{2.6}$$

and a transport equation that describes the change in amplitude along the ray path,

$$2\boldsymbol{\nabla} A \boldsymbol{\cdot} \boldsymbol{\nabla}\Gamma + A\nabla^2\Gamma = 0. \tag{2.7}$$

From Eqns. (2.6) and (2.7), one can obtain the phase and intensity fluctuation along the rays, the diffusion coefficient, and the angular distribution of the rays.[40]

Application of ray theory to nonlinear acoustic propagation was introduced by Ostrovsky[41] and developed extensively by several authors including Pelinovskii et al.[42] and Rudenko et al.[43,44] Consider the general form of Westervelt's nonlinear wave equation for inhomogeneous media used by Rudenko:[43]

$$\nabla^2 p - \frac{1}{c^2}\frac{\partial^2 p}{\partial t^2} = \boldsymbol{\nabla}\ln\rho\boldsymbol{\cdot}\boldsymbol{\nabla}p - \frac{\beta}{\rho c^4}\frac{\partial^2 p^2}{\partial t^2}, \tag{2.8}$$

where β is the nonlinearity coefficient, and β, ρ, and c are functions of $\mathbf{R}$. In their analyses, the variations in density and nonlinearity coefficient are taken into account. With the transformation

$$p = p(\mathbf{R}, t'), \qquad t' = t - \Gamma(\mathbf{R})/c_0\,, \tag{2.9}$$

and for high frequency, the eikonal given by Eqn. (2.6) is obtained, together with the new nonlinear transport equation

$$2\boldsymbol{\nabla}p\boldsymbol{\cdot}\boldsymbol{\nabla}\Gamma + p\nabla^2\Gamma - \boldsymbol{\nabla}\ln\rho\boldsymbol{\cdot}\boldsymbol{\nabla}\Gamma p - \frac{2\beta n}{\rho c^3}p\frac{\partial p}{\partial t'} = 0. \tag{2.10}$$

When the transport equation is integrated along the ray path, it reduces to a generalized Burgers equation,

$$\frac{\partial p}{\partial s} + \frac{p}{2}\frac{d}{ds}\ln\left(\frac{D}{\rho c}\right) = \frac{\beta}{\rho c^3}p\frac{\partial p}{\partial t'}\,, \tag{2.11}$$

where s is distance along the ray path, and D is the Jacobian of the transformation from Cartesian coordinates into ray coordinates.[43]

Equations (2.6) and (2.11) have been used to analyze sawtooth waves in a smoothly varying inhomogeneous medium.[43,44] The ray theory approach has been used by a number of authors, including Blanc-Benon and Lipkins et al.,[45] to study sonic boom propagation through turbulence.

Ray theory is successful in many problems, but since it does not account for diffraction, it is not appropriate for analysis of beam propagation. To take diffraction into account the following methods are introduced, which are also very frequently encountered in the literature: the Born approximation, Rytov's approximation, and phase screen method.

2.2 Born approximation

The Born approximation accounts for diffraction in inhomogeneous media. It is used when relative changes in amplitude and phase are small over the entire propagation path. In this case the sound speed fluctuation is small compared to its mean value, and the inhomogeneous Helmholtz equation, Eqn. (2.3), is solved using a perturbation method. The refractive index $n(\mathbf{R})$ can now be expressed as

$$n(\mathbf{R}) = \frac{c_0}{c(\mathbf{R})} = 1 + n'(\mathbf{R}), \tag{2.12}$$

where $n'(\mathbf{R})$ is a small variation proportional to the sound speed variation:

$$\frac{c'(\mathbf{R})}{c_0} = \frac{c(\mathbf{R}) - c_0}{c_0} \sim O(n') \ll 1\,. \tag{2.13}$$

The solution of Eqn. (2.3) can be written in the series form

$$q \approx q^{(0)} + q^{(1)} + ... + q^{(n)}, \qquad \frac{q^{(n)}}{q^{(0)}} \sim O[(n')^n], \tag{2.14}$$

where

$$\begin{aligned} \nabla^2 q^{(0)} + k^2 q^{(0)} &= 0 && (2.15)\\ \nabla^2 q^{(1)} + k^2 q^{(1)} &= -2k^2 n'(\mathbf{R}) q^{(0)}, && (2.16)\\ \nabla^2 q^{(2)} + k^2 q^{(2)} &= -2k^2 n'(\mathbf{R}) q^{(1)} - k^2 n'^2(\mathbf{R}) q^{(0)}, && (2.17)\\ &\;.... \end{aligned}$$

The 0th order solution $q^{(0)}$ satisfies the homogeneous wave equation. It is often called the coherent field. The nth order scattered field is $q^{(n)}$, which is a correction to $q^{(0)}$. The scattered field $q^{(n)}$ is an integral solution involving the medium inhomogeneity. Multiple scattering can be included by evaluating higher-order scattering terms, but usually only $q^{(1)}$ is calculated. The statistics of the scattered field can be written as function of the statistics of $n'(\mathbf{R})$.[36,40]

If nonlinearity is included, we may use the following form of the Westervelt equation:

$$\nabla^2 p - \frac{1}{c^2(\mathbf{R})}\frac{\partial^2 p}{\partial t^2} = -\frac{\beta}{\rho_0 c_0^4}\frac{\partial^2 p^2}{\partial t^2}\,. \tag{2.18}$$

This equation is different from Eqn. (2.8) used in nonlinear ray theory. We neglect the change of density and use mean density and mean sound speed in the nonlinear term. Also, the nonlinearity coefficient β is assumed to be a constant. This equation is thus a simplified form of Eqn. (2.8) that is convenient for grouping terms according to their smallness. Equation (2.18) is valid under conditions that the fluctuations of medium properties are small. To analyze second-harmonic generation we let

$$p \approx p_1 + p_2\,, \tag{2.19}$$

$$p_m = \frac{1}{2j} q_m e^{jm\omega t} + \text{c.c.}, \qquad m = 1, 2, \tag{2.20}$$

where p_1 and q_1 represent the real and complex fundamental pressures at frequency ω, while p_2 and q_2 represent the second-harmonic pressures at frequency 2ω. Assuming $|q_2| \ll |q_1|$, we may substitute Eqns. (2.19) and (2.20) into Eqn. (2.18) to obtain

$$\nabla^2 q_1 + k^2 n^2(\mathbf{R}) q_1 = 0, \tag{2.21}$$

$$\nabla^2 q_2 + 4k^2 n^2(\mathbf{R}) q_2 = -\frac{j2k^2\beta q_1^2}{\rho_0 c_0^2}\,, \tag{2.22}$$

which can be solved sequentially.

The next step is to expand both q_1 and q_2 as in Eqn. (2.14). If we designate q_n as being $O(\epsilon^n)$, where ϵ is the acoustic Mach number (which is proportional in magnitude to acoustic pressure), and designate n as being $O(\mu)$, then the expansion and ordering terms appear as follows:

$$\begin{aligned} q_1 &\approx q_1^{(0)} + q_1^{(1)}, \qquad q_1^{(0)} \sim O(\epsilon),\ \ q_1^{(1)} \sim O(\mu\epsilon)\,, \\ q_2 &\approx q_2^{(0)} + q_2^{(1)}, \qquad q_2^{(0)} \sim O(\epsilon^2),\ \ q_2^{(1)} \sim O(\mu\epsilon^2)\,, \end{aligned} \tag{2.23}$$

where $q_1^{(0)}$ and $q_2^{(0)}$ are the coherent fields for the fundamental and second harmonic, respectively. They satisfy the homogeneous wave equations, i.e. Eqns. (2.21)–(2.22) when $n(\mathbf{R}) = 1$, with $q_1^{(1)}$ and $q_2^{(1)}$ the first-order scattering corrections for $q_1^{(0)}$ and $q_2^{(0)}$, respectively. The scattering term $q_2^{(1)}$ for the second harmonic has two components,

$$q_2^{(1)} = q_2^{(1A)} + q_2^{(1B)}\,,$$

where

$$\nabla^2 q_2^{(1A)} + 4k^2 q_2^{(1A)} = -8k^2 n' q_2^{(0)}, \tag{2.24}$$

$$\nabla^2 q_2^{(1B)} + 4k^2 q_2^{(1B)} = -\frac{j4k^2 \beta q_1^{(0)} q_1^{(1)}}{\rho_0 c_0^2}. \tag{2.25}$$

Thus $q_2^{(1A)}$ accounts for scattering of the second-harmonic component generated by the coherent field of the fundamental, and $q_2^{(1B)}$ is the second-harmonic component generated by the nonlinear interaction of the coherent and first-order scattered components of the fundamental field. The solution for $q_2^{(1)}$, in principle, can be carried out term by term, but it is quite tedious, even for plane waves. To the author's knowledge, no literature is available describing the use of this method for analysis of nonlinear propagation.

2.3 Rytov approximation

The Rytov approximation[46] is an extension of the Born approximation. It requires the change of amplitude and phase over one wavelength to be small. In this method, a new set of transformed wave equations and field variables is used to formulate the problem. Starting from Eqn. (2.3), applying Rytov's transformation to the pressure q,[46] we write

$$q(\mathbf{R}) = q_0 e^{\psi(\mathbf{R})}, \tag{2.26}$$

with the constant q_0 introduced as a reference amplitude. We arrive at the nonlinear Riccati equation,

$$\nabla^2 \psi + \boldsymbol{\nabla}\psi \cdot \boldsymbol{\nabla}\psi = -k^2 n^2(\mathbf{R}), \tag{2.27}$$

where

$$\psi(\mathbf{R}) = \ln A(\mathbf{R}) + i\phi(\mathbf{R}), \tag{2.28}$$

with $A(\mathbf{R})$ and $\phi(\mathbf{R})$ being the amplitude and phase variations of $q(\mathbf{R})$. The same perturbation method as used in the Born approximation can be used to solve Eqn. (2.28):

$$\psi \approx \psi^{(0)} + \psi^{(1)} + ... + \psi^{(n)}, \tag{2.29}$$

where

$$\begin{aligned}\nabla^2\psi^{(0)} + \boldsymbol{\nabla}\psi^{(0)}\boldsymbol{\cdot}\boldsymbol{\nabla}\psi^{(0)} &= -k^2, &(2.30)\\ \nabla^2\psi^{(1)} + 2\boldsymbol{\nabla}\psi^{(0)}\boldsymbol{\cdot}\boldsymbol{\nabla}\psi^{(1)} &= -2k^2 n'\,, &(2.31)\\ &\cdots\end{aligned}$$

Here $\psi^{(0)}$ is the unperturbed solution, and

$$\psi - \psi^{(0)} = \ln\left|\frac{A(\mathbf{R})}{A_0(\mathbf{R})}\right| + i[\phi(\mathbf{R}) - \phi_0(\mathbf{R})]. \tag{2.32}$$

From Eqn. (2.32) we can see that ψ provides the statistics on the log amplitude and the phase variations of the wave field. This method has been used for the analysis of laser beam propagation through turbulent media.[46,47] Rytov's method can also be extended to nonlinear propagation. The procedure is the same as in Sec. 2.2, so it is not written out here. Again, the solution for the scattered second-harmonic field is very tedious to evaluate, and we have not seen it used in the literature.

2.4 Phase screen method

The phase screen method is often used for modeling random media.[37] This theory is not restricted to small fluctuations of properties of the medium. It can easily include diffraction and multiple scattering. Compared to other methods, the phase screen model provides a more clear physical picture of the process involved. It is this method that we will use as the basis of our analysis in Chapter 4. The classical description of this method is presented here.

As shown in Fig. 2.1, an extended random medium can be separated into a series of slabs with thickness Δz. The phase variations ϕ inside the slab is projected onto a screen of zero thickness, situated in the center of the slab. The phase fluctuation introduced by one such screen is

$$\phi(\mathbf{r}) = -k\int_z^{z+\Delta z} n'(\mathbf{r}, z')\, dz'\,, \tag{2.33}$$

where $\mathbf{r} = (x, y)$ is the 2D transverse coordinate vector. The extended medium is thus approximated by a series of such screens. The phase screen approach requires that the phase change over the length scale l of the inhomogeneity (often referred to as the correlation length of the inhomogeneity) is small, and the slab thickness Δz is of order l. Under these conditions, the phase screens are statistically independent of each other.[37]

Statistical equations describing the propagation of moments can be derived directly from this model. The moments are statistical averages of the field quantities. The first moment is

$$m_1 = \langle q(\mathbf{r}, z) \rangle \,, \tag{2.34}$$

where $\langle \cdot \rangle$ means the ensemble average. This moment is often used to determine wave attenuation due to scattering. The second moment has two forms, one of which is

$$m_2 = \langle q(\mathbf{r}_1, z) q^*(\mathbf{r}_2, z) \rangle \,, \tag{2.35}$$

which is referred to as the correlation function. With $\mathbf{r}_1 = \mathbf{r}_2$, m_2 characterizes the statistical intensity of the wave field. Another form of the second moment is

$$m_2' = \langle q(\mathbf{r}_1, z) q(\mathbf{r}_2, z) \rangle \,. \tag{2.36}$$

Other higher-order moments are defined in a similar way.

For plane wave incidence, differential equations can be derived for evolution of the moments of the wave field at distances much greater than the correlation length. The equation describing the propagation of m_2 is shown here as an example:[37]

$$\frac{\partial m_2}{\partial z} = -\frac{j}{2k} \left(\nabla^2_{\mathbf{r}_1} - \nabla^2_{\mathbf{r}_2} \right) m_2 - k^2 \mu^2 [\sigma_{n'}(0) - \sigma_{n'}(\mathbf{r}_1 - \mathbf{r}_2)] m_2 \,, \tag{2.37}$$

where

$$\nabla^2_{\mathbf{r}_1} = \frac{\partial^2}{\partial x_1^2} + \frac{\partial^2}{\partial y_1^2} \,, \qquad \nabla^2_{\mathbf{r}_2} = \frac{\partial^2}{\partial x_2^2} + \frac{\partial^2}{\partial y_2^2} \,. \tag{2.38}$$

The variance μ is defined by

$$\mu^2 = \langle n'^2(\mathbf{r}, z) \rangle \,, \tag{2.39}$$

(a) Random medium

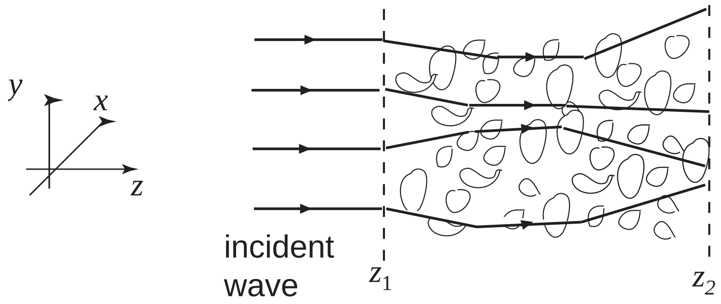

(b) Phase screen approximation

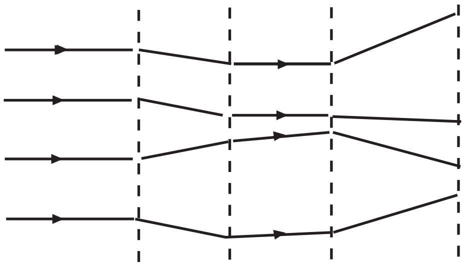

(c) Construction of phase screen

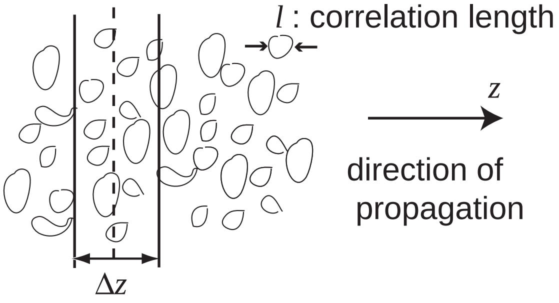

Figure 2.1: An extended random medium with correlation length l can be modeled as set of phase screens. (a) Continuous random medium between z_1 and z_2. (b) Approximation of continuous random medium by discrete phase screens. (c) Illustration of one phase screen representing slab of thickness Δz.

and

$$\sigma_{n'}(\mathbf{r}_1 - \mathbf{r}_2) = \int_{-\infty}^{\infty} C_{n'}(\mathbf{r}_1 - \mathbf{r}_2, \xi)\, d\xi \tag{2.40}$$

is the 2D correlation function for the phase screen, obtained as an integral over the following 3D correlation function for the medium:

$$C_{n'}(\mathbf{r}_1 - \mathbf{r}_2, z_1 - z_2) = \frac{\langle n'(\mathbf{r}_1, z_1) n'(\mathbf{r}_2, z_2)\rangle}{\langle n'^2(\mathbf{r}, z)\rangle}\,. \tag{2.41}$$

The first term on the right-hand side of Eqn. (2.37) accounts for diffraction, and the second term accounts for medium inhomogeneity. Statistical equations for other moments can be found in the book by Uscinski.[37]

Without the diffraction operator and for plane wave incidence, the following solutions for different orders of the moments are obtained:

$$\langle q\rangle = q_0 \mathrm{exp}\left[-\frac{1}{2}k^2\mu^2\sigma_{n'}(0)z\right], \tag{2.42}$$

$$\langle q^2\rangle = q_0^2 \mathrm{exp}\left[-2k^2\mu^2\sigma_{n'}(0)z\right], \tag{2.43}$$

$$\langle |q|^2\rangle = q_0^2, \tag{2.44}$$

$$\langle q^4\rangle = q_0^4 \mathrm{exp}\left[-8k^2\mu^2\sigma_{n'}(0)z\right], \tag{2.45}$$

$$\langle |q|^4\rangle = q_0^4\,, \tag{2.46}$$

where q_0 is the pressure amplitude at $z = 0$. The exclusion of diffraction is similar to applying ray theory, for which the propagation distance must satisfy $l \ll z \ll kl^2$, where k is the wave number. The lower limit is connected with the definition of Eqn. (2.40), which requires the slabs in the medium shown in Fig. 2.1(c) to be statistically independent of each other. Under this assumption the solutions are valid. The solutions $\langle q\rangle$, $\langle q^2\rangle$ and $\langle q^4\rangle$ reveal exponential decay with propagation distance. This decay is due to the incoherent addition of the phase terms. As the wave propagates further, the scattered field becomes stronger and the coherent field becomes weaker. The decay of the moments increases with μ and $\sigma_{n'}$. For the second moment, $\langle |q|^2\rangle = \langle qq^*\rangle$, we notice that it is proportional to the expected value of the acoustic intensity:

$$\langle I\rangle = \frac{\langle |q|^2\rangle}{2\rho_0 c_0}\,. \tag{2.47}$$

From Eqn. (2.44), we have $\langle I\rangle = q_0^2/2\rho_0 c_0^2$, a constant. The same is true for the quantity $\langle |q|^4\rangle$. These results indicate that the total energy of the wave is conserved during propagation through a phase changing medium, but the coherent energy decays, indicating that the scattered energy increases.

The phase screen method can also be extended to include nonlinear propagation. Again, if we exclude diffraction, we may obtain the following equations for the moments of the second harmonic:

$$\frac{d\langle q_2\rangle}{dz} + 2k^2\mu^2\sigma_{n'}(0)\langle q_2\rangle = \frac{j\beta k}{2\rho_0 c_0^2}\left\langle q_1^2\right\rangle, \tag{2.48}$$

$$\frac{d^2\langle q_2^2\rangle}{dz^2} + 16k^2\mu^2\sigma_{n'}(0)\frac{d\langle q_2^2\rangle}{dz} + 64k^4\mu^4\sigma_{n'}^2(0)\langle q_2^2\rangle = -\frac{\beta^2 k^2}{2\rho_0^2 c_0^4}\langle q_1^4\rangle, \tag{2.49}$$

$$\frac{d^2\langle |q_2|^2\rangle}{dz^2} = \frac{\beta^2 k^2}{2\rho_0^2 c_0^4}\langle |q_1|^4\rangle\,. \tag{2.50}$$

From Eqn. (2.48) we can see that the 1st order moment for the second harmonic involves second-order moments of the fundamental, and from Eqns. (2.49) and (2.50) we see that its second-order moments involve fourth-order moments of the fundamental. For plane wave incidence, the solutions for the moments are

$$\langle q_2\rangle = \frac{j\beta k q_0^2}{2\rho_0 c_0^2} z\exp[-2k^2\mu^2\sigma_{n'}(0)z], \tag{2.51}$$

$$\langle q_2^2\rangle = -\frac{\beta^2 k^2 q_0^4}{4\rho_0^2 c_0^4} z^2\exp[-8k^2\mu^2\sigma_{n'}(0)z], \tag{2.52}$$

$$\langle |q_2|^2\rangle = \frac{\beta^2 k^2 q_0^4}{4\rho_0^2 c_0^4} z^2. \tag{2.53}$$

The solution for $\langle |q_2|^2\rangle$ has the same value as in the case of propagation in homogeneous media. It is also proportional to the mean intensity. According to Eqn. (2.53), phase perturbations do not change the total energy in the second harmonic field under the conditions we investigated. For the moments of $\langle q_2\rangle$ and $\langle q_2^2\rangle$, at small z the nonlinear generation dominates and the moments grow with distance, whereas at large z the scattering dominates and the moments decay. This is different from the case for the moments of the fundamental, which decay continuously in the z direction. The change in these moments along the z axis is shown in Fig. 2.2. The maximum point of $\langle q_2\rangle$ is at $z = 1/2k^2\mu^2\sigma_{n'}(0)$, and the maximum of $\langle q_2^2 \rangle$ is at $z = 1/4k^2\mu^2\sigma_{n'}(0)$. Because of the increase in scattering with increasing frequency, $\langle q_2 \rangle$ and $\langle q_2^2 \rangle$ have faster decay rates than those of $\langle q_1 \rangle$ and $\langle q_1^2 \rangle$.

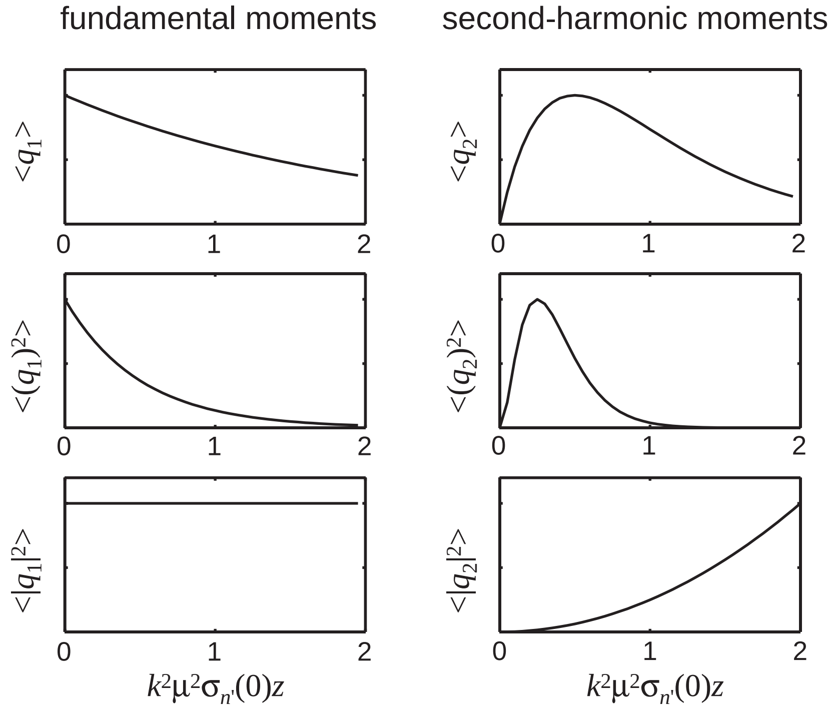

Figure 2.2: Change of fundamental and second-harmonic moments with distance for a plane wave propagating through a random medium.

To the author's knowledge, the solutions for the moments of the second-harmonic field, given by Eqns. (2.51)–(2.53), are not available in the literature. Although they are based on a simple model, they provide useful comparisons with linear theory, as well as with solutions derived later for diffracting beams.

2.5 Discussion

As shown in this chapter, although classical theories are successful in solving linear wave propagation problems, the corresponding nonlinear propagation problems prove to be much more difficult. Using Born's or Rytov's method to obtain the scattered component of the second-harmonic field introduces many more terms in the expansion. In the phase screen method, the statistical equation governing the moments of the second-harmonic field involves higher-order moments of the fundamental wave. Although results were obtained for a plane wave, the problem of beam propagation with diffraction is very difficult to solve. Even in the linear case, it has been proved that no analytical solutions exist for the fourth-order moments.[37]

In this dissertation we use a phase screen approach to analyze beam propagation including diffraction and nonlinearity. Instead of deriving an equation for the propagation of statistical moments, we express the mean intensity of the second-harmonic field in an integral form similar to that encountered in Born's approximation. In the theoretical model, only one screen is considered, with the remainder of the medium assumed to be homogeneous. An analytical expression for the evolution of the mean intensity is obtained. In the plane wave limit, the beam solution reduces to the plane wave solution given by Eqn. (2.53).

Chapter 3

Integral and numerical descriptions of second-harmonic generation in diffracting beams

In this chapter we discuss in detail the nonlinear model equations used for both theoretical and numerical analysis in later chapters. We have shown in Chap. 2 that Eqn. (2.18) can be used to model nonlinear wave propagation through inhomogeneous media, in which the sound speed varies continuously over the propagation path. The theoretical predictions of propagation in inhomogeneous media that follow in subsequent chapters are based primarily on the phase screen model described in Sec. 2.4. The phase screen introduces a random phase distribution across the beam in a plane at some distance from the source. At all other locations the medium is presumed to be homogeneous. Analytical and numerical solutions in this case can be based on the wave equation for homogeneous media, with effects of inhomogeneity introduced through appropriate boundary conditions at the locations of the phase screens. The purpose of the present chapter is to present the wave equation, together with its integral and numerical solutions, for both the fundamental and second harmonic fields, to be used in later chapters. These results have been reviewed by others,[33,48–51] and therefore this section is mainly a review of known theory. The results presented here will establish the notation and specific formulations to be used in the present work.

Basically, two nonlinear wave equations are used in this dissertation. One is the Westervelt equation,[50] obtained from Eqn. (2.18) by letting $c(\mathbf{R})$ be a constant. Another is the KZK equation,[33,50,52] which can be obtained from the Westervelt equation by using the Fresnel approximation (or parabolic approximation) of the diffraction term. The KZK equation has been used by several authors to model nonlinear beam distortion in inhomogeneous medium.[44,45] It will be used to derive integral solutions for the second-harmonic field in Sec. 3.1. The numerical scheme for the phase screen model is an angular spectrum method based on the Westervelt equation. The angular spectrum method has been used to calculate the nonlinear field in a variety of problems involving diffraction.[53–55] In Sec. 3.2, the angular spectra for the fundamental and second-harmonic fields are derived, and their numerical implementations are discussed. For the numerical scheme of beam propagation through a continuous inhomogeneous medium, a time domain KZK algorithm is used. The time domain KZK algorithm accounts for continuous 3D sound speed variations. This algorithm is introduced in Sec. 3.3. In Chap. 5 this time-domain KZK code is used to simulate beam propagation through a continuous inhomogeneous medium. The purpose is to compare with the single screen model to discussed the validity of using a single screen to approximate an extended inhomogeneous medium.

3.1 Integral solutions

The KZK nonlinear progressive wave equation is used as the basis of the integral solutions presented in this section. It is an appropriate equation for directional sound beams such as those considered here. The most important advantage of using the KZK equation is that for radiation from a source with Gaussian amplitude shading, closed-form solutions can be obtained for the fundamental and second harmonic.[49] Tractable integral solutions can be obtained for more general cases.[48,56,57] These advantages make the KZK equation suitable for the basis of our analytical work. If inhomogeneity is included, the KZK equation is valid provided energy is scattered mainly in the forward direction, and provided the forward scattering is localized near the axis of the beam, such that the condition of directional radiation continues to be satisfied. We thus exclude the following two cases from consideration: First, in which the length scale of the inhomogeneity is very small compared to one wavelength. In such cases, the scattering is isotropic in all directions. Second, in which the sound speed fluctuation is sufficiently large that strong scattered components are radiated at large angles with respect to the beam axis. In the phase screen model we make the weak scattering assumption, and use of the KZK equation is justified.

The KZK equation describing a sound beam that propagates in the positive z direction, shown by Fig. 3.1, can be written as

$$\frac{\partial p}{\partial z} = \frac{c_0}{2}\int_{\infty}^{t'} \nabla_{\perp}^2 p \, dt'' + \frac{\beta}{2\rho_0 c_0^3}\frac{\partial p^2}{\partial t'} + L_{t'}(p) \,, \tag{3.1}$$

where $t' = t - z/c_0$ is the retarded time, c_0 is a reference sound speed, and $\nabla_{\perp}^2 = \partial^2/\partial x^2 + \partial^2/\partial y^2$. The first term on the right-hand side of Eqn. (3.1) accounts for diffraction, and the second term accounts for nonlinearity. Frequency dependent absorption and the accompanying sound speed dispersion are represented by the third term, assumed to be a linear operator. For fresh water this operator becomes $L_{t'} = (\delta/2c_0^3)\partial^2/\partial t'^2$, where δ is the sound diffusivity of water taking into account viscosity and thermal conductivity. For tissue, it is typically characterized by the frequency dependence of an absorption coefficient obeying a power law, and by the corresponding dispersion law.[60]

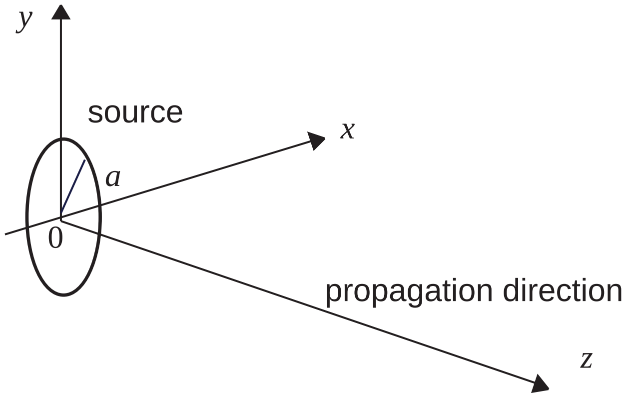

Figure 3.1: Geometry for a sound beam. The source is located in the plane $z = 0$ with radius a, and propagation is along the z axis.

The solution of Eqn. (3.1) is sought in the form of the simple perturbation

$$p = p_1 + p_2 \,,$$

where p_1 represents the fundamental pressure, p_2 represents the second harmonic, and $|p_2| \ll |p_1|$ is assumed throughout the nonlinear interaction region. This quasilinear approximation transforms Eqn. (3.1) into two linear equations:

$$\frac{\partial p_1}{\partial z} = \frac{c_0}{2}\int_{\infty}^{t'} \nabla_{\perp}^2 \, p_1 \, dt'' + L_{t'}(p_1)\,, \tag{3.2}$$
$$\frac{\partial p_2}{\partial z} = \frac{c_0}{2}\int_{\infty}^{t'} \nabla_{\perp}^2 \, p_2 \, dt'' + \frac{\beta}{2\rho_0 c_0^3}\frac{\partial p_1^2}{\partial t'} + L_{t'}(p_2)\,. \tag{3.3}$$

We now let[49]

$$p_n(\mathbf{r}, z, t) = \frac{1}{2j} q_n(\mathbf{r}, z) e^{j\omega_n t'} + \text{c.c.} \qquad n = 1, 2\,, \tag{3.4}$$

where $\omega_n = n\omega_0$ with ω_0 the source frequency, and q_n is the complex pressure at frequency ω_n. The vector $\mathbf{r} = (x, y)$ is in the plane perpendicular to the propagation axis z. Thus the reference sound speed c_0 in Eqns. (3.1)–(3.3) is taken to be the sound speed at source freqnecy $\omega_1 = \omega_0$, i.e. $c_0 = c_1$. In general, the effect of the operator $L_{t'}$ on retarded time t' is to introduce a complex multiplicative constant,[58] i.e.,

$$L_{t'}(e^{j\omega_n t'}) = \tilde{\alpha}_n e^{j\omega_n t'}\,, \qquad \tilde{\alpha}_n = \alpha_n + j\omega_n(c_n^{-1} - c_1^{-1})\,. \tag{3.5}$$

The real part α_n is the absorption coefficient at frequency ω_n, and the imaginary part is associated with sound speed dispersion, where c_n is the phase speed at frequency ω_n.[58] When we substitute Eqns. (3.4) and (3.5) into Eqns. (3.2) and (3.3), we obtain

$$\frac{\partial q_1}{\partial z} + \frac{j}{2k}\nabla_{\perp}^2 \, q_1 + \tilde{\alpha}_1 q_1 = 0\,, \tag{3.6}$$
$$\frac{\partial q_2}{\partial z} + \frac{j}{4k}\nabla_{\perp}^2 \, q_2 + \tilde{\alpha}_2 q_2 = \frac{k\beta}{2\rho_0 c_0^2} q_1^2\,, \tag{3.7}$$

where $k = \omega_0/c_0$.

We consider the case of radiation at frequency ω_0, in which case the boundary conditions are

$$q_1(\mathbf{r}, 0) = q_{10}(\mathbf{r}), \qquad q_2(\mathbf{r}, 0) = 0\,, \tag{3.8}$$

where $q_{10}(\mathbf{r})$ is a complex source function determining the amplitude and phase distribution in the plane $z = 0$. A random phase distribution corresponds to the presence of a phase screen immediately in front of the source. The solution for q_1 can be written in the integral form[59]

$$q_1(\mathbf{r},z) = \frac{jke^{-\tilde{\alpha}_1 z}}{2\pi z}\int_{\mathbf{r}'} q_{10}(\mathbf{r}')\exp\left[-\frac{jk|\mathbf{r}-\mathbf{r}'|^{\mathbf{2}}}{2z}\right]d\mathbf{r}'\,, \tag{3.9}$$

and the solution for q_2 is[59]

$$\begin{aligned} q_2(\mathbf{r},z) = &-\frac{\beta k^3}{8\pi^2\rho_0 c_0^2 z}e^{-jkr^2/z-\tilde{\alpha}_2 z}\int_{\mathbf{r}_c}\int_{\mathbf{r}_d} q_{10}\left(\mathbf{r}_c+\frac{\mathbf{r}_d}{2}\right)q_{10}\left(\mathbf{r}_c-\frac{\mathbf{r}_d}{2}\right)\\ &\times H(r_d,z)\,\exp\left[-\frac{jkr_c^2-2jk\mathbf{r}\boldsymbol{\cdot}\mathbf{r}_c}{z}\right]d\mathbf{r}_c d\mathbf{r}_d\,, \end{aligned} \tag{3.10}$$

where

$$H(r_d,z) = \int_0^z \frac{1}{z'}\exp\left[-\frac{jkr_d^2}{4z'}+(\tilde{\alpha}_2-2\tilde{\alpha}_1)z'\right]dz'\,, \tag{3.11}$$

with $r_c^2 = \mathbf{r}_c\boldsymbol{\cdot}\mathbf{r}_c$, $r_d^2 = \mathbf{r}_d\boldsymbol{\cdot}\mathbf{r}_d$. Note that solution q_2 is expressed as an integral over the source function q_{10}, i.e., the solution for q_1 is not needed to determine q_2, even though the second harmonic is generated by the cumulative distortion of the beam as it propagates. This simple formulation is due to the fact that the propagation path is taken to be through a homogeneous medium.

If the medium is tissue, the absorption coefficient is approximately proportional to frequency, i.e., $\alpha_2 \approx 2\alpha_1$. The corresponding sound speed dispersion is then very weak, with the difference between c_2 and c_1 being less than 1% in the low MHz range.[60] This means that in tissue $\tilde{\alpha}_2 \approx 2\tilde{\alpha}_1$, and the term $(\tilde{\alpha}_2 - 2\tilde{\alpha}_1)z'$ in Eqn. (3.11) can be neglected. The solution for q_2 can then be reduced to

$$\begin{aligned} q_2(\mathbf{r},z) = &-\frac{\beta k^3}{8\pi^2\rho_0 c_0^2 z}e^{-jkr^2/z-\tilde{\alpha}_2 z}\int_{\mathbf{r}_c}\int_{\mathbf{r}_d} q_{10}\left(\mathbf{r}_c+\frac{\mathbf{r}_d}{2}\right)q_{10}\left(\mathbf{r}_c-\frac{\mathbf{r}_d}{2}\right)\\ &\times E_1\left(\frac{jkr_d^2}{4z}\right)\,\exp\left[-\frac{jkr_c^2-2jk\mathbf{r}\boldsymbol{\cdot}\mathbf{r}_c}{z}\right]d\mathbf{r}_c d\mathbf{r}_d\,, \end{aligned} \tag{3.12}$$

where $E_1(z)$ is exponential integral defined as

$$E_1(z) = \int_1^\infty \frac{e^{-zt}}{t}dt\,. \tag{3.13}$$

From Eqns. (3.9)–(3.12) we see that the tissue absorption and dispersion appear only in the exponential terms outside the integral. Except for decreasing the overall amplitude, they have no effect on the beam pattern. A simulation was performed for beam propagation through liver medium based on the absorption and dispersion laws[60]

$$\alpha_n = \alpha_0 \left(\frac{\omega_n}{\omega_1}\right)^\eta , \qquad \frac{c(\omega_n) - c_1}{c_1} = \frac{2c_1\alpha_0[(\omega_n/\omega_1)^{\eta-1} - 1]}{\pi(\eta - 1)\omega_1} . \tag{3.14}$$

Using the parameters given in the literature,[6] $\alpha_0 = 0.03$ Np/cm, $f_1 = 1$ MHz, $\eta = 1.3$, $c_1 = 1570$ m/s, we find that the resulting beam patterns for the fundamental and second harmonic field are indistinguishable from when absorption and dispersion are not considered. The only difference is the overall decrease in amplitude when absorption and dispersion are considered. Therefore in tissue, if we are only interested in the beam pattern distortion, we can neglect the effects of absorption and dispersion, and $\tilde{\alpha}_n$ is set to zero in all equations and solutions that follow.

For an axially symmetric beam, and for $\tilde{\alpha}_n = 0$, Eqn. (3.12) can be written as

$$\begin{aligned} q_2(r,z) = & -\frac{\beta k^3}{2\pi\rho_0 c_0^2 z} e^{-jkr^2/z} \int_0^\infty \int_0^\infty \int_0^\pi q_{10}(r_1)\ q_{10}(r_2) \\ & \times E_1\left[\frac{jk}{4z}(r_1^2 + r_2^2 - 2r_1 r_2 \cos\Phi)\right] \\ & \times \exp\left(-\frac{jkg}{4z}\right) J_0\left(\frac{kr}{z}\sqrt{g}\right) r_1 r_2 d\Phi dr_1 dr_2 , \end{aligned} \tag{3.15}$$

where $g = r_1^2 + r_2^2 + 2r_1r_2\cos\Phi$, and J_0 is the 0th order Bessel function. Equation (3.15) is equivalent to Eqn. (8) of Berntsen et al.[48] Closed form expressions for q_1 and q_2 can be derived for Gaussian beams[49] from Eqns. (3.9) and (3.12), respectively.

3.2 Angular spectrum method

Several numerical schemes have been developed for solving the KZK equation. They include the frequency-domain algorithm first developed by Aanonsen et al.,[61] which is convenient for periodic signals, and the time-domain algorithm developed by Lee and Hamilton,[62] which is suitable for pulses and random waveforms. Later Christopher and Parker[63] improved the frequency-domain approach by avoiding the parabolic approximation and accounting for full diffraction by incorporating the Kirchhoff-Helmholtz integral. These algorithms were developed originally for axisymmetric sound beams. Extensions of the KZK codes to nonaxisymmetric sound beams were developed in the frequency domain by Kamakura et al.,[64] and Baker et al.[57] and in the time domain by Averkiou and Khokhlova.[32]

Another numerical scheme, developed by Landsberger and Hamilton,[54] accounts for full diffraction during the process of second-harmonic generation in sound beams reflected from and transmitted through interfaces. Their numerical scheme propagates the angular spectrum of the field using integral solutions obtained by Tjøtta et al.[59,65] This angular spectrum method was first introduced by Alais and Hennion[53] to analyze sum- and difference frequency generation by a parametric array. The advantage of this approach is that, like Eqn. (3.12), the second-harmonic field at an arbitrary distance requires only a single calculation based on the primary wave field in the source plane. However, use of the angular spectrum makes the numerical computation more efficient, and moreover one is not restricted to the parabolic approximation. This numerical scheme is therefore suitable for calculations incorporating phase screens.

To set up the numerical scheme, we first define the angular spectrum of a complex pressure field. The angular spectrum Q_n is obtained by taking the 2D spatial Fourier transform of q_n in the (x, y) plane:[66]

$$Q_n(\boldsymbol{\kappa}, z) = \int_{-\infty}^{\infty}\int_{-\infty}^{\infty} q_n(\mathbf{r}, z) \exp(-j\boldsymbol{\kappa}\cdot\mathbf{r})\, d\mathbf{r}, \tag{3.16}$$

where $\boldsymbol{\kappa} = (k_x, k_y)$ is the wave vector in the (x, y) plane. The inverse Fourier transform is used to reconstruct q_n from its spectrum Q_n,

$$q_n(\mathbf{r}, z) = \frac{1}{4\pi^2} \int_{-\infty}^{\infty}\int_{-\infty}^{\infty} Q_n(\boldsymbol{\kappa}, z) \exp(j\boldsymbol{\kappa}\cdot\mathbf{r})\, d\boldsymbol{\kappa}\,. \tag{3.17}$$

Equation (3.17) indicates that any pressure field $q_n(\mathbf{r}, z)$ can be represented as a group of plane waves. The angular spectrum $Q_n(\boldsymbol{\kappa}, z)$ is identified as the complex amplitude of a plane wave traveling in the direction defined by the wave vector $(\boldsymbol{\kappa}, k_z)$, where k_z is the wavenumber in the z direction:

$$k_z = \sqrt{k^2 - \kappa^2}\,, \tag{3.18}$$

with $\kappa = |\boldsymbol{\kappa}|$. Any plane wave for which k_z is real is a propagating wave, whereas imaginary k_z corresponds to an evanescent wave. In the parabolic approximation, $\kappa^2 \ll k^2$ is assumed, and k_z is given by the first two terms in the binomial expansion of Eqn. (3.18):

$$k_z = k - \frac{\kappa^2}{2k}\,. \tag{3.19}$$

This approximation can therefore be used only for wave fields with narrow angular spectra, which is consistent with the restriction on use of the KZK parabolic wave equation.

We now review very briefly the main features of the numerical algorithm in order to point out parameters that are important for computation. Reference is made to parameters that are incorporated for numerical results presented later. The algorithm is based on the Westervelt equation,[50]

$$\nabla^2 p - \frac{1}{c_0^2}\frac{\partial^2 p}{\partial t^2} = -\frac{\beta}{\rho_0 c_0^4}\frac{\partial^2 p^2}{\partial t^2}\,. \tag{3.20}$$

Substitution of Eqn. (3.4) yields, in place of Eqns. (3.6) and (3.7),

$$\nabla^2 q_1 + k^2 q_1 = 0\,, \tag{3.21}$$

$$\nabla^2 q_2 + 4k^2 q_2 = -\frac{j2\beta k^2}{\rho_0 c_0^2} q_1^2\,. \tag{3.22}$$

These equations are the same as Eqns. (2.21) and (2.22) in Chap. 2 when the latter are applied to a homogeneous medium $[n(\mathbf{R}) = 1]$. The boundary conditions for q_1 and q_2 are given by Eqns. (3.8). In the following discussion, the wavenumber k_z associated with q_1 is denoted by k_1, and when associated with q_2 it is denoted by k_2. Taking the Fourier transform of Eqn. (3.21) and considering wave propagation in the positive z direction, one arrives at the solution

$$Q_1(\boldsymbol{\kappa}, z) = Q_1(\boldsymbol{\kappa}, 0)e^{-jk_1 z} = Q_{10}(\boldsymbol{\kappa})e^{-jk_1 z}\,. \tag{3.23}$$

where Q_{10} is the spectrum of the source function q_{10}, and

$$k_1 = \begin{cases} \sqrt{k^2 - \kappa^2}, & k^2 \geq \kappa^2 \,, \\ -j\sqrt{\kappa^2 - k^2}, & k^2 < \kappa^2 \,. \end{cases} \tag{3.24}$$

Numerical implementation of Eqn. (3.23) is straightforward. The angular spectrum $Q_{10}(\boldsymbol{\kappa})$ is obtained by taking the 2D FFT of the source function $q_{10}(\mathbf{r})$. The FFT algorithm requires the function q_{10} to be sampled above the Nyquist rate in both the x and y directions, i.e.,

$$\Delta x \leq \frac{1}{B_x} \,, \qquad \Delta y \leq \frac{1}{B_y} \,, \tag{3.25}$$

where Δx, Δy are the sampling intervals in the x, y directions, and B_x, B_y are the bandwidths that $Q_{10}(\boldsymbol{\kappa})$ projects on the k_x, k_y axes, respectively. In all computations we chose $\Delta x = \Delta y$. The sampling interval Δx (or Δy) determines the spectral range, i.e., the computation range of $\boldsymbol{\kappa}$ is defined by $[\pm k_{xmax}, \pm k_{ymax}]$, where

$$k_{xmax} = \max(|k_x|) = \pi/\Delta x, \qquad k_{ymax} = \max(|k_y|) = \pi/\Delta y. \tag{3.26}$$

The range of $\boldsymbol{\kappa}$ affects the discretization of the function $\exp(-jk_1 z)$.[55] The variation of this exponential as a function of $\boldsymbol{\kappa}$, for $|\boldsymbol{\kappa}| < k$ (propagating waves), can be seen by differentiating Eqn. (3.24):

$$\frac{dk_1}{d\kappa} = -\frac{\kappa/k}{\sqrt{1 - \kappa^2/k^2}} \,. \tag{3.27}$$

As κ increases toward k, $|dk_1/d\kappa|$ increases to infinity, and the oscillation of the exponential reaches infinity at $\kappa = k$. The k_x and k_y for which $\kappa = k$ defines what is called the radiation circle. Outside the radiation circle the function $\exp(-jk_1 z)$ decays exponentially. This is shown graphically in Fig. 3.2(a), where the real part of the exponential is plotted versus κ/k for an unfocused piston with $ka = 50$ (a is the piston radius), and z is at Rayleigh distance $z_0 = ka^2/2$.

When κ falls inside the radiation circle, where $k_{xmax}^2 + k_{ymax}^2 < k^2$, the function $\exp(-jk_1 z)$ can be discretized at the rate[55]

$$\Delta k_x = \Delta k_y \leq \frac{\pi\sqrt{k^2 - (k_{xmax}^2 + k_{ymax}^2)}}{2k_{xmax} z} \,. \tag{3.28}$$

A different numerical scheme must be used for $\kappa > k$.[55] In all of our cases, i.e., for a high-frequency ultrasound beam (large ka), κ always falls inside the radiation circle.

In principle, we need to satisfy both Eqn. (3.25) in the spatial domain and Eqn. (3.28) in the spectral domain. However, to satisfy Eqn. (3.28) requires many more sample points than necessary. For an unfocused piston source with $ka = 50$, at $z = z_0$, the function $\exp(-jk_1 z)$ and the spectrum $Q_{10}(\kappa)$ are plotted in Fig. 3.2(a) and (b). As indicated in Fig. 3.2(a), the phase oscillation is slow when $|\kappa/k|$ is small, and becomes faster when $|\kappa/k|$ increases. From Fig. 3.2(b) we see that $|Q_{10}|$ becomes small when $|\kappa/k|$ becomes large. The angular spectrum Q_{10} indicates that most of the energy is confined to small transverse wavenumbers, i.e., along axis of the beam. Equation (3.28) requires the exponential to be sampled above the Nyquist rate for every point in the $\boldsymbol{\kappa}$ domain. At the edge of this domain, however, Q_{10} becomes negligibly small, such that even if $\exp(-jk_1 z)$ is undersampled near the edge, the aliasing introduced by it is so small that the calculated beam pattern is virtually unaffected.

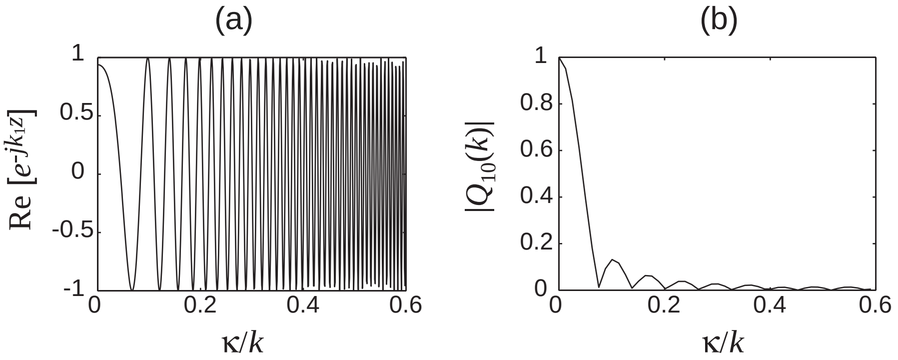

Figure 3.2: (a) Plot of the real part of $e^{-jk_1 z}$ vs spatial frequency κ/k at distance $z = z_0$. (b) The spectrum Q_{10} for an unfocused piston with $ka = 50$.

Take the same source as an example. The beam pattern is to be calculated at $z = z_0$. The spatial discretization according to Eqn. (3.25) is chosen as $\Delta x = \Delta y = 0.1a$, which sets the range of the dimensionless spectrum $\boldsymbol{\kappa}a$ as $(\pm 30.9, \pm 30.9)$. Equation (3.28) requires the spectrum discretization to be

$\Delta(k_x a) = \Delta(k_y a) \leq 0.06$. At this rate, we need 1024 × 1024 points to sample $\exp(-jk_1 z)$ and $Q_{10}(\boldsymbol{\kappa})$. Moreover by using 512 × 512 samples, for which $\Delta(k_x a) = \Delta(k_y a) = 0.12$, the resulting aliasing error is negligible, and the beam pattern is no different from the one obtained with 1024 × 1024 samples. Figure 3.3 shows the two beam patterns corresponding to the 512 × 512 samples (solid line) and 1024 × 1024 samples (dashed line). They are found to be indistinguishable in the region of interest. Hence, in the later calculations, the spectrum sampling rate is determined by the criterion that when doubled, no differences are observed. It is found that this rate can be reduced to about one third or one half of the rate required by Eqn. (3.28). This can save considerable computation time and memory.

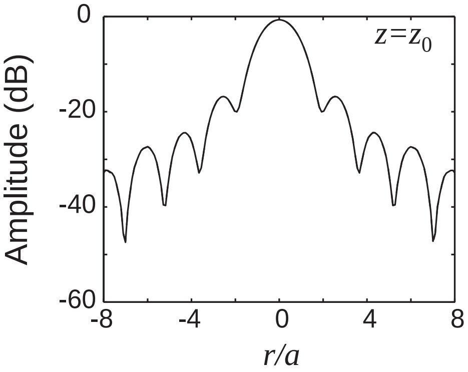

Figure 3.3: Plots of beam patterns at $z = z_0$ for an unfocused piston source using two spectrum discretizations. Dashed line: Nyquist rate of $\Delta(k_x a) = 0.06$, Solid line: $\Delta(k_x a) = 0.12$.

The angular spectrum for the second harmonic can be obtained by applying the Fourier transform directly to Eqn. (3.22). This method yields a result equivalent to Eqns. (39) and (40) of Landsberger and Hamilton.[54] A detailed derivation is produced in App. A, and the result for Q_2 is

$$Q_2 = \frac{j\beta k^2}{2\pi^2 \rho_0 c_0^2} e^{-jk_2 z} \int\int \frac{Q_{10}(\boldsymbol{\kappa} - \boldsymbol{\kappa}') Q_{10}(\boldsymbol{\kappa}') [e^{-j(k_A + k_1 - k_2)z} - 1]}{(k_A + k_1 - k_2)(k_A + k_1 + k_2)} d\boldsymbol{\kappa}' \,, \tag{3.29}$$

where $k_A = k_1(\boldsymbol{\kappa} - \boldsymbol{\kappa}')$, and k_2 is

$$k_2 = \begin{cases} \sqrt{4k^2 - \kappa^2}\,, & 4k^2 \geq \kappa^2\,, \\ -j\sqrt{\kappa^2 - 4k^2}\,, & 4k^2 < \kappa^2\,. \end{cases} \tag{3.30}$$

Similar formulations of Eqn. (3.29) have also been presented by Alais and Hennion[53] and by Naze Tjøtta and Tjøtta.[65] Notice in Eqn. (3.29) that when $k_A + k_1 = k_2$,

$$\frac{e^{-j(k_A+k_1-k_2)z} - 1}{k_A + k_1 - k_2} = -jz\,.$$

The sampling rate of $Q_{10}(\boldsymbol{\kappa}')$ and the exponential terms should be doubled, since they involve multiplication.

Following the same procedure we can also derive the corresponding angular spectra for the KZK equation, Eqns. (3.6) and (3.7) (with $\tilde{\alpha}_1 = \tilde{\alpha}_2 = 0$). The spectra Q_1 and Q_2 are

$$Q_1(\kappa, z) = Q_{10}(\kappa)\exp\left(\frac{jz\kappa^2}{2k}\right)\,, \tag{3.31}$$

and

$$\begin{aligned} Q_2(\kappa, z) = {} & \frac{k\beta}{2\rho_0 c_0^2} \int\!\!\int \frac{Q_{10}(\boldsymbol{\kappa} - \boldsymbol{\kappa}')Q_{10}(\boldsymbol{\kappa}')}{j|\boldsymbol{\kappa} - 2\boldsymbol{\kappa}'|^2/4k} \\ & \times \left[\exp\left(\frac{jz|\boldsymbol{\kappa} - \boldsymbol{\kappa}'|^2 + jz\kappa'^2}{2k}\right) - \exp\left(\frac{jz\kappa^2}{4k}\right)\right] d\boldsymbol{\kappa}'\,. \end{aligned} \tag{3.32}$$

When $\boldsymbol{\kappa}$ equals $2\boldsymbol{\kappa}'$, the following relation is used:

$$\frac{1}{j|\boldsymbol{\kappa} - 2\boldsymbol{\kappa}'|^2/4k}\left[\exp\left(\frac{jz|\boldsymbol{\kappa} - \boldsymbol{\kappa}'|^2 + jz\kappa'^2}{2k}\right) - \exp\left(\frac{jz\kappa^2}{4k}\right)\right] = z\exp(jz\kappa^2/4k).$$

Once Q_1 and Q_2 are obtained from Eqn. (3.23) and (3.29), the complex pressures q_1 and q_2 are obtained through the inverse Fourier transform in Eqn. (3.17).

If the complex pressure in the source plane has a second-harmonic component, then its propagation obeys a linear diffraction law. The radiated second-harmonic associated with this source condition can be obtained using Eqn. (3.23) by replacing k_1 with k_2. The total second harmonic pressure at the target plane is composed of the linear propagation part and the nonlinear generation by the fundamental wave radiated from the source, which is computed through Eqn. (3.29).

As mentioned before, the angular spectrum method is particularly suitable for phase screen calculations. Since the medium between the screens is homogeneous, only one calculation is needed to numerically propagate the field between screens. If medium inhomogeneity continuously varies over the propagation path, the angular spectrum approach is unsuitable, and a time domain KZK algorithm is used for this type of simulation. It is a marching algorithm and can incorporate continuous sound speed changes. This algorithm is discussed in the next section.

3.3 Time-domain KZK algorithm

The methods described in Sec. 3.1 and 3.2 are appropriate when modeling inhomogeneity by one or just a few phase screens, because the algorithms apply fundamentally to propagation in homogeneous media. Inhomogeneity enters only through boundary conditions. For continuously inhomogeneous media, and when nonlinearity is included, it becomes necessary to march through the medium incrementally, introducing diffraction and scattering at each step in the calculations. For this approach, it is most convenient to use the KZK equation, for which numerical solution algorithms are available. For weakly inhomogeneous media, the KZK equation assumes the form,[45]

$$\frac{\partial p}{\partial z} = \frac{c_0}{2}\int_{-\infty}^{t'} \nabla_\perp^2 \, p \, dt'' + \frac{\delta}{2c_0^3}\frac{\partial^2 p}{\partial t'^2} + \frac{\beta p}{\rho_0 c_0^3}\frac{\partial p}{\partial t'} + \frac{c'(\mathbf{r},z)}{c_0^2}\frac{\partial p}{\partial t'}\,, \tag{3.33}$$

where $c'(\mathbf{r},z) = c(\mathbf{r},z) - c_0$ is the sound speed fluctuation.

The effect of random inhomogeneity entering through $c'(\mathbf{r},z)$ ensures that radiation from an axisymmetric source cannot remain axisymmetric. Therefore a fully 3D algorithm must be used to solve this equation. The algorithm we began with is one developed by Averkiou and Khokhlova[32] for radiation from asymmetric (e.g., rectangular) sources in homogeneous media. Theirs is a time-domain algorithm that generalized the axisymmetric code developed by Lee and Hamilton.[62] These algorithms march forward in time including diffraction, absorption, and nonlinearity separately at each step in the z direction. Finite difference methods evaluate the diffraction and absorption terms, and an analytical solution is used to evaluate the nonlinear term. The computation region is a rectangular tube defined by $-x_{max} \leq x \leq x_{max}$, $-y_{max} \leq x \leq y_{max}$. The dimensions x_{max} and y_{max} must be sufficiently large that reflections from these boundaries do not affect the solution in the region of interest.

We modified Averkiou and Khokhlova's code to include the last term in Eqn. (3.33). Like the other effects, inhomogeneity is included independently at each step. This effect is included analytically. Without the diffraction, absorption, and nonlinearity terms, Eqn. (3.33) reduces to

$$\frac{\partial p}{\partial z} = \frac{c'(\mathbf{r}, z)}{c_0^2} \frac{\partial p}{\partial t'} \, . \tag{3.34}$$

The analytical solution of Eqn. (3.34) is, in parametric form,

$$p(z, t') = f(t' + \Delta t) \, , \qquad \Delta t = \int_0^z \frac{c'(\mathbf{r}, z')}{c_0^2} dz' \, , \tag{3.35}$$

where f is an arbitrary function of time. Equation (3.35) indicates that the inhomogeneity advances or delays the waveform by time Δt. Therefore, we only need to shift the waveform by that amount during each propagation step. The numerical implementation of shifting the waveform is outlined as follows. Suppose the time base t' is discretized to have time interval $\delta t' = t'_i - t'_{i-1}$, as in Fig. 3.4. The amount of time to be shifted during propagation from $k\Delta z$ to $(k+1)\Delta z$, with Δz the step size in z axis, is expressed as

$$\Delta t^k = M\delta t' + \Delta\xi^k = \int_{k\Delta z}^{(k+1)\Delta z} \frac{c'(\mathbf{r}, z')}{c_0^2} dz' \, , \tag{3.36}$$

where M is an integer number, and $0 \leq \Delta\xi^k \leq \delta t'$. The shift of $M\delta t'$ can be realized by moving the samples of the waveform by M points along the time axis. The shift of $\Delta\xi^k$ is realized by interpolating the waveform on a new time base (see Fig. 3.4):

$$p_i^{k+1} = C \left[\frac{\Delta\xi^k}{\delta t'} (p_{i+1}^k - p_i^k) + p_i^k \right] \, , \tag{3.37}$$

$$C = 1 + \frac{\Delta\xi^k (\delta t' - \Delta\xi^k)}{2} \, , \tag{3.38}$$

where p_i^{k+1} is the pressure at propagation distance $z = (k+1)\Delta z$, and at time $t' = i\delta t'$. The constant C is a correction factor to compensate for the numerical absorption introduced by interpolation.[67]

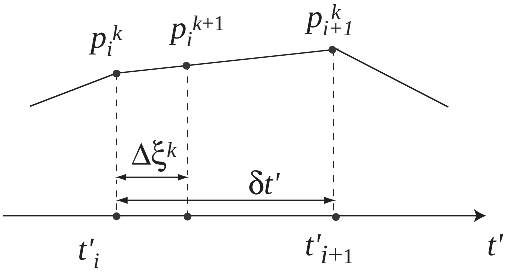

Figure 3.4: Interpolation of time waveform to realize a fractional time shift $\Delta\xi^k$.

The inclusion of the inhomogeneity term in time domain KZK code was checked by comparison to an analytical solution obtained for linear propagation of an unfocused Gaussian beam through a medium that has a parabolic sound speed variation in the transverse direction, i.e., $c'(\mathbf{r}, z) \propto r^2$. This medium creates a waveguide that periodically modulates the beam pattern and its axial amplitude along the propagation direction. Figure 3.5 shows the comparison of the analytical axial pressure[68] with the computation result using the KZK code for Eqn. (3.33) with $\delta = 0$ and $\beta = 0$. The close agreement between the analytical result and the computations verifies the algorithm for solving the KZK code with inclusion of the inhomogeneity term. In Chap. 5 this code is used to model beam propagation through an extended inhomogeneous medium.

3.4 Summary

The integral solutions, Eqns. (3.9) and (3.12), derived in this chapter form the starting point for the derivation of statistical perturbation solutions in Chap. 4. The analytical results are compared to the numerical realizations based on angular spectrum method. Since the angular spectrum method includes full diffraction, it is valid for cases in which scattering from inhomogeneities is strong, and

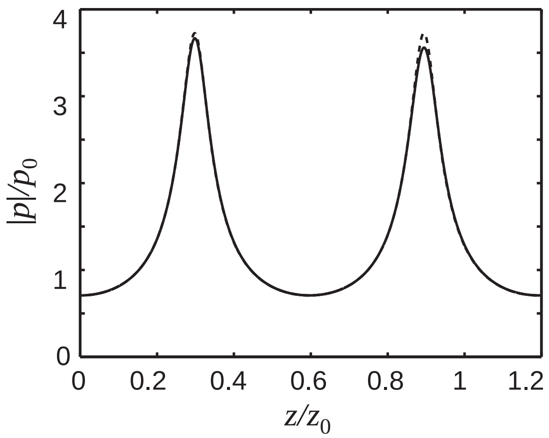

Figure 3.5: Analytical (dashed line) and computational (solid line) axial pressures amplitude for Gaussian beam propagation through a medium that has a parabolic sound speed variation in the transverse plane.

therefore it can be used to assess the accuracy of the statistical perturbation solutions derived under conditions of weak scattering. The KZK code which includes 3D sound speed variations lays the ground work for analysis of scattering due to an extended inhomogeneous medium. This analysis is important for assessing the phase screen approximation that we use throughout the dissertation.

Chapter 4

Statistical solution for scattering of a Gaussian beam by a phase screen

In this chapter we employ a phase screen model and the field integrals in Sec. 3.1 to develop a statistical model for second-harmonic generation in a sound beam that propagates through an inhomogeneous layer. Of particular interest is the expected value of the intensity beam pattern after propagation through a thin layer just in front of the source transducer. This result is applicable to tissue harmonic imaging, the geometry for which is depicted in Fig. 4.1(a). The body wall layer adjacent to the transducer is modeled by the phase screen depicted in Fig. 4.1(b). The function $\phi(\mathbf{r})$ that characterizes the screen is defined in Eqn. (2.33). Its variation in the x-y plane is illustrated with the gray scale in Fig. 4.1(c), and its statistics shall be described by its variance σ and spatial correlation length l, with a zero mean. These statistics may be obtained, for example, from the measurements provided by Hinkelman et al.[22] Except for the phase screen, the remainder of the propagation path is assumed to be in a homogeneous medium.

Our theoretical model is similar to the classical phase screen method described in Sec. 2.4, except that it is simplified to only one screen. The method for determining the scattered component of the second-harmonic field is similar to the method used in the Born approximation. Under the weak scattering assumption ($|\phi(\mathbf{r})| \ll 1$), the total field separates into a coherent component and a scattered component. The terms associated with scattering can be written as integrals involving $\phi(\mathbf{r})$. Based on this model we can derive the ensemble averaged second-harmonic intensity (second moments) as a function of the statistics of $\phi(\mathbf{r})$ for a source with a Gaussian amplitude profile. This derivation is carried out in Sec. 4.1. From the statistical solutions, the evolution of the scattered second-harmonic beam profile, and its change in energy content along the prop-

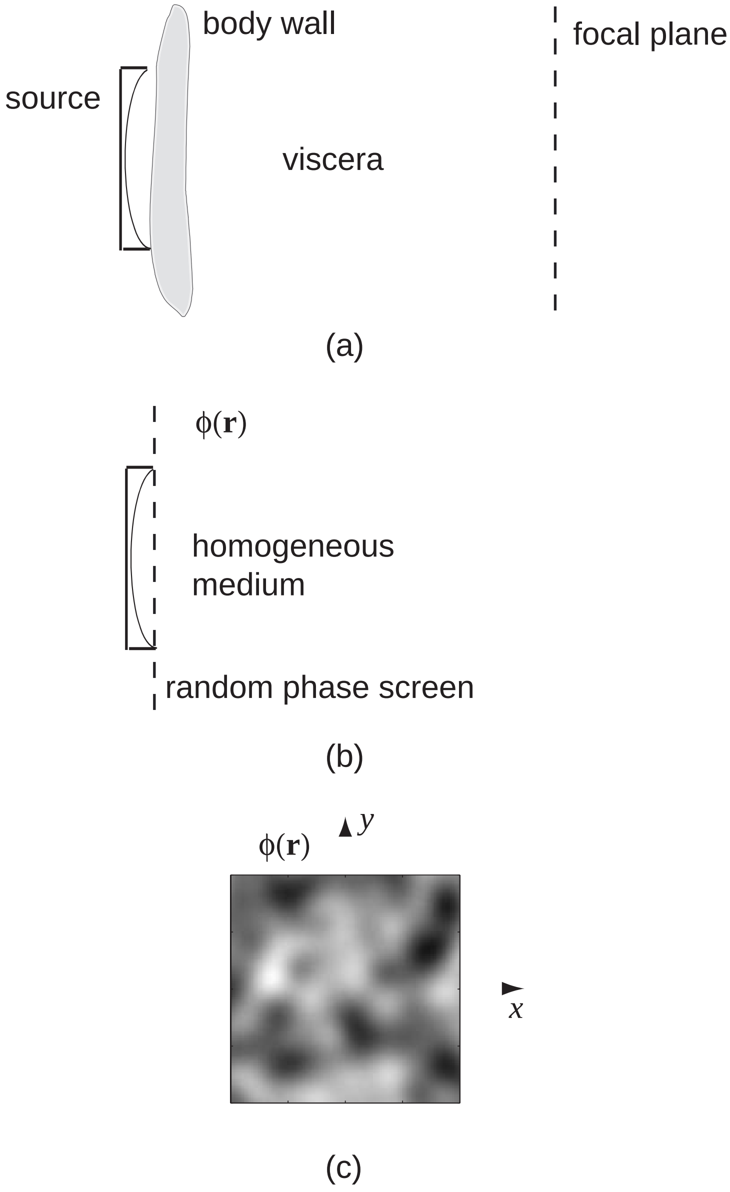

Figure 4.1: Single phase screen model for analysis of nonlinear propagation through a body wall layer.

agation axis, can be analyzed.

In Sec. 4.2 the derived solutions are simplified by evaluating them in the focal plane. Statistical properties of the beam intensity are discussed in this section. In Sec. 4.3 the focused beam solutions are compared with direct numerical simulations to test their validity. In Sec. 4.4, following Tabei et al.,[35] we introduce a focusing quality factor to quantify the influence of the phase screen on the beam patterns. The parameter indicates the amount of energy that is scattered away from the propagation axis due to the presence of the phase screen. In Sec. 4.5 the weak scattering condition required by the statistical solution is assessed by comparing with direct numerical simulations.

The analysis in Secs. 4.1–4.5 is based on the geometry in Fig. 4.1, in which the phase screen located directly in front of the radiating transducer. In Sec. 4.6 this restriction is relaxed, and the statistical solution is generalized to account for a phase screen positioned an arbitrary distance away. The cost of generalization is an increase in complexity, which involves matching individual solutions for the fields on the two sides of the phase screen. The resulting solution is used to investigate the effect of distance between source and phase screen on the expected values of the intensity beam patterns.

4.1 Statistical solutions for a Gaussian source

In this section we derive the statistical solutions for the intensities of the fundamental and second-harmonic components in a Gaussian beam with the random phase screen located directly in front of the source. In this case one may think of a random phase $\phi(\mathbf{r})$ being applied to the source itself, with the remaining propagation medium taken to be homogeneous. The source function $q_{10}(\mathbf{r})$ in Eqn. (3.8) is taken to be

$$q_{10}(\mathbf{r}) = p_0 \exp\left[-A\frac{r^2}{a^2} + jB\frac{r^2}{a^2} + j\phi(\mathbf{r})\right] , \tag{4.1}$$

where p_0 and a are the pressure amplitude and radius, respectively. The coefficients A and B account for amplitude and phase shading, specifically,

$$A = 1, \qquad B = 0, \qquad \text{unfocused beam} \tag{4.2}$$

$$A = 1, \qquad B = G, \qquad \text{focused beam} \tag{4.3}$$

where $G = ka^2/2d$ is the focusing gain, and d is the distance to the focal plane. The purpose of introducing this notation here is that for a phase screen located some distance away from the source, the coefficients A and B become coefficients that depend on this distance. Separation between the source and phase screen is considered in Sec. 4.6. Introducing A and B here facilitates that investigation.

Because of the random nature of $\phi(\mathbf{r})$, the phase of the wave front radiated by the source becomes partially incoherent. We assume that $\phi(\mathbf{r})$ obeys the following statistics:

$$\langle \phi(\mathbf{r}) \rangle = 0\,, \tag{4.4}$$

$$\langle \phi^2(\mathbf{r}) \rangle = \sigma^2\,, \tag{4.5}$$

$$C_\phi(\mathbf{r}_1, \mathbf{r}_2) = \frac{\langle \phi(\mathbf{r}_1)\phi(\mathbf{r}_2) \rangle}{\langle \phi(\mathbf{r})^2 \rangle} = \exp\left(-\frac{|\mathbf{r}_1 - \mathbf{r}_2|^2}{l^2} \right). \tag{4.6}$$

That is, $\phi(\mathbf{r})$ possesses a mean value of zero, variance σ, and Gaussian correlation function $C_\phi(\mathbf{r}_1, \mathbf{r}_2)$. The correlation length is l. Since $\phi(\mathbf{r})$ accounts for all phase fluctuations accumulated in the tissue layer, its variance can be obtained from Eqn. (2.33) using the definitions in Eqns. (2.39)–(2.41):

$$\sigma^2 = k^2 \mu^2 L \sigma_{n'}(0)\,, \tag{4.7}$$

where L is the thickness of the layer. Equations (4.4)–(4.6) identify $\phi(\mathbf{r})$ as a homogeneous, isotropic random process in space. Isotropy of the phase fluctuation caused by human body wall has been observed in experiments.[22,26]

We now seek an ensemble averaged beam intensity (or second moment) for the fundamental and second-harmonic fields, specifically,

$$\langle I_1 \rangle = \frac{\langle |q_1|^2 \rangle}{2\rho_0 c_0} = \frac{\langle q_1 q_1^* \rangle}{2\rho_0 c_0}\,, \tag{4.8}$$

$$\langle I_2 \rangle = \frac{\langle |q_2|^2 \rangle}{2\rho_0 c_0} = \frac{\langle q_2 q_2^* \rangle}{2\rho_0 c_0}\,. \tag{4.9}$$

We start with Eqn. (3.9), neglecting the absorption and dispersion coefficients. Substitution of Eqn. (3.9) into Eqn. (4.8) yields

$$\begin{aligned}\langle I_1 \rangle = & \frac{k^2}{8\pi^2 \rho_0 c_0 z^2} \int_{\mathbf{r}_1} \int_{\mathbf{r}_2} \langle q_{10}(\mathbf{r}_1) q_{10}^*(\mathbf{r}_2) \rangle \\ & \times \exp\left[-\frac{jk|\mathbf{r}-\mathbf{r}_1|^2}{2z} + \frac{jk|\mathbf{r}-\mathbf{r}_2|^2}{2z} \right] d\mathbf{r}_1 d\mathbf{r}_2 \,. \end{aligned} \tag{4.10}$$

Substitution of Eqn. (4.1) in (4.10) yields

$$\begin{aligned}\langle I_1 \rangle = & \frac{k^2 p_0^2}{4\pi^2 z^2} \int_{\mathbf{r}_1} \int_{\mathbf{r}_2} \exp\left[-\left(\frac{A - jB}{a^2} + \frac{jk}{2z} \right) r_1^2 - \left(\frac{A + jB}{a^2} - \frac{jk}{2z} \right) r_2^2 \right. \\ & \left. + \frac{jk}{z} \mathbf{r} \cdot (\mathbf{r}_1 - \mathbf{r}_2) \right] \langle \exp[j\phi(\mathbf{r}_1) - j\phi(\mathbf{r}_2)] \rangle \, d\mathbf{r}_1 d\mathbf{r}_2 \,. \end{aligned} \tag{4.11}$$

Further progress can be made analytically by supposing the phase perturbation to be small. For $|\phi| \ll 1$ and $\sigma^2 \ll 1$, the expected value in Eqn. (4.11) can be expanded in the following series:

$$\begin{aligned}\langle \exp[j\phi(\mathbf{r}_1) - j\phi(\mathbf{r}_2)] \rangle \approx \; & 1 + j\langle \phi(\mathbf{r}_1) \rangle - j\langle \phi(\mathbf{r}_2) \rangle - \frac{1}{2} \langle [\phi(\mathbf{r}_1) - \phi(\mathbf{r}_2)]^2 \rangle \\ = \; & 1 - \frac{1}{2} \langle \phi^2(\mathbf{r}_1) \rangle - \frac{1}{2} \langle \phi^2(\mathbf{r}_2) \rangle + \langle \phi(\mathbf{r}_1) \phi(\mathbf{r}_2) \rangle \\ = \; & 1 - \sigma^2 + \sigma^2 \exp\left(-\frac{|\mathbf{r}_1 - \mathbf{r}_2|^2}{l^2} \right) \,. \end{aligned} \tag{4.12}$$

Thus $\langle I_1 \rangle$ can be separated into two integrals. One integral involves $1 - \sigma^2$. This part is called the coherent field, and it yields the same beam pattern as if no phase distortion occurs. The second part involves integration of the exponential function in Eqn. (4.12). This part is the scattered term, and it broadens the beam pattern. The scattered beam radius is directly related to the correlation length l. Substitution of Eqn. (4.12) into (4.11) yields

$$\langle I_1 \rangle = (1 - \sigma^2) \, I_1^{\mathrm{coh}} + \sigma^2 \, I_1^{\mathrm{sc}} \,, \tag{4.13}$$

where

$$I_1^{\mathrm{coh}} = \frac{p_0^2 k^2 a^4 / 8\rho_0 c_0 z^2}{A^2 + (B - ka^2/2z)^2} \exp\left[-\frac{(Ak^2 a^4 / 2z^2)(r^2/a^2)}{A^2 + (B - ka^2/2z)^2} \right] , \tag{4.14}$$

$$I_1^{\mathrm{sc}} = \frac{p_0^2 k^2 a^4 / 8\rho_0 c_0 z^2}{A^2 + (B - ka^2/2z)^2 + 2A\nu^2} \exp\left[-\frac{(Ak^2 a^4 / 2z^2)(r^2/a^2)}{A^2 + (B - ka^2/2z)^2 + 2A\nu^2} \right] . \tag{4.15}$$

We note the new parameter

$$\nu = a/l \tag{4.16}$$

that appears in Eqn. (4.15). The ratio of source radius to phase correlation length is the dimensionless quantity that characterizes the effect of inhomogeneity.

For $\nu = 0$, Eqns. (4.14) and (4.15) reveal that $I_1^{\mathrm{sc}} = I_1^{\mathrm{coh}}$, and therefore $\langle I_1 \rangle = I_1^{\mathrm{coh}}$ from Eqn. (4.13). The quantity I_1^{coh} corresponds to the intensity field that would be observed in the absence of the phase screen, and hence it is referred to as the coherent field. Its coefficient $(1 - \sigma^2)$ accounts for energy loss from the coherent field to the scattered field, represented by I_1^{sc}. The total energy is conserved in Eqn. (4.13), as shown by integrating the intensity across the beam:

$$\int_0^\infty \langle I_1(r,z) \rangle 2\pi r dr = \frac{\pi a^2 p_0^2}{4A\rho_0 c_0} \,. \tag{4.17}$$

The energy in the beam is thus independent of distance from the source. From Eqns. (4.14) and (4.15) we see that both the coherent and the scattered beam have a Gaussian profile in the transverse plane. The width of the scattered beam is greater than that of the coherent beam. The larger the value of ν is, the wider will be the scattered beam. Larger ν corresponds to smaller l, meaning that the phase is less coherent in space, which results in broadening of the beam.

The same expansion of the intensity as in Eqns. (4.13)–(4.15) has appeared in the work of Clarke[69] on propagation of a Gaussian laser beam through a turbulent atmosphere. No phase screen approximation is made in his analysis, and the entire space between the source and receiver is occupied by the randomly inhomogeneous medium. The beam was unfocused, which corresponds to setting $A = 1$ and $B = 0$ in our equations. In place of Eqn. (4.13), his expression for the mean intensity is his Eqn. (47):[69]

$$\langle I \rangle = e^{-\sigma^2} I_0 + I_s \,. \tag{4.18}$$

Here, σ is again the variance of the phase fluctuations in the medium, as given by Eqn. (4.7) but now with L being the total path length from source to receiver. The quantity I_0 is the intensity of the coherent field. In our notation, it is equivalent to Eqn. (4.14) with $A = 1$ and $B = 0$. The mean scattered intensity I_s obtained by Clarke is given by[69]

$$I_s = \frac{k^2a^2p_0^2}{8\pi z^2}e^{-\sigma^2}\int_{-\infty}^{\infty}\!\!\int_{-\infty}^{\infty}\exp\left[-\left(\frac{1}{2a^2}+\frac{k^2a^2}{8z^2}\right)(\xi^2+\eta^2)+\frac{jk(\xi x+\eta y)}{z}\right] \times\{\exp[\sigma^2C_\phi(\xi,\eta)]-1\}d\xi d\eta \tag{4.19}$$

when expressed using our notation, where C_ϕ is the phase correlation function in Eqn. (4.6). In contrast with our analysis, the coherent and scattered intensities in Clarke's analysis may be of the same order. When the path length L is short enough to make $\sigma^2 \ll 1$, expansion of the exponential in Eqn. (4.18) yields

$$\langle I\rangle = (1-\sigma^2)I_0 + I_s\,, \tag{4.20}$$

and the corresponding expansions in Eqn. (4.19) give[69]

$$I_s = \frac{\sigma^2k^2a^2p_0^2}{8\pi z^2}\int_{-\infty}^{\infty}\!\!\int_{-\infty}^{\infty}\exp\left[-\left(\frac{1}{2a^2}+\frac{k^2a^2}{8z^2}\right)(\xi^2+\eta^2)+\frac{jk(\xi x+\eta y)}{z}\right]C_\phi(\xi,\eta)d\xi d\eta\,. \tag{4.21}$$

If a Gaussian correlation function is assumed for $C_\phi(\xi,\eta)$ as in Eqn. (4.6), Eqns. (4.20) and (4.21) become equivalent to Eqns. (4.13) and (4.15) with $A = 1$ and $B = 0$. Our result is thus the limiting form of Clarke's result for a layer that is sufficiently thin, or a phase perturbation that is sufficiently weak, that $\sigma^2 \ll 1$. In this limit, the mean intensity of the scattered radiation is a small correction to the intensity of the coherent radiation.

To obtain the solution for the second-harmonic intensity $\langle I_2\rangle$, we begin by substituting Eqn. (3.12) into Eqn. (4.9) to obtain

$$\begin{aligned}\langle I_2\rangle = {}& \frac{k^6\beta^2}{128\pi^4\rho_0^3c_0^5z^2}\int_{\mathbf{r}_{c1}}\int_{\mathbf{r}_{d1}}\int_{\mathbf{r}_{c2}}\int_{\mathbf{r}_{d2}}E_1\left(\frac{jkr_{d1}^2}{4z}\right)E_1\left(-\frac{jkr_{d2}^2}{4z}\right)\\ &\times\left\langle q_{10}\left(\mathbf{r}_{c1}+\frac{\mathbf{r}_{d1}}{2}\right)q_{10}\left(\mathbf{r}_{c1}-\frac{\mathbf{r}_{d1}}{2}\right)q_{10}^*\left(\mathbf{r}_{c2}+\frac{\mathbf{r}_{d2}}{2}\right)q_{10}^*\left(\mathbf{r}_{c2}-\frac{\mathbf{r}_{d2}}{2}\right)\right\rangle\\ &\times\exp\left[\frac{-jk(r_{c1}^2-r_{c2}^2)+2jk\mathbf{r}\cdot(\mathbf{r}_{c1}-\mathbf{r}_{c2})}{z}\right]d\mathbf{r}_{c1}d\mathbf{r}_{d1}d\mathbf{r}_{c2}d\mathbf{r}_{d2}\,,\end{aligned} \tag{4.22}$$

which requires integration over the fourth-order moment of the source function. Substitution of Eqn. (4.1) in (4.22) yields an expression for what is formally a ten-dimensional integral, counting two-dimensions for each vector and recalling the definition of the exponential integral E_1 in Eqn. (3.13). An expansion similar to that in Eqn. (4.12) is used again to permit integration over the phase ϕ. Even with this substitution, we have so far been unable to evaluate every integral.

As shown in App. B, the assumption of small ϕ and σ^2, followed by extensive manipulation, permits Eqn. (4.22) to be expressed as

$$\langle I_2 \rangle = (1 - 2\sigma^2) I_2^{\mathrm{coh1}} - \sigma^2 I_2^{\mathrm{coh2}} + \sigma^2 I_2^{\mathrm{sc}} \,, \tag{4.23}$$

where

$$\begin{aligned}
I_2^{\mathrm{coh1}} &= \frac{k^6 \beta^2 p_0^4 a^8}{128 \rho_0^3 c_0^5 z^2} \frac{1}{A^2 + (B - ka^2/2z)^2} \exp\left[-\frac{(Ak^2 a^4/z^2)(r/a)^2}{A^2 + (B - ka^2/2z)^2} \right] \\
&\quad \times \frac{|\ln[1 - j2z(A - jB)/ka^2]|^2}{A^2 + B^2} \,, && (4.24) \\
I_2^{\mathrm{coh2}} &= \frac{k^6 \beta^2 p_0^4 a^8}{64 \rho_0^3 c_0^5 z^2} \frac{1}{A^2 + (B - ka^2/2z)^2} \exp\left[-\frac{(Ak^2 a^4/z^2)(r/a)^2}{A^2 + (B - ka^2/2z)^2} \right] \\
&\quad \times \mathrm{Re} \left\{ \frac{\ln[1 - j2z(A - jB + 2\nu^2)/ka^2] \, \ln[1 + j2z(A + jB)/ka^2]}{(A - jB + 2\nu^2)(A + jB)} \right\} \,, \\
& && (4.25) \\
I_2^{\mathrm{sc}} &= \frac{k^6 \beta^2 p_0^4 a^8}{32 \rho_0^3 c_0^5 z^2} \exp\left[-\frac{(Ak^2 a^4/z^2)(r^2/a^2)}{A^2 + (B - ka^2/2z)^2} \right] \\
&\quad \times \int_1^\infty \int_1^\infty \frac{dt_1 dt_2}{t_1 t_2 \eta_1 \eta_2 M(t_1, t_2)} \exp\left\{ \frac{(\nu^2 A^2 k^2 a^4/z^2)(r^2/a^2)}{M(t_1, t_2) \left[A^2 + (B - ka^2/2z)^2 \right]} \right\} && (4.26)
\end{aligned}$$

In Eqn. (4.26), we have defined

$$M(t_1, t_2) = \left[A^2 + \left(B - ka^2/2z \right)^2 \right] \left[\frac{\nu^2}{2} \left(\frac{1}{\eta_1} + \frac{1}{\eta_2} \right) + 1 \right] + A\nu^2 \,, \tag{4.27}$$

$$\eta_1(t_1) = A - jB + \frac{jka^2 t_1}{2z} \,, \qquad \eta_2(t_2) = A + jB - \frac{jka^2 t_2}{2z} \,. \tag{4.28}$$

A two-dimensional integral thus remains in the expression for I_2^{sc}. Each of the three components I_2^{coh1}, I_2^{coh2}, and I_2^{sc} is a real and positive function. The total field $\langle I_2 \rangle$ is the combination of Eqns. (4.23)–(4.28).

To interpret the components we consider first the limit $\nu \to 0$, for which

$$I_2^{\mathrm{coh2}} = 2 I_2^{\mathrm{coh1}} \,, \qquad I_2^{\mathrm{sc}} = 4 I_2^{\mathrm{coh1}} \,, \tag{4.29}$$

and thus

$$\langle I_2 \rangle = I_2^{\text{coh1}} \,. \tag{4.30}$$

For this reason we label the first component I_2^{coh1}, because it is the second-harmonic intensity field in the absence of a phase screen. This notation is consistent with that used for the intensity of the primary beam, Eqn. (4.13). The terms I_1^{coh} and I_2^{coh1} do not depend on ν and σ. Unlike Eqn. (4.13), however, Eqn. (4.23) contains a second term associated with the coherent field, labeled I_2^{coh2}. Comparison of Eqns. (4.25) and (4.24) reveals that I_2^{coh2} and I_2^{coh1} exhibit the same dependence on r and thus describe the same radiation pattern at any distance from the source. The integral of $\sigma^2(2I_2^{\text{coh1}} + I_2^{\text{coh2}})$ across the beam is therefore the energy that is removed from the field that would have existed in the absence of the phase screen. However, it does not equal the integral of $\sigma^2 I_2^{\text{sc}}$ across the beam. That is, there is no simple energy conservation law relating the coherent and scattered components, as there is in the primary field. Energy considerations are discussed in greater detail in Sec. 4.2.

The main focus shall be on the scattering term I_2^{sc}. The 2D integrals must be performed numerically. The integrand decays with increasing t_1 or t_2, and therefore the upper limits t_1 and t_2 can be approximated by $t_{\max}$, with $t_{\max} \gg 1$. The integral converges as $t_{\max} \to \infty$. The solution I_2^{sc} changes the beam pattern of the second harmonic due to scattering. The exponential term outside the integral describes the transverse beam profile in the absence of the phase screen. This is the same exponential that appears in I_2^{coh1} and I_2^{coh2}. The integral accounts for the beam broadening due to scattering. Numerical calculation shows that the scattered beam does not possess a Gaussian profile in the transverse plane. This is different from the case of linear scattering, where the scattered beam always possesses a Gaussian shape. The shape of the scattered beam for the second harmonic has no analytical expression.

We may also compare with the simple phase screen results presented in Sec. 2.4. To obtain the plane wave limit, we first set $A = 1$ and $B = 0$ according to Eqn. (4.2) to eliminate focusing in the beam, and then set $a \to \infty$. For propagation distances $z \ll kl^2$, where it is valid to ignore the diffraction, the solution of $\langle I_2\rangle$ reduces to Eqn. (2.53).

In the next section, the solution for $\langle I_2\rangle$ is evaluated for the case of a focused Gaussian beam. For simplicity, the focal plane is taken as the target plane.

4.2 Focused Gaussian source

For a focused Gaussian source, we set $A = 1$ and $B = G$ as given in Eqn. (4.3). The propagation distance z is normalized by focal distance, $\zeta = z/d$, and the transverse radial coordinate is normalized by source radius, $\rho = r/a$. Substituting these parameters into Eqns. (4.13)–(4.15) and Eqns. (4.23)–(4.28), we arrive at

$$\begin{aligned}\langle I_1\rangle = {} & \frac{(1-\sigma^2)G^2p_0^2/2\rho_0c_0}{\zeta^2+G^2(\zeta-1)^2}\exp\left[-\frac{2G^2\rho^2}{\zeta^2+G^2(\zeta-1)^2}\right] \\ & + \frac{\sigma^2G^2p_0^2/2\rho_0c_0}{(1+2\nu^2)\zeta^2+G^2(\zeta-1)^2}\exp\left[-\frac{2G^2\rho^2}{(1+2\nu^2)\zeta^2+G^2(\zeta-1)^2}\right],\end{aligned} \tag{4.31}$$

and

$$\begin{aligned}\langle I_2\rangle = {} & \frac{G^2P_2^2/2\rho_0c_0}{\zeta^2+G^2(\zeta-1)^2}\exp\left[-\frac{4G^2\rho^2}{\zeta^2+G^2(\zeta-1)^2}\right]\left\{\frac{(1-2\sigma^2)|\ln[1-(1+j/G)\zeta]|^2}{(1+G^2)}\right. \\ & \left. -2\sigma^2\,\mathrm{Re}\left[\frac{\ln[1-j\zeta(1-jG+2\nu^2)/G]\,\ln[1+j\zeta(1+jG)/G]}{(1+2\nu^2-jG)(1+jG)}\right]\right\} \\ & + \frac{4\sigma^2G^2P_2^2}{2\rho_0c_0\zeta^2}\exp\left[-\frac{4G^2\rho^2}{\zeta^2+G^2(\zeta-1)^2}\right]\int_1^\infty\int_1^\infty \chi(\rho,\zeta,t_1,t_2,\nu)dt_1dt_2\,, \qquad (4.32)\end{aligned} \tag{4.33}$$

where

$$\chi = \frac{1}{t_1t_2\eta_1\eta_2M(t_1,t_2)}\exp\left\{\frac{4G^2\nu^2\rho^2}{M(t_1,t_2)\,[\zeta^2+G^2(\zeta-1)^2]}\right\}, \tag{4.34}$$

$$M = \left[1+G^2\left(1-\frac{1}{\zeta}\right)^2\right]\left[\frac{\nu^2}{2}\left(\frac{1}{\eta_1}+\frac{1}{\eta_2}\right)+1\right]+\nu^2\,, \tag{4.35}$$

$$\eta_1 = 1-jG+\frac{jGt_1}{\zeta}\,, \qquad \eta_2 = 1+jG-\frac{jGt_2}{\zeta}\,. \tag{4.36}$$

and $P_2 = \beta p_0^2 k^2 a^2 / 4\rho_0 c_0^2$. Special interest in this case is the beam pattern in the focal plane, where $\zeta = 1$. Equations (4.31) and (4.32) become

$$\langle I_1\rangle = (1-\sigma^2)\frac{G^2 p_0^2}{2\rho_0 c_0}\exp(-2G^2\rho^2) + \frac{\sigma^2 G^2 p_0^2}{2\rho_0 c_0(1+2\nu^2)}\exp\left(-\frac{2G^2\rho^2}{1+2\nu^2}\right), \quad (4.37)$$

and

$$\begin{aligned}\langle I_2\rangle = {}& \frac{P_2^2}{2\rho_0 c_0}\exp(-4G^2\rho^2)\Bigg\{(1-2\sigma^2)\left[\frac{\ln(-j/G)\ln(j/G)}{(1+G^2)/G^2}\right] \\ & -2\sigma^2\,\mathrm{Re}\left[\frac{\ln[(-j-2j\nu^2)/G]\,\ln(j/G)}{(1+2\nu^2-jG)(1+jG)/G^2}\right]\Bigg\} \\ & +4\sigma^2\frac{G^2{P_2}^2}{2\rho_0 c_0}\exp(-4G^2\rho^2)\int_1^\infty\int_1^\infty \chi(\rho,1,t_1,t_2,\nu)dt_1 dt_2\,, \quad (4.38)\end{aligned}$$

respectively, with

$$\begin{aligned}\chi &= \frac{1}{t_1 t_2 \eta_1 \eta_2 M(t_1,t_2)}\exp\left[\frac{4G^2\nu^2\rho^2}{M(t_1,t_2)}\right], \\ M &= \frac{\nu^2}{2}\left(\frac{1}{\eta_1}+\frac{1}{\eta_2}\right)+1+\nu^2\,, \\ \eta_1 &= 1-jG+jGt_1\,, \qquad \eta_2 = 1+jG-jGt_2\,.\end{aligned}$$

Numerical evaluation of the integral in Eqn. (**??**) is performed by choosing an upper limit $t_{\max} = 400$ for t_1 and t_2. This upper limit provides sufficient accuracy. Equations (4.37) and (4.38) show that with fixed G, the scattered beam profiles for the fundamental and second harmonic depend only on ν. This dependence is shown in Fig. 4.2. The value $\nu = 0$ represents the beam pattern in the absence of a phase screen. The focal gain of the source is chosen to be $G = 10$. The scattered beam patterns for linear propagation at twice the source frequency are also included for comparison. This comparison emphasizes the difference between the second harmonic generated nonlinearly by a beam with frequency f, and linear radiation from the same source and under the same conditions at frequency $2f$. Double the source frequency results in double the focal gain, keeping the focal length the same. For example, if the focusing gain is chosen to be $G = 10$ at frequency f, the value of the gain is 20 for linear

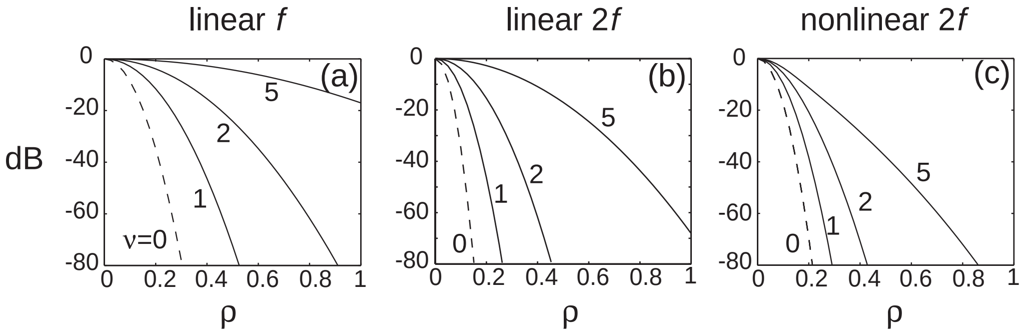

Figure 4.2: Normalized focal beam patterns for the scattered field of (a) linear f, (b) linear $2f$, (c) nonlinear $2f$ beams as a function of ν ($G = 10$ for linear f beam).

radiation at frequency $2f$. Also, from Eqn. (2.33) one can see that the phase change doubles at frequency $2f$. The scattered beam pattern associated with the linear radiation at frequency $2f$ can be obtained from the last term in Eqn. (4.37) by setting $G = 20$ and doubling the variance σ. In the following discussion, the fundamental component with source frequency f is called the "linear f" beam, the nonlinearly generated second harmonic is called the "nonlinear $2f$" beam, and the linear second-harmonic component with source frequency $2f$ is called the "linear $2f$" beam. All scattered beam profiles in Fig. 4.2 are normalized to their on-axis value and are plotted in the same dynamic range, from 0 to -80 dB.

From Fig. 4.2 we can see that for the same value of ν, the scattered beams are narrower for the linear $2f$ and nonlinear $2f$ beams than for the linear f beam. The shorter wavelength at frequency $2f$ accounts for their narrower beam width. For small ν ($\nu = 1, 2$), the scattered beam width is roughly the same for the linear $2f$ and nonlinear $2f$ beams. When ν becomes large ($\nu = 5$), the linear $2f$ beam has a larger scattered beam width than the nonlinear $2f$ beam.

Whereas I_2^{coh1} and I_2^{coh2} have Gaussian beam profiles, I_2^{sc} depends on the integral in Eqn. (4.38). To assess the extent to which the profile of I_2^{sc} deviates from Gaussian we introduce the following shape factor for the scattered beam:

$$C_2^{\mathrm{sc}}(\rho) = -\frac{1}{4G^2\rho^2}\ln\left[\frac{I_2^{\mathrm{sc}}(\rho)}{I_2^{\mathrm{sc}}(0)}\right] . \tag{4.39}$$

For beam profiles given by $\exp(-4G^2\rho^2)$ as exhibited by the expressions for I_2^{coh1} and I_2^{coh2}, one would obtain C_2^{coh1}=C_2^{coh2}=1, a constant. The variation of C_2^{sc} with ρ thus indicates the extent to which I_2^{sc} deviates from $\exp(-4G^2\rho^2)$. Curves for C_2^{sc} are plotted in Fig. 4.3(a) for different ν. For fixed ν, C_2^{sc} decreases as ρ increases. Observe first that the smaller the shape factor, the wider the beam. Deviation from a Gaussian profile is determined by the derivative of C_2^{sc}, shown in Fig. 4.3(b). It is seen that the deviation from Gaussian occurs near the axis, and it increases with ν.

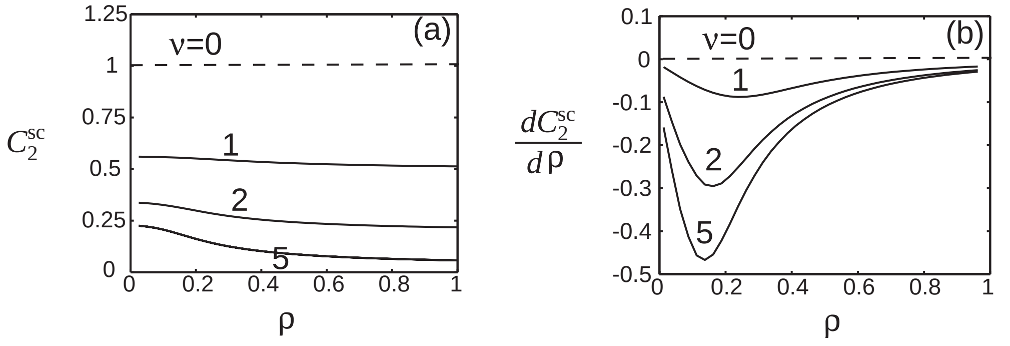

Figure 4.3: The shape factor C_2^{sc} (a) and its derivative (b) for second-harmonic scattering with different values of ν.

We now consider axial propagation curves as functions of both ν and σ. In Fig. 4.4 the axial curves for the scattered field I_n^{sc} (dashed lines) and the total field $\langle I_n \rangle$ (solid lines) are plotted for the fundamental ($n = 1$) and second harmonic ($n = 2$) for different values of σ and ν. The increase in scattering with increasing σ is readily seen from this figure. In all of the plots the axial curves are normalized to the maximum value of the total field. The focal plane is at $\zeta = 1$.

From Fig. 4.4 we see that the scattered fields increase with σ for both the fundamental and second harmonic, with the second harmonic exhibiting stronger

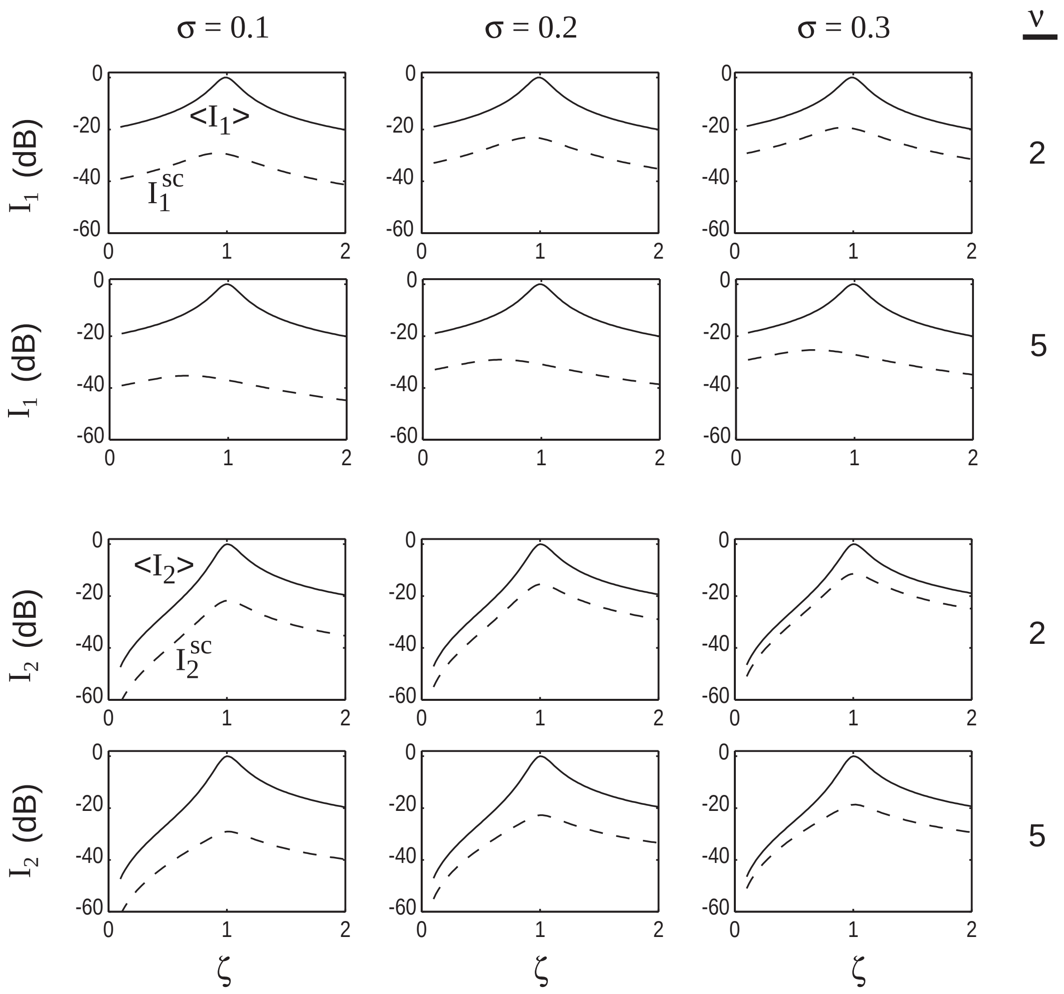

Figure 4.4: Comparison of axial intensity of the total field $\langle I_n \rangle$ (solid lines) with contribution due to the scattered field I_n^{sc} (dashed lines) for the fundamental (first two rows) and second harmonic (second two rows), for a focused Gaussian beam with gain $G = 10$, and for different combinations of the statistical parameters of the phase screen: $\sigma = 0.1, 0.2, 0.3$ (organized by columns) and $\nu = 2, 5$ (organized by rows).

dependence than the fundamental. For the second harmonic, the total and scattered axial fields are much less in the pre-focal region compared to the fundamental since there is little nonlinear generation in this region. It is also apparent from this figure that for fixed σ, the second harmonic seems to possess higher axial scattered pressure relative to the total axial pressure in comparison with the fundamental. However, this does not mean that second-harmonic scattering is strong. As will be shown later, it indicates that the scattered field tends to concentrate more along the beam axis for the second harmonic than for the fundamental. This is consistent with observations of the linear field. For example, for fixed σ, the scattered energy stays the same for different ν, but for $\nu = 2$, the axial intensity of the scattered field is larger than for $\nu = 5$. This is because for $\nu = 5$ the scattered field tends to spread out more in the transverse plane, and hence decrease its axial field amplitude. For the same reason, the scattered axial intensity for $\nu = 2$ is higer than for $\nu = 5$ of the second harmonic field.

Another observation of Fig. 4.4 is that there is almost no change in the total field with respect to σ and ν. Since the scattered field is a small perturbation, its effect on the total field is insignificant on a dB scale. The total field is nevertheless shown in each figure to provide a point of reference. However, the axial distribution of the scattered field is quite different for different ν. For the second harmonic, the maximum amplitude in the scattered field is at the focus. Since the generation and scattering of the second harmonic occurs in a region bounded by the fundamental beam, and they are approximately proportional to the fundamental amplitude squared, their amplitudes increase toward the focus. Both the total and scattered fields of the second harmonic are strongest in the focal region. For the fundamental, we can see that the maximum scattered pressure occurs before the focus, especially for $\nu = 5$. When the scattered field propagates along ζ axis, diffraction due to the phase aberration $\phi(\mathbf{r})$ tends to broaden the beam pattern and cause the axial pressure to decrease. Although diffraction due to the coherent part of the phase Gr^2/a^2 tends to focus the scattered field (i.e., increase the axial pressure), this effect is weakened by the incoherent phase aberration. The aberration causes defocusing of the scattered field. This competition between focusing and spreading causes the maximum pressure along the axis to occur before the focus. For strong aberration (large ν, small l), the initial phase front is less coherent in space, spreading is stronger than focusing, so the maximum in the scattered field moves closer to the source plane.

Evolution of the beam profiles along the propagation axis calculated using Eqns. (4.31) and (4.32) is shown in Fig. 4.5 for $\nu = 5$ and $\sigma = 0.2$. Again, total intensity fields are represented by solid lines, scattered fields by dashed lines. Figure 4.5 shows that at all distances the linear f beam has the largest scattered beam width, and the nonlinear $2f$ beam has the smallest scattered beam width. The scattered linear $2f$ beam falls in between. In addition, the scattered fields for the $2f$ beams have higher amplitudes than for the f beam. By comparison, the nonlinear scattered beam is concentrated more along the axis than the linear scattered beam. Its reduced scattered field off axis reduces unwanted artifacts during diagnostic imaging. At the same time, transverse resolution is improved by the smaller beam width of the total field.

The energy in the coherent, scattered and total field components can be obtained by integrating elements of Eqns. (4.13) and (4.23) across the beam, as was done in Eqn. (4.17) to calculate the total energy in the fundamental. One thus obtains the energy of the coherent field for the nth harmonic, denoted by E_n^{coh}, the energy of the scattered field, denoted by E_n^{sc}, and the total energy, denoted by E_n^{tot}, which is the sum of E_n^{coh} and E_n^{sc}. For the fundamental these energies are found to be

$$E_1^{\mathrm{coh}} = (1-\sigma^2)\frac{\pi a^2 p_0^2}{4\rho_0 c_0}\,, \qquad E_1^{\mathrm{sc}} = \sigma^2 \frac{\pi a^2 p_0^2}{4\rho_0 c_0}\,, \tag{4.40}$$

and thus

$$E_1^{\mathrm{tot}} = E_1^{\mathrm{coh}} + E_1^{\mathrm{sc}} = \frac{\pi a^2 p_0^2}{4\rho_0 c_0}. \tag{4.41}$$

The total energy E_1^{tot}, equivalent to Eqn. (4.17) with $A = 1$, is a constant. It is independent of ν and σ, and is equal to the energy at the source. The total energy is unaffected by ν and σ because the aberration plane in front of the source alters only the phase, such that the energy is not affected by it. The

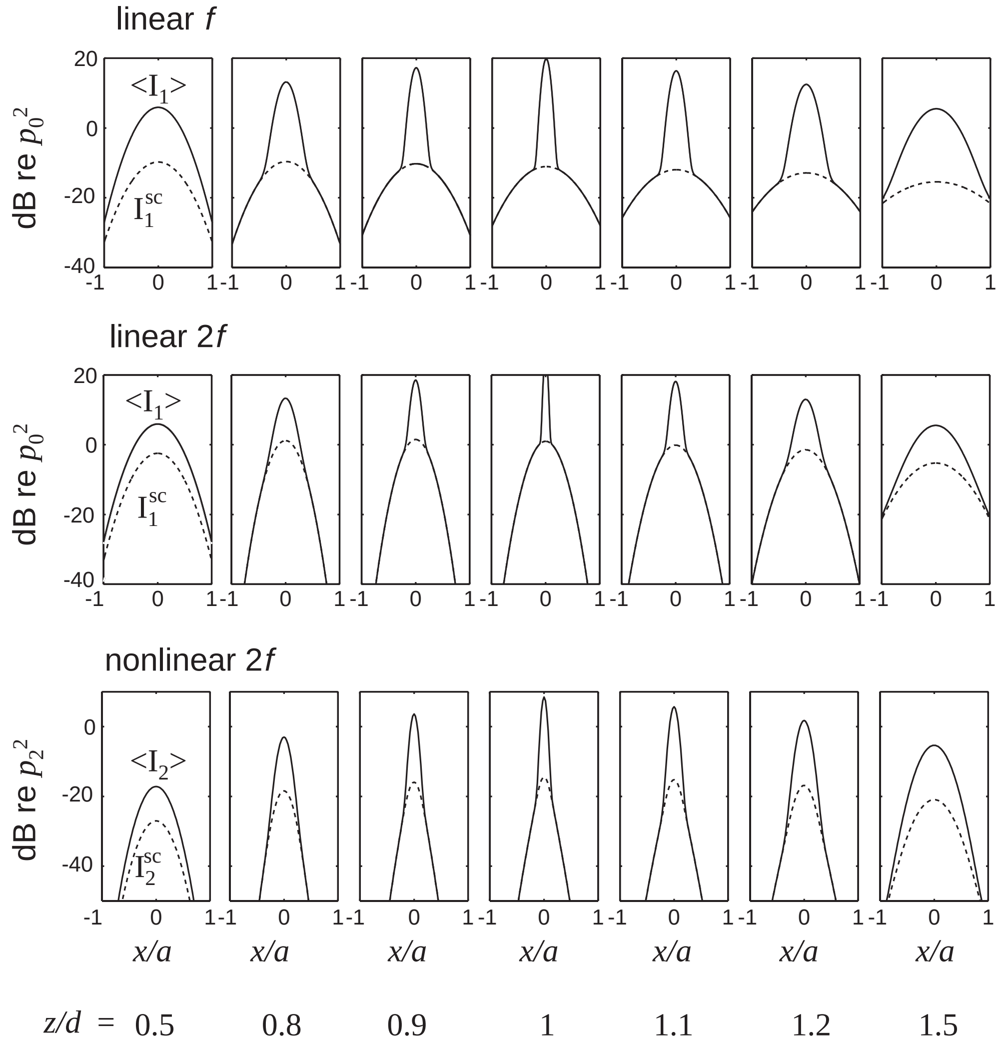

Figure 4.5: Evolution of scattered fields (dashed lines) and total fields (solid lines) for a focused Gaussian beam with $G = 10$ and a phase screen parameters $\nu = 5$ and $\sigma = 0.2$. The axisymmetric beam pattern is represented by its 1D beam profile along x direction.

variance σ alters the relative levels of $E_1^{\rm coh}$ and $E_1^{\rm sc}$, and ν alters the distribution of these energies in the transverse plane. However, ν does not change the values of $E_1^{\rm coh}$ and $E_1^{\rm sc}$.

For the second harmonic one obtains, from Eqns. (4.23) and (4.32),

$$E_2^{\rm tot} = E_2^{\rm coh1} + E_2^{\rm coh2} + E_2^{\rm sc}\,, \tag{4.42}$$

where

$$E_2^{\rm coh1} = (1-2\sigma^2)\frac{\pi a^2 P_2^2}{8\rho_0 c_0}\frac{|\ln[1-(1+j/G)\zeta]|^2}{1+G^2}\,, \tag{4.43}$$

$$E_2^{\rm coh2} = \frac{\sigma^2\pi a^2 P_2^2}{4\rho_0 c_0}{\rm Re}\left\{\frac{\ln[1-j\zeta(1-jG+2\nu^2)/G]\ln[1+j\zeta(1+jG)/G]}{(-1-2\nu^2+jG)(1+jG)}\right\}\,, \tag{4.44}$$

$$E_2^{\rm sc} = \frac{\sigma^2\pi a^2 P_2^2}{2\rho_0 c_0}\int_1^\infty\!\!\int_1^\infty \frac{dt_1 dt_2/t_1 t_2}{\nu^2[1+jG(t_1-t_2)/2\zeta]+(1-jG+jGt_1/\zeta)(1+jG-jGt_2/\zeta)}\,. \tag{4.45}$$

In contrast to $E_1^{\rm tot}$, $E_2^{\rm tot}$ is not a constant. It depends on ν and σ, i.e., the phase perturbation at the source affects nonlinear generation of the second harmonic. This is different from the result given by Eqn. (2.53) for propagation in one dimension without diffraction, where energy in the second harmonic is unaffected by the random phase screen. The reason for the difference is that even though the random phase screen does not change the energy in the fundamental beam, it does change its spatial distribution. Since the second harmonic is generated throughout the region occupied by the fundamental beam, the spatial distribution of the fundamental will affect the total energy in the second harmonic. Therefore $E_2^{\rm tot}$ depends on all parameters, i.e., ζ, σ, ν, and G. Similarly $E_2^{\rm coh1}$, $E_2^{\rm coh2}$, and $E_2^{\rm sc}$ also depend on each of these parameters.

Figure 4.6 shows the dependence of $E_2^{\rm coh}$, $E_2^{\rm sc}$ and $E_2^{\rm tot}$ on ζ for different values ν and σ, where we have defined the total coherent field by

$$E_2^{\rm coh} = E_2^{\rm coh1} + E_2^{\rm coh2}\,. \tag{4.46}$$

In Fig. 4.6, all energies are normalized by the reference energy $\pi a^2 P_2^2/4\rho_0 c_0$. From this figure we can see that $E_2^{\rm coh}$, $E_2^{\rm sc}$ and $E_2^{\rm tot}$ grow in the prefocal region,

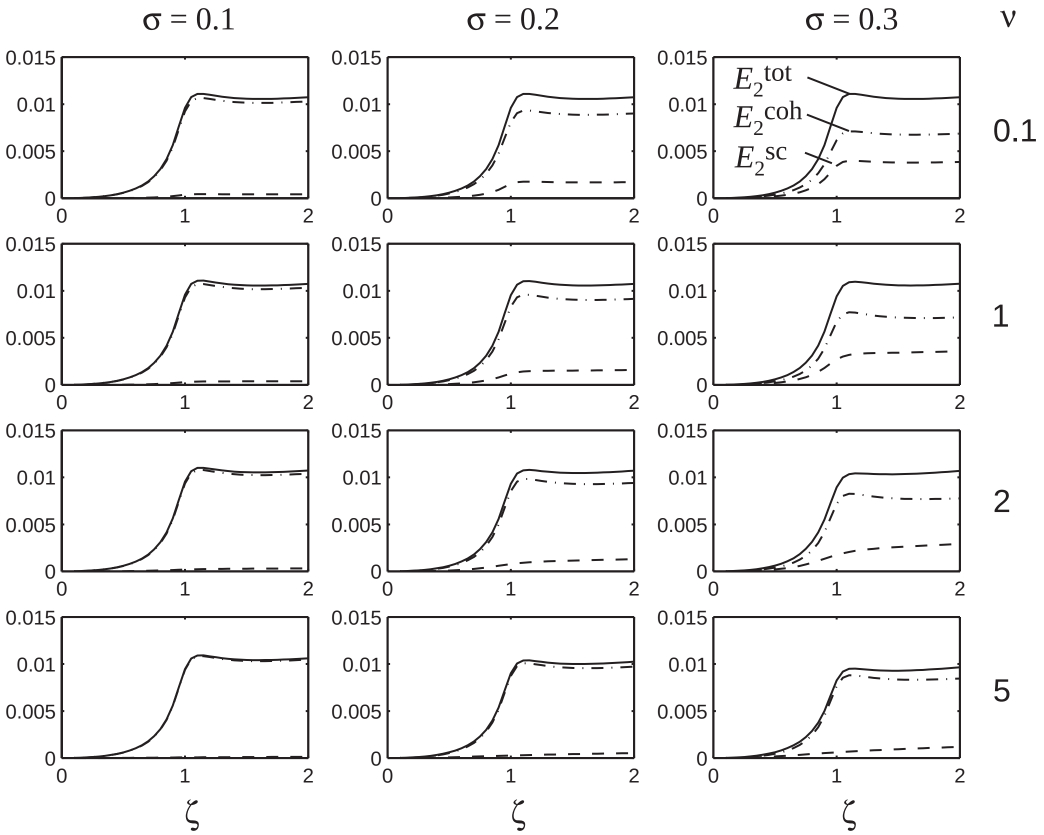

Figure 4.6: Dependence of $E_2^{\rm tot}$ (solid lines), $E_2^{\rm coh}$ (dot-dash lines) and $E_2^{\rm sc}$ (dashed lines) on distance ζ for a focused Gaussian beam with $G = 10$ and a phase screen with different values of ν and σ.

reach their maxima around the focus, and are almost constant after the focus. This is because nonlinear generation of both the coherent and scattered fields occurs mainly in the prefocal region, after which the second harmonic propagates essentially as a small signal (linear) wave. The nonlinear generation by the fundamental field is very small. For any given value of ν (i.e., across any row), increase in σ is seen to cause E_2^{sc} to increase and E_2^{coh} to decrease. For fixed σ, however, as ν increases, E_2^{sc} decreases and E_2^{coh} increases. The reason for the second phenomenon, although a weaker effect than the first, is explained as follows. The scattered energy in the fundamental field does not depend on ν, but as ν increases the fundamental beam becomes broader. Less concentration of the fundamental field results in less capability of generating the second harmonic, and E_2^{sc} decreases accordingly.

The statistical results derived above will be compared with direct numerical simulations in Sec. 4.3 to assess the validity of the statistical solutions.

4.3 Comparison with numerical simulations

In this section, the angular spectrum method described in Sec. 3.2 is used to compute the fundamental and second-harmonic fields produced in the focal plane due to radiation from a Gaussian source through a random phase screen. The phase screen is created on the basis of prescribed statistics. The method we used to generate such a random phase screen is described in the book by Viniotis.[70] We outline the procedure here. The goal is to create a 2D distribution $\phi(\mathbf{r})$ with zero mean, variance σ, and a Gaussian correlation function $C_\phi(\mathbf{r})$ as described by Eqn. (4.6). To do this, the following filter function $H(f_x, f_y)$ is introduced:

$$H(f_x, f_y) = \sqrt{\mathcal{F}\{C_\phi(|\mathbf{r}_1 - \mathbf{r}_2|)\}} = \sqrt{\mathcal{F}\{C_\phi(\mathbf{r})\}}\,, \tag{4.47}$$

where $\mathcal{F}$ represents the spatial Fourier transform defined as in Eqn. (3.16). A 2D random noise function $\eta(\mathbf{r})$ having zero mean and variance σ is the input to this filter, such that

$$\Phi(f_x, f_y) = H(f_x, f_y)\mathcal{F}\{\eta(\mathbf{r})\}\,, \tag{4.48}$$

where $\Phi(f_x, f_y)$ is the output spectrum. When the inverse Fourier transform, defined as in Eqn. (3.17), is applied to $\Phi(f_x, f_y)$, the result is a single sample $\phi(\mathbf{r})$ that has zero mean, variance σ, and correlation function $C_\phi(\mathbf{r})$. The 2D random noise input $\eta(\mathbf{r})$ can be generated using a built-in function in MATLAB. The entire procedure is illustrated in Fig. 4.7.

We thus generate four random screens in this way, two for the parameters $\nu = 5$, $\sigma = 0.2$, and the other two for $\nu = 2$, $\sigma = 0.2$. The two values of ν chosen here correspond to the measured correlation length produced by the human abdominal wall.[22] In the measurements, the reported correlation length varies from 3.7 mm to 11 mm.[22] For a typical transducer, such as a 1.5 in. diameter focused source, the corresponding value of ν varies roughly between 2 and 5. These two extreme values are chosen here as the parameters for computation.

The simulations in Fig. 4.8 are for phase screens with $\nu = 5$ and $\sigma = 0.2$. The first row shows the amplitude distribution of the source and the phase distributions of the two random screens, A and B, having the same statistics. The phase plots have a dynamic range from -0.8 rad to 0.8 rad. The black circles have the same radius a as the source, which is introduced to provide a relative sense of the correlation length (inhomogeneity length scale) l. Since $\nu = 5$, the correlation length is about 10% of the source diameter. Rows 2–4 are the focal beam patterns for the linear f, linear $2f$, and nonlinear $2f$ beams, respectively, with the first column showing the focal beam patterns without the phase screen. The second and third columns show the distorted focal beam patterns corresponding to screens A and B. All beam patterns are normalized to their maximum value and are plotted in the same dynamic range, from -60 dB to 0 dB.

From this figure one can see that the beam patterns are no longer symmetric, and that a considerable amount of energy is scattered away from the main lobes. We see qualitatively that less energy is scattered from the central lobe of the beam for linear radiation at $2f$ compared with that at f, and less still in the nonlinear $2f$ component. Since the weak scattered fundamental components generate even weaker second harmonics, most of the second-harmonic energy is confined to the central lobe of the fundamental, and its scattered field decays very quickly

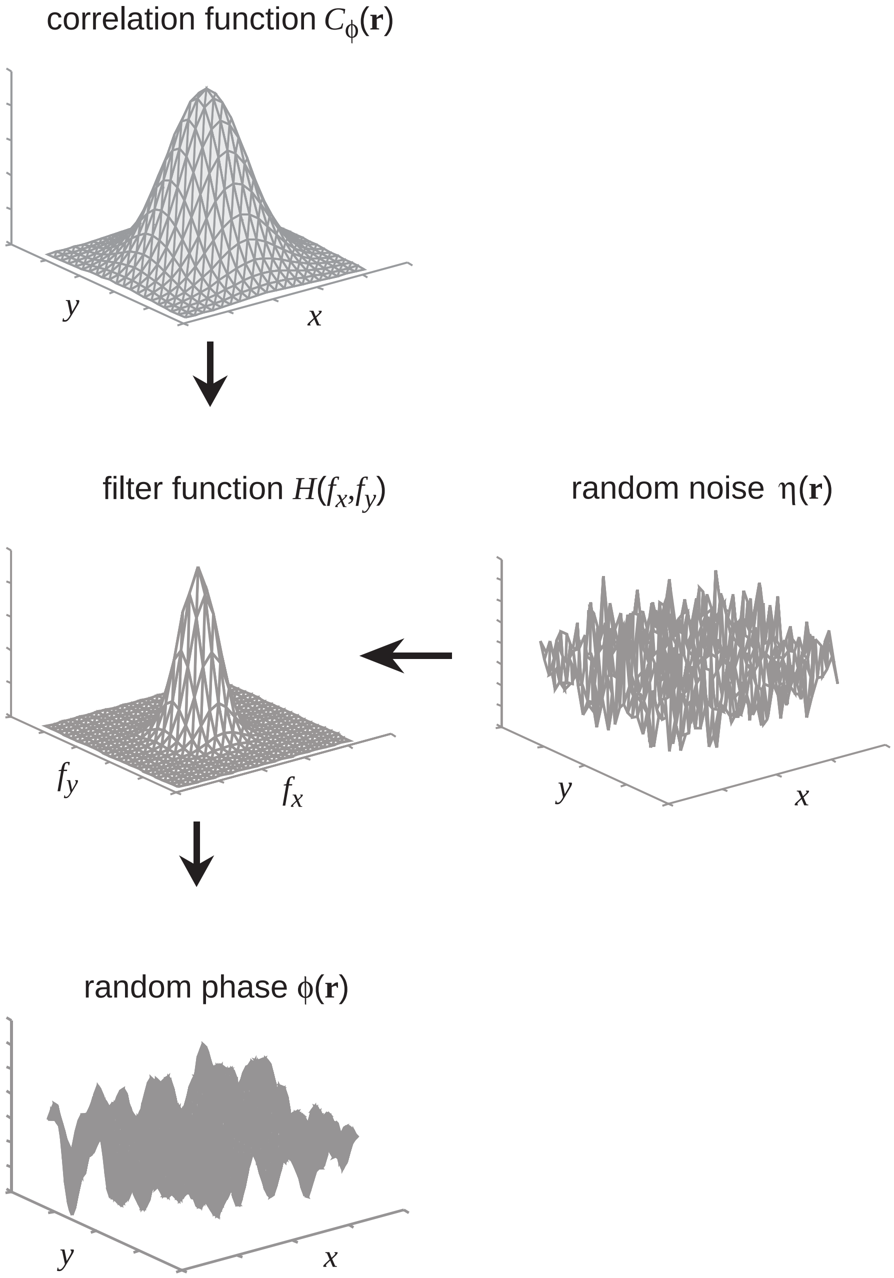

Figure 4.7: Procedure for the generation of random phase screens.

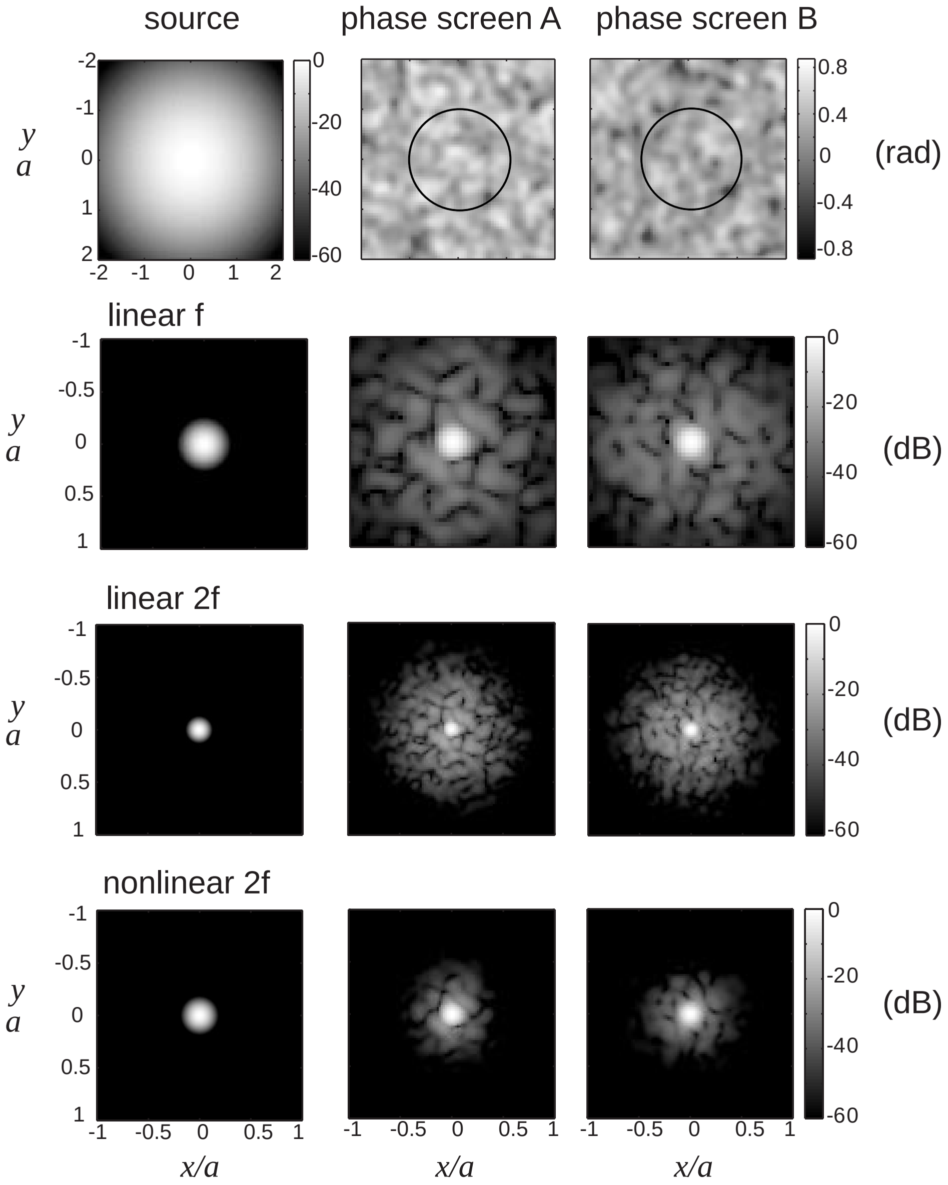

Figure 4.8: Top row: amplitude distribution of the source and phase distributions of the two screens ($\nu = 5$, $\sigma = 0.2$). Second row: linear f field in the focal plane with no phase screen (left), and then with the two phase screens in the first row (middle and right). Third and fourth rows: corresponding results for the linear $2f$ field and the nonlinear $2f$ field.

with distance from axis. Although the linear $2f$ beam has the sharpest main lobe, which can increase scan resolution, compared to the nonlinear $2f$ beam its scattering lobes introduce more artifacts and haze during image formation. The nonlinear $2f$ beam is better than linear beam, in the sense of least scattering off axis, which is a main contributor to artifacts and haze in image formation.

A detailed comparison of the beam profiles with the statistical solutions is presented in Fig. 4.9. The top two rows are for comparisons with phase screen A in Fig. 4.8, and the bottom two rows are for phase screen B. The beam profiles (dotted lines) are plotted along the x and y axes in the focal plane. From a statistical point of view, since the random variation in field amplitudes is isotropic in the x-y plane, the distributions along the x and y axes through the focus have the same statistical behavior as distributions along any other axes through the focus. They are therefore representative of the general scattering of the corresponding 2D beam patterns in Fig. 4.8. The dashed curves are the beam patterns in the absence of a phase screen, and the solid lines are the statistical solutions, Eqn. (4.37) for the linear f and linear $2f$ beams, and Eqn. (4.38) for the nonlinear $2f$ beam.

We see that in all cases, the sampled beam profiles oscillate around the statistical solutions, and closely follow the trend predicted by the latter. It can also be seen that in the beam center the scattering is not prominent and the beam patterns maintain their undistorted shape, given by the dashed lines. Most of the energy in the beam center is due to the coherent field. Further off axis, scattering becomes apparent and side lobes are generated. We can see the scattered side lobe levels are lowest for the nonlinear $2f$ beams. The rate at which the scattered field decays off axis is also largest for the nonlinear $2f$ beams. The slowest decay rate occurs for the linear f beam. The linear $2f$ beam falls in between. The decay rate for the scattered field mainly depends on the parameter ν. The dependence on σ will be seen below to be very weak. Also from this figure, one can see that the linear $2f$ beam has the largest variance in the scattered field. Its side lobes are more oscillatory around the statistical solutions.

We now investigate how well the statistical solutions agree with ensemble

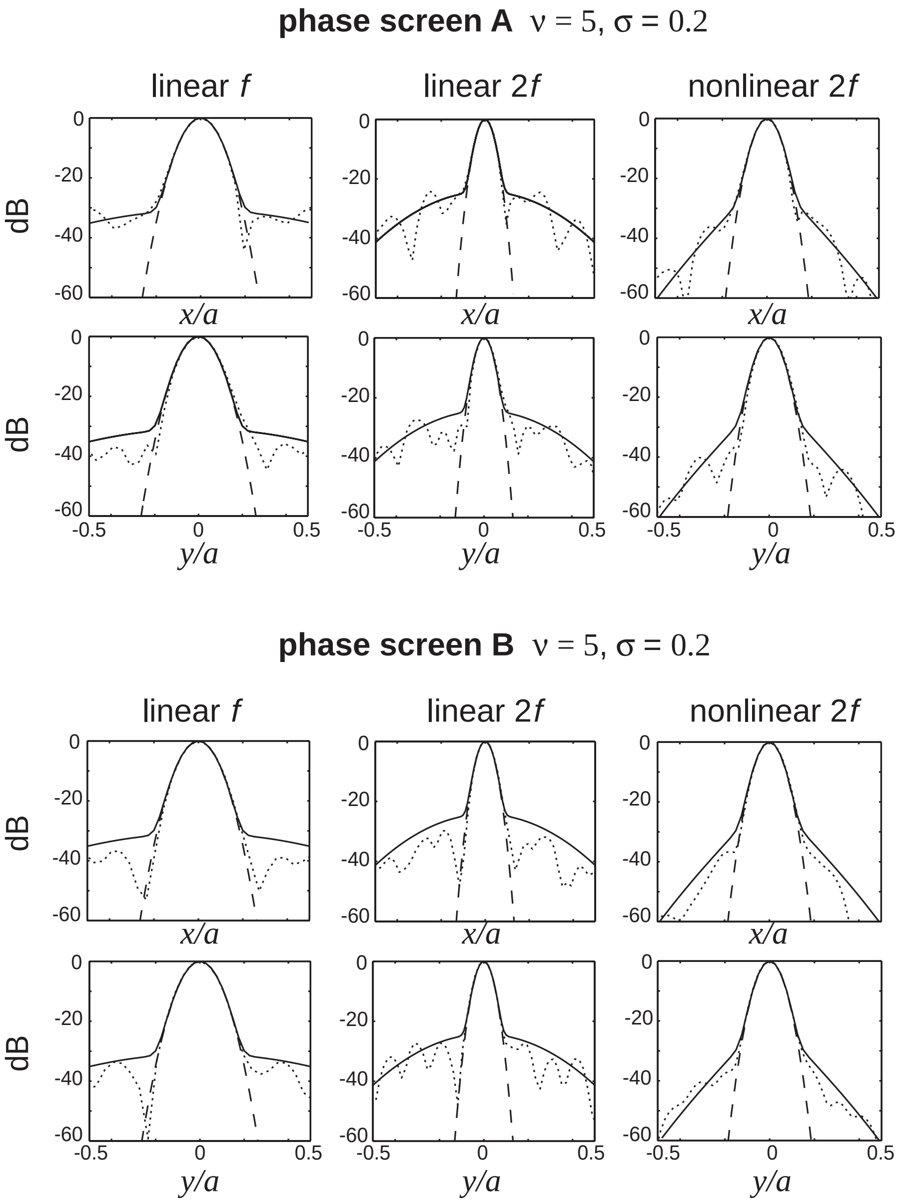

Figure 4.9: Comparison of normalized linear f, nonlinear $2f$ and linear $2f$ focal beam profiles (dotted lines) with statistical solutions (solid lines) and the aberration free beam profiles (dashed lines). The first two rows are the results with screen A, and the second two rows are with screen B, with x and y representing perpendicular axes passing through the focus.

averages of numerically computed individual realizations. The ensemble averages are computed using a single realization of the beam pattern computed in the focal plane, as depicted in Fig. 4.10. The beam pattern represented by $q(x, y)$ is averaged along rings with different radius ρ, from $\rho = 0$ to a chosen $\rho_{\max}$. A ring with radius ρ and thickness $d\rho$ is drawn in the x-y plane, any data points that fall inside the ring are averaged, and their mean is the averaged pressure at radius ρ. The same averaging procedure has been used by Christopher[6] to show the general behavior of a distorted beam pattern. In our case, each distorted 2D beam pattern is a realization with the corresponding random phase screen, and the ensemble average of large number of such realizations should result in a symmetric beam pattern, having the same dependence on ρ as obtained using the method described above for a single 2D beam pattern. We hence use the averaged beam profile obtained from one sample 2D beam pattern to serve as an estimate of the mean beam profile. The equivalence of these two averaging procedures is explained as follows. Since the distortion of the beam pattern is a stationary random process in space, it can be shown to be mean ergodic.[70] For an ergodic process, estimating the mean by performing a spatial average over one realization is equivalent to performing an ensemble average of many realizations.

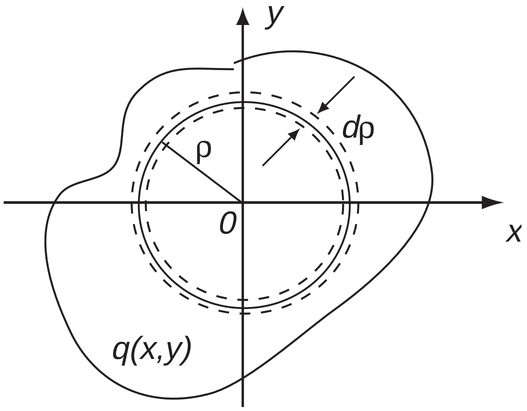

Figure 4.10: Illustration of the method for performing an ensemble average of numerically generated field patterns $q(x, y)$.

This is a convenient relation because we only need to compute single 2D beam pattern to estimate the mean, rather than perform many 2D beam computations.

An averaged beam profile is calculated for each of the 2D beams associated with phase screen A. The results are shown as the dotted lines in Fig. 4.11, together with solid lines for the statistical solutions, and dashed lines for the solutions in the absence of a phase screen. The plots show close agreement between numerically averaged profiles and the statistical solutions. From this figure it is apparent that there is a transition radius ρ_t such that for $|\rho| < \rho_t$ the beam maintains an undistorted shape. In this region, the beam profile is dominated by the coherent field. For $|\rho| > \rho_t$, the beam profile follows the trend predicted by the scattered field. As illustrated by Fig. 4.11, ρ_t is roughly where the scattered field amplitude equals the coherent field amplitude. One may thus express ρ_t as a function of ν, σ and G. For a linear beam, we obtain

$$\rho_t = \frac{1}{2G\nu}\sqrt{(1+2\nu^2)\ln\left[(1+2\nu^2)/\sigma^2\right]}\,. \tag{4.49}$$

One obtains $\rho_t = 0.19$ for the linear f beam, and $\rho_t = 0.09$ for the linear $2f$ beam. For the second harmonic, ρ_t has no analytical expression and must be determined numerically. For the nonlinear $2f$ beam, $\rho_t = 0.12$.

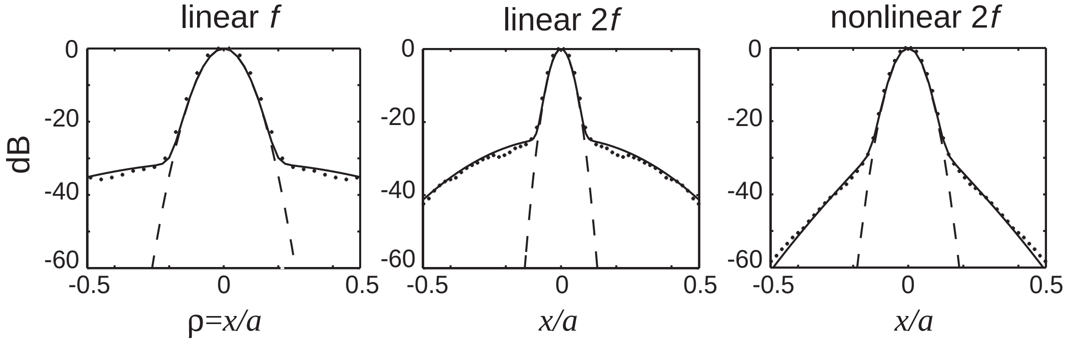

Figure 4.11: Averaged beam profiles (dotted lines) for the beam patterns in Fig. 4.8 associated with phase screen A compared with the statistical solutions (solid lines) and the aberration-free profiles (dashed lines).

In the second simulation, shown in Fig. 4.12, we use the two phase screens with $\nu = 2$ and $\sigma = 0.2$, and keep all other conditions the same. The only difference with the previous case is that ν has been decreased from 5 to 2, corresponding to an increase in the correlation length l of the phase screen (compare the top rows in Figs. 4.12 and 4.8). From this figure, we see the scattered area decreased for all beams, compared with the $\nu = 5$ case. However, the scattered fields for the linear and nonlinear $2f$ beams appear similar in both level and radial extent. In addition, the main lobes (central spots) of the linear and nonlinear $2f$ beams are comparable.

The sampled and averaged beam profiles are plotted in Figs. 4.13 and 4.14, respectively. They correspond to Figs. 4.9 and 4.11 for $\nu = 5$. As before, the scattered field is accurately predicted by the statistical solutions. The transition radii are $\rho_t = 0.17$ for the linear f beam, $\rho_t = 0.08$ for the linear $2f$ beam, and $\rho_t = 0.1$ for the nonlinear $2f$ beam. Compared to the corresponding beam profiles for $\nu = 5$, ρ_t is a little smaller, but the scattered field decreases much faster in the radial direction. This is due to the narrower beam width and the increased axial pressure of the scattered field for $\nu = 2$ compared to $\nu = 5$.

The angular spectra for the focal beam patterns and the phase screens corresponding to the two statistical examples are shown in Fig. 4.15. From this figure, one can see that a smaller correlation length (large ν) for the phase screen results in a broader angular spectrum, and the corresponding spectra for the focal beam patterns are more distorted. The angular spectrum for the nonlinear $2f$ beam is much less affected by the phase screen than the spectra of the linear f and linear $2f$ beams.

From the above comparisons we conclude that the statistical solutions given by Eqns. (4.37) and (4.38) are accurate for the cases considered, i.e., $\sigma = 0.2$ and $\nu = 2, 5$. For these parameters, which introduce scattering and distortion of the beams, ensemble averaging of direct numerical simulations converges to the statistical solutions. For larger phase perturbations (larger σ), the weak scattering assumption breaks down and the statistical solutions ultimately fail. This issue is investigated in Sec. 4.5. The statistical solutions nevertheless reveal the relation between the phase aberration and the scattered beam pattern. For $\nu = 5$, which is the case of a relatively stronger scattering, the nonlinearly

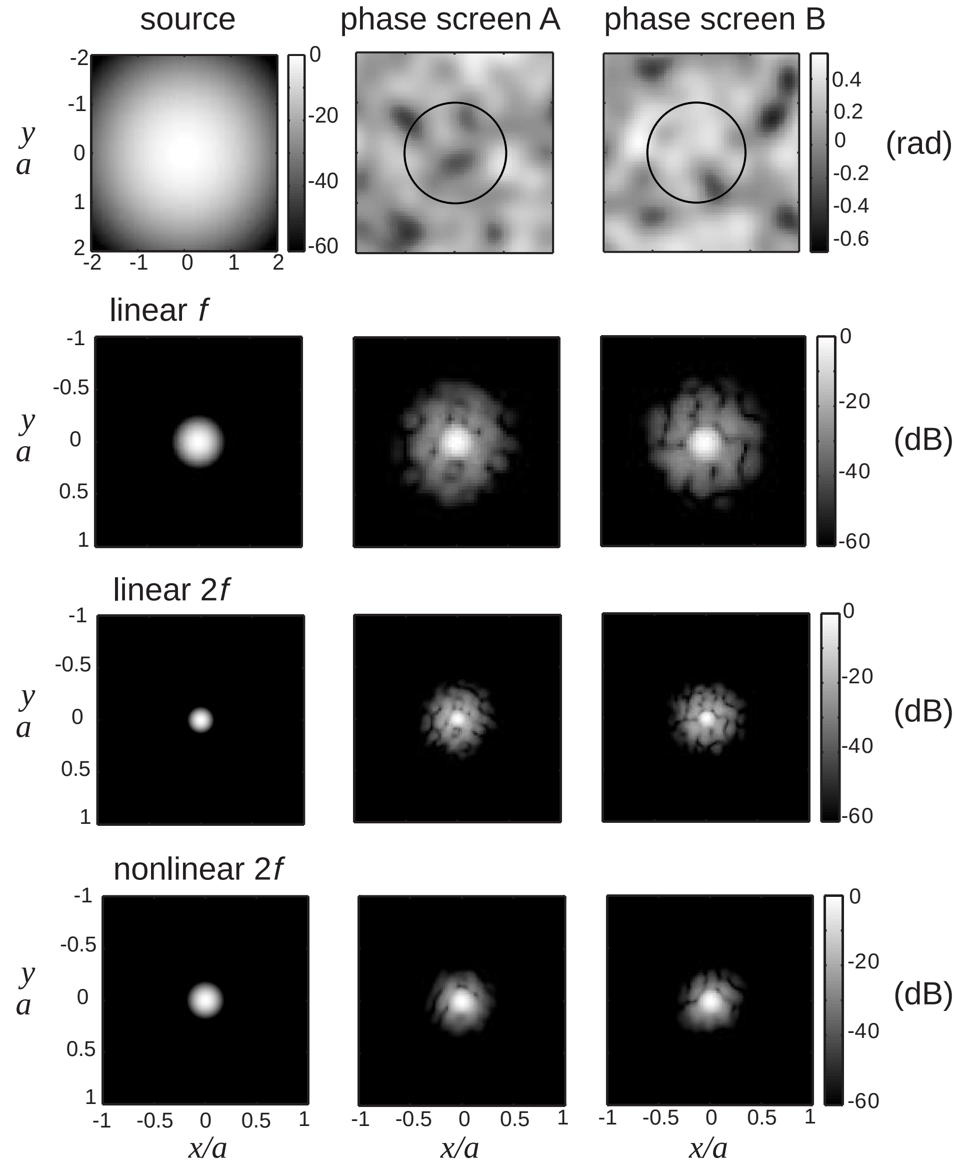

Figure 4.12: Top row: amplitude distribution of the source and phase distributions of the two screens ($\nu = 2, \sigma = 0.2$). Second row: linear f field in the focal plane with no phase screen (left), and then with the two phase screens in the first row (middle and right). Third and fourth rows: corresponding results for the linear $2f$ field and the nonlinear $2f$ field.

phase screen A ν = 2, σ = 0.2

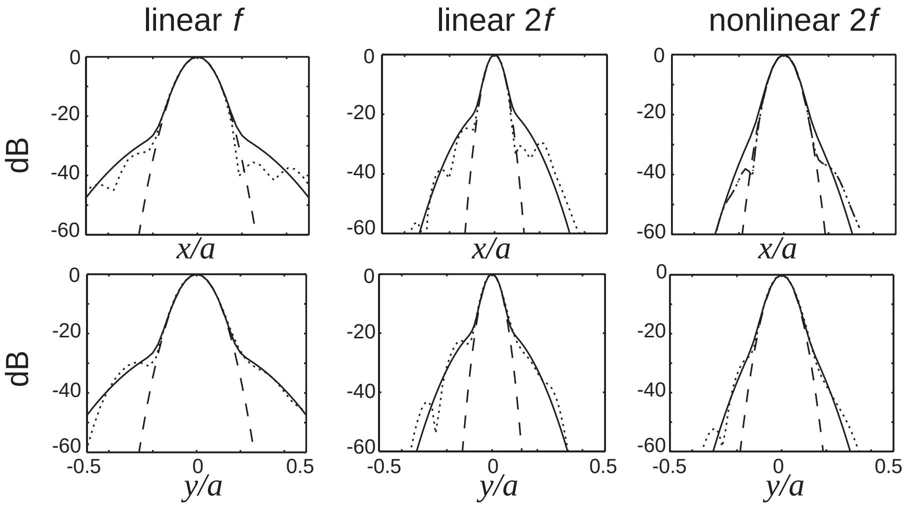

phase screen B ν = 2, σ = 0.2

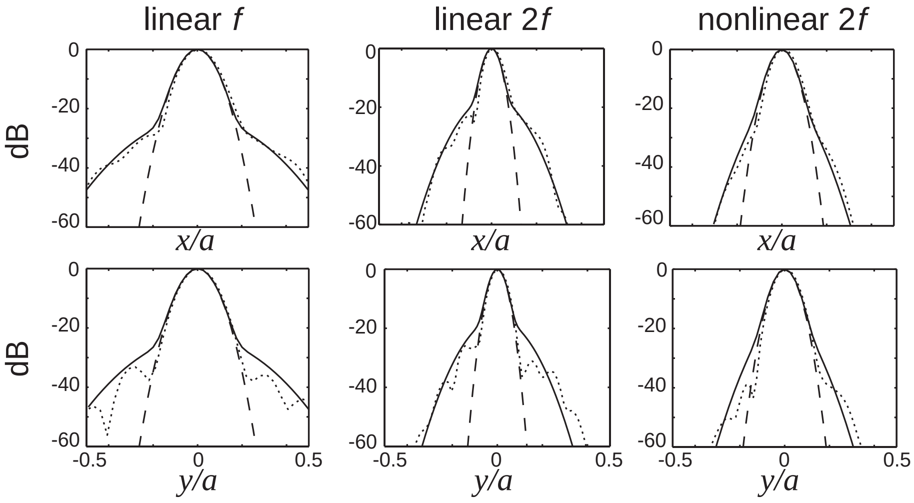

Figure 4.13: Comparison of normalized linear f, nonlinear $2f$ and linear $2f$ focal beam profiles (dotted lines) with statistical solutions (solid lines) and the aberration free beam profiles (dashed lines). The first two rows are the results with screen A, and the second two rows are with screen B, with x and y representing perpendicular axes passing through the focus.

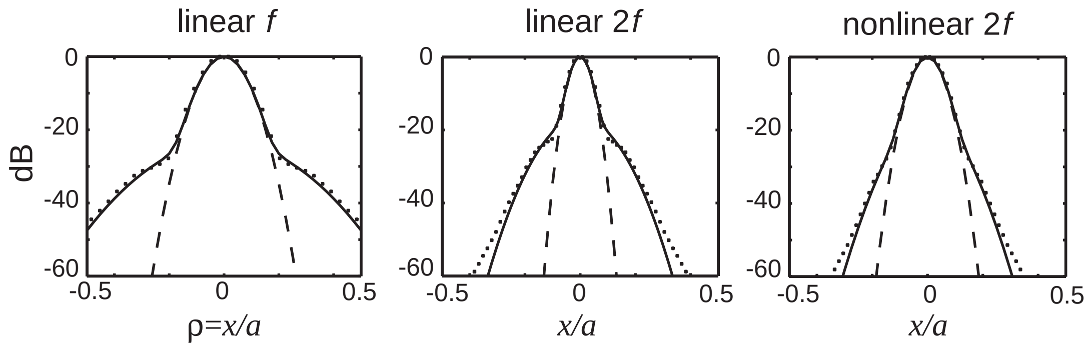

Figure 4.14: Averaged beam profiles (dotted lines) compared with statistical solutions (solid lines) and the aberration-free profiles (dashed lines).

generated second-harmonic beam at frequency $2f$ is less distorted than both the fundamental at frequency f and a field radiated linearly at frequency $2f$. To further quantify the distortion, metrics are proposed in the next section showing the beam's focus quality and the influence of this quality by phase screen.

4.4 Measure of focusing quality

The distortion of beam patterns can also be quantified by calculating their focus quality. In a recent paper, Tabei et al.[35] defined a metric to measure the focus quality for a distorted beam pattern after propagation through a tissue layer. They define a Peripheral Energy Ratio (PER) as the ratio of acoustic energy in the peripheral area to the energy in the focal area, i.e., $E_{\mathrm{per}}/E_{\mathrm{foc}}$. Their focal area is defined as the region where the level in the main lobe is within 10 dB of its peak value. In this section, a similar measure is used, denoted as Q, to quantify the focus quality of the beam patterns. We define Q as the ratio of the focal energy to the peripheral energy, which is the reciprocal of the metric defined by Tabei, i.e.,

$$Q = \frac{E_{\mathrm{foc}}}{E_{\mathrm{per}}} \tag{4.50}$$

The parameter Q is a measure of the concentration of energy in the beam pattern. Larger values of Q indicate that more energy is concentrated in the focal area,

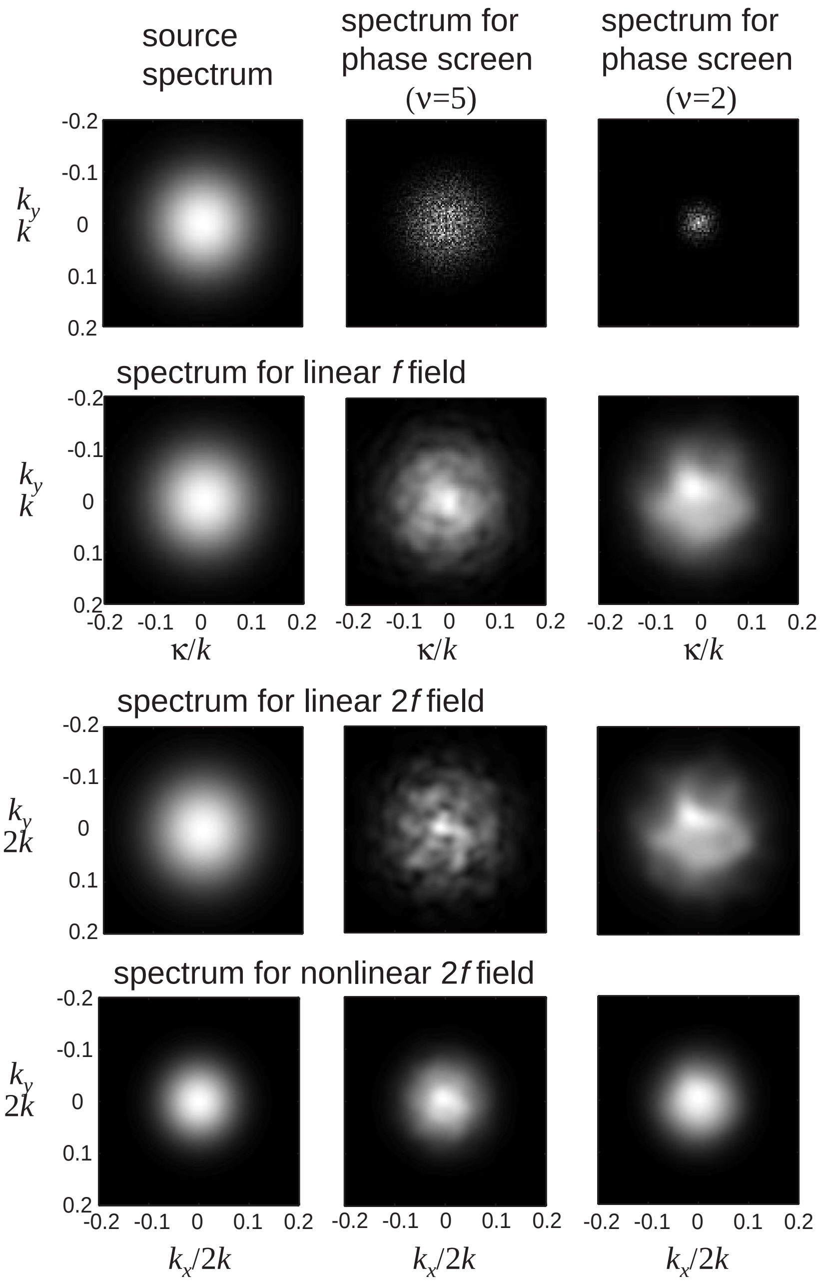

Figure 4.15: Top row: amplitude of the angular spectra for the Gaussian source and for the two phase screens with $\nu = 5, \sigma = 0.2$ and $\nu = 2, \sigma = 0.2$ (sample screen A in Fig. 4.8 and Fig. 4.12). Second row: angular spectrum for linear f field with no phase screen (left), and the spectra with two phase screens in the first row (middle and right). Third and fourth rows: corresponding results for the linear $2f$ field and the nonlinear $2f$ field.

which also indicate that less energy is scattered into the peripheral area.

In addition, we also introduce a measure of the change of Q from an undistorted beam pattern to a distorted beam pattern as a result of the phase aberration. We label this as the normalized focus quality Q_{norm} defined as

$$Q_{\mathrm{norm}} = \frac{E_{\mathrm{foc}}/E_{\mathrm{per}}}{E_{\mathrm{foc0}}/E_{\mathrm{per0}}}\times 100\%\,, \tag{4.51}$$

where the numerator is calculated using the distorted beam pattern, the denominator using the undistorted beam pattern (the notation foc0 and per0 indicate quantities calculated in the absence of aberration). The parameter Q_{norm} is thus a measure of the decrease in the focus quality Q caused by phase aberration, with $Q_{\mathrm{norm}} = 1$ corresponding to a beam pattern without aberration. Smaller values of Q_{norm} indicate larger effects of aberration.

The threshold level that defines the focal area is somewhat arbitrary. First of all, the threshold should be larger than the maximum side lobe levels so that the side lobe energy is excluded from the focal energy. To determine the threshold it is helpful to rewrite Eqn. (4.51) in terms of the energy ΔE scattered from the focal region to the peripheral region. In linear theory the energy in the beam remains constant, and therefore $E_{\mathrm{foc}} = E_{\mathrm{foc0}} - \Delta E$, $E_{\mathrm{per}} = E_{\mathrm{per0}} + \Delta E$, such that Eqn. (4.50) becomes

$$Q_{\mathrm{norm}}^{\mathrm{fund}} = \frac{1-\Delta E/E_{\mathrm{foc0}}}{1+\Delta E/E_{\mathrm{per0}}}\,, \tag{4.52}$$

where the superscript "fund" indicates that this relation is strictly valid only in linear theory. Recall from Eqns. (4.37) that the scattered energy is a very small fraction of the total energy in the beam (also see first row of Fig. 4.5, and therefore a reasonable approximation of Eqn. (4.52) is

$$Q_{\mathrm{norm}}^{\mathrm{fund}} \approx \frac{1}{1+\Delta E/E_{\mathrm{per0}}}\,. \tag{4.53}$$

For $Q_{\mathrm{norm}}^{\mathrm{fund}}$ to be a sensitive measure of energy scattered out of the focal region, the threshold level should be chosen to maximize the ratio $\Delta E/E_{\mathrm{per0}}$ for the class of cases under consideration. On the basis of Figs. 4.8 and 4.12, we feel that a threshold level set at -20 dB, roughly where the scattered field begins to cause noticeable distortion of the beam profiles, is appropriate for our purposes here.

The values of Q and Q_{norm} for every 2D beam pattern shown in Figs. 4.8 and 4.12 are presented in Fig. 4.16. Figure 4.16(a) and (c) corresponds to Fig. 4.8 ($\nu = 5$), and Fig. 4.16(b) and (d) corresponds to Fig. 4.12 ($\nu = 2$). At the threshold of 20 dB, the values of Q indicate that the nonlinear $2f$ beam has the largest concentration of energy in the focal area, whereas the values of Q_{norm} indicates the nonlinear $2f$ beam is least influenced by the phase screen. From Fig. 4.16, one can see that the values of Q and Q_{norm} for $\nu = 2$ are larger than the corresponding values for $\nu = 5$.

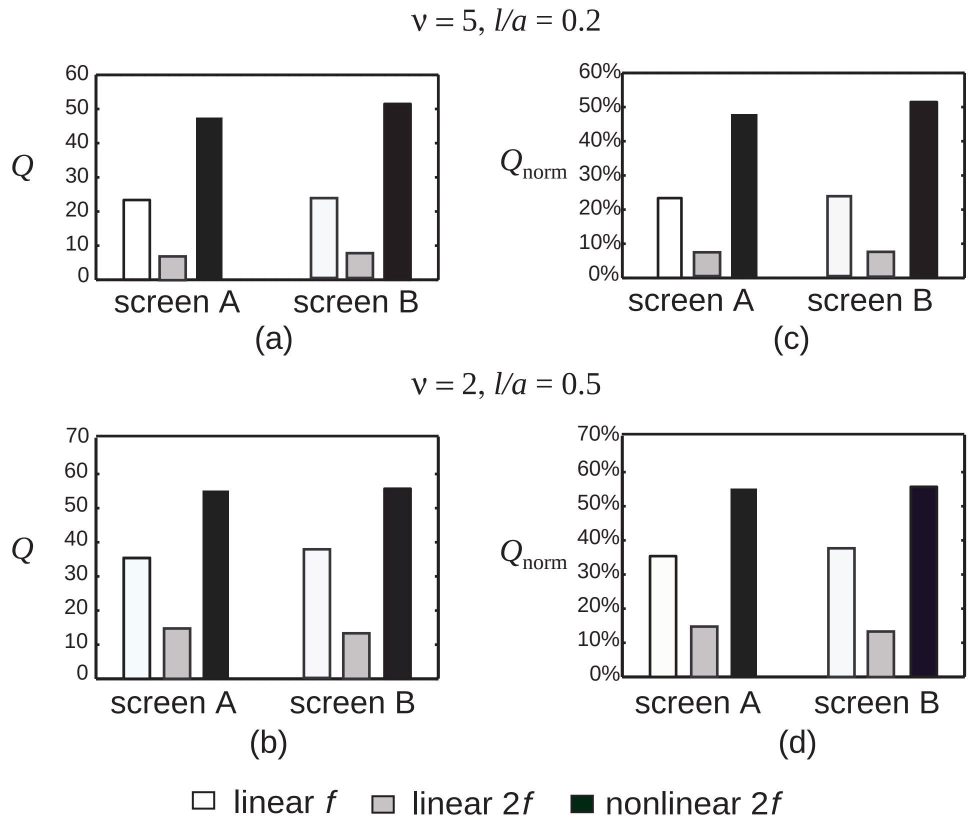

Figure 4.16: The focusing quality Q and Q_{norm} for the 2D beam patterns in Figs. 4.8 and 4.12, with screen A and B, respectively.

4.5 Validity of the statistical solution

The statistical solutions derived in Secs. 4.1 and 4.2 are based on the assumption $|\phi| \ll 1$, i.e., the weak scattering condition. This condition puts a restriction on the phase variance σ. The statistical solutions are expected to break down for large σ. A corollary of the weak scattering assumption is that the scattered energy should be small compared to the coherent energy over the propagation path.

In this section, we show how the statistical solutions change and ultimately fail with increasing σ. We assess the accuracy of the statistical solutions via comparison with beam patterns calculated by ensemble averaging direct numerical simulations. Of course, σ cannot increase without bound, because at the very least we must have $\sigma < 1$ on the basis of the expansions used in Eqn. (4.12) for obtaining $\langle I_1 \rangle$ and Eqn. (B.2) for obtaining $\langle I_2 \rangle$.

The two random phase screens denoted by A in Sec. 4.3 with $\nu = 5, 2$ are used in this investigation. Results for $\nu = 5$ are presented in Fig. 4.17. In the calculations, the angular spectrum method employing full diffraction is used. Additional calculations using the parabolic approximation of the diffraction term give the same beam patterns in all these examples. This shows that any deviation between the calculations and statistical solutions is not due to the parabolic approximation inherent in the solutions. From these plots we can see that the solutions for $\langle I_1 \rangle$ and $\langle I_2 \rangle$ (solid lines) deviate from the numerical solutions (dotted lines) in different ways. For the fundamental, the error is manifest as a small, relatively uniform overprediction of the scattering. For the second harmonic, the error is in mostly underpredicting the scattering, with the error increasing rapidly with distance from the axis, and beginning closer to the axis with increasing σ. For $\sigma = 0.2$, the solution for $\langle I_2 \rangle$ can accurately predict the total field down to -60 dB. For $\sigma = 0.7$ the range is reduced to -30 dB, and for $\sigma = 0.8$ the solution may be considered to fail entirely, even for the main lobe.

Comparisons for $\nu = 2$ are shown in Fig. 4.18. In this case, the statistical solutions for $\langle I_1 \rangle$ fail for smaller values of sigma than with $\nu = 5$. Moreover, the nature of the error is also different. Here, the error in $\langle I_1 \rangle$ is not uniform across fundamental :

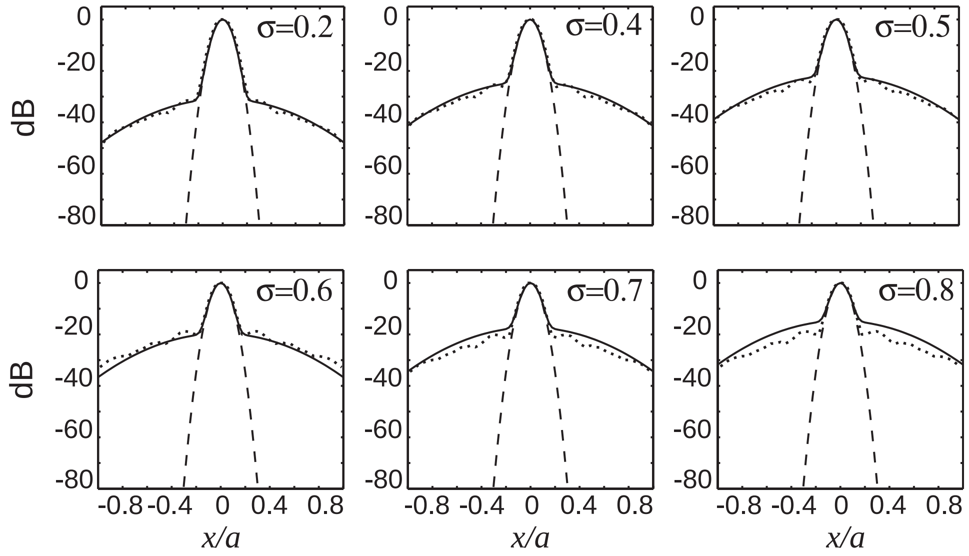

second harmonic :

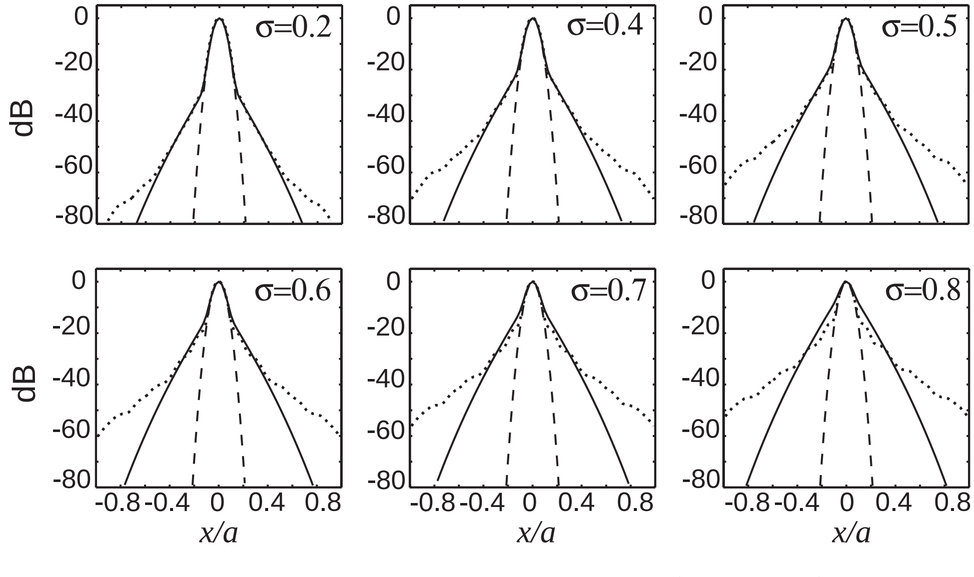

Figure 4.17: Comparison of statistical solutions (solid lines) with ensemble averages of numerical simulations (dotted lines) for $\nu = 5$. Dashed lines show the beam pattern without aberration for reference.

the beam, and it manifests mainly as an underprediction of the scattered field. However, the error in $\langle I_2 \rangle$ resembles that in Fig. 4.17, except that the range of validity is somewhat less for $\nu = 2$. Although for $\sigma = 0.2$ the statistical solution is accurate down to -60 dB, this range is reduced to -30 dB at $\sigma = 0.6$. At $\sigma = 0.7$, the solution completely fails.

The statistical solutions predict, as σ increases, that the scattered component tends to increase uniformly until it achieves the same level as the coherent field, such as the case for the second-harmonic beam when $\nu = 5$, $\sigma = 0.8$, where the main lobe is almost buried in the scattered field. The total beam pattern seems to have a broadened main lobe. However, the numerical solution reveals that the main lobe still stands out from the scattered field, and its shape remains almost the same. The scattered field dominates only at about -15 dB. The scattered field also decays with r at a much slower rate than that predicted by the solution. The reason is that the approximation in the expansions appearing in Eqns. (4.12) and (B.2) become poor for large σ. Higher order terms should be included in the expansions. These higher order terms are associated with scattering, which are omitted in Eqns. (4.37) and (4.38). When σ is small these additional terms are much smaller and make their presence felt only far off axis, where the total field amplitude is negligibly small. When σ increases these terms are no longer small compared to the previous terms in the expansion. They account for the scattered field in the peripheral region of the beam, and their interference with the coherent terms and other scattered terms will decrease the radiated scattered field in the main lobe. The errors of the statistical solutions arise mainly from the expansions in Eqns. (4.12) and (B.2). For large σ, higher powers of ϕ should be included, leading to higher-order moments that must be calculated for ϕ. Not only is the integral is more difficult to perform, but one would also need more information on higher-order moments for the phase screen.

4.6 Change of screen position

The statistical solutions presented in previous sections are for a phase screen located in the source plane. These solutions form the basis for investigating the fundamental :

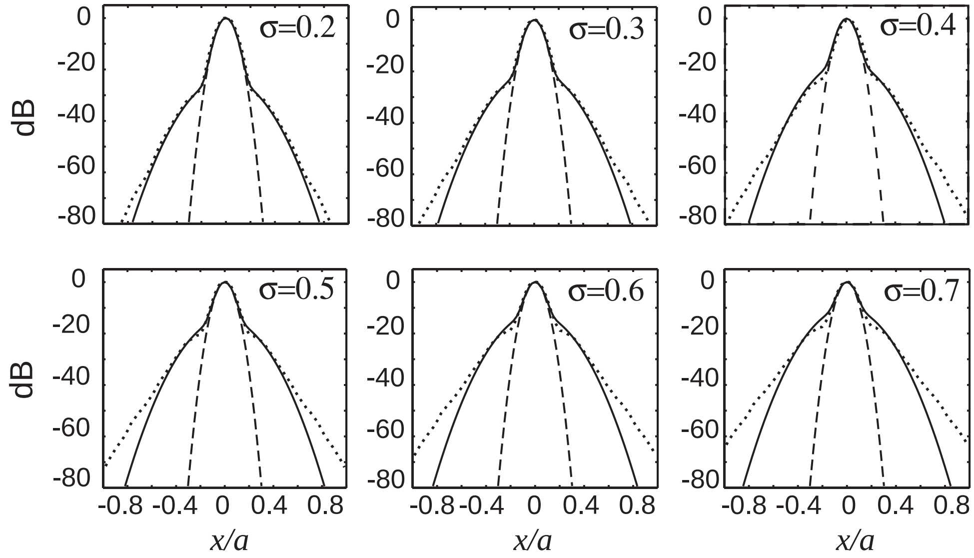

second harmonic :

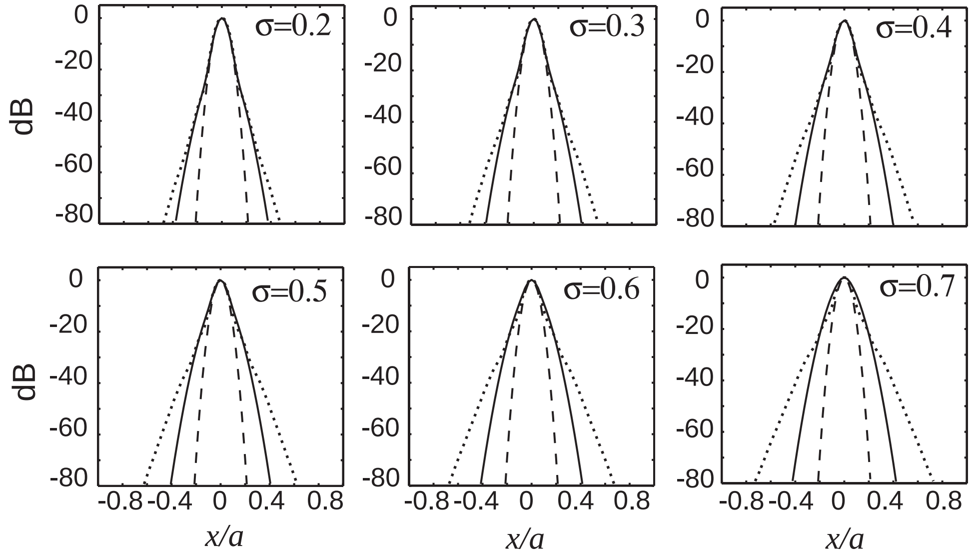

Figure 4.18: Comparison of statistical solutions (solid lines) with ensemble averages of numerical simulations (dotted lines) for $\nu = 2$. Dashed lines show the beam patterns without aberration for reference.

effect of phase screens located an arbitrary distance from the source plane, as depicted in Fig. 4.19. The screen is at distance b_1 from the source plane, and the beam pattern is to be obtained in the focal plane at distance d. Although the target plane can be at any distance from the screen, the physics involved in the scattering is the same and the calculation of the scattered field is similar to that obtained in the focal plane. Here we choose the target plane to be the focal plane as an example. In this case, the field at b_1 consists of not only the component from the source frequency but also some amount of nonlinearly generated second harmonic.

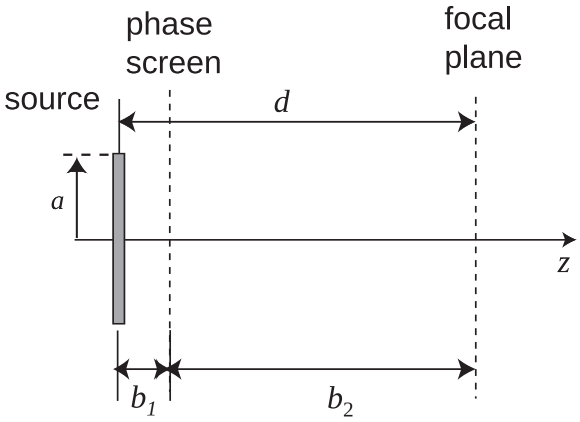

Figure 4.19: Geometry for phase screen at distance b_1 from source.

The solution procedure is as follows. The linear f and nonlinear $2f$ fields incident on the phase screen are treated as a secondary source radiating at both of these frequencies. The resulting radiation fields are treated independently. The radiation at frequency f is treated just as before. It produces a linear f and a nonlinear $2f$ field in the focal plane, each containing a coherent and scattered component. The radiation at frequency $2f$ is considered as a second fundamental beam. Linear theory is used to obtain its solution, which also contains both a coherent and scattered component. The corresponding second-harmonic generation at frequency $4f$ is not of interest, and it is ignored.

Let $q_{10}(\mathbf{r})$ and $q_{20}(\mathbf{r})$ denote the complex fundamental and second-harmonic pressures, respectively, at $z = b_1$. As before, a Gaussian source is assumed at $z = 0$, the pressure for which is given again by

$$q_0(\mathbf{r}) = p_0 \exp\left[-\frac{r^2}{a^2} + jG\frac{r^2}{a^2}\right] . \tag{4.54}$$

The pressure distribution at $z = b_1$ for the fundamental field q_{10} can be written as[49]

$$q_{10} = P_1 \mathrm{exp}\left[-A\frac{r^2}{a^2} + jB\frac{r^2}{a^2} + j\phi(\mathbf{r})\right] , \tag{4.55}$$

where

$$P_1 = \frac{p_0}{b_2/d - jb_1/Gd}, \qquad A = \frac{d^2}{b_2^2 + b_1^2/G^2} , \qquad B = d\frac{Gb_2 - b_1/G}{b_2^2 + b_1^2/G^2} . \tag{4.56}$$

The complex pressure q_{10} represents a new source condition with frequency f at $z = b_1$, and it possesses Gaussian amplitude shading. The solution for $\langle I_1 \rangle$ in the focal plane can be obtained from Eqns. (4.13)–(4.15) by substituting A and B in Eqn. (4.56) and letting $z = d - b_1 = b_2$:

$$\langle I_1 \rangle = (1-\sigma^2)\frac{\tilde{G}^2\tilde{p}_0^2}{2\rho_0 c_0}\mathrm{exp}(-2\tilde{G}^2\tilde{\rho}^2) + \frac{\sigma^2\tilde{G}^2\tilde{p}_0^2/2\rho_0 c_0}{1 + 2\tilde{\nu}^2}\mathrm{exp}\left(-\frac{2\tilde{G}^2\tilde{\rho}^2}{1 + 2\tilde{\nu}^2}\right) , \tag{4.57}$$

where

$$\tilde{\rho} = \frac{r}{\tilde{a}} , \qquad \tilde{G} = \frac{k\tilde{a}^2}{2\tilde{d}} , \qquad \tilde{\nu} = \frac{\tilde{a}}{l} , \tag{4.58}$$

with

$$\tilde{a} = \frac{b_2}{d}a , \qquad \tilde{d} = \frac{b_2}{d}d = b_2 , \qquad \tilde{p}_0 = \frac{d}{b_2}p_0 . \tag{4.59}$$

The transformation in Eqn. (4.59) has a simple explanation in terms of geometrical acoustics. Note that Eqn. (4.57) can be obtained from Eqn. (4.37) for an effective source having radius $\tilde{a}$, focal length $\tilde{d}$, and source pressure $\tilde{p}_0$ situated in the plane of the phase screen. This new effective source can be viewed as a projection of the original source at $z = 0$ onto the plane of the screen at $z = b_1$ according to the laws of geometrical acoustics, as shown in Fig. 4.20 and represented by Eqn. (4.59). The statistical intensity $\langle I_1 \rangle$ can thus be obtained with this new source, assuming the screen is directly on its surface and keeping all other parameters the same. One finds that the effective focal gain $\tilde{G}$ and the parameter $\tilde{\nu}$ decrease due to the decrease in the effective source radius and focal length. Thus a phase screen that is close to the source has a much larger impact on the wave field than one that is near the observing plane, as has already been reported by Berkhoff.[71]

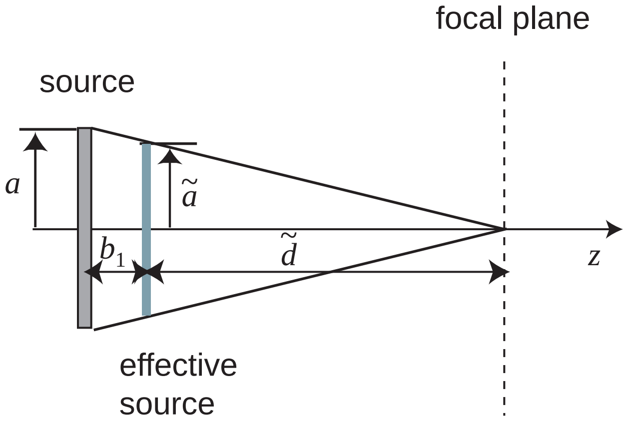

Figure 4.20: Geometrical acoustic interpretation of an effective source that accounts for a phase screen located distance b_1 in front of the real source. The effective source has radius $\tilde{a} = b_2 a/d$ and focal length $\tilde{d} = b_2$.

For the second harmonic, the pressure distribution at $z = b_1$ is[49]

$$q_{20} = P_{b1}\exp\left[-2A\frac{r^2}{a^2} + j2B\frac{r^2}{a^2} + j2\phi(\mathbf{r})\right] , \tag{4.60}$$

where

$$P_{b1} = \frac{jP_2 \ln[1-(1+j/G)b_1/d]}{(1-jG)[1-(1+j/G)b_1/d]} . \tag{4.61}$$

The pressure q_{20} also has a Gaussian amplitude shading. The total field of the second harmonic q_2 at $z = d$ is the combination of a linear field q_{2l} and a nonlinear field q_{2n}, as depicted in Fig. 4.21. The linear field q_{2l} is due to the linear propagation of q_{20} through the phase screen. The nonlinear field q_{2n} is due to the nonlinear interaction of fundamental field from $z = b_1$ to $z = d$. Each field has a coherent part and scattered part. Therefore the total field q_2 can be

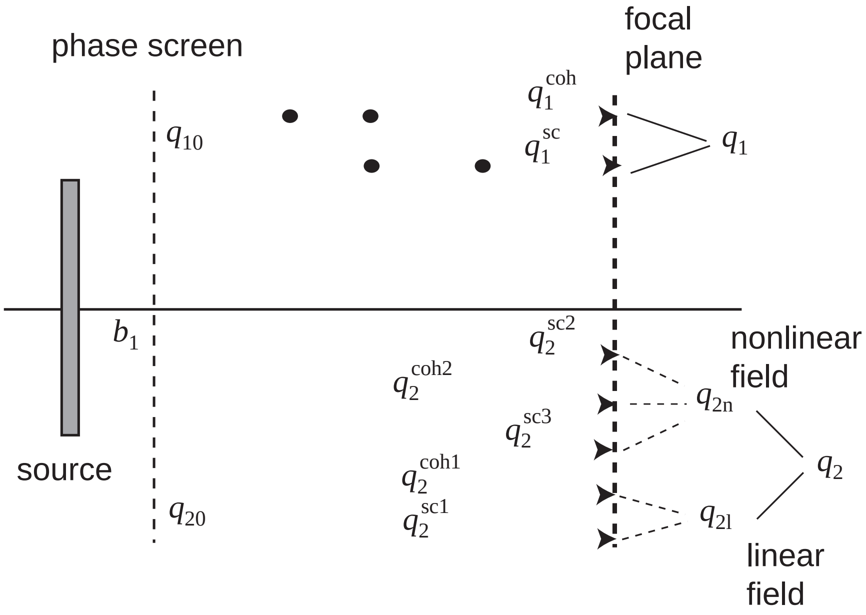

Figure 4.21: Illustration of second-harmonic generation due to scattering through a phase screen a distance b_1 from the source.

written as

$$q_2 = q_{2l} + q_{2n}\,, \tag{4.62}$$

and the intensity $\langle I_2 \rangle$ can be written as

$$\begin{aligned}\langle I_2 \rangle &= \frac{1}{2\rho_0 c_0}\langle (q_{2l} + q_{2n})(q_{2l}^* + q_{2n}^*)\rangle \\ &= I_{2l} + I_{2n} + I_{2ln}\,,\end{aligned} \tag{4.63}$$

where

$$I_{2l} = \frac{\langle q_{2l} q_{2l}^* \rangle}{2\rho_0 c_0}\,, \qquad I_{2n} = \frac{\langle q_{2n} q_{2n}^* \rangle}{2\rho_0 c_0}\,, \qquad I_{2ln} = \frac{\langle q_{2l} q_{2n}^* \rangle}{2\rho_0 c_0} + \text{c.c.}\,. \tag{4.64}$$

Because they are somewhat bulky, the solution for each intensity term in Eqn. (4.64) is given in App. D.

Usually the body wall tissue is very close to the transducer, and the approximation $b_1 \ll d$ is assumed for the phase screen. Under this approximation the intensity I_{2l} is observed to be $O(b_1^2/d^2)$, and I_{2ln} is $O(b_1/d)$, which are small compared to I_{2n}, see App. D. The total intensity $\langle I_2 \rangle$ is dominated by the nonlinear intensity I_{2n}, which can be written as

$$\begin{aligned}\langle I_2 \rangle \approx I_{2n} \approx \frac{P_2^2}{2\rho_0 c_0}\Bigg\{&\left[(1-2\sigma^2)\frac{|\ln(-j/\tilde{G})|^2}{(1+\tilde{G}^2)/\tilde{G}^2} - 2\sigma^2 \mathrm{Re}\left\{\frac{\ln[-j(1+2\tilde{\nu}^2)/\tilde{G}]\,\ln(j/\tilde{G})}{(1-j\tilde{G}+2\tilde{\nu}^2)(1+j\tilde{G})/\tilde{G}^2}\right\}\right] \\ &+4\sigma^2\tilde{G}^2\int_1^\infty\!\!\int_1^\infty \frac{\exp(4\tilde{G}^2\tilde{\nu}^2\tilde{\rho}^2/M_{nn})\,dt_1 dt_2}{t_1 t_2(1-j\tilde{G}+j\tilde{G}t_1)(1+j\tilde{G}-j\tilde{G}t_2)M_{nn}}\Bigg\}\exp(-4\tilde{G}^2\tilde{\rho}^2),\end{aligned} \tag{4.65}$$

where

$$M_{nn} = \frac{\tilde{\nu}^2}{2}\left(\frac{1}{1-j\tilde{G}+j\tilde{G}t_1} + \frac{1}{1+j\tilde{G}-j\tilde{G}t_2}\right) + 1 + \tilde{\nu}^2\,, \tag{4.66}$$

and the remaining quantities are defined in Eqn. (4.58). Thus the solution I_{2n} also has a simple geometrical explanation. It is found that the statistical solution for $\langle I_2 \rangle$ derived in Sec. 4.1 can be used for $b_1 > 0$ simply by using the effective values $\tilde{G}$, $\tilde{\nu}$ and $\tilde{\rho}$ in Eqn. (4.58). However, the transformation for $\langle I_1 \rangle$ is exact, whereas for I_{2n}, it is an approximation based on the assumption $b_1 \ll d$.

It is interesting to see the validity of this simple geometrical acoustic approximation relation for the second-harmonic intensity $\langle I_2 \rangle$ as a function of b_1. The exact solution in Eqn. (4.63) written explicitly in App. D, is compared to I_{2n} in Eqn. (4.65) for different values of b_1. This comparison is shown in Fig. 4.22. One can see that I_{2n} can fairly well approximate $\langle I_2 \rangle$ for $b_1 < 0.5d$. For $b_1 \geq 0.5d$, I_{2n} shows an underprediction of $\langle I_2 \rangle$. In these ranges, the components I_{2l} and I_{2ln} that account for the second-harmonic field generated before the screen cannot be neglected.

One may also notice that there is only a slight change in the statistical curves for $b_1/d \leq 0.3$, which indicate that for $b_1 \ll d$ the expected values of the beam patterns exhibit little dependence on b_1. Since the body wall tissue is close to the transducer surface, modeling it as a phase aberration directly on the transducer plane is thus justified.

4.7 Summary

In this chapter we focused our analysis on Gaussian source radiation and derived the expected values of the intensities $\langle I_1 \rangle$ for the fundamental and $\langle I_2 \rangle$ for the second harmonic. The solutions are validated for small phase variances σ by comparison with numerical simulations. For a beam radiated by a piston source, however, the scattered field is different and far more complicated because of the side lobe structure. The solutions for $\langle I_1 \rangle$ and $\langle I_2 \rangle$ cannot be reduced to simple forms as was done for Gaussian beams. For the analysis of piston radiation, numerical simulation is necessary. In Chap. 5, we will use numerical solutions to study nonlinear scattering for a piston beam. The emphasis is on the influence of phase aberration on the main lobe and side lobes. The dependence of the beam pattern on the statistical properties of the phase screen are discussed. Computations are not restricted to a single phase screen model, and hence we consider also multiple screens between the source and receiver. The beam patterns obtained for several screens are compared with computations for a single phase screen. The analysis supplements our understanding of scattering for different beam structures.

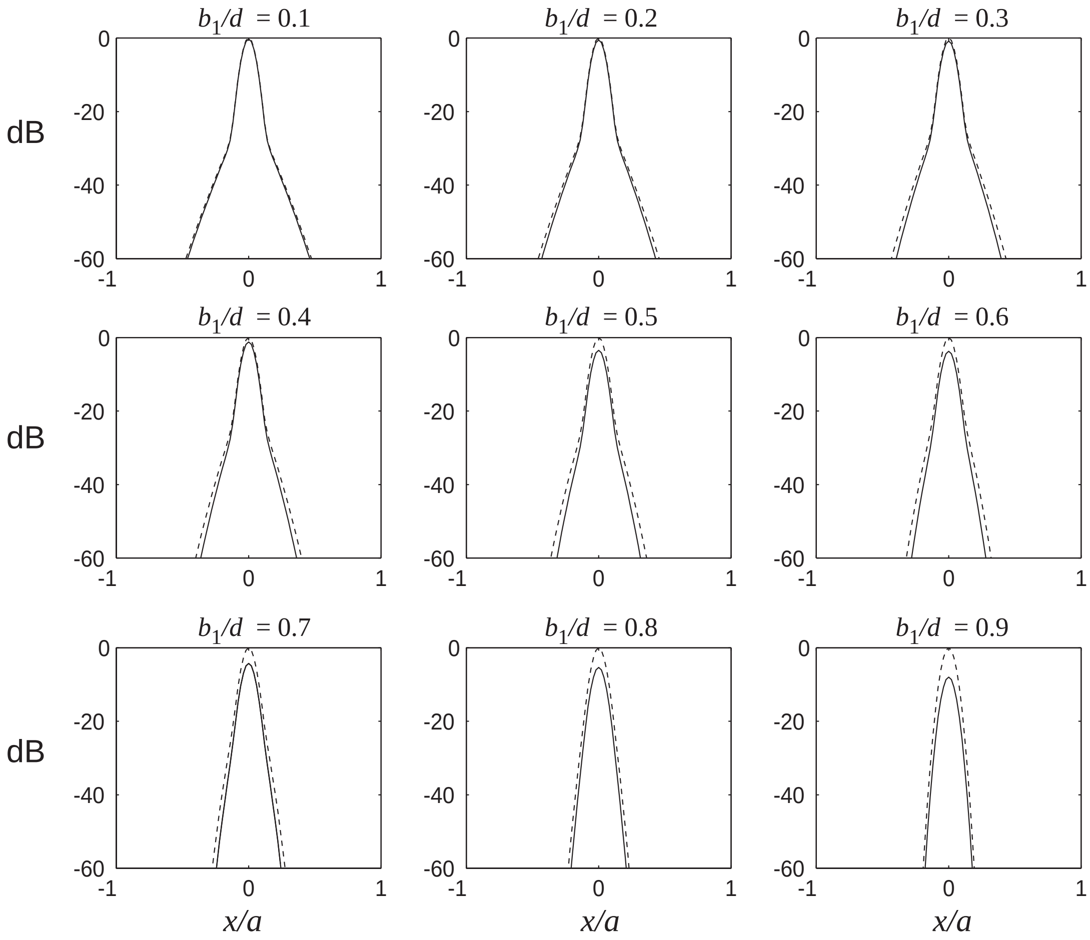

Figure 4.22: Comparison of exact solution of $\langle I_2 \rangle$ (dashed lines) with approximation of I_{2n} based on Eqn. (4.65) (solid lines) for different b_1. All plots are normalized to the maximum value of $\langle I_2 \rangle$. The phase screen's statistical parameters are: $\nu = 5$, $\sigma = 0.2$.

Chapter 5

Scattering of a beam radiated by a focused circular piston

The scattering of a beam radiated from a focused circular piston through a phase screen is discussed in this chapter. The corresponding nonlinear propagation in a homogeneous medium, mainly second-harmonic generation, has been studied by Lucas and Muir.[72,73] In the focal plane the fundamental field has a Bessel directivity pattern. However, there is no closed form solution for the beam pattern of the fundamental in any other plane, and there is no closed form solution for the second-harmonic anywhere in the field. For the single phase screen model, we are therefore unable to obtain simple forms of the statistical solutions for $\langle I_1 \rangle$ and $\langle I_2 \rangle$. The scattered fields are thus analyzed numerically.

The distortions of the focal beam patterns are investigated for a single phase screen as a function of correlation length l, phase variance σ, and position of the screen. The analysis is mostly qualitative, and our focus is on the general trends of the behavior of the scattered field, in particular whether they are consistent with the results for Gaussian beam scattering. We have special interest in the distortion of the main lobe and the structure of the side lobes. The latter are not present in a Gaussian beam in a homogeneous medium. In addition, we also investigate the effect of volume scattering, in which the phase change is distributed over an extended length in the propagation path.

In the following simulations, the source is a circular piston of radius a vibrating at frequency f. The focusing gain $G = ka^2/2d$ is taken to be 10. As before, for comparison, we consider also linear radiation from the same source but at frequency $2f$, with a focusing gain $G = 20$. In Sec. 5.1, the screen is placed in the source plane with fixed variance σ and different correlation lengths l. In Sec. 5.2, the correlation length l is fixed but σ is varied. In Sec. 5.3, l and σ are fixed but the position of the screen is varied between the source plane and the focal plane.

In Sec. 5.4, modeling of body wall tissue using single-screen and multi-screen approximations is discussed. Following that, in Sec. 5.5, comes a discussion of using a single-screen model to approximate an extended inhomogenous medium. Except for the simulation of propagation through an extended inhomogeneous medium using a finite difference algorithm to solve the KZK equation, all other simulations in this chapter are computed using the angular spectrum algorithm described in Sec. 3.2.

5.1 Dependence on correlation length l

In this section, screens with three different phase correlation lengths l ($\nu = a/l = 2, 5, 10$) but the same variance $\sigma = 0.4$ are used for the computations. The phase distributions of the three screens are shown in Fig. 5.1. The maximum phase change introduced by these screens is approximately π (i.e., $-1.5 \leq \phi \leq 1.5$).

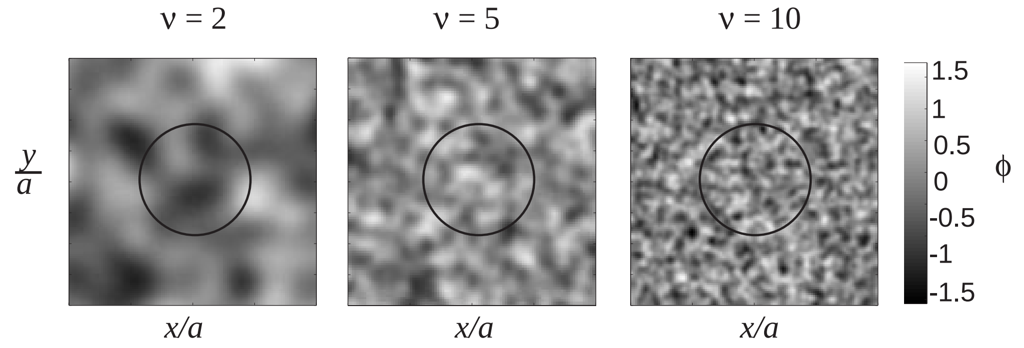

Figure 5.1: Phase screens with different correlation lengths that were used in the calculations: $\nu = a/l = 2, 5, 10$, with variance $\sigma = 0.4$. The circles indicate the relative size of the piston.

The resulting normalized focal beam patterns are shown in Fig. 5.2. The beam profiles in the x and y directions are given in Fig. 5.3. All plots have the same 60 dB dynamic range. The beam patterns without phase screens, equivalent to $\nu = 0$, are shown in Fig. 5.2(a)–(c). In this case, the amplitude distributions for the linear f and linear $2f$ beam patterns in the focal plane are

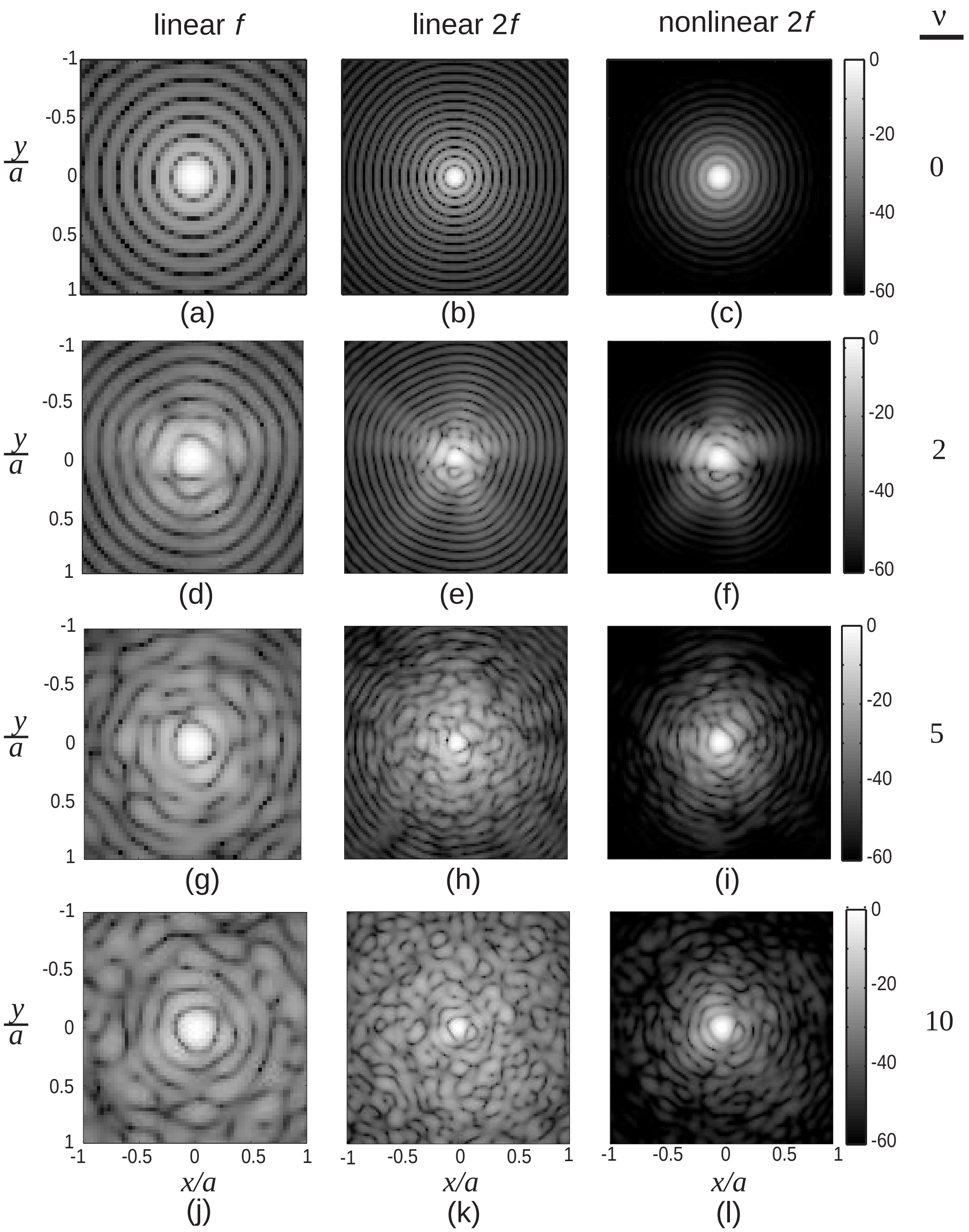

Figure 5.2: Top row: focal beam patterns without phase screen ($\nu = 0$). Second to fourth rows: focal beam patterns with phase screens in Fig. 5.1, respectively. The grayscale indicates relative intensity in dB.

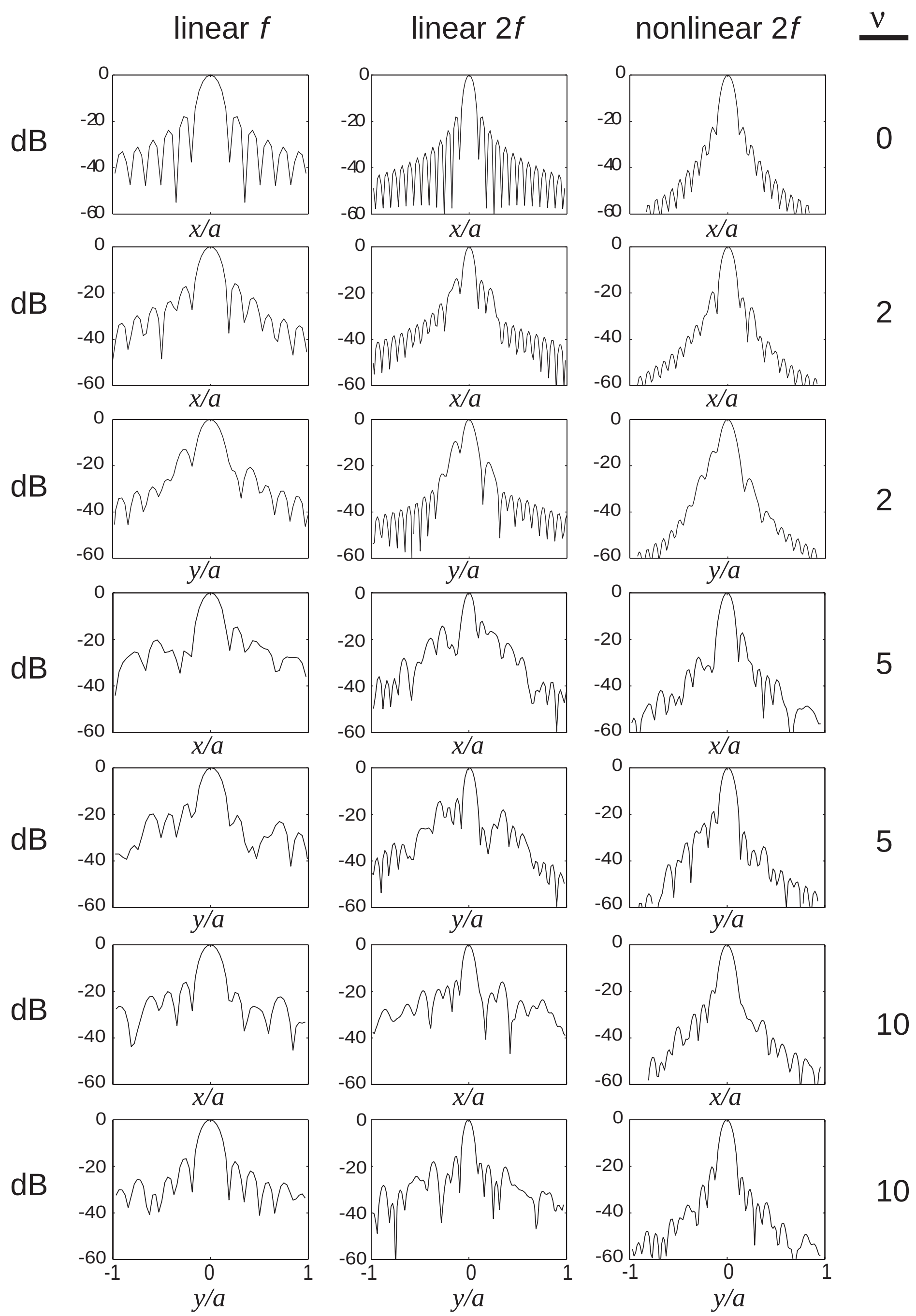

Figure 5.3: Focal beam profiles in the x and y directions corresponding to the beam patterns in Fig. 5.2.

given by

$$D(\rho) = \frac{J_1(2G\rho)}{\rho}\,. \tag{5.1}$$

For the second harmonic the amplitude is given in integral form by Lucas and Muir,[72,73] or it can be obtained from Eqn. (3.15) by setting $z = d$. In these undistorted beam patterns, the side lobe ring structures are clearly defined. The side lobe levels for the nonlinear $2f$ beam are lower compared to those of the linear beams. The first side lobe in the nonlinear $2f$ beam is about -22 dB below the main lobe, compared to -17 dB for the linear beams. When $\nu = 2$ ($l = 0.5a$), the main lobes for all three beams are slightly distorted, and the structure of the first few side lobes is destroyed. The higher-order side lobes are only slightly affected. This is also demonstrated by the beam profiles shown in Fig. 5.3. According to the discussion in Chap. 4, the distribution of the scattered field in the transverse plane is determined by the correlation length l. When l is large, corresponding to small ν, the scattered field is concentrated near the propagation axis, such that most of the beam distortion occurs near the main lobe. In the peripheral area, the scattered field amplitude is so small that the higher-order side lobes are virtually unaffected. In Fig. 5.2(d)–(f), the maximum side lobe levels are the same for the linear f and the nonlinear $2f$ beams, about -12 dB, lower than that of the linear $2f$ beam, which is -8 dB. When ν increases to 5 (l decreases to $0.2a$), shown in Fig. 5.2(g)–(i) and the forth and fifth rows in Fig. 5.3, the scattered fields spread out across larger areas. For all three beams, the side lobes are fully distorted. The maximum side lobe level is about -12 dB for the linear f beam, -15 dB for the nonlinear $2f$ beam, and -8 dB for the linear $2f$ beam. When ν increases to 10, shown in Fig. 5.2(j)–(l) and the last two rows in Fig. 5.3, the scattered region becomes even larger for the linear beams, but there is not so much change for the nonlinear beam. The amplitude of the scattered field near the beam center is reduced, and hence we can see that near the main lobe, the side lobe distortion is reduced a bit, and the ring structure of the side lobes tends to be restored. The maximum side lobe level is about -13 dB for the linear f beam, -15 dB for the nonlinear $2f$ beam, and -9 dB for the linear $2f$ beam.

Averages of the beam patterns in Fig. 5.2 are plotted in Fig. 5.4. The procedure used to average the distorted beam was described in connection with Fig. 4.10. The beam profiles without the phase screen (top row in Fig. 5.2) are represented by dashed lines. From Fig. 5.4 we can see that the deviation of the averaged beam profiles for the linear f and nonlinear $2f$ beams are not much different from the undistorted profiles. The linear $2f$ beam shows greater deterioration. In the presence of phase screen, the nonlinear $2f$ beam does not show obvious improvement over linear f beam compared to the undistorted situation. However, the linear $2f$ beam shows considerable degradation due to phase screen.

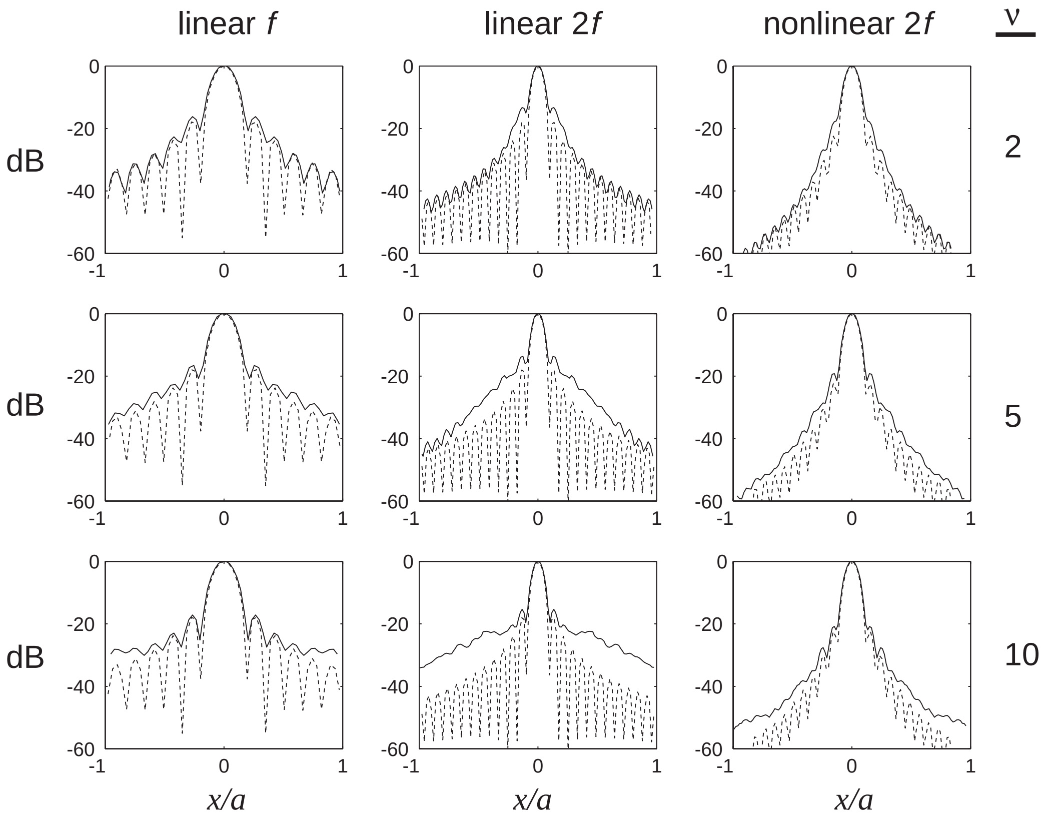

Figure 5.4: Averaged beam profiles for the linear f, linear $2f$, and nonlinear $2f$ beams (solid lines) displayed in Fig. 5.2. Dashed lines are the beam profiles without a phase screen, i.e., $\nu = 0$.

Compared to the undistorted beam profile, the major change of the statistical beam profile is the smoothing of the side lobe structure due to the incoherent contributions from the scattered field. When $\nu = 2$, the statistical beam profile for the linear f beam differs little from the unperturbed beam profile, except that the depths of the nulls between the side lobes are diminished. One may also notice a slight increase in the first side lobe level. For the linear $2f$ beam, since the phase changes doubles, the increase of the lower side lobe level is more prominent. For the nonlinear $2f$ beam, since its scattered field is more concentrated near the propagation axis than that of the linear f beam, we see more distortion near the beam center. There is appreciable increase in the lower-order side lobe level.

As ν increases, the scattered field diverges more in the transverse plane. This begins to substantially affect the higher-order side lobes. There is an increase of higher-order side lobe levels in all of the beam profiles. The side lobes for the linear $2f$ and the nonlinear $2f$ beams are smoothed out by the scattered fields. For the linear f beam, side lobes remain but the nulls between them are further diminished. When ν increases to 10, further spreading of the scattered field decreases its amplitude near the beam axis, such that distortion near the beam center is reduced, and more distortion occurs off axis. For all statistical beam profiles, except the first few side lobes, higher-order side lobes have disappeared. We can clearly see the increase of the scattered field amplitude in these regions.

From Fig. 5.4, and recalling the results for Gaussian beams in Figs. 4.11 and 4.14, we see that the scattered field of a piston beam cannot be easily separated from that of the coherent field. For an undistorted piston beam pattern, there is a certain amount of energy in the side lobe region, as shown by dashed lines in Fig. 5.4. Against this background, the scattered field only appears to diminish the nulls and slightly increase the side lobe levels judging from the averaged filed. Only when the scattered energy is much greater than the side lobe energy can we see clearly its behavior, such as the case for the linear $2f$ beam. For a Gaussian beam, however, we can easily distinguish the scattered field from the coherent field. There are no side lobes in a Gaussian beam, and therefore the scattered field becomes prominent outside the transition radius. Its statistical behavior is easier to analyze than that of the piston beam. Despite this difference, the general features of their scattered fields are similar. Basically, the phase correlation length l changes the distribution of the scattered field. With smaller correlation length (larger ν), the scattered field becomes broader. Also, the nonlinear scattered field becomes more concentrated near the beam center in comparison with the linear scattered field.

We now consider the focusing quality Q and corresponding Q_{norm} defined in Eqns. (4.50) and (4.51). It was argued there, on the basis of how scattering manifests itself in Gaussian beam patterns, that the focal region for a Gaussian beam should be defined as the nominal radius at which the level is 20 dB relative to the peak level in the beam. Since even in the absence of a phase screen the side lobe levels in piston radiation are within 20 dB of the peak level in the beam (for the linear f and nonlinear $2f$ beams, although not for the nonlinear $2f$ beam), the 20 dB threshold used for Gaussian beams is not appropriate for piston radiation. Instead we choose 6 dB as the threshold, since in the presence of a phase screen the maximum scattered side lobe that appears in the simulation is well beyond -20 dB if normalized to the peak value of the beam pattern, but not exceeding -6 dB (see Fig. 5.3). In order to exclude the side lobes in the focal area, we raised our threshold to 6 dB for piston beams. The values of Q and Q_{norm} for the beam patterns in Fig. 5.2 are presented in Fig. 5.5.

With this threshold we see that values of Q_{norm} are roughly the same for the linear f and nonlinear $2f$ beams, and they are both much larger than the linear $2f$ beam. The values of Q for the nonlinear $2f$ beam are much larger than those of the linear f and linear $2f$ beams. This is supported by observation of Fig. 5.4. One may also observe that as ν decreases (l increases), the values of Q (or Q_{norm}) for all the linear beams increase, which indicates a decrease in phase distortions. For the nonlinear $2f$ beam, however, the trend is reversed. The largest value of Q (or Q_{norm}) occurs when ν is largest (l is smallest), and the smallest value of Q (or Q_{norm}) occurs when ν is smallest (l is largest). The reason behind this lays in the fact that the energy in the nonlinear scattered field changes with different ν. It decreases when ν becomes large. This has

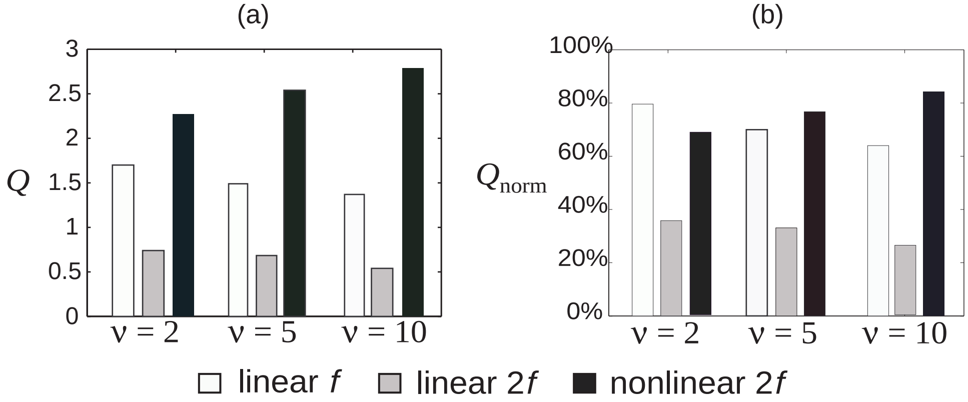

Figure 5.5: The focusing quality Q and Q_{norm} for the linear f, linear $2f$, and nonlinear $2f$ beams calculated for the beam patterns in Fig. 5.2.

been predicted by the Gaussian beam solution. Even though the scattered field has spread out more into the peripheral area with larger ν, the total scattered energy in the peripheral area actually decrease due to a decreased in the total scattered energy. In comparison to the linear beams, in which the scattered energy is independent of ν, when ν is large more scattered energy is present in the peripheral area, causing a decrease in Q, and hence in Q_{norm}. Despite this difference in the change of Q with parameter ν, Q is always larger for the nonlinear $2f$ beam than those of the linear beams, which is consistent with the observation in Gaussian beam. Moreover for the piston beam, relative decrease in focusing quality by the phase aberration, indicated by the parameter Q_{norm}, are roughly the same for the linear f and nonlinear $2f$ beams for $\nu = 2, 5$, but with $\nu = 10$, linear f beam has a larger decrease in its focusing quality.

5.2 Dependence on phase variance σ

In this discussion, the phase screen has a fixed correlation length l, but different values of the variance σ. The phase distribution of the screen, situated in the source plane, is shown in Fig. 5.6. It has $\nu = 5$ with σ increased from 0 rad to

1 rad (this screen has the same phase distribution as screen A in Fig. 4.8). The corresponding beam patterns in the focal plane are shown in Fig. 5.7. The beam profiles in the x and y directions are given by Fig. 5.8.

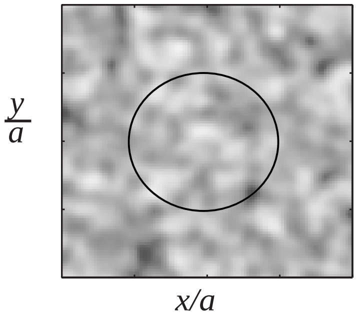

Figure 5.6: The phase screen with $\nu = 5$ used for investigating the effects of σ. The circle indicates the size of the piston.

From Figs. 5.7 and 5.8, one can see that as σ increases, scattering for both the linear and nonlinear beams increases. When $\sigma = 0.2$, side lobe distortion occurs, while the main lobe is only slightly affected. For the linear f and the nonlinear $2f$ beams, the scattered fields are not strong enough to fully distort the side lobe structures, especially in the peripheral area. The maximum side lobe level is about -14.5 dB for the linear f beam, about -12.5 dB for the linear $2f$ beam, and about -18.5 dB for nonlinear $2f$ beam. When $\sigma = 0.4$, the scattering is stronger, all beams lose their side lobe structures, and distortion is observed in the main lobes too. In this case, the maximum side lobe level for the linear f beam is -12 dB, for the linear $2f$ beam it is -8 dB, and for the nonlinear beam it is -14.5 dB. When $\sigma = 1$ rad, not only the side lobes, but also the main lobes have appreciable distortion. We see a substantial energy increase in the peripheral area, which is dominated by the scattered field. The maximum side lobe level is -6 dB for the linear f beam, and -7 dB for the nonlinear $2f$ beam. Particularly, for the linear $2f$ beam, the focal beam pattern is totally destroyed by the phase screen. The main lobe no longer seems to exist. The energy is distributed almost evenly over the outer region.

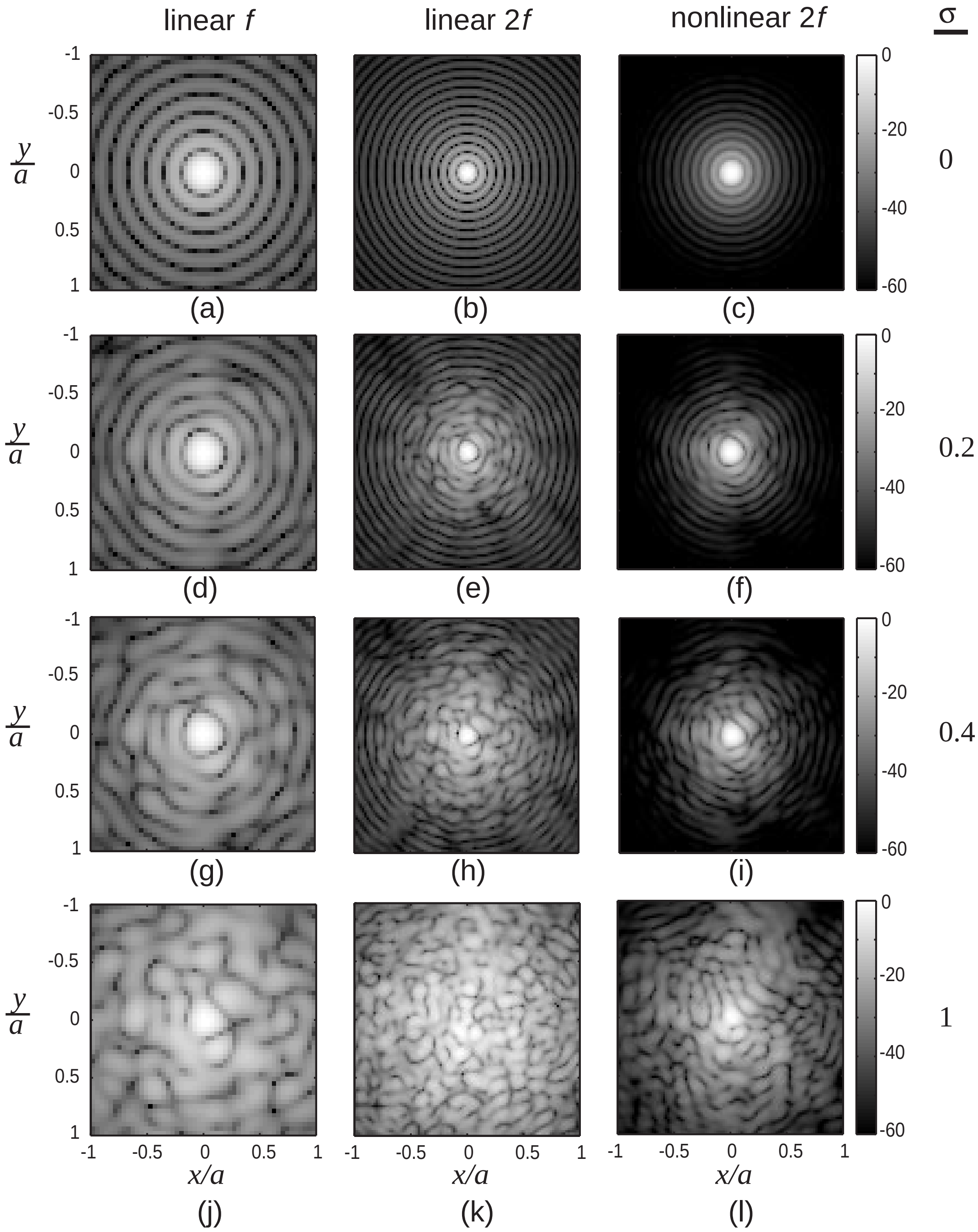

Figure 5.7: Focal beam patterns for the linear f, linear $2f$, and nonlinear $2f$ beams with the phase screen in Fig. 5.6. Top row: beam pattern without phase screen ($\sigma = 0$). Second to fourth row: beam patterns with phase screen having different values of σ, with $\nu = 5$. The grayscale indicates relative intensity in dB.

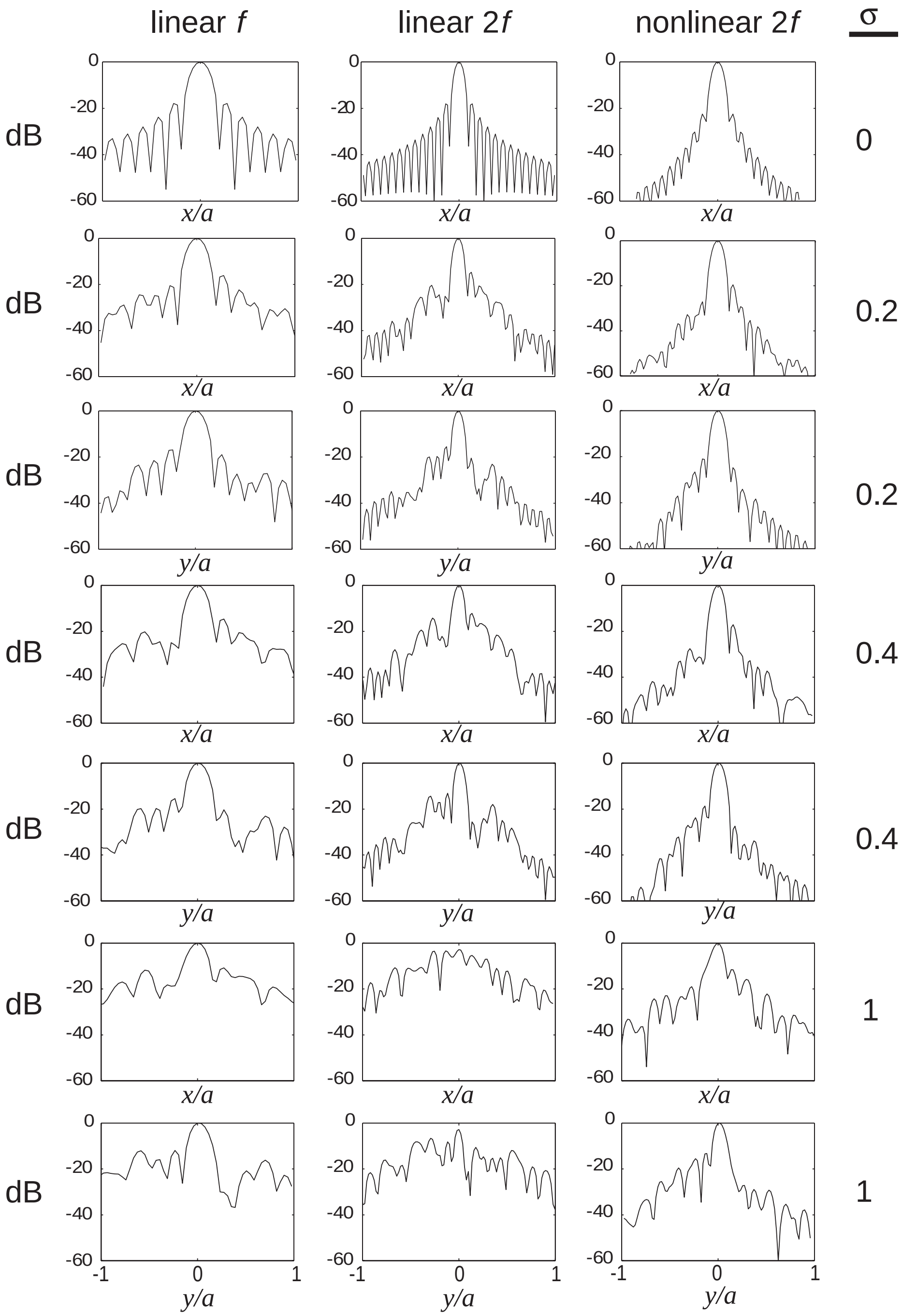

Figure 5.8: Beam profiles in the x and y directions correspond to beam patterns in Fig. 5.7, with $\nu = 5$.

The averaged beam profiles are shown in Fig. 5.9, where the dashed lines are the beam patterns without the screen, i.e., $\sigma = 0$. We see that for $\sigma = 0.2$, the scattered field amplitude is low, and except for the diminishing of the side lobe nulls, the averaged beam profiles are close to those without a screen. For $\sigma = 0.4$ the scattering level is increased, and higher-order side lobes have disappeared in the linear $2f$ and nonlinear $2f$ beams. Except for the linear $2f$ beam, the increase in side lobe level is not large. For $\sigma = 1$ there is considerable increase in energy in the scattered field. The increase is more or less uniform across the beam. For all three beams, the main lobes are somewhat buried in the scattered field. For the linear f and the nonlinear $2f$ beams, except for the first side lobes, all others have virtually disappeared. For the linear $2f$ beam the scattered field totally obscures the side lobe structure.

The focusing quality Q and Q_{norm} calculated for the cases $\sigma = 0.2, 0.4$ in Fig. 5.7 are given here as examples. The case $\sigma = 1$ is excluded because the scattering is so strong in this case that it is unreasonable to characterize the fields as beams. The threshold for setting the focal area is 6 dB. The results are shown in Fig. 5.10. The values of Q indicate that the nonlinear $2f$ beam is noticeably better than the linear f and linear $2f$ beams. The values of Q_{norm} indicates that the decrease in focusing quality Q for the nonlinear $2f$ beam is slightly less than the linear f beam. Compared to them, the linear $2f$ beam has a dramatic decrease in its focusing quality.

5.3 Dependence on screen position

In this section, the influence of the position of the phase screen is considered. The phase screen used here has the same distribution as the one shown in Fig. 5.6, with $\nu = 5$ and $\sigma = 0.4$. The focal beam patterns associated with different positions b_1 are shown in Fig. 5.11. Calculations of the nonlinear $2f$ beam is performed in two parts, as described generally in Sec. 4.6. First, the second harmonic incident on the screen at $z = b_1$ is calculated, then the random phase $2\phi(\mathbf{r})$ is applied, after which the field propagates linearly to the focal plane at $z = d$. The second part is calculated based on the fundamental pressure at $z = b_1$

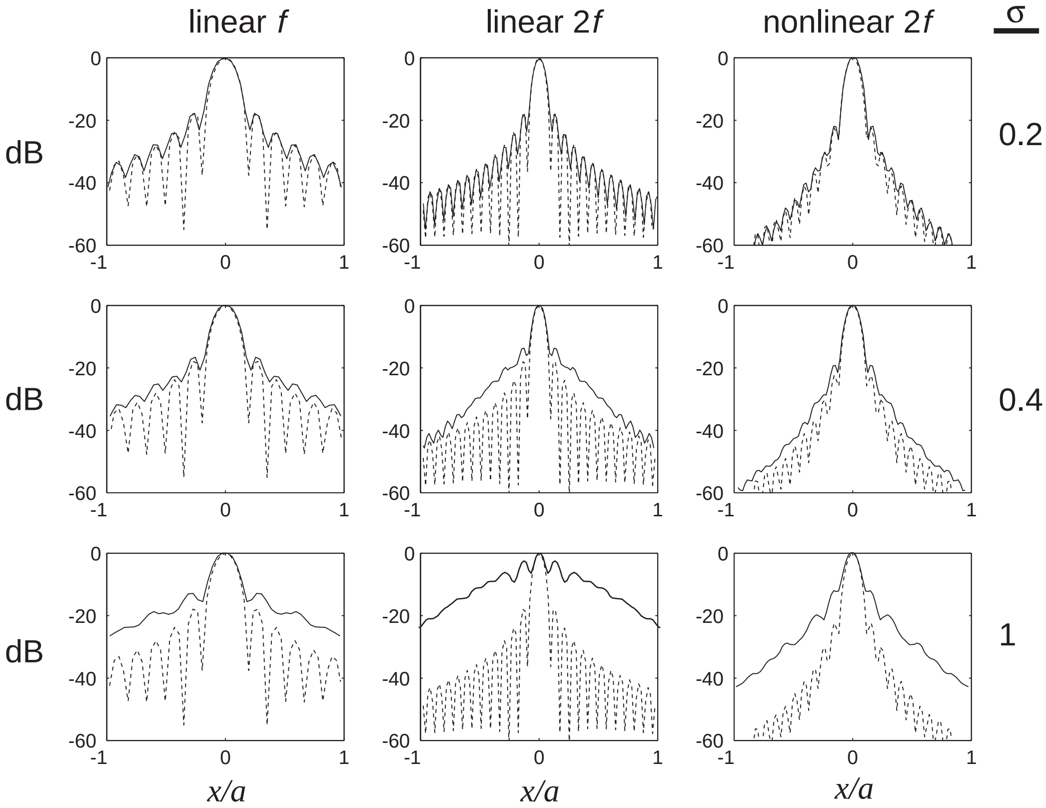

Figure 5.9: Averaged beam profiles for the linear f, linear $2f$, and nonlinear $2f$ beams (solid lines) displayed in Fig. 5.7, for $\nu = 5$. Dashed lines are the beam profiles without a phase screen.

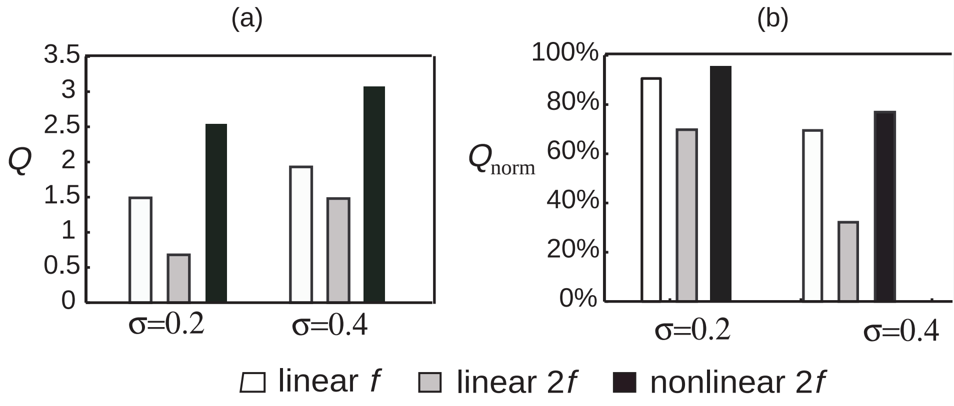

Figure 5.10: The focusing quality Q and Q_{norm} for the linear f, linear $2f$, and nonlinear $2f$ beam for $\sigma = 0.2, 0.4$ rad and $\nu = 5$.

with random phase $\phi(\mathbf{r})$ applied to it. Nonlinear propagation of this pressure generates a second harmonic in the focal plane. The total second-harmonic field is the sum of these two parts.

From Fig. 5.11, it is clearly seen that the beam pattern distortion is reduced as the screen is moved toward the focal plane. There is little difference between the beam patterns for $b_1 = 0$ and $b_1 = 0.2d$. But for $b_1 = 0.5d$ we see appreciable changes. The influence of scattering is confined more near the beam center. As b_1 increases to $0.7d$, the scattering region becomes further reduced. The side lobe rings can be seen for all the three beams. When $b_1 = 0.9d$, the beam patterns are close to the ones without the screen.

As mentioned in Sec. 4.6, when the screen is at distance b_1 from the source, the focal beam pattern can be approximated by the beam pattern radiated from an effective source with transformed radius and focal length situated at b_1, shown in Fig. 4.20. This geometric relation has been demonstrated by the statistical solutions for Gaussian beams. It was surprising to find that for a nonlinear $2f$ Gaussian beam this geometrical approxiamtion works quite well up to $b_1 = 0.5d$. For a beam radiated from a piston source, it is also interesting to investigate this relation. The averaged beam profiles based on the 2D calculations of beam pattern with an effective source having transformed radius and focal length situated

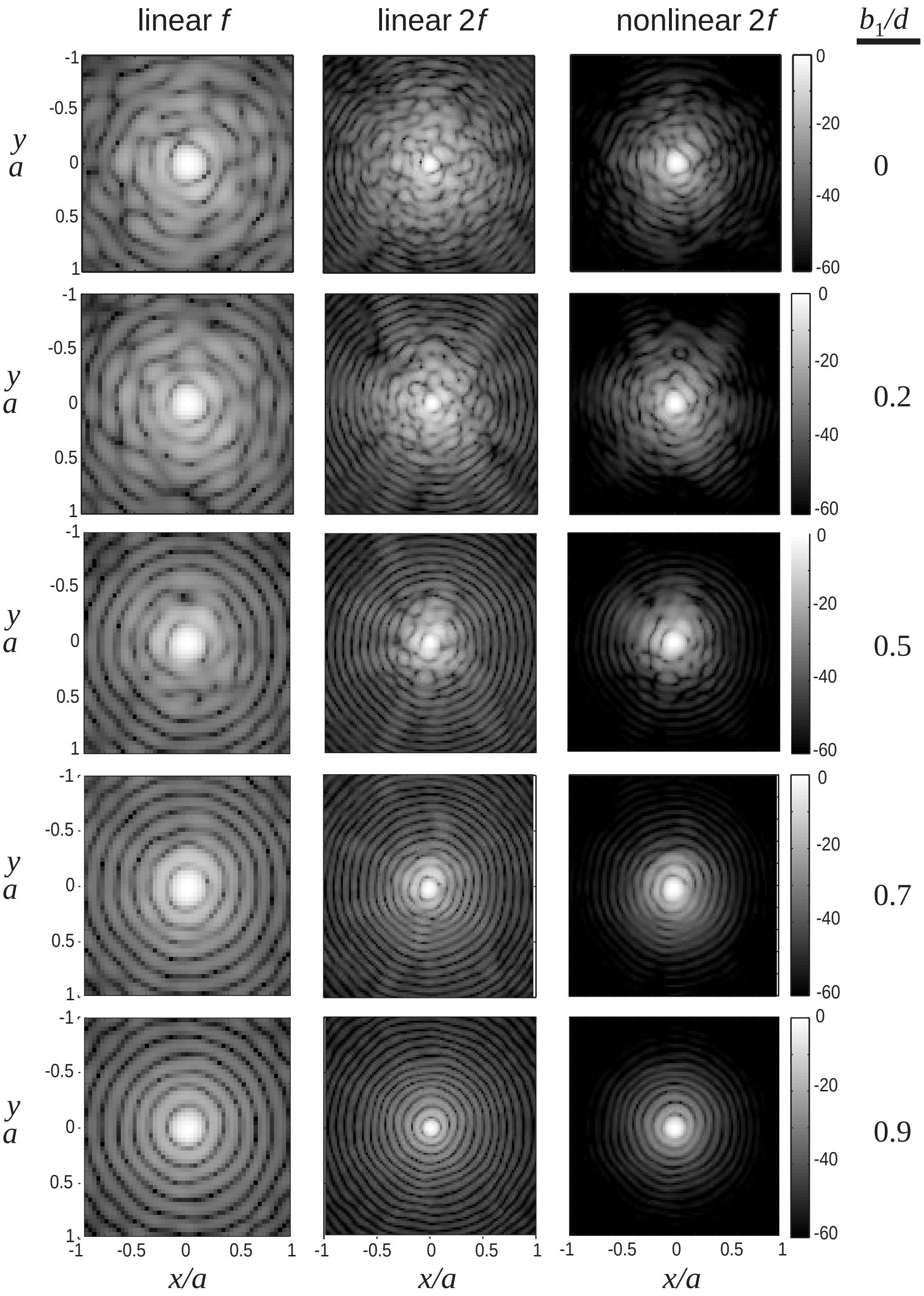

Figure 5.11: Focal beam patterns with a phase screen for which $\nu = 5$, $\sigma = 0.4$, positioned at different distances b_1 from the source plane. The grayscale indicates relative intensity in dB.

at $z = b_1$ ($b_1 = 0.2d \sim 0.9d$) are shown in Fig. 5.12. The results are compared to the averaged beam profiles associated with the beam patterns in Fig. 5.11.

From Fig. 5.12, one can see that similar to a Gaussian beam, the geometrical acoustics approximation works well up to $b_1 = 0.5d$ for both the linear f and nonlinear $2f$ beam. At greater distance, for the nonlinear $2f$ beam, the approximation underpredicts the statistical beam profile. For the linear f beam this geometrical approximation works fine even at $b_1 = 0.9d$. For the examples we show here, the transformation of source dimension based on geometrical acoustics can be used to predict the statistical beam patterns from $b_1 = 0$ to $0.5d$. Beyond this position, the transformation gives underprediction of the amplitude of the nonlinear $2f$ beam. For the linear f beam, the amplitude level can be predicted using this transformation all the way to $b_1 = 0.9d$. It should be mentioned here that this geometrical acoustics approximation cannot predict the actual pressure amplitude at any particular point in the wave field. The sample beam profiles obtained from this approximation and the phase screen calculations are different. This approximation can only predict the expected values of the beam patterns under proper condition.

5.4 Multi-phase screen model

In the previous analysis, a single phase screen was used to model the body wall layer. Although this is an idealized model it reveals the basic physics. A more sophisticated approach is to represent the layer as series of phase screens, which is multi-screen model. It has been briefly introduced in Sec. 2.4. Multi-screen methods have been used to model an extended tissue theoretically in linear imaging by Huang and Tsao[31] and computationally in nonlinear imaging by Christopher.[6] In this section, we follow the approach of Christopher to set up the multi-screen model. In this model, the phase distortion is distributed evenly over the thickness of the body wall represented by series of phase screens. The effect of this volume phase distortion on the focal beam pattern is compared to the effect of a lumped phase distortion represented by single screen model.

The method used to construct the multi-screens is the same as the one used

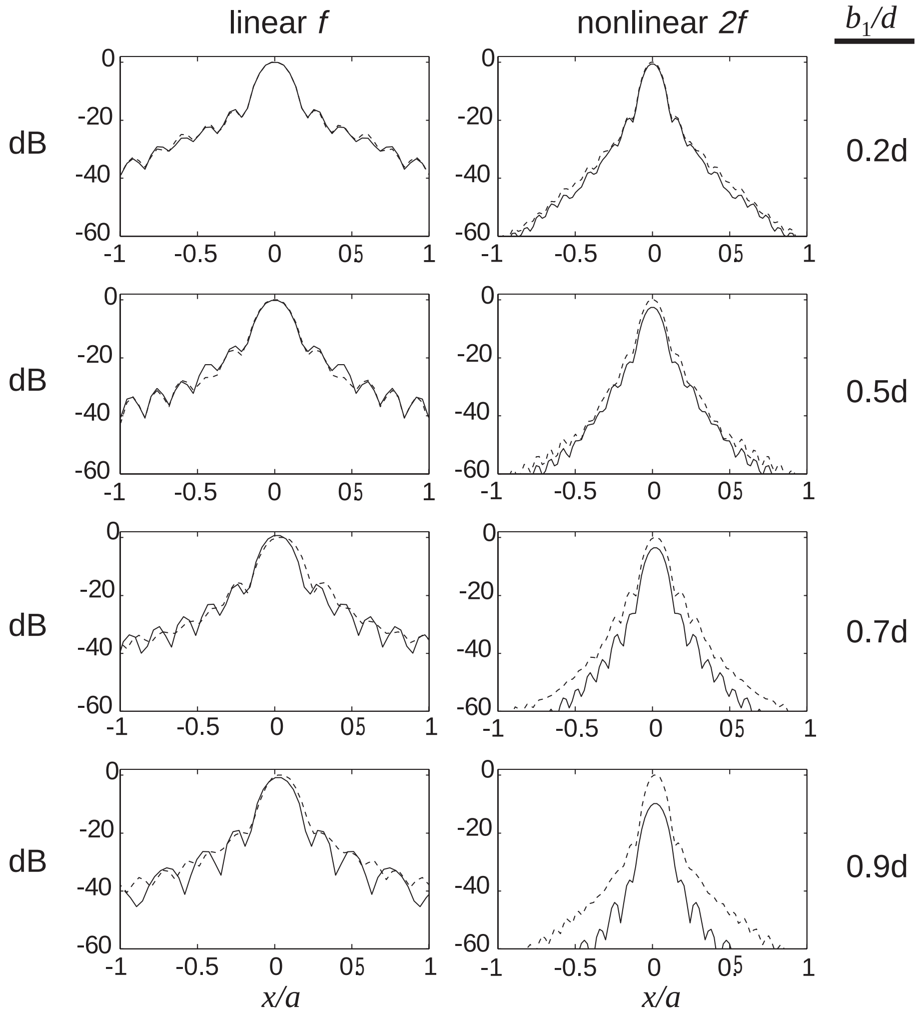

Figure 5.12: Comparisons of averaged beam profiles based on calculations of phase screen at different distances from the source plane corresponds to Fig. 5.11 (dashed lines), with calculations based on geometrical acoustics approximation for a phase screen at the source plane (solid lines). The phase screen has $\nu = 5$ and $\sigma = 0.4$.

by Christopher.[6] As shown in Fig. 5.13, We consider a tissue layer of thickness L. The cumulative phase distortion can be approximated by a single screen with phase variations $\phi(\mathbf{r})$ in the middle of the tissue layer, as shown in Fig. 5.13(a). Alternatively, N screens can be used, which are evenly spaced in the tissue layer as shown by Fig. 5.13(b)–(c). In this case each "subscreen" has a phase variation ϕ/N, where ϕ possesses the same distribution as the phase for the single screen. The phase variance of each subscreen thus becomes σ/N. For example, as shown by Fig. 5.13(a), the single screen with phase variation ϕ is placed in the middle of the layer. In Fig. 5.13(b), the two screens are placed at distances $L/3$ and $2L/3$ from the source, etc.

The phase distribution of a single screen is shown in Fig. 5.6, for which $\nu = 5$ and $\sigma = 0.4$. The thickness of the tissue layer $L = 0.4d$. The computation of the fundamental field requires N intermediate steps. Each steps requires the calculation of pressure at the kth subscreen based on the pressure distribution in the $(k-1)$th screen $(k = 1, 2..N)$. When the pressure at the Nth screen is obtained, an additional calculation is needed to propagate this pressure to the focal plane. The computation of the second harmonic field is based on the method described in Sec. 5.3, where the propagation through one screen is discussed. The same procedure is repeated from screen to screen in the multi-screen model. The computed beam patterns in the focal plane associated with single, double and quadruple screens are plotted in Fig. 5.14.

From Fig. 5.14 it can be seen that the three models generate very similar field patterns in the focal plane for both the linear and nonlinear beams. Indeed, it is hard to tell the differences between the three models, as even the details of the distortion are quite similar. Comparisons are also made of the averaged beam profiles, which are shown in Fig. 5.15. The results are virtually indistinguishable.

In this example, we see that a lumped single screen that accumulates the phase distortion in a finite layer produces the same scattering effects as when the phase distortion is evenly distributed over the same length L which is represented by serie of phase screens. Berkhoff and Thijssen[71] reached a similar conclusion in their development of a scheme to correct for aberration in linear imaging. They

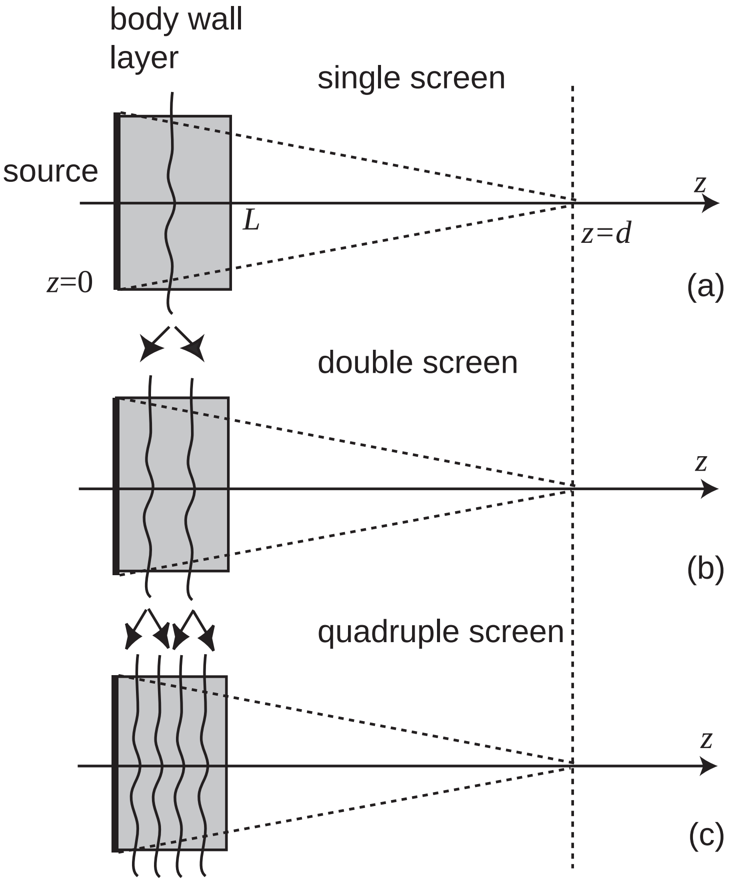

Figure 5.13: Construction of the multi-phase screen model. The phase screens are positioned evenly over a finite length L ($L = 0.4d$). (a) single screen, (b) double screen, (c) quadruple screen.

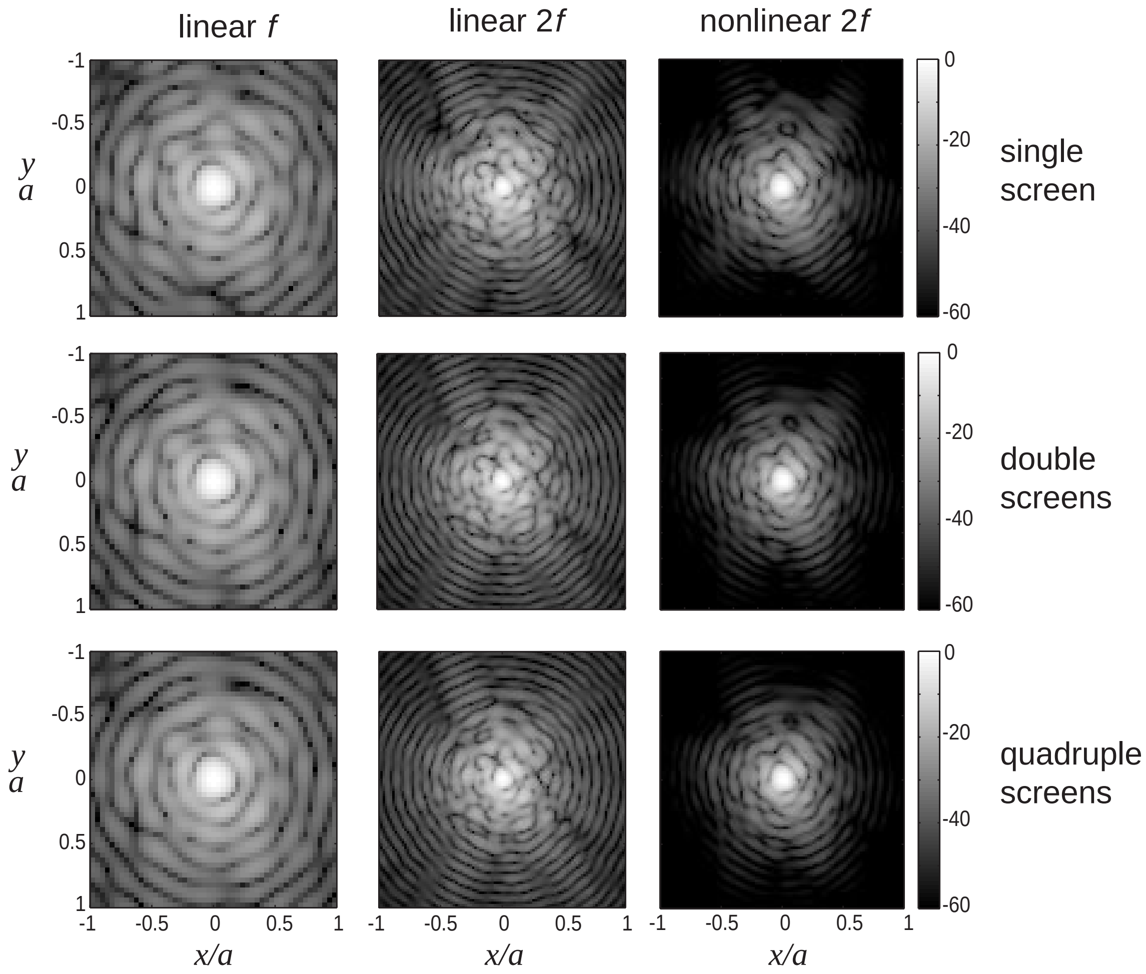

Figure 5.14: Focal beam patterns for the linear f, linear $2f$, and nonlinear $2f$ beams computed using single screen, double screen, and quadruple screen approximations of a random layer of finite thickness. The grayscale indicates relative intensity in dB.

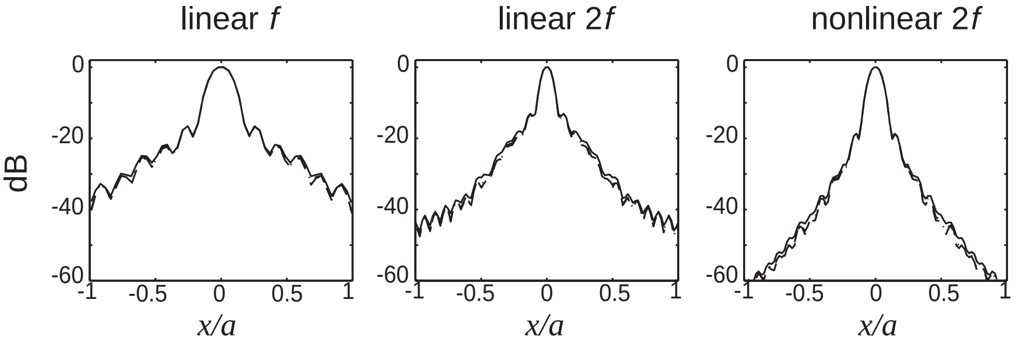

Figure 5.15: Averaged focal beam profiles for the linear f, linear $2f$, and nonlinear $2f$ beams based on single screen (solid line), double screen (dash-dot line), and quadruple screen (dashed line) models.

found that the correction algorithm intended for a single screen method can be used to reduce effects due to distributed aberration, which are modeled as series of phase screens. In the correction scheme, these screens were approximated by one concentrated single screen placed in the center of the aberrations. The correction based on this assumption was shown to work just as well.

5.5 3D random layer

The phase screen model discussed up to here is based on the assumption that phase variations in an extended tissue layer can be lumped into a single screen. As shown in Sec. 5.4, this single screen model is equivalent in the sense of producing scattered focal beam patterns to a multi-screen model in which the lumped phase variations are evenly distributed over the tissue thickness L represented by series of subscreens. In the multi-screen model, the subscreens all have the same phase distributions, which means that the phase is coherently distributed over the thickness L. If the thickness of the layer is on the order of correlation length of the medium in the z direction, then this is a reasonable assumption. If the thickness is much larger than the correlation length, coherence in the distribution of phase inside the layer would result in a poor approximation. To investigate the validity of the phase screen model when thickness of the layer is several correlation lengths we performed a calculation with a 3D random medium in which the sound speed varies continously in both the transverse and axial directions. To make this calculation we use the algorithm described in Sec. 3.3 for solving the KZK equations.

In our computations, the 3D random layer is isotropic with the same correlation length in all directions. The generation of this 3D random medium is similar to the procedure of generating 2D random screen which is shown in Fig. 4.7. Here, the correlation function and the filtering process are all in 3D domain. The correlation length is again normalized to the transducer radius with $\nu = a/l = 5$ and the source is a focused circular piston with focusing gain $G = 10$. Two comparisons are made, first with $L = 5l$, and second with $L = 10l$. In each case, the 3D random layer occupies the region $0 < z < L$. The focal beam patterns obtained with the 3D random layer are compared with those obtained with a single screen model, in which the total phase variations inside the layer are lumped into one screen placed in the source plane. The resulting focal beam patterns for the linear f and nonlinear $2f$ fields are shown in Fig. 5.16. The corresponding beam profiles along the x and y axes through the focus and the averaged beam profiles are shown in Figs. 5.17 and 5.18.

From Figs. 5.16–5.18, one can see that for the layer with thickness $L = 5l$ the single screen model provides a good approximation of the 3D medium in terms of the scattered field level and averaged beam profiles. Individual pressures are less predicted as expected. For $L = 10l$ the single screen model is not a good approximation in all respects. As seen from the beam patterns in Fig. 5.16, the single phase screen model underpredicts the scattered field levels. Inspection of the averaged beam profiles shows that single screen predictions slightly underestimate the levels off axis

From this comparison, one can see that when the thickness of the random layer is much larger than the correlation length (e.g., $L > 10l$) the validity of the single screen model is questionable. When the thickness is on the order of just few correlation lengths, however, the single sceen model provides an accurate

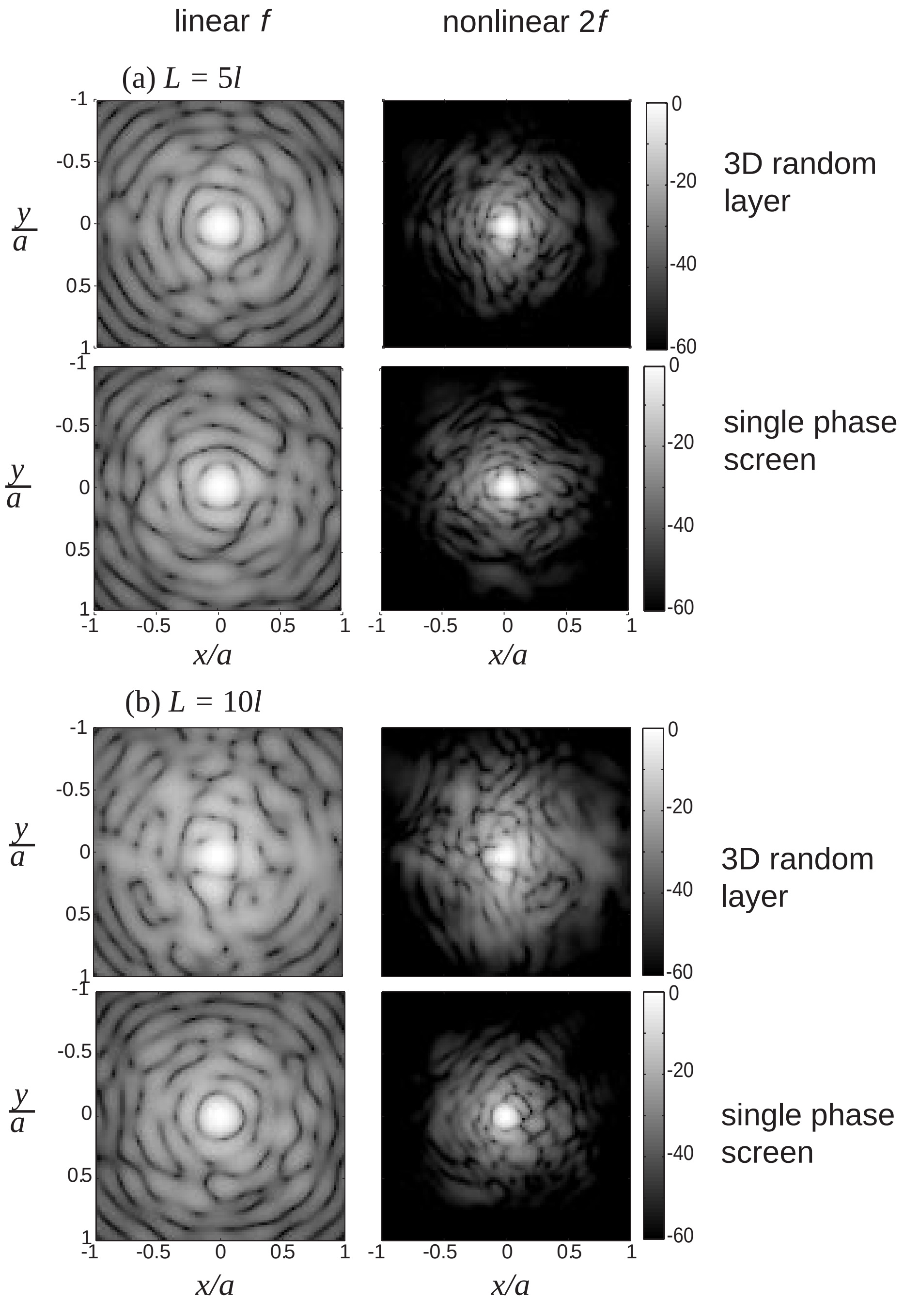

Figure 5.16: Comparisons of focal beam patterns for the linear f and nonlinear $2f$ beams passing through 3D random layer of thickness L and single phase screen with zero thickness. (a) $L = 5l$, (b) $L = 10l$. The grayscale indicates relative intensity in dB.

(a) $L = 5l$

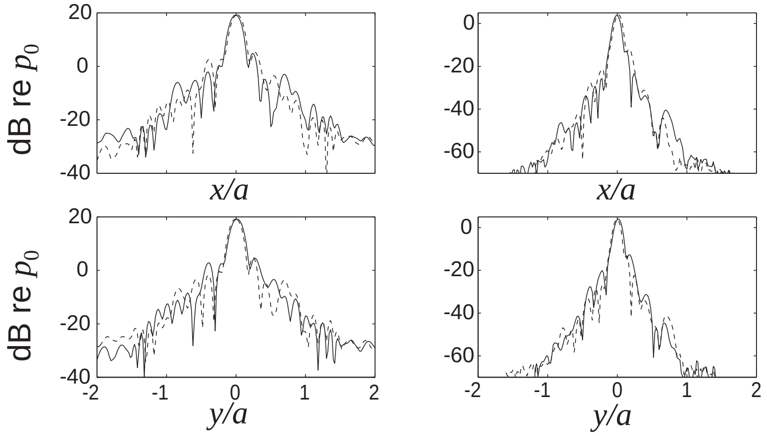

(b) $L = 10l$

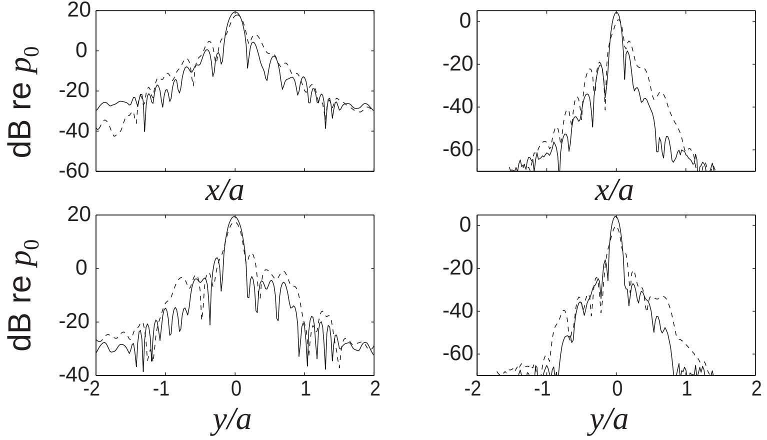

Figure 5.17: Comparisons of focal beam profiles along x and y directions for the 2D patterns in Fig. 5.16. The dashed lines are beam profiles obtained with 3D random layer. The solid lines are with single screen. (a) $L = 5l$, (b) $L = 10l$.

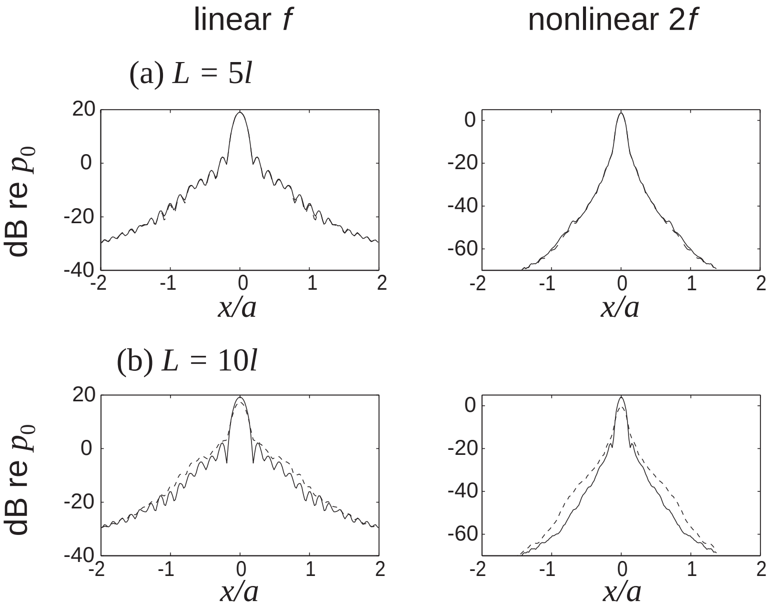

Figure 5.18: Comparisons of averaged focal beam profiles for the 2D patterns in Fig. 5.16. The dashed lines are beam profiles obtained with 3D random layer. The solid lines are with single screen. (a) $L = 5l$, (b) $L = 10l$.

representation of the statistical behavior of the scattered field.

Finally, in the example where the single screen model is used for approximating the 3D medium with $L = 5l$, we provide a figure to illustrate the change of beam profiles along the propagation axis. In Figs. 5.16(a) and 5.17(a), only the focal beam patterns are shown, whereas in Fig. 5.19, the beam patterns before and after the focus are also plotted and compared with the corresponding beam patterns without the phase screen.

As we see from this section when the medium thickness is much larger than its correlation length, single screen does not provide a good approximation. In this case multilayer phase screens with independent phase distributions are shown to be a more reasonable model. Here we make a comparison of the focal beam patterns with 3D random layer propagation with layer thickness $L = 10l$, shown in Fig. 5.16(b) with the result of using two phase screens. The two phase screens are statistically independent of each other and each accumulates the phase variations in the 3D layer within half of the thickness. The position of the phase screen is evenly distributed over the layer thickness L. With the two phase screen model we obtain the focal beam patterns for the linear f and the nonlinear $2f$ beams, together with the sample beam profiles and the averaged beam profiles, shown in Fig. 5.20. From this figure we can see the multilayer screen model can predict the scattered field level caused by the 3D random layer with a thickness much larger than correlation length.

5.6 Discussion

In this chapter we investigated numerically the scattered field for a piston beam. Compared to the results for a Gaussian beam, the relatively large energy associated with the side lobes complicates the analysis. However, the general trend of the scattered field is the same as what is observed for a Gaussian beam. For a fixed value of the phase variance σ, different values of the correlation length l change the rate at which the relative importance of the scattered field increases with distance off axis. For fixed l, increasing σ increases the level of the scattered field. From the statistical beam profiles, we can see that the side lobes are more

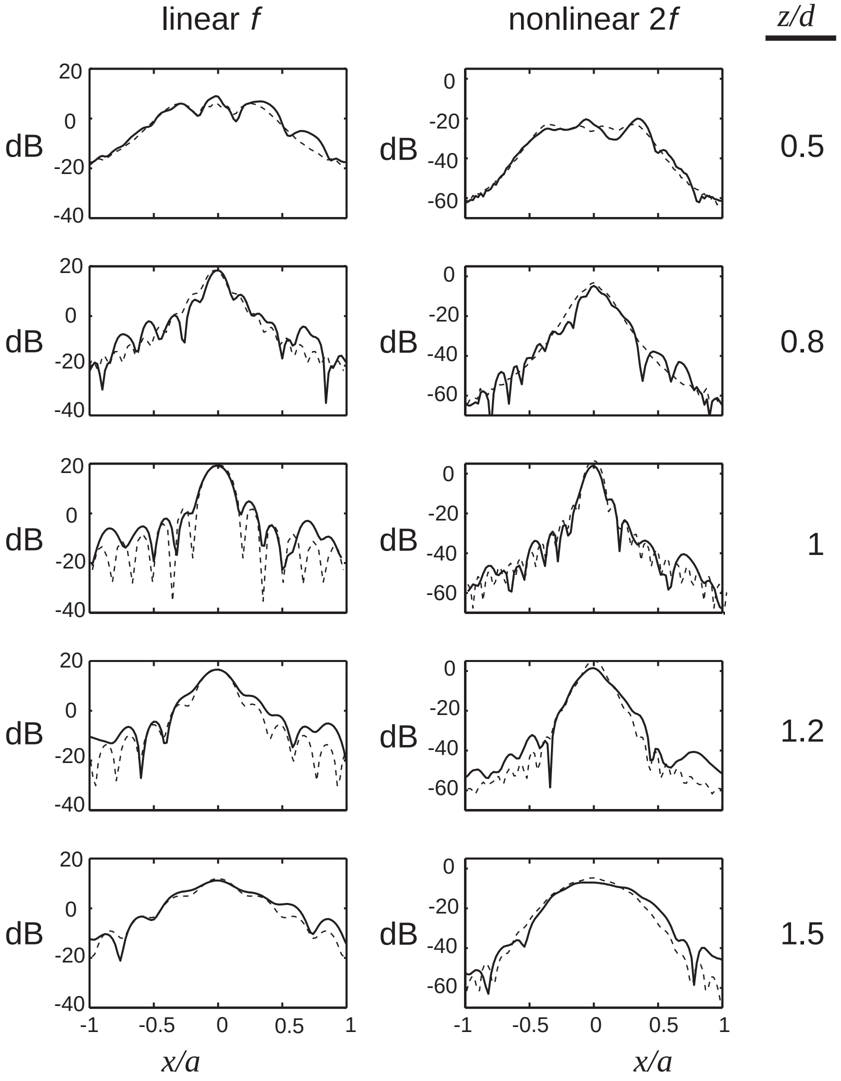

Figure 5.19: Beam patterns at different propagation distances obtained with single screen model shown in Fig. 5.16(a). Solid lines represent the beam patterns with phase screen, dashed lines represent beam patterns without phase screen.

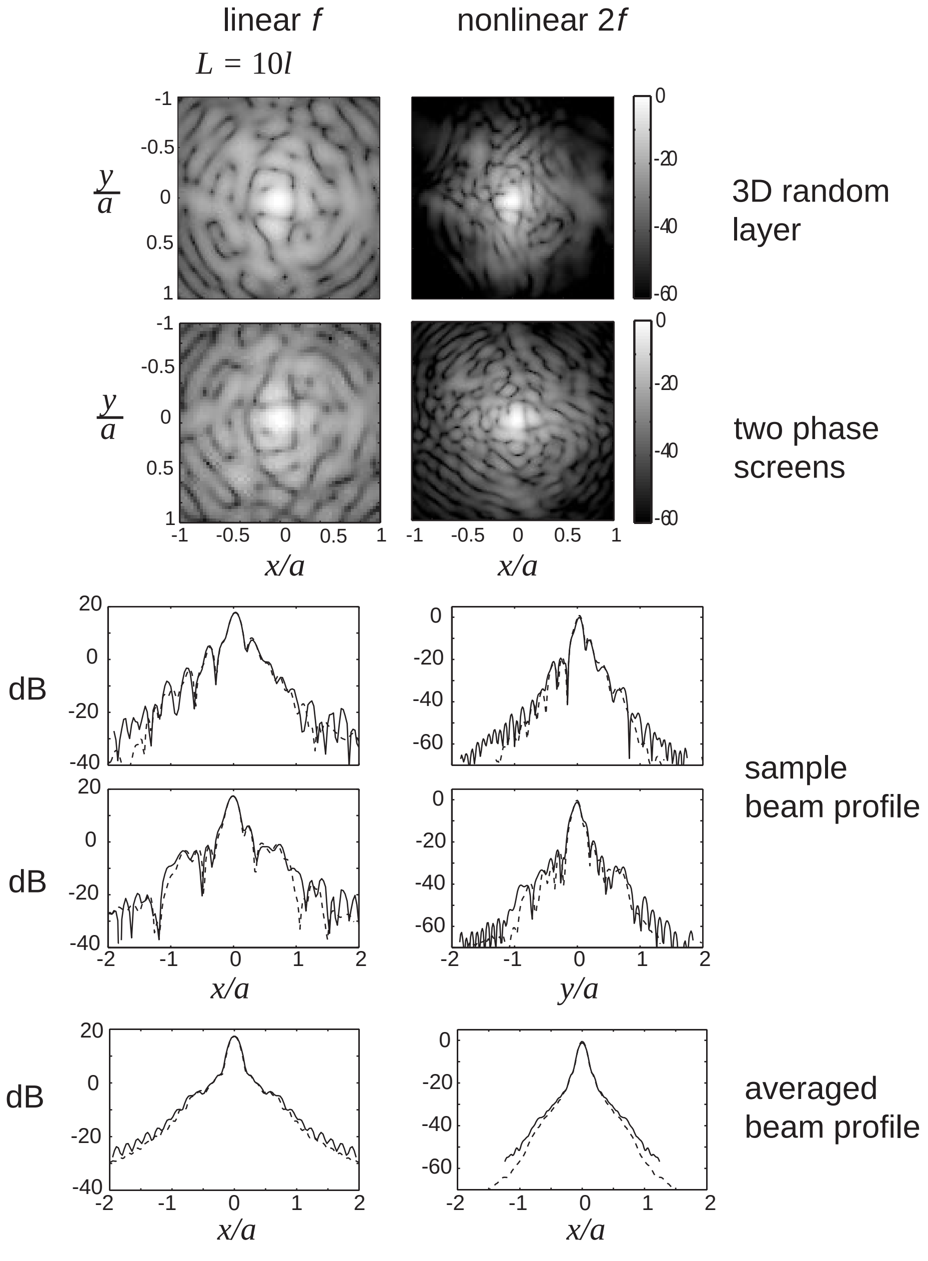

Figure 5.20: Comparisons of focal beam patterns for the linear f and nonlinear $2f$ beams passing through 3D random layer of thickness $L = 10l$ and two phase screens with zero thickness and independent phase distributions. The grayscale indicates relative intensity in dB. For all the beam profiles the solid lines represent two-screen model, the dashed lines represent 3D layer calculation.

sensitive than the main lobe to the phase aberration. The side lobe nulls and peaks are the results of coherent phase addition, so they are more sensitive to the phase changes. The relatively high energy level in the main lobe makes it more immune to phase aberrations.

The focusing quality Q and the sample beam profiles investigated in this chapter reveal advantages of the nonlinear $2f$ beam over the linear f and $2f$ beams when subject to the same phase screen perturbation. In comparison, the linear $2f$ beam suffers the greatest degradation. This is consistent with the observation of the focusing quality Q for Gaussian beams. Comparing of Fig. 4.16 with Fig. 5.10 as an example, we see that the second harmonic is noticeably better than the fundamental and linear second harmonic radiation for both the Gaussian beam and the piston beam. This conclusion follows from the comparison of the values of Q for the three beams.

An investigation of the screen position shows a reduction in the effect of phase aberration when the screen is moved closer to the target plane. A comparison of the beam patterns obtained with the effective source based on the geometrical acoustics approximation and the two-step phase screen calculations is made for screen position that varies from 20% to 90% of the distance to the focal plane. In these examples, the transformation predicts the scattered field well for screen positions less than half way to the focal plane.

Finally, an investigation of the multi-screen model in which phase distortion is coherently and evenly distributed over the medium thickness in the direction of propagation suggests that it has the same effect as the lumped phase distortion represented by a single screen. This leads to another investigation in which the phase distribution is not coherent in the propagation direction, but rather randomly distributed. In the simulations, the single phase screen model is found to be a good approximation of a 3D random layer if the layer thickness is on the order of the correlation length. For medium thickness is much larger than correlation length, multilayer screen model should be used instead.

The analysis of scattering in a beam radiated by a circular piston is supplemented by phase screen measurements presented in Chap. 6. Strictly speaking, the phase variations in the screen used in the experiments is not totally random, but rather it is formed by a random distribution of regular patterns. However, these manufactured phase screens provide a good basis for comparison with the analysis presented in this chapter.

Chapter 6

Phase screen experiments

In this chapter we report an experimental investigation of the scattered field from a circular piston source. A phase screen was used to distort the beam. The goal of our experiments was to measure accurately the distortion of the linear f and nonlinear $2f$ beam patterns due to radiation from a typical focused piston source through a random phase screen. All measurements were taken in the Ultrasonics Laboratory in the Mechanical Engineering Department at The University of Texas at Austin. General details of the tank set-up are described by Landsberger.[51] Our specific set-up is shown in Fig. 6.1. A thin (with maximum thickness $h = 3.17$ mm) low density polyethylene plate with varying thickness serves as the phase screen. The screen was created by cutting a random pattern into the surface of the plate. The polyethylene is a plastic material that has a specific acoustic impedance of about 1.9 Mrayls and a sound speed of about 2100 m/s. The reason for selecting this material was because of the relation of these parameters to those of water, in which the experiments were performed, and for which the specific acoustic impedance is 1.48 Mrayls and the sound speed is 1486 m/s. The goal was to find a material having a specific acoustic impedance as close as possible to that of water in order to minimize transmission loss, but having a sound speed as different as possible from that of water in order to maximize phase changes due to variations in thickness of the material. The polyethylene appeared to provide the best compromise in satisfying these criteria, providing a plane wave transmission coefficient of $T = 1.12$ for the acoustic pressure at the water-plastic interface.

By cutting a pattern into the plastic sheet, one may obtain a phase variation across the surface as a function of the local plate thickness, thus producing the phase screen. The plate is placed in the prefocal region of a focused circular piston transducer, perpendicular to the transducer axis. The beam patterns are

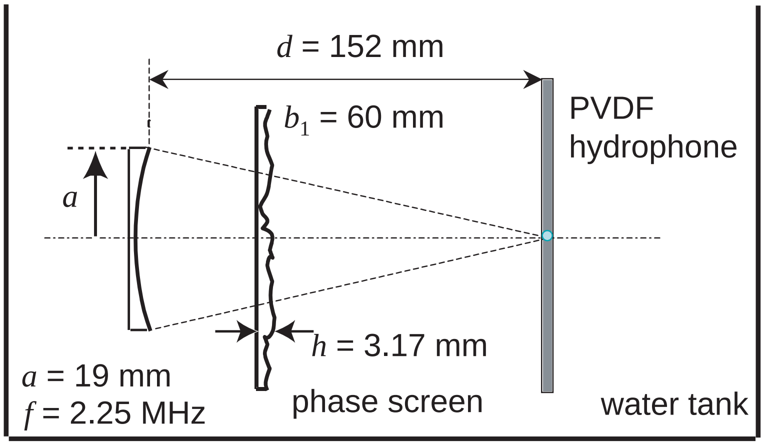

Figure 6.1: The set-up for the phase screen measurements.

measured in the focal plane using a broadband PVDF membrane hydrophone. The source transducer is made by Panametrics and has a diameter of $2a = 38.1$ mm, a focal length of $d = 152$ mm, and a center frequency of $f = 2.25$ MHz. The PVDF membrane hydrophone is made by Marconi and has a receiving element 1 mm in diameter. The hydrophone is calibrated by the National Physical Laboratory (Teddington, Middlesex, England) from 0.5 MHz to 20 MHz at about 1 MHz steps in frequency. The positioning apparatus of the hydrophone is controlled via computer and has a spatial resolution of 20 μm. The source, hydrophone and plate are all immersed in a water tank containing de-ionized, degassed fresh water. A block diagram of the entire measurement system, including electronic and mechanical parts, is shown in Fig. 6.2.

The transmitted signals are CW pulses (around 15 cycles) at 2.25 MHz frequency generated by a HP 3314A function generator, which are sent to the ENI model 2100L RF power amplifier, which produces 50 dB amplification. The amplified signal is then sent to the transducer. The signal received by the hydrophone is sent to the EG&G model 115 wideband preamplifier providing 20 dB gain, after which it is sent to the Sony/Tektronix RTD 710 digitizer. The digitizer has 10-bit dynamic range and maximum sampling rate of 5 ns, which

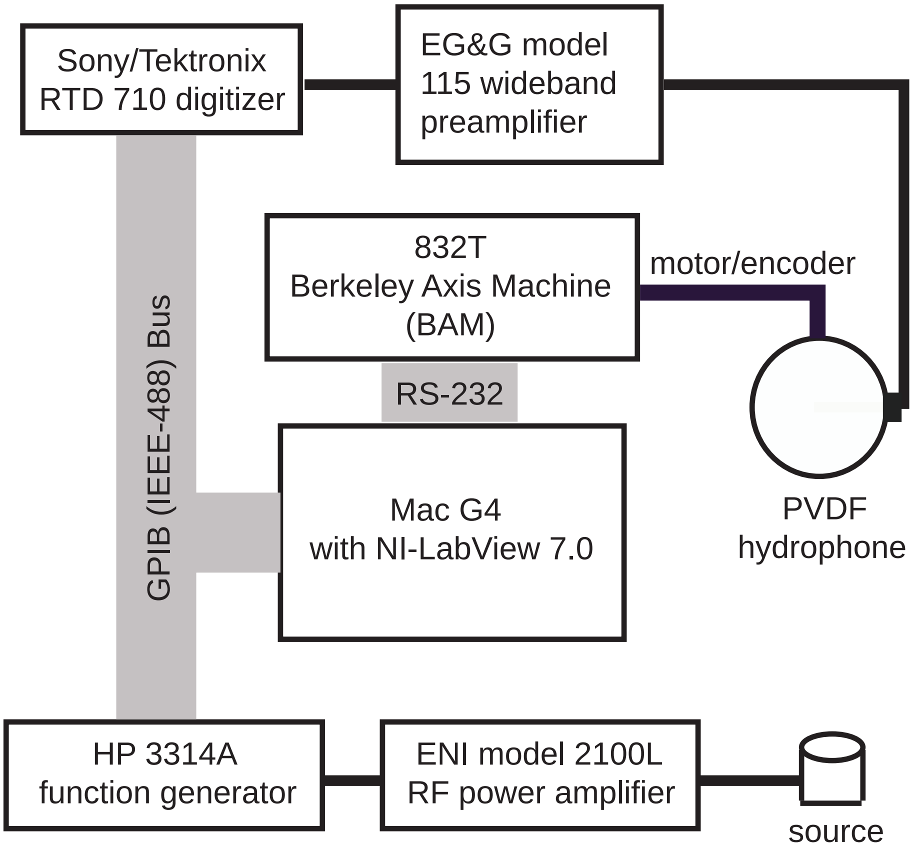

Figure 6.2: Block diagram of the entire system.

permits sampling up to 100 MHz. The digitized waveform is finally sent to the computer to be analyzed. The positioning apparatus for the hydrophone is controlled by a 832T Berkeley Axis Machine (BAM). The computer controls all instruments and the BAM through LabVIEW virtual control. The communication between the computer and instruments is through a GPIB bus (IEEE 488), and the communication between the computer and BAM is through a serial port RS-232.

Before all phase screen measurements, the influence on the focal beam pattern arising from the impedance mismatch between the plate and water and from the plate thickness was investigated. In an ideal situation, the phase plate should have zero thickness and introduce only a phase variation, with a unity amplitude transmission coefficient. In our experiments, depicted in Fig. 6.1, the plate has a maximum thickness of $h = 3.17$ mm, and its impedance is higher than that of water. The transmission loss introduced by the plate for plane wave incidence is[74]

$$\mathrm{TL} = 10\log_{10}\left[\cos^2 k_p h + \frac{1}{4}\left(\frac{z_p}{z_w} + \frac{z_w}{z_p}\right)^2 \sin^2 k_p h\right]\,(\mathrm{dB})\,, \tag{6.1}$$

where $z_p = 1.91$ Mrayls and $z_w = 1.48$ Mrayls are the specific acoustic impedance of the plate and water, respectively. The wavenumber $k_p = 2\pi f/c_p$ is obtained with the polyethylene sound speed $c_p = 2100$ m/s. The transmission loss obtained from Eqn. (6.1) is 0.27 dB at 2.25 MHz. Therefore the impedance mismatch between the plate and water is such a weak effect that it can be neglected in the measurements. Therefore the only amplitude change that introduced by the plate comes from the loss of the polyethylene material, which can be compensated by increasing the source pressure level.

One may also calculate the wavelength inside the plate to be 0.93 mm. The maximum thickness of the plate is therefore around three wavelengths. The diffraction effect over such a small propagation distance is assumed to be very small. To check this conclusion, we performed a measurement with a uniform 3.17 mm thick plate placed in the prefocal region 60 mm away from the source. This position is where the phase screen is to be placed in the subsequent measurements. The focal beam patterns obtained with the plate are compared to those without the plate, as shown in Fig. 6.3. One observes that except a decrease in amplitude caused by plate loss, the shape of the two beam patterns are similar. Moreover if all beam patterns are normalized to their maximum value, the ones with insertion of plate are virtually identical to the ones without plate. This comparison confirms that the insertion of the plate does not affect the diffraction. The plate can therefore be well approximated by a phase screen with zero thickness.

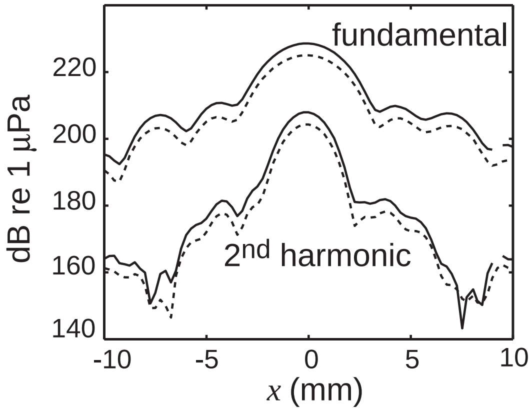

Figure 6.3: Focal beam patterns for fundamental and second-harmonic pressures with and without a uniform thickness plate at distance 60 mm from the source. The solid lines represent the beam pattern with no plate, and dashed lines represent the beam pattern with a plate.

6.1 Beam patterns without phase screen

The focal beam patterns radiated from the focused circular piston were measured without any scattering medium in between. These beam patterns serve as reference for comparison with the phase screen measurements. The 2D beam pattern measurements were taken in an area of $[-10, 10]$ mm $\times$ $[-10, 10]$ mm. The beam profiles in the x and y directions were also measured. The measurements were compared with the computations using the angular spectrum method discussed in Sec. 3.2. The 2D focal beam patterns for the fundamental and second harmonic are shown in Figs. 6.4 and 6.5. The beam profiles in the x and y directions are shown in Fig. 6.6.

In the next two sections we report measurements of beam patterns taken first with a periodic phase grating plate, and then with two random phase plates with different correlation lengths. The purpose of using a plate with a periodic phase grating is to confirm the validity of our manufactured phase screen by comparison with known results. The scattered lobes can be clearly seen in the experiments with the periodic plate. The measurements with the random phase plates illustrate the statistical properties of the scattered field. All measurements are compared to numerical simulations using the angular spectrum method, in which the exact phase variations of the plate can be incorporated into the program.

6.2 Scattering by a periodic phase grating

Measurements were made with a plate with periodic rectangular grooves, as shown in Fig. 6.7(a). The grooves were 2 mm wide and 1 mm deep. The change in phase introduced by a groove of depth Δz is

$$\Delta\phi = (k_w - k_p)\Delta z = \left(\frac{1}{c_w} - \frac{1}{c_p}\right) 2\pi f \Delta z \,, \tag{6.2}$$

where k_w, k_p, c_w and c_p are wave number and sound speed for the water and the polyethylene plate, respectively. For $\Delta z = 1$ mm, one obtains $\Delta\phi = 2.7$ rad at the fundamental frequency of 2.25 MHz. The groove pattern repeats every 4 mm. Although there is small amount of amplitude variation across the plate due to the loss of the plate and the indentation of the groove. This amplitude variation is within 10% of the total amplitude change caused by the plate loss, which can be compensated by increasing source level and it has negligible influence on the diffraction of the beam pattern. In the following calculations this amplitude variation is neglected.

The phase plate was placed in the prefocal region, 60 mm away from the source. The hydrophone was placed in the geometric focal plane, 152 mm away

Fundamental Component

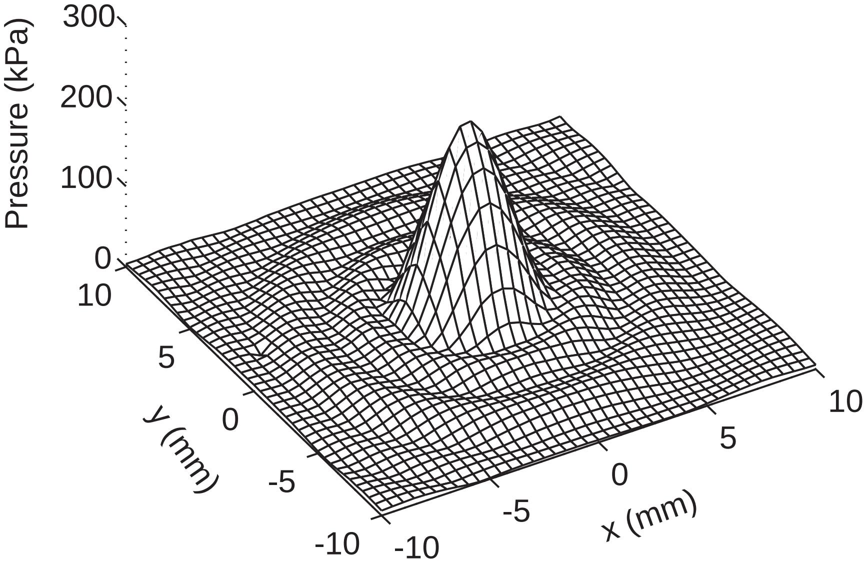
(a) Measurement

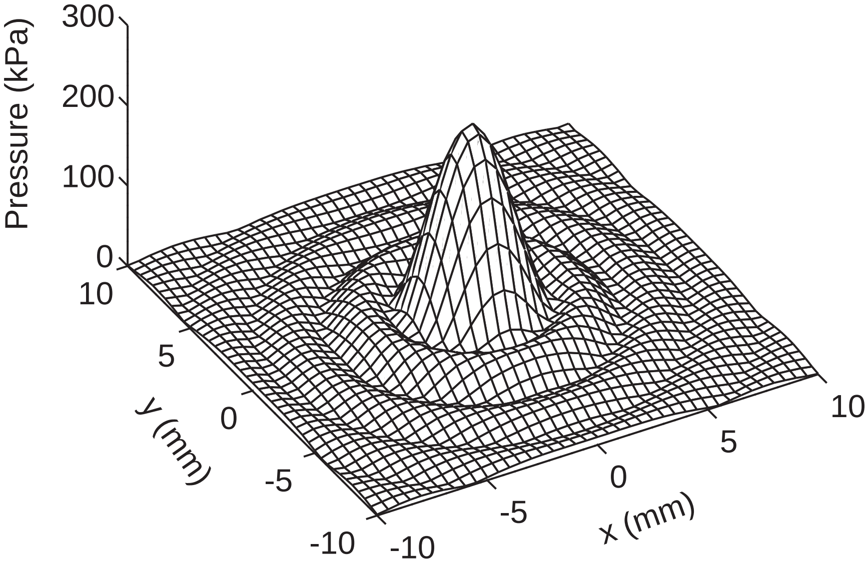
(b) Computation

Figure 6.4: (a) Measured and (b) computed fundamental beam patterns in the focal plane, in the absence of a phase screen.

Second Harmonic Component

(a) Measurement

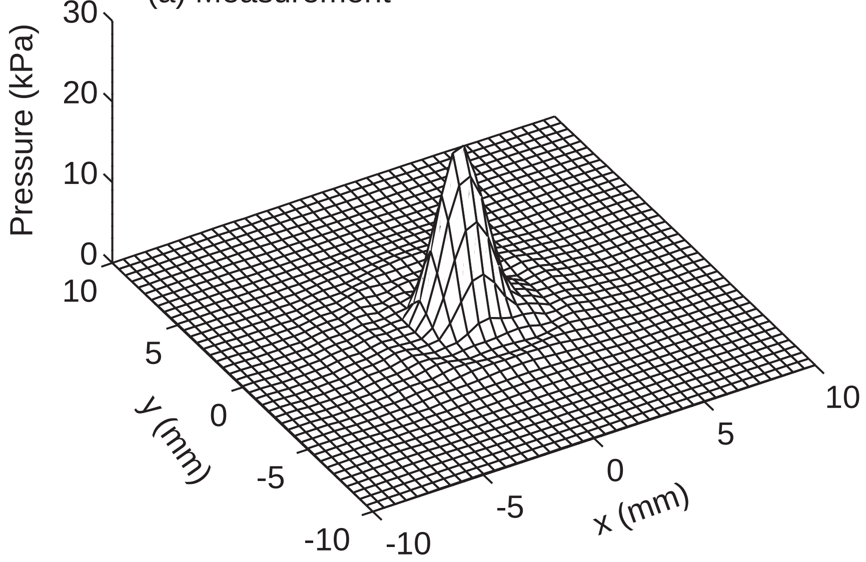

(b) Computation

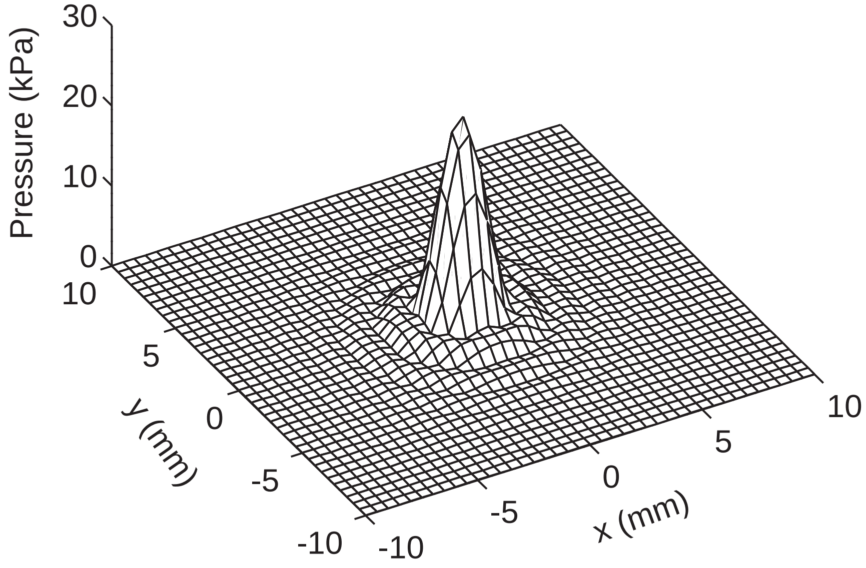

Figure 6.5: (a) Measured and (b) computed second-harmonic beam patterns in the focal plane, in the absence of a phase screen.

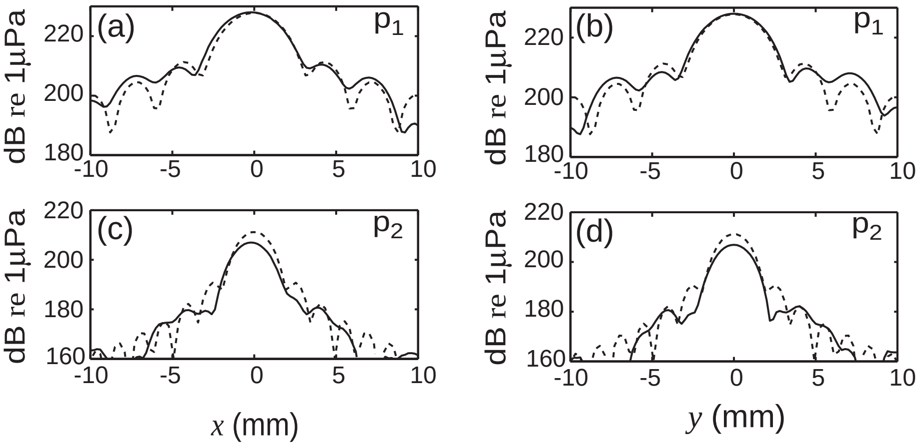

Figure 6.6: Measured (solid lines) and computed (dashed lines) beam patterns in the focal plane, in the absence of a phase screen, for the fundamental (top row) and second harmonic (bottom row) components, in the x (left column) and y (right column) directions.

from the source. The experimental set-up is shown in Fig. 6.7(b). With this geometry, the scattering is in the x-z plane. In the y direction there is no phase change, and no scattering lobes appear.

Beam patterns were measured along the x and y axes in the focal plane. In the x direction the measurements were taken from -20 mm to 20 mm, and from -10 mm to 10 mm in the y direction. The measured and computed pressure amplitudes are shown in Fig. 6.8. In the computations, the plate is assumed to be an ideal phase screen. From Fig. 6.8(a) we see that in the x direction there exist at $x = \pm 15$ mm two scattering lobes with large amplitudes. Computations reveal more pairs of lobes located further off axis. The locations of these side lobes are determined by the period of the phase grating. In the y direction, shown in Fig. 6.8(b), there are no side lobes, and the beam pattern is the same as in the absence of the phase grating (see Fig. 6.6). The computation based on the phase screen model can predict very well the locations and amplitudes of the scattering lobes.

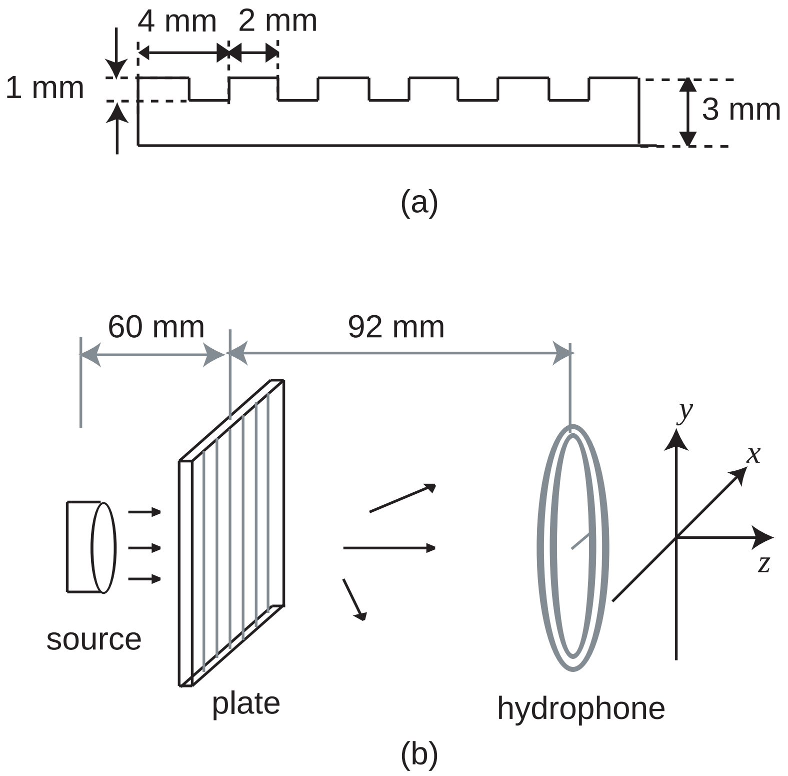

Figure 6.7: (a) Structure of the periodic phase grating plate and (b) the geometry of the measurement.

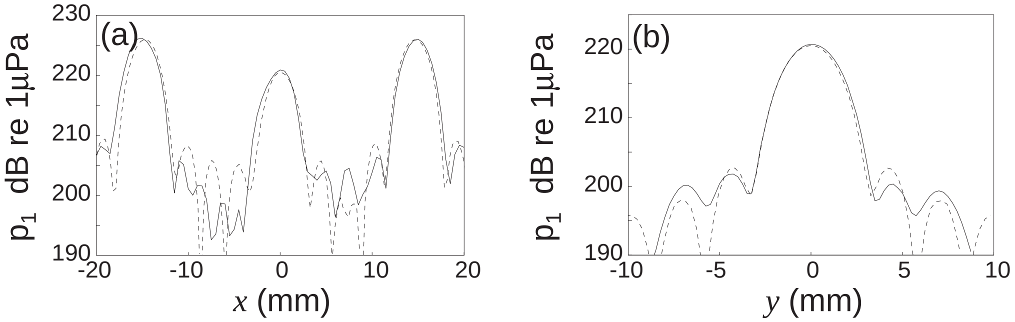

Figure 6.8: Measured (solid line) and computed (dashed line) linear beam patterns along the x and y axes through the focus for radiation from a focused piston source through a periodic phase grating plate.

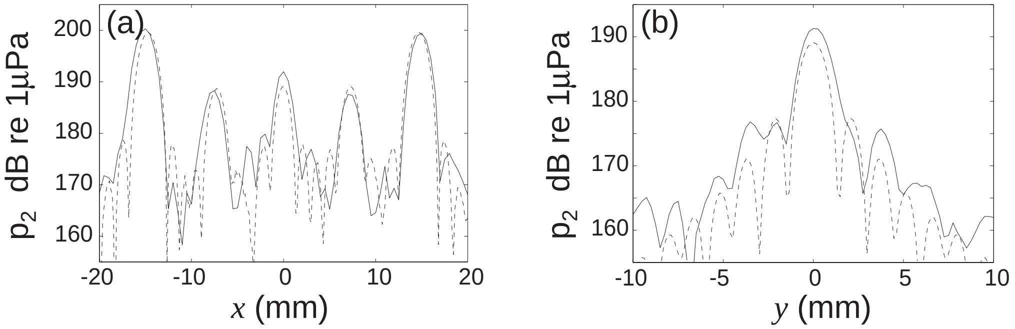

Figure 6.9: Measured (solid line) and computed (dashed line) second harmonic beam patterns along the x and y axes through the focus for radiation from a focused piston source through a periodic phase grating plate.

Beam patterns for the second harmonic were also measured and compared to computations. As the fundamental main lobe is scattered into several side lobes, the efficiency of second-harmonic generation is decreased. Compared to Fig. 6.6, where the maximum second-harmonic amplitude is about 20 dB below the maximum fundamental amplitude, the amplitude of the second harmonic in this measurement is more than 26 dB lower than that of the fundamental with the grating plate. The second-harmonic beam profiles in the x and y directions are shown in Fig. 6.9. One can see that the second harmonic has a more complicated scattering structure than the fundamental. In the x direction there are two pairs of side lobes, one at ±7.5 mm, which is denoted the 1st scattering lobe, and the other at ±15 mm, which is denoted the 2nd scattering lobe. The 1st scattering lobe is generated from two sources. One is from the linear scattering of the second harmonic generated before the phase screen. The other is from the nonlinear interactions of the main lobe and the 1st scattering lobe associated with the fundamental. The 2nd scattering lobe is mainly due to the nonlinear generation by the 1st fundamental scattering lobe. There is also a small contribution from linear scattering of the second harmonic. In the y direction, since there are no phase changes, no scattering lobes appear.

6.3 Scattering by a random phase screen

In this section, measurements of scattering produced by random phase screens are presented. The phase screen was created by cutting the surface of the polyethylene plate with many randomly distributed circles, which in cross section resemble the indentations shown in Fig. 6.7 for the periodic phase grating. Two phase screens were created, having different circle diameters and different spatial distributions as shown in Fig. 6.10. Screen A has 200 small circles with diameter of 3.18 mm. The indentation of every circle is 1 mm. The correlation length of this phase screen was determined by calculating its autocorrelation function and then fitting it with a Gaussian curve. The Gaussian curve matches the autocorrelation function by their half power width. The autocorrelation function for screen A and the Gaussian curve is shown in Fig. 6.11(a). It turns out that screen A has a correlation length about the same as the radius of the indentation circle, i.e., $l = 1.6$ mm. Screen B has 40 circles with diameter 12.7 mm and 1 mm indentation. Using the same curve fitting method, shown in Fig. 6.11(b), it's correlation length was found to be $l = 6.3$ mm.

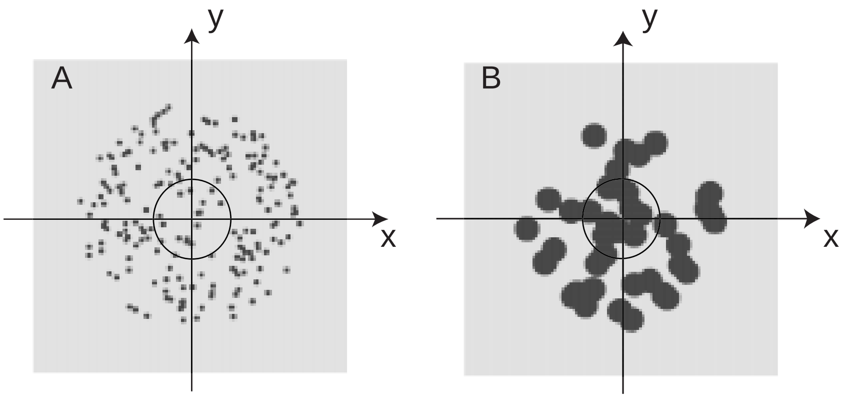

$\nu=12$ $\nu=3$

Figure 6.10: Geometry of circular indentations in the random phase plates used as the phase screens. The big circle indicates the size of the focused piston source.

The experimental set-up is illustrated in Fig. 6.1. The random plate was placed 60 mm away from the source, which is the same position as in the experiment in Sec. 6.2, and beam patterns were measured in the focal plane. We did not place the plate directly in front of the source in order to avoid the contact nonlinearity introduced by the gap between the plate and the source. Also, in order to avoid the overlap of pulses reflected between the source and plate, the distance between them should be at least larger than the pulse length, which in our case turns out to be 10 mm for the 15 cycles at 2.25 MHz. In addition, the basic physics we are investigating is not affected by the precise position of the plate, as long as it is in the prefocal region and introduces enough phase aberration to make the beam pattern distortion observable. We chose 60 mm as a convenient position for the experiments. At this position, the plate introduces enough aberration to distort the focal beam patterns.

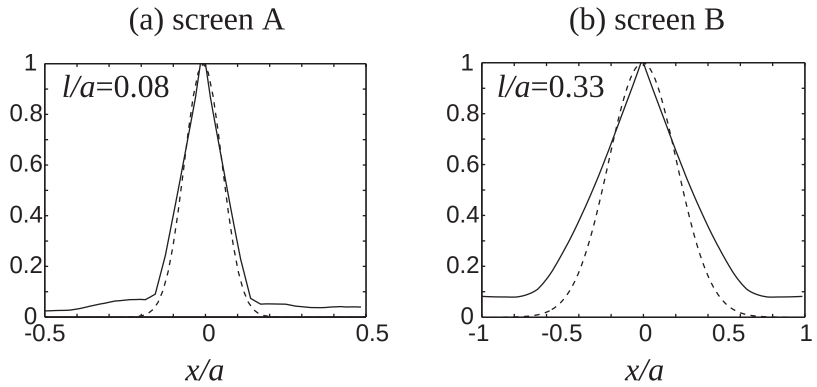

Figure 6.11: Normalized autocorrelation functions for phase screens A and B (solid lines), together with Gaussian curve fittings (dashed lines). Each Gaussian curve has the same half power width as the corresponding autocorrelation function.

The measurements of focal beam patterns obtained for phase screen A were compared to the computations. The 2D beam patterns for the fundamental pressure are shown in Fig. 6.12. The second harmonic beam patterns are shown in Fig. 6.13. The 1D beam profiles in the x and y directions are shown in Fig. 6.14. In all comparisons, the computations are seen to be in agreement with the measurements.

From observations of these figures, we see for both the fundamental and second-harmonic fields that the side lobes adjacent to the main lobe are increased, while the main lobe stays unchanged. The maximum side lobe level for the fundamental is found to be 8.2 dB below the peak level of the main lobe. For the second harmonic, the scattered field level is lower than that of the fundamental. Its maximum side lobe level is -12.2 dB. For screen A, the phase correlation length is small compared to the source radius, and from the beam pattern measurement we can see distortions occur mainly in the side lobe area, whereas the main lobe is relatively unaffected.

The measured and computed 2D beam patterns associated with screen B are shown in Figs. 6.15 and 6.16. The 1D beam profiles in the x and y directions are shown in Fig. 6.17. From these figures one can see that the field scattered

Fundamental Component

(a) Measurement

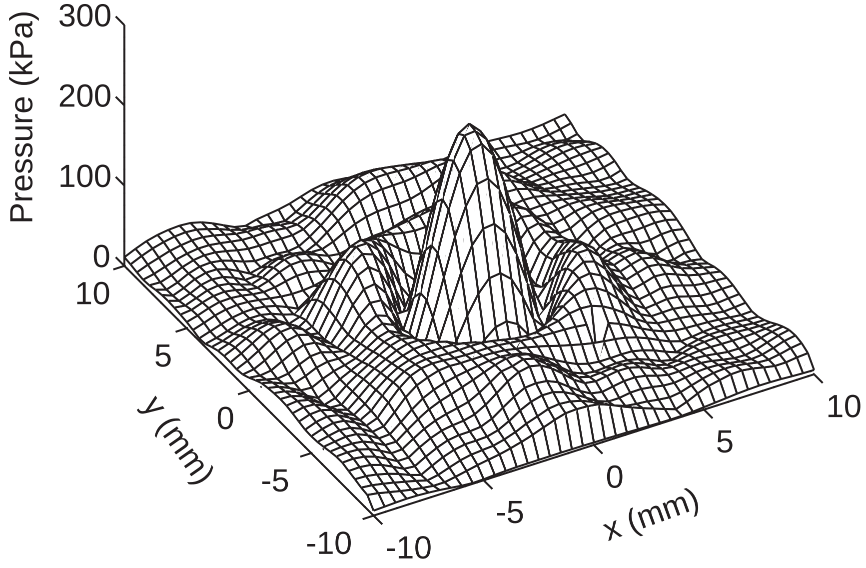

(b) Computation

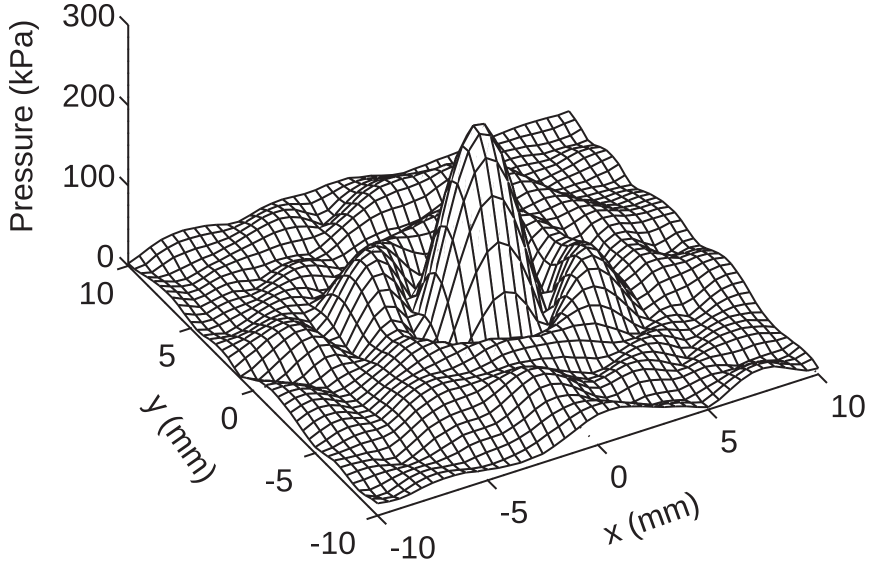

Figure 6.12: (a) Measured and (b) computed fundamental beam patterns in the focal plane, with phase screen A at $b_1/d = 0.4$.

Second Harmonic Component

(a) Measurement

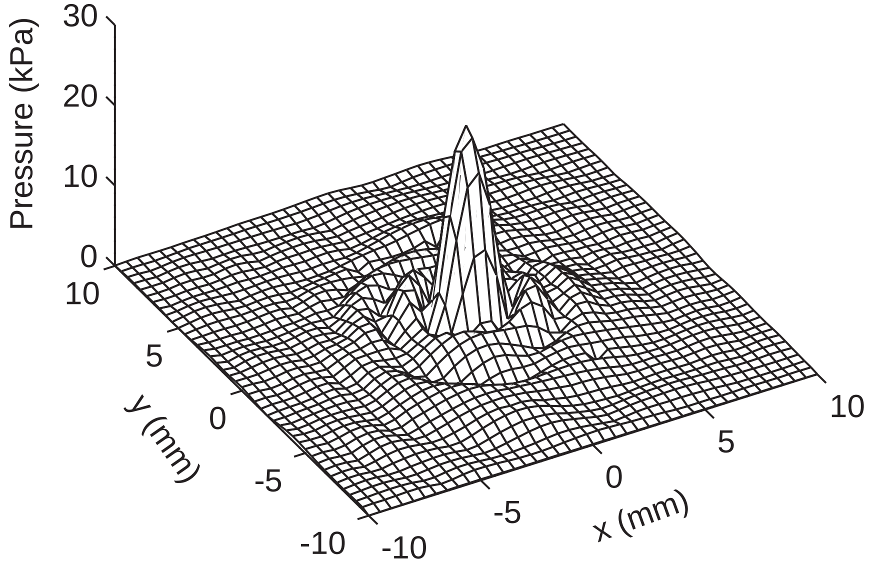

(b) Computation

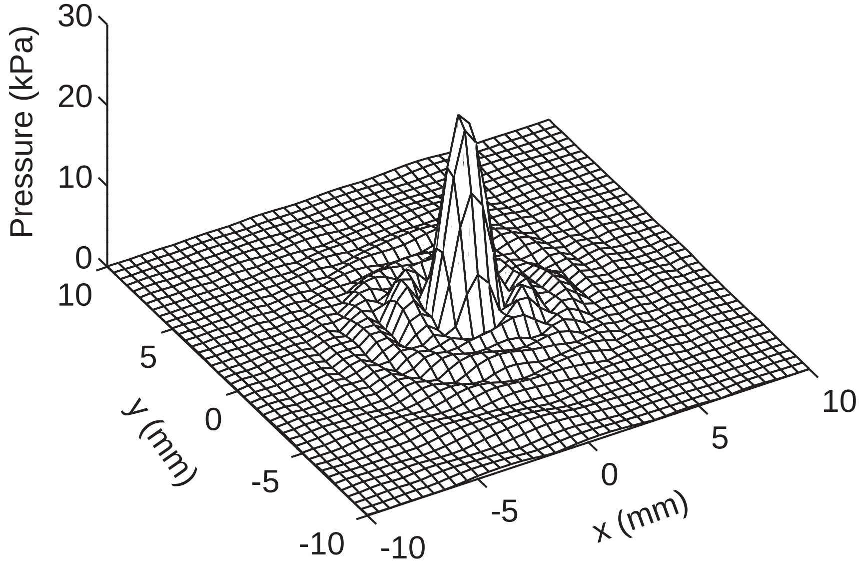

Figure 6.13: (a) Measured and (b) computed second-harmonic beam patterns in the focal plane, with phase screen A at $b_1/d = 0.4$.

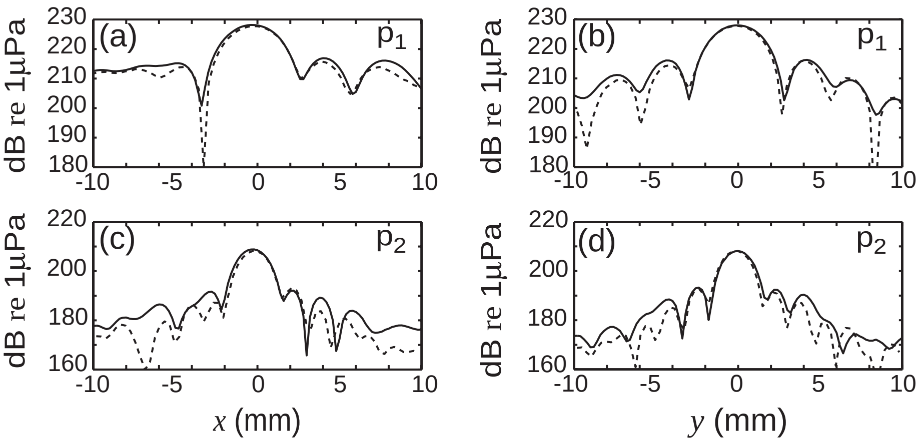

Figure 6.14: Measured (solid lines) and computed (dashed lines) beam patterns in the focal plane, with phase screen A at $b_1/d = 0.4$, for the fundamental (top row) and second harmonic (bottom row) components, in the x (left column) and y (right column) directions.

by screen B not only distorts the side lobe but also increases the main lobe width. The increase in side lobe level is not as high as for screen A, but the main lobe is much wider. The increase in beam width and decrease in side lobe levels compared to that of screen A are due to the increase of the phase correlation length. As the correlation length increases, the scattered field tends to concentrate more along the propagation axis. Thus the distortion of the main lobe becomes prominent and the distortion of the side lobe is reduced. For screen A, the correlation length is small, and the scattered field tends to spread out in the focal plane. The relatively low scattered field level near the beam axis cannot distort the main lobe, while in the side lobe area, the scattered field is relatively larger and thus distortion of the side lobes is more prominent. This explains the larger side lobe level and narrower main lobe beam width in the beam patterns with screen A.

The focusing quality Q and Q_{norm} with 6 dB threshold was also calculated for the measured beam patterns. Their values for the fundamental and second

Fundamental Component

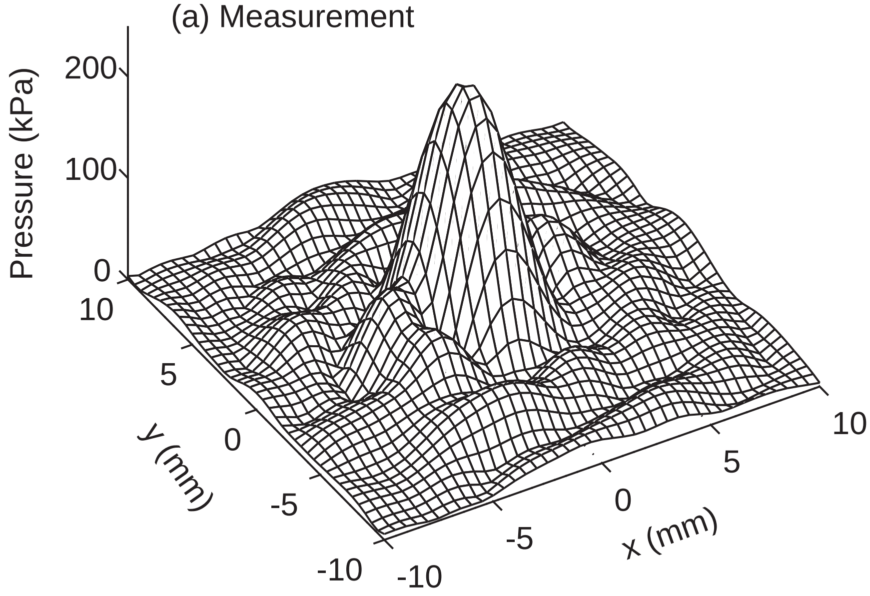
(a) Measurement

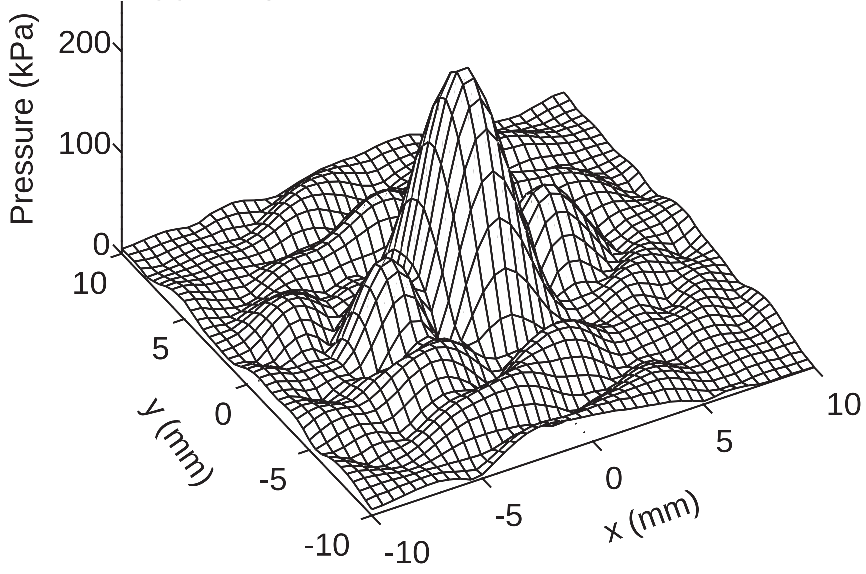
(b) Computation

Figure 6.15: (a) Measured and (b) computed fundamental beam patterns in the focal plane, with phase screen B at $b_1/d = 0.4$.

Second Harmonic Component

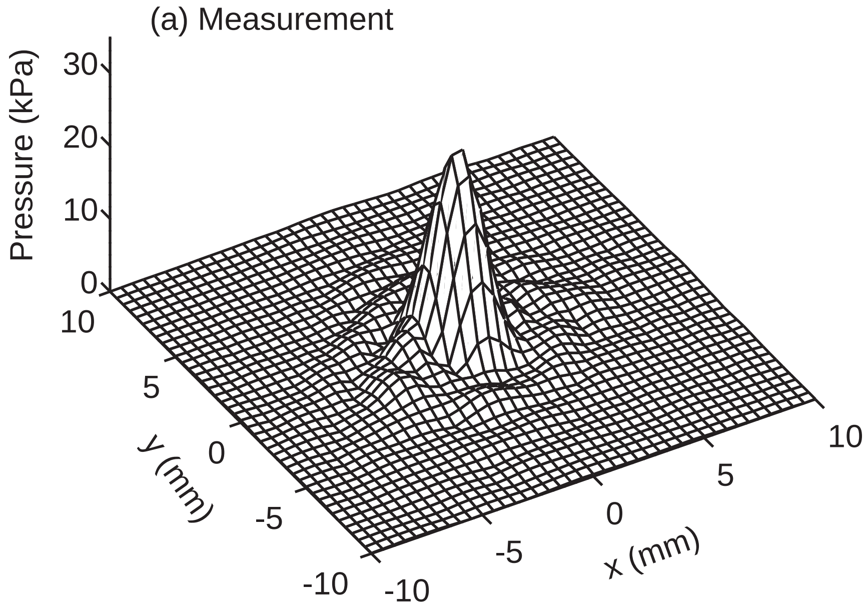
(a) Measurement

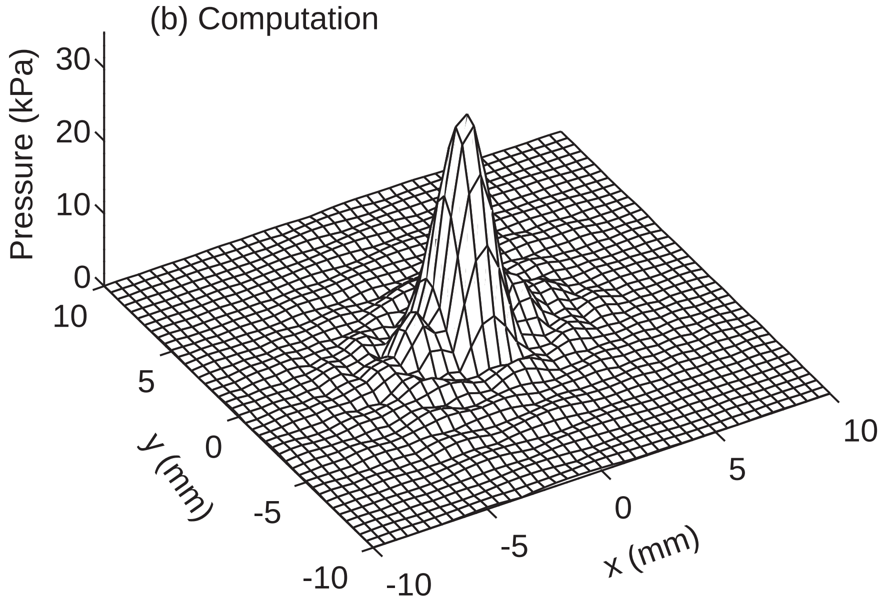
(b) Computation

Figure 6.16: (a) Measured and (b) computed second-harmonic beam patterns in the focal plane, with phase screen B at $b_1/d = 0.4$.

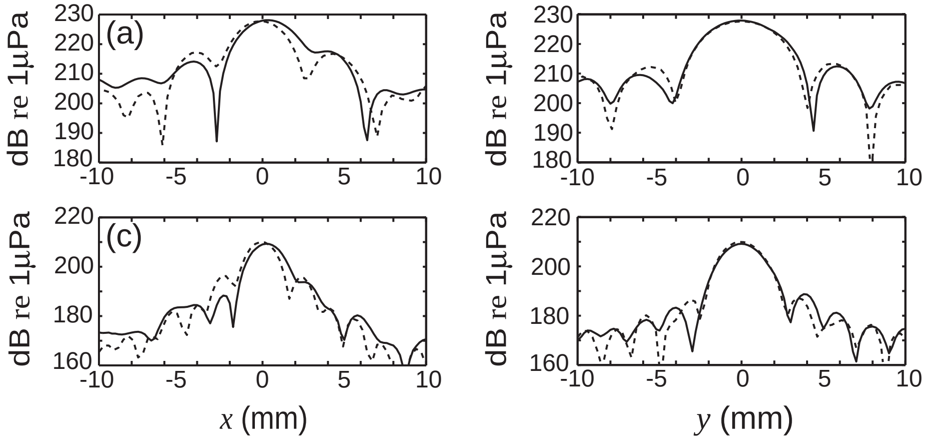

Figure 6.17: Measured (solid lines) and computed (dashed lines) beam patterns in the focal plane, with phase screen B at $b_1/d = 0.4$, for the fundamental (top row) and second harmonic (bottom row) components, in the x (left column) and y (right column) directions.

harmonic beam patterns associated with the two phase screens A and B are shown in Fig. 6.18. Figure 6.18 indicates that second harmonic beam has larger focusing quality than that of fundamental. The two phase screens A and B have less influence on the second harmonic than on the fundamental, whereas phase screen A introduces more distortion than phase screen B. This conclusion is supported by the 2D view of the beam patterns.

Up to now we have compared all measurements with the computations based on the phase screen depicted in Fig. 6.10. The phase changes in these two screens are quasi-random, and their correlation lengths are about the diameter of the small circles indented into the plate. In order to make a comparison with a truly random phase screen, like the ones used in Chap. 5, we performed a computation with the same source and a random phase screen having the same correlation length as the screen used in the experiment. The phase screens used in this computation are shown in Fig. 6.19. Screens A′ and B′ in Fig. 6.19 have the same correlation lengths as screens A and B in Fig. 6.10, respectively. Screens A′ and

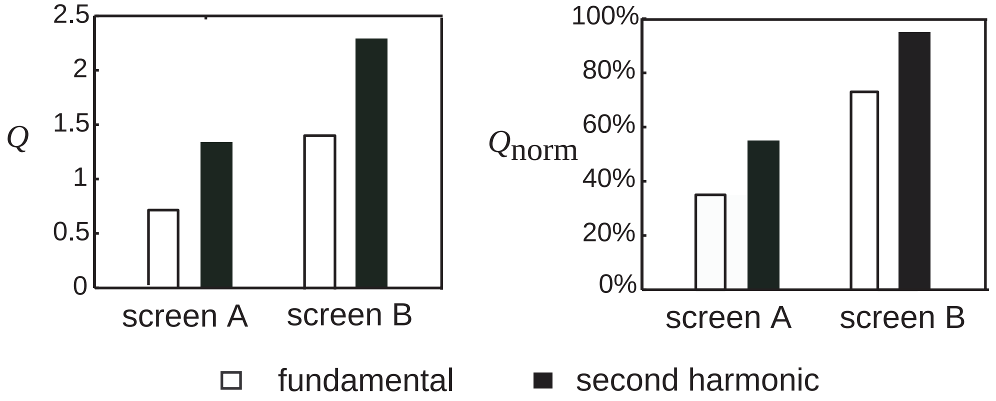

Figure 6.18: Focusing quality Q and Q_{norm} for the fundamental and second harmonic beam patterns perturbed by the two random phase screens in Fig. 6.10.

B′ also possess the same maximum phase changes as screens A and B. In the experiment the screen is positioned at distance $b_1 = 0.4d$ from the source, within half a focal length, we can use the effective source with the transformed radius and focal length as discussed in Sec. 4.6 for the computation. The focal beam patterns for fundamental and second-harmonic are computed with screen A′ (or B′) placed directly in front of the effective source. The calculated beam patterns are not expected to agree with measurements, but they should show similar statistical behavior. The averaged beam profiles obtained from computations with screen A′ (and B′) are compared with those obtained from the measurements, as shown in Fig. 6.20. In this figure we also include the averaged beam profiles based on exact computations using screens A and B shown in Fig. 6.12(b)–6.13(b) and Fig. 6.15(b)–6.16(b). From Fig. 6.20, one can see from the comparisons that the approximations based on a truly random screen are in general agreement with the measurements and the exact computations. A broadening of the main lobe was observed with the larger phase correlation length. Although the side lobe levels predicted by the approximation are not in agreement to the measurements, the general trend in the variation of the statistical beam patterns are consistent to the measurements. The exact computations based on phase screens in Fig. 6.10 give much better fits to the measurements.

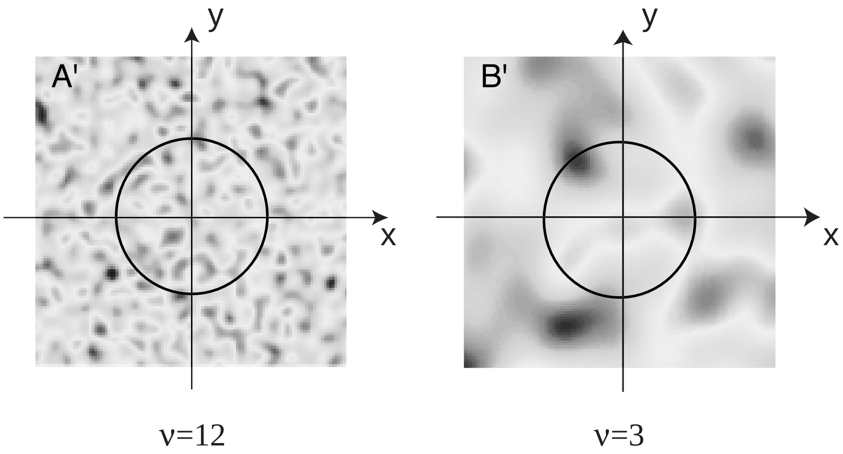

Figure 6.19: The two random phase screens used for the comparison. They have the same correlation length as the screens depicted in Fig. 6.10. The circle indicates the size of the effective piston source.

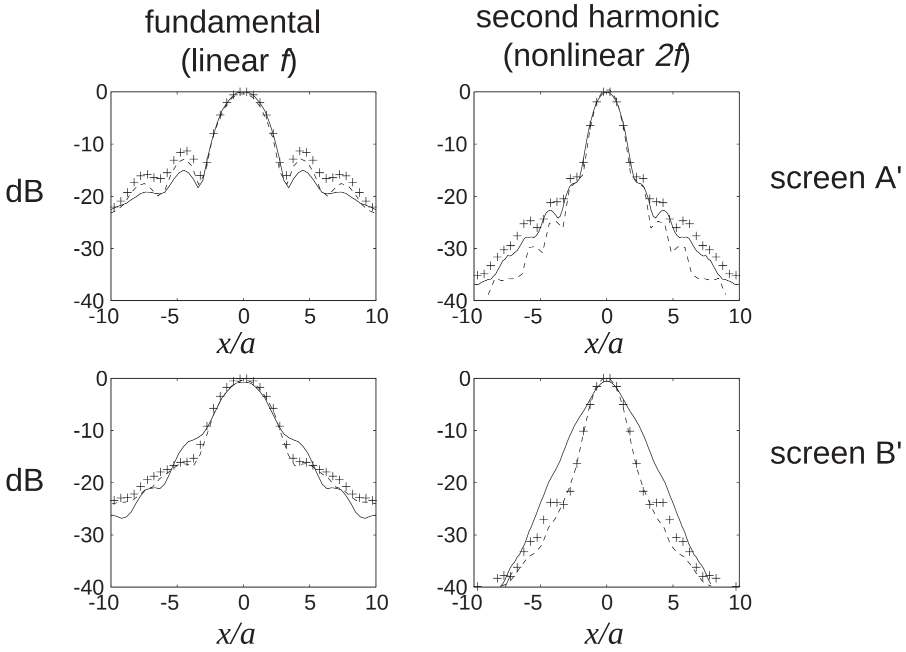

Figure 6.20: Solid lines: averaged beam profiles obtained from approximations with random phase screens in Fig. 6.19. Crosses: averaged beam profiles obtained from measurements with phase screens in Fig. 6.10. Dashed lines: averaged beam profiles obtained from exact calculations with random phase screens in Fig. 6.10.

Chapter 7

Summary and conclusions

This dissertation reports both theoretical and experimental investigations on scattering in a weakly nonlinear sound beam due to phase perturbations introduced by an inhomogeneous layer. The phase changes in the layer were modeled as a random phase screen characterized by zero mean, small variance and Gaussian correlation function in the spatial domain. The mean intensity for the second harmonic field of a Gaussian beam was derived under weak forward scattering conditions. These solutions reveal the relation between the statistics of the scattered second-harmonic field and the statistics of the phase screen. In contrast to direct numerical realizations, the statistical solutions predict the general behavior of the scattered field. Although the mean intensity is obtained analytically only for a Gaussian beam, numerical simulations and experiments reveal similar behavior for a sound beam radiated by a circular piston.

This investigation was motivated by the increasing interest in tissue harmonic imaging used in medical ultrasound. The reduction in scattering of the nonlinearly generated second-harmonic component by body wall tissue makes THI a better imaging technique in most cases than conventional imaging based on transmission and reception at the source frequency. However, as mentioned in Chap. 1, previous analyses of scattering in the second-harmonic field has been restricted exclusively to numerical simulations and experiments. Descriptions of the nonlinear scattered fields based on such investigations are qualitative in nature. The results obtained in this dissertation provide a more quantitative description of the scattered nonlinear field, including evolution of the beam pattern, change in scattered and coherent energy along the propagation axis, etc., which are not presented in the literature.

In Chap. 2 we briefly reviewed the classical methods used to treat linear wave propagation in an inhomogeneous medium. We described the difficulties and restrictions involved in extending these methods to nonlinear wave propagation. The focus is on the phase screen method, which is used to obtain theoretical results for second-harmonic generation in subsequent chapters. The whole investigation in this dissertation, including analysis, numerical simulation, and experiments, is based on this phase screen approach.

In Chap. 3 we discussed the model equations used to obtain the mean intensity for the second-harmonic field. They are based on quasilinear solutions of the KZK equation. Integral relations for the beam intensity for both the fundamental and the second-harmonic fields are obtained for arbitrary sources propagating through a homogeneous medium. These integral forms are the basis for deriving the mean intensity with phase screen perturbations that appear in the next chapter. Also in this chapter, the numerical scheme based on the angular spectrum method that we used to perform all phase screen simulations is discussed. Another finite difference algorithm used to solve KZK equation is also briefly discussed in this chapter. This algorithm is used to obtain the field pressure when beam propagates through an extended inhomogeneous medium with a continuous sound speed variation.

Chapter 4 is devoted entirely to Gaussian beam analysis. In this chapter we derived the mean beam intensity for both the fundamental and second-harmonic fields resulting from propagation through a single random phase screen. The beam is radiated from a focused source that has Gaussian amplitude shading. The solutions reveal that the nonlinear scattered field has a narrower beam profile than that of the linear scattered field. This property explains why less image clutter due to side lobes is observed in practice with the nonlinearly generated second-harmonic. Compared to the linear scattered field, which possesses a Gaussian beam profile, the nonlinear scattered field does not exhibit a Gaussian profile. The mean value of the second-harmonic beam pattern is complicated and does not admit an analytical expression. Energy generated at the second-harmonic frequency is affected by the correlation length l and variance σ of the phase screen. In general, as σ increases, the amplitude of the scattering increases. As l increases, the total nonlinear scattered energy increases, and its beam pattern is more localized around the beam axis. The solutions for the mean beam intensities are compared to ensemble averages of direct numerical simulations, and the two results agree very well. The influence of phase perturbation on distortion of beam patterns can be quantified by calculating a relative focusing quality Q. A similar parameter has been used to quantify the focusing quality of a linear beam.[35] Here it is used for comparison of linear and nonlinear beams. The factor Q, obtained with a 20 dB threshold, indicates that the second-harmonic beam pattern is less distorted by the random phase perturbation than is the beam pattern at the source frequency. Further investigation of the influence of screen position on the beam pattern distortion reveals a interesting result. When the screen is at an arbitrary distance between the source and focal plane, the statistical beam intensity for the fundamental field can be obtained with an effective source that is placed directly behind the screen with a transformed radius and focal length according to geometrical acoustics. The solution for the statistical intensity of the second-harmonic can be fairly well approximated by the result using the same transformation, as long as the screen is within half the focal length from the source.

In Chaps. 5 and 6 we report numerical simulations and experiments, respectively, for radiation from a focused circular piston source that propagates through a random phase screen. Analysis of the scattered field is more difficult than for a Gaussian beam because of the side lobe structure. However, the changes in the statistical beam patterns due to changes of the screen's correlation length and variance are consistent with the analytical solutions based on Gaussian beam theory. The values of the relative focusing quality Q, obtained with a 6 dB threshold, indicate that the phase screen has a comparative influence on the fundamental and second-harmonic beam pattern distortions, but a large influence on the linear beam with twice the source frequency. We also found that the geometrical acoustics transformation works for the fundamental and second harmonic when the distance from the source to the screen is less than half the focal length. In this chapter we also used numerical simulations to investigate a multi-screen model, in which the phase variations inside a tissue medium are distributed evenly over its thickness (40% of the transducer focal length), and represented by N subscreens ($N = 2, 4$). This model produces the same scattered focal beam pattern as if all the phase distortions are lumped into a single screen placed in the center of the medium. When the phase variations are randomly distributed over the thickness, one finds that the single screen model is valid if the thickness is on the order of the correlation length in the propagation direction. If thickness is much larger than one correlation length, the single screen model underpredicts the level of the scattered field. In subsequent experiments, scattered beam patterns were generated by propagation of ultrasound in water through a phase plate with random thickness. The variation in thickness over the plate surface introduces phase changes. Preliminary experiments proved that the phase plate provides a good approximation of an ideal phase screen with zero thickness. The scattered beam patterns were measured and compared to computations. Two phase screens with different phase correlation length were used. The measurements were consistent with numerical simulations.

In this dissertation, the theoretical and experimental investigations of second-harmonic beam scattering by a phase screen support the long observed phenomena in tissue harmonic imaging. In addition to interpretation of the physics in the THI, some new problems may deserve better understanding. One is the geometrical acoustics transformation in prediction of statistical focal beam patterns for both the fundamental and second harmonic with the phase screen away from the transducer. This geometrical acoustics approximation is unable to predict the actual field amplitude but can predict the statistical beam patterns. This means that the statistical average of the field intensity eliminates some diffraction effects. It will be interesting to provide a physical explanation for this.

Another issue that can be extended is the statistical beam patterns obtained with a multilayer phase screen model in which different subscreens have different phase distributions and they are independent of each other. These multiple screens can be used to model an extended inhomogeneous medium with thickness much larger than its correlation length. In this case the single screen model fails to predict the scattered field. In the multi-phase screen model, scattering becomes more complicated because the linear scattering of the second harmonic by the phase screens also enters the problem. Unlike the case when the screen is in the source plane, in which there is no linear scattering of the second harmonic by the screen, in the multi-screen model the linear field of the second harmonic generated before a particular subscreen is subject to scattering by all the subscreens in its propagation path. Also, nonlinear generation by the fundamental field becomes much more complicated to analyze.

A third issue may be the extension of the statistical solutions $\langle I_1 \rangle$ and $\langle I_2 \rangle$ from a Gaussian source to a rectangular Gaussian source. The extension would be similar to what has been carried out in Secs. 4.1 and 4.2. A rectangular Gaussian source is more close in shape to the imaging transducers used clinically. The results may provide more information related to these imaging transducers.

In general, the phase screen method can be used in many other areas. For example, in underwater acoustics, where the ocean environment is also inhomogeneous, one may investigate the fluctuation of the acoustic field due to the spatial variation of the sound speed of the water column. This study could be valuable for assessing the performance of the underwater sonar. In addition, in the use of parametric array sonar, changes in the beam intensity for the difference frequency field due to the inhomogeneity of the environment may be interesting to explore.

Appendix A

Solution for the angular spectrum of the second-harmonic

In this appendix we derive Eqn. (3.29), the angular spectrum of the second harmonic in a homogeneous fluid. The angular spectrum method was introduced by Alais and Hennion[53] and subsequently extended by Tjøtta et al.[59,65] Later, it was used by Landsberger and Hamilton[54] to analyze the reflection and transmission phenomena of second harmonic field between interfaces. In their algorithm, the angular spectrum $Q_2(\boldsymbol{\kappa}, z)$ related to a certain plane wave is obtained through the analytical solutions for second-harmonic generation by a pair of noncolinear plane waves associated with the fundamental field. All the second-harmonic plane waves are then superposed to construct $q_2(\mathbf{r})$.[51]

Here we apply the Fourier transform directly to the differential equation for the second harmonic, given by Eqn. (3.22). The Fourier transform of Eqn. (3.22) [recall Eqn. (3.16)] yields the following ordinary differential equation for Q_2:

$$\frac{d^2Q_2}{dz^2} + (4k^2 - \kappa^2)Q_2 = \alpha M(\boldsymbol{\kappa}, z)\,, \qquad \alpha = -\frac{j\beta k^2}{2\pi^2\rho_0 c_0^2}\,, \tag{A.1}$$

where

$$M(\boldsymbol{\kappa}, z) = \int\!\!\int Q_1(\boldsymbol{\kappa} - \boldsymbol{\kappa}', z)Q_1(\boldsymbol{\kappa}', z)\, d\boldsymbol{\kappa}'\,. \tag{A.2}$$

The boundary (source) condition is taken to be

$$Q_2(\boldsymbol{\kappa}, 0) = 0\,. \tag{A.3}$$

Linear theory described in Sec. 3.2 accounts for radiation due to a nonzero source condition. The general solution of Eqn. (A.1) is composed of homogeneous and particular solutions,

$$Q_2 = Ae^{-jk_2 z} + Be^{jk_2 z} + Q_{2p}\,, \tag{A.4}$$

where A and B are constants, and Q_{2p} is the particular solution. The wavenumber k_2 is defined by Eqn. (3.30). Let the particular solution be expressed as

$$Q_{2p} = e^{-jk_2 z}\bar{Q}_{2p}\,, \tag{A.5}$$

and substitute into Eqn. (A.1) to obtain

$$\frac{d^2\bar{Q}_{2p}}{dz^2} - j2k_2\frac{d\bar{Q}_{2p}}{dz} = \alpha M(\boldsymbol{\kappa}, z)e^{jk_2 z}\,. \tag{A.6}$$

With $P = d\bar{Q}_{2p}/dz$ Eqn. (A.6) becomes

$$\frac{dP}{dz} - 2jk_2 P = \alpha M(\boldsymbol{\kappa}, z)e^{jk_2 z}\,, \tag{A.7}$$

and with the additional substitution $P = e^{j2k_2 z}\bar{P}$, Eqn. (A.7) becomes

$$\frac{d\bar{P}}{dz} = \alpha M(\boldsymbol{\kappa}, z)e^{-jk_2 z}\,. \tag{A.8}$$

The solution is

$$\bar{P} = \alpha\int_0^z M(\boldsymbol{\kappa}, z')e^{-jk_2 z'}dz' + \bar{P}(\boldsymbol{\kappa}, 0)\,, \tag{A.9}$$

and thus

$$P = \alpha e^{2jk_2 z}\int_0^z M(\boldsymbol{\kappa}, z')e^{-jk_2 z'}dz' + \bar{P}(\boldsymbol{\kappa}, 0)e^{j2k_2 z}\,. \tag{A.10}$$

Noting that

$$\bar{P}(\boldsymbol{\kappa}, 0) = P(\boldsymbol{\kappa}, 0) = \left.\frac{d\bar{Q}_{2p}}{dz}\right|_{z=0}\,,$$

one obtains

$$\frac{d\bar{Q}_{2p}}{dz} = \alpha e^{j2k_2 z}\int_0^z M(\boldsymbol{\kappa}, z')e^{-jk_2 z'}dz' + \left.\frac{d\bar{Q}_{2p}}{dz}\right|_{z=0} e^{j2k_2 z}\,, \tag{A.11}$$

the integral of which is

$$\bar{Q}_{2p} = \alpha\int_0^z e^{j2k_2 z'}\int_0^{z'} M(\boldsymbol{\kappa}, z'')e^{-jk_2 z''}dz''dz' + \left.\frac{d\bar{Q}_{2p}}{dz}\right|_{z=0}\frac{e^{j2k_2 z} - 1}{j2k_2} + \bar{Q}_{2p}|_{z=0}. \tag{A.12}$$

From Eqn. (A.5) we have the relation

$$\left.\frac{dQ_{2p}}{dz}\right|_{z=0} = \left.\frac{d\bar{Q}_{2p}}{dz}\right|_{z=0} - jk_2 Q_{2p}|_{z=0} \,. \tag{A.13}$$

Substituting in Eqn. (A.12), using Eqn. (A.5), we get

$$\begin{aligned} Q_{2p} &= \alpha e^{-jk_2 z}\int_0^z e^{j2k_2 z'}\int_0^{z'} M(\boldsymbol{\kappa}, z'')e^{-jk_2 z''}dz''dz' \\ &\quad + \left.\frac{dQ_{2p}}{dz}\right|_{z=0}\frac{e^{jk_2 z} - e^{-jk_2 z}}{j2k_2} + Q_{2p}|_{z=0}(e^{jk_2 z} + e^{-jk_2 z}) \,. \end{aligned} \tag{A.14}$$

The second and third terms in Eqn. (A.14) are the homogeneous solutions of Eqn. (A.1), so they are merged into the first two terms of Eqn. (A.4). Equation (A.4) can thus be rewritten as

$$Q_2 = Ae^{-jk_2 z} + Be^{jk_2 z} + Q_{2p} \,, \tag{A.15}$$

where

$$Q_{2p} = e^{-jk_2 z}\int_0^z e^{2jk_2 z'}\left[\alpha\int_0^{z'} M(\boldsymbol{\kappa}, z'')e^{-jk_2 z''}dz''\right] dz' \,. \tag{A.16}$$

Applying the boundary condition Eqn. (A.3) to Eqn. (A.15), we arrive at $A = -B$. Substitute A and B into Eqn. (A.15), and expand $M(\boldsymbol{\kappa}, z'')$ in terms of Q_{10}, to arrive at

$$\begin{aligned} Q_2 &= B(e^{jk_2 z} - e^{-jk_2 z}) - \frac{\alpha(e^{jk_2 z} - e^{-jk_2 z})}{2k_2}\int\int \frac{Q_{10}(\boldsymbol{\kappa} - \boldsymbol{\kappa}')Q_{10}(\boldsymbol{\kappa}')}{k_A + k_1 + k_2}\, d\boldsymbol{\kappa}' \\ &\quad - \alpha e^{-jk_2 z}\int\int \frac{Q_{10}(\boldsymbol{\kappa} - \boldsymbol{\kappa}')Q_{10}(\boldsymbol{\kappa}')[e^{-j(k_A + k_1 - k_2)z} - 1]}{(k_A + k_1 - k_2)(k_A + k_1 + k_2)} d\boldsymbol{\kappa}', \end{aligned} \tag{A.17}$$

where $k_A = k_1(\boldsymbol{\kappa} - \boldsymbol{\kappa}')$. Components of the solution for Q_2 that contain $\exp(jk_2 z)$ are associated with linear waves propagating in the $-z$ direction. These waves should not be included in Q_2, since we only consider wave propagation in the $+z$ direction. After omitting these terms we have

$$\begin{aligned} Q_2 &= -Be^{-jk_2 z} + \frac{\alpha e^{-jk_2 z}}{2k_2}\int\int \frac{Q_{10}(\boldsymbol{\kappa} - \boldsymbol{\kappa}')Q_{10}(\boldsymbol{\kappa}')}{(k_A + k_1 + k_2)}\, d\boldsymbol{\kappa}' \\ &\quad - \alpha e^{-jk_2 z}\int\int \frac{Q_{10}(\boldsymbol{\kappa} - \boldsymbol{\kappa}')Q_{10}(\boldsymbol{\kappa}')[e^{-j(k_A + k_1 - k_2)z} - 1]}{(k_A + k_1 - k_2)(k_A + k_1 + k_2)} d\boldsymbol{\kappa}' \,. \end{aligned} \tag{A.18}$$

Applying the boundary condition to Eqn. (A.18), we arrive at

$$B = \frac{\alpha}{2k_2} \int\int \frac{Q_{10}(\boldsymbol{\kappa} - \boldsymbol{\kappa}')Q_{10}(\boldsymbol{\kappa}')}{k_A + k_1 + k_2} d\boldsymbol{\kappa}' .$$

Substituting into Eqn. (A.18), we obtain the final expression for Q_2,

$$Q_2 = \frac{j\beta k^2}{2\pi^2 \rho_0 c_0^2} e^{-jk_2 z} \int\int \frac{Q_{10}(\boldsymbol{\kappa} - \boldsymbol{\kappa}')Q_{10}(\boldsymbol{\kappa}')[e^{-j(k_A+k_1-k_2)z} - 1]}{(k_A + k_1 - k_2)(k_A + k_1 + k_2)} d\boldsymbol{\kappa}' , \quad \text{(A.19)}$$

which is Eqn. (3.29)

Appendix B

Derivation of the averaged second-harmonic intensity components

This appendix fills in the steps between Eqn. (4.22) and the final result for the average intensity of the second harmonic given by Eqns. (4.23)–(4.28). Equation (4.22) can be reduced to a much simpler form under the assumption made in Eqns. (4.4)–(4.6). Since the statistics of ϕ are independent of orientation, the intensity $\langle I_2 \rangle$ should also be independent of orientation. This assumption is used to eliminate many integrals in Eqn. (4.22).

We begin by evaluating the fourth-order moment in Eqn. (4.22). Substitution of Eqn. (4.1) yields

$$\begin{aligned} m_4 = \; & \langle q_{10}(\mathbf{r}_\alpha)\, q_{10}(\mathbf{r}_\beta)\, q_{10}^*(\mathbf{r}_\gamma)\, q_{10}^*(\mathbf{r}_\delta) \rangle \\ = \; & p_0^4 \exp\Big[-\frac{A - jB}{a^2} \left(|\mathbf{r}_\alpha|^2 + |\mathbf{r}_\beta|^2 \right) - \frac{A + jB}{a^2} \left(|\mathbf{r}_\gamma|^2 + |\mathbf{r}_\delta|^2 \right) \Big] \\ & \times \langle \exp[j\phi(\mathbf{r}_\alpha) + j\phi(\mathbf{r}_\beta) - j\phi(\mathbf{r}_\gamma) - j\phi(\mathbf{r}_\delta)] \rangle \,, \end{aligned} \tag{B.1}$$

where the temporary notation

$$\mathbf{r}_\alpha = \mathbf{r}_{c1} + \frac{\mathbf{r}_{d1}}{2}\,, \quad \mathbf{r}_\beta = \mathbf{r}_{c1} - \frac{\mathbf{r}_{d1}}{2}\,, \quad \mathbf{r}_\gamma = \mathbf{r}_{c2} + \frac{\mathbf{r}_{d2}}{2}\,, \quad \mathbf{r}_\delta = \mathbf{r}_{c2} - \frac{\mathbf{r}_{d2}}{2}\,,$$

permits Eqn. (B.1) to be written more compactly to clarify the terms involved. Under the weak scattering condition ($|\phi| \ll 1$), the ensemble averaged term may be expanded as

$$\begin{aligned} & \langle \exp[j\phi(\mathbf{r}_\alpha) + j\phi(\mathbf{r}_\beta) - j\phi(\mathbf{r}_\gamma) - j\phi(\mathbf{r}_\delta)] \rangle \\ & \qquad \approx 1 - 2\sigma^2 - \sigma^2 \exp\left(-\frac{r_{d1}^2}{l^2} \right) - \sigma^2 \exp\left(-\frac{r_{d2}^2}{l^2} \right) \\ & \qquad\quad + \sigma^2 \exp\left[-\frac{1}{l^2} \left| \mathbf{r}_{c1} - \mathbf{r}_{c2} + \frac{\mathbf{r}_{d1}}{2} - \frac{\mathbf{r}_{d2}}{2} \right|^2 \right] \end{aligned}$$

$$
\begin{aligned}
&+\sigma^2\exp\left[-\frac{1}{l^2}\left|\mathbf{r}_{c1}-\mathbf{r}_{c2}+\frac{\mathbf{r}_{d1}}{2}+\frac{\mathbf{r}_{d2}}{2}\right|^2\right]\\
&+\sigma^2\exp\left[-\frac{1}{l^2}\left|\mathbf{r}_{c1}-\mathbf{r}_{c2}-\frac{\mathbf{r}_{d1}}{2}-\frac{\mathbf{r}_{d2}}{2}\right|^2\right]\\
&+\sigma^2\exp\left[-\frac{1}{l^2}\left|\mathbf{r}_{c1}-\mathbf{r}_{c2}-\frac{\mathbf{r}_{d1}}{2}+\frac{\mathbf{r}_{d2}}{2}\right|^2\right]\ ,
\end{aligned}
\tag{B.2}
$$

where we have made use of the statistical properties of ϕ defined in Eqns. (4.4)-(4.6). If the variable transform

$$
\mathbf{r}_{c3}=\frac{1}{2}(\mathbf{r}_{c1}+\mathbf{r}_{c2}),\qquad\qquad \mathbf{r}_{d3}=(\mathbf{r}_{c1}-\mathbf{r}_{c2}),
$$

is introduced, then substitution of Eqn. (B.2) in (B.1) and the latter in Eqn. (4.22) yields the expression for $\langle I_2\rangle$

$$
\begin{aligned}
\langle I_2\rangle =\ &\alpha p_0^4\int_{\mathbf{r}_{d1}}\int_{\mathbf{r}_{d2}}\int_{\mathbf{r}_{d3}}\int_{\mathbf{r}_{c3}} d\mathbf{r}_{c3}d\mathbf{r}_{d3}d\mathbf{r}_{d2}d\mathbf{r}_{d1}\,\exp\left[-\frac{j2k\mathbf{r}_{c3}\cdot\mathbf{r}_{d3}}{z}+\frac{j2k\mathbf{r}\cdot\mathbf{r}_{d3}}{z}\right.\\
&\left.-\frac{2A}{a^2}\left(2r_{c3}^2+\frac{r_{d3}^2}{2}\right)+\frac{4jB}{a^2}\mathbf{r}_{c3}\cdot\mathbf{r}_{d3}-\frac{A-jB}{2a^2}r_{d1}^2-\frac{A+jB}{2a^2}r_{d2}^2\right]\\
&\times E_1\left(\frac{jkr_{d1}^2}{4z}\right)E_1\left(-\frac{jkr_{d2}^2}{4z}\right)\left\{1-2\sigma^2-\sigma^2\exp\left(-\frac{r_{d1}^2}{l^2}\right)-\sigma^2\exp\left(-\frac{r_{d2}^2}{l^2}\right)\right.\\
&+\sigma^2\exp\left[-\frac{1}{l^2}\left|\mathbf{r}_{d3}+\frac{(\mathbf{r}_{d1}-\mathbf{r}_{d2})}{2}\right|^2\right]+\sigma^2\exp\left[-\frac{1}{l^2}\left|\mathbf{r}_{d3}+\frac{(\mathbf{r}_{d1}+\mathbf{r}_{d2})}{2}\right|^2\right]\\
&\left.+\sigma^2\exp\left[-\frac{1}{l^2}\left|\mathbf{r}_{d3}-\frac{(\mathbf{r}_{d1}+\mathbf{r}_{d2})}{2}\right|^2\right]+\sigma^2\exp\left[-\frac{1}{l^2}\left|\mathbf{r}_{d3}-\frac{(\mathbf{r}_{d1}-\mathbf{r}_{d2})}{2}\right|^2\right]\right\}\ ,
\end{aligned}
\tag{B.3}
$$

where

$$
\alpha=\frac{k^6\beta^2}{128\pi^4\rho_0^3c_0^5z^2}\ .
\tag{B.4}
$$

The integration over $\mathbf{r}_{c3}$ is carried out first. The result is

$$
\begin{aligned}
\langle I_2\rangle =\ &\frac{\alpha p_0^4\pi a^2}{4A}\int_{\mathbf{r}_{d1}}\int_{\mathbf{r}_{d2}}\int_{\mathbf{r}_{d3}}\exp\left\{\left[-\frac{A}{a^2}-\frac{(B-ka^2/2z)^2}{Aa^2}\right]r_{d3}^2\right.\\
&\left.+\frac{2jk\mathbf{r}\cdot\mathbf{r}_{d3}}{z}-\frac{(A-jB)r_{d1}^2}{2a^2}-\frac{(A+jB)r_{d2}^2}{2a^2}\right\}\\
&\times E_1\left(\frac{jkr_{d1}^2}{4z}\right)E_1\left(-\frac{jkr_{d2}^2}{4z}\right)\{1-2\sigma^2+....\}d\mathbf{r}_{d3}d\mathbf{r}_{d2}d\mathbf{r}_{d1}\ ,
\end{aligned}
\tag{B.5}
$$

where the expression inside the braces, $\{1 - 2\sigma^2 + ...\}$, is the same as that in Eqn. (B.3). Next, we separate the coherent and scattered fields according to Eqn. (4.23),

$$\langle I_2 \rangle = (1 - 2\sigma^2) I_2^{\mathrm{coh1}} - \sigma^2 I_2^{\mathrm{coh2}} + \sigma^2 I_2^{\mathrm{sc}} \,.$$

The coherent intensity I_1^{coh1} is expressed as

$$\begin{aligned} I_2^{\mathrm{coh1}} = \frac{\alpha p_0^4 \pi a^2}{4A} \int_{\mathbf{r}_{d1}} \int_{\mathbf{r}_{d2}} \int_{\mathbf{r}_{d3}} & \exp\Bigg\{ \left[-\frac{A}{a^2} - \frac{(B - ka^2/2z)^2}{Aa^2} \right] r_{d3}^2 \\ & + \frac{2jk\mathbf{r}\cdot\mathbf{r}_{d3}}{z} - \frac{(A - jB) r_{d1}^2}{2a^2} - \frac{(A + jB) r_{d2}^2}{2a^2} \Bigg\} \\ & \times E_1\left(\frac{jkr_{d1}^2}{4z} \right) E_1\left(-\frac{jkr_{d2}^2}{4z} \right) d\mathbf{r}_{d3} d\mathbf{r}_{d2} d\mathbf{r}_{d1} \,. \end{aligned} \tag{B.6}$$

Evaluating the integrals in Eqn. (B.6) yields

$$\begin{aligned} I_2^{\mathrm{coh1}} = & \frac{k^6 \beta^2 p_0^4 a^8}{128 \rho_0^3 c_0^5 z^2} \frac{|\ln[1 - j2z(A - jB)/ka^2]|^2}{(A^2 + B^2)[A^2 + (B - ka^2/2z)^2]} \\ & \times \exp\left[-\frac{(Ak^2 a^4/z^2)(r/a)^2}{A^2 + (B - ka^2/2z)^2} \right] , \end{aligned} \tag{B.7}$$

which has been presented in Eqn. (4.24).

The intensity I_2^{coh2} is expressed as

$$\begin{aligned} I_2^{\mathrm{coh2}} = \frac{\alpha p_0^4 \pi a^2}{4A} \int_{\mathbf{r}_{d1}} \int_{\mathbf{r}_{d2}} \int_{\mathbf{r}_{d3}} & \exp\Bigg\{ \left[-\frac{A}{a^2} - \frac{(B - ka^2/2z)^2}{Aa^2} \right] r_{d3}^2 \\ & + \frac{2jk\mathbf{r}\cdot\mathbf{r}_{d3}}{z} - \frac{(A - jB) r_{d1}^2}{2a^2} - \frac{(A + jB) r_{d2}^2}{2a^2} \Bigg\} \\ & \times E_1\left(\frac{jkr_{d1}^2}{4z} \right) E_1\left(-\frac{jkr_{d2}^2}{4z} \right) \left(e^{-r_{d1}^2/l^2} + e^{-r_{d2}^2/l^2} \right) d\mathbf{r}_{d3} d\mathbf{r}_{d2} d\mathbf{r}_{d1} \,. \end{aligned} \tag{B.8}$$

By carrying out the integration one can obtain the solution

$$\begin{aligned} I_2^{\mathrm{coh2}} = & \frac{k^6 \beta^2 p_0^4 a^8}{128 \rho_0^3 c_0^5 z^2} \frac{1}{A^2 + (B - ka^2/2z)^2} \exp\left[-\frac{(Ak^2 a^4/z^2)(r/a)^2}{A^2 + (B - ka^2/2z)^2} \right] \\ & \times \left\{ \frac{\ln[1 - j2z(A - jB + 2\nu^2)/ka^2] \, \ln[1 + j2z(A + jB)/ka^2]}{(A - jB + 2\nu^2)(A + jB)} + \mathrm{c.c.} \right\} , \end{aligned} \tag{B.9}$$

which is Eqn. (4.25).

The scattered intensity I_2^{sc} is expressed as

$$\begin{aligned}
I_2^{\mathrm{sc}} = {} & \frac{\alpha p_0^4 \pi a^2}{4A} \int_{\mathbf{r}_{d1}} \int_{\mathbf{r}_{d2}} \int_{\mathbf{r}_{d3}} \exp\Bigg\{ \left[-\frac{A}{a^2} - \frac{(B - ka^2/2z)^2}{Aa^2} \right] r_{d3}^2 \\
& + \frac{j2k\mathbf{r}\cdot\mathbf{r}_{d3}}{z} - \frac{(A - jB) r_{d1}^2}{2a^2} - \frac{(A + jB) r_{d2}^2}{2a^2} \Bigg\} \\
& \times E_1\!\left(\frac{jkr_{d1}^2}{4z} \right) E_1\!\left(-\frac{jkr_{d2}^2}{4z} \right) \left\{ \exp\left[-\frac{1}{l^2} \left| \mathbf{r}_{d3} + \frac{(\mathbf{r}_{d1} - \mathbf{r}_{d2})}{2} \right|^2 \right] \right. \\
& + \exp\left[-\frac{1}{l^2} \left| \mathbf{r}_{d3} + \frac{(\mathbf{r}_{d1} + \mathbf{r}_{d2})}{2} \right|^2 \right] + \exp\left[-\frac{1}{l^2} \left| \mathbf{r}_{d3} - \frac{(\mathbf{r}_{d1} + \mathbf{r}_{d2})}{2} \right|^2 \right] \\
& \left. + \exp\left[-\frac{1}{l^2} \left| \mathbf{r}_{d3} - \frac{(\mathbf{r}_{d1} - \mathbf{r}_{d2})}{2} \right|^2 \right] \right\} d\mathbf{r}_{d3} d\mathbf{r}_{d2} d\mathbf{r}_{d1} \, .
\end{aligned} \tag{B.10}$$

It can be seen that the dependence of the integrand on $\mathbf{r}_{d3}$ is Gaussian. Integration over $\mathbf{r}_{d3}$ thus yields

$$\begin{aligned}
I_2^{\mathrm{sc}} = {} & \frac{\alpha p_0^4 \pi^2 a^2}{2AF(z)} \exp\left[-\frac{k^2 r^2}{z^2 F(z)} \right] \int_{\mathbf{r}_{d1}} \int_{\mathbf{r}_{d2}} E_1\!\left(\frac{jkr_{d1}^2}{4z} \right) E_1\!\left(-\frac{jkr_{d2}^2}{4z} \right) \\
& \times \exp\left[\left(\frac{1}{4l^4 F(z)} - \frac{1}{4l^2} - \frac{A - jB}{2a^2} \right) r_{d1}^2 + \left(\frac{1}{4l^4 F(z)} - \frac{1}{4l^2} - \frac{A + jB}{2a^2} \right) r_{d2}^2 \right] \\
& \times \left\{ \exp\left[-\left(\frac{1}{2l^4 F(z)} - \frac{1}{2l^2} \right) \mathbf{r}_{d1}\cdot\mathbf{r}_{d2} \right] \cos\left[\frac{k\mathbf{r}\cdot(\mathbf{r}_{d1} - \mathbf{r}_{d2})}{zl^2 F(z)} \right] \right. \\
& \left. + \exp\left[\left(\frac{1}{2l^4 F(z)} - \frac{1}{2l^2} \right) \mathbf{r}_{d1}\cdot\mathbf{r}_{d2} \right] \cos\left[\frac{k\mathbf{r}\cdot(\mathbf{r}_{d1} + \mathbf{r}_{d2})}{zl^2 F(z)} \right] \right\} d\mathbf{r}_{d2} d\mathbf{r}_{d1} \, ,
\end{aligned} \tag{B.11}$$

where

$$F(z) = \frac{A}{a^2} + \frac{(B - ka^2/2z)^2}{Aa^2} + \frac{1}{l^2} \, .$$

It is now helpful to introduce the polar coordinates

$$\mathbf{r} = (\rho, \theta) \, , \qquad \mathbf{r}_{d1} = (\rho_1, \theta_1) \, , \qquad \mathbf{r}_{d2} = (\rho_2, \theta_2) \, ,$$

such that

$$\begin{aligned}
\mathbf{r}_{d1}\cdot\mathbf{r}_{d2} &= \rho_1 \rho_2 \cos(\theta_1 - \theta_2) \, , \\
\mathbf{r}\cdot(\mathbf{r}_{d1} - \mathbf{r}_{d2}) &= \rho\rho_1 \cos(\theta - \theta_1) - \rho\rho_2 \cos(\theta - \theta_2) \, , \\
\mathbf{r}\cdot(\mathbf{r}_{d1} + \mathbf{r}_{d2}) &= \rho\rho_1 \cos(\theta - \theta_1) + \rho\rho_2 \cos(\theta - \theta_2) \, .
\end{aligned}$$

Substituting the polar coordinates into Eqn. (B.11), and performing the integrations over θ_1 and θ_2, we arrive at

$$\begin{aligned} I_2^{\mathrm{sc}} = \frac{\alpha p_0^4 \pi^2 a^2}{2AF(z)} \exp\left[-\frac{k^2 r^2}{z^2 F(z)}\right] \int_0^\infty \int_0^\infty \exp\Big(m_1 \rho_1^2 + m_1^* \rho_2^2\Big) \\ \times E_1\left(\frac{jk\rho_1^2}{4z}\right) E_1\left(-\frac{jk\rho_2^2}{4z}\right) \rho_1 \rho_2 T(\rho_1, \rho_2)\, d\rho_1 d\rho_2 \,, \end{aligned} \tag{B.12}$$

with

$$\begin{aligned} T(\rho_1, \rho_2) = \int_0^{2\pi} \int_0^{2\pi} [\exp[\xi_1 \rho_1 \rho_2 \cos(\theta_1 - \theta_2)]\ \cos\{\xi_2[\rho\rho_1 \cos(\theta - \theta_1) - \rho\rho_2 \cos(\theta - \theta_2)]\} \\ + \exp[-\xi_1 \rho_1 \rho_2 \cos(\theta_1 - \theta_2)] \cos\{\xi_2[\rho\rho_1 \cos(\theta - \theta_1) + \rho\rho_2 \cos(\theta - \theta_2)]\}]\ d\theta_1 d\theta_2 \,, \end{aligned} \tag{B.13}$$

and

$$\xi_1 = -\frac{1}{2l^4 F(z)} + \frac{1}{2l^2} \,, \qquad \xi_2 = \frac{k}{z l^2 F(z)} \,, \qquad M_1 = \frac{1}{4l^4 F(z)} - \frac{1}{4l^2} - \frac{A - jB}{2a^2} \,.$$

The integrations over θ_1 and θ_2 are cumbersome, and they are carried out in App. C. The result is

$$T = \int_0^{2\pi} \int_0^{2\pi} \ldots\ldots d\theta_1 d\theta_2 = 8\pi^2 \sum_{m=-\infty}^{\infty} J_m(\xi_2 \rho \rho_1) J_m(\xi_2 \rho \rho_2) I_m(\xi_1 \rho_1 \rho_2) \,, \tag{B.14}$$

where J_m is mth order Bessel function, and I_m is the mth order modified Bessel function.

Equation (B.12) now becomes

$$\begin{aligned} I_2^{\mathrm{sc}} = S(r, z) \sum_{m=-\infty}^{\infty} \int_0^\infty \int_0^\infty E_1\left(\frac{jk\rho_1^2}{4z}\right) E_1\left(-\frac{jk\rho_2^2}{4z}\right) \exp\Big(M_1 \rho_1^2 + M_1^* \rho_2^2\Big) \\ \times J_m(\xi_2 \rho \rho_1)\ J_m(\xi_2 \rho \rho_2)\ I_m(\xi_1 \rho_1 \rho_2)\ \rho_1 \rho_2\ d\rho_1 d\rho_2 \,, \end{aligned} \tag{B.15}$$

with

$$S(r, z) = \frac{4\alpha p_0^4 \pi^4 a^2}{AF(z)} \exp\left[-\frac{k^2 r^2}{z^2 F(z)}\right] .$$

With the definition of E_1 in Eqn. (3.13), Eqn. (B.15) can be written as

$$\begin{aligned} I_2^{\mathrm{sc}} = S(r,z) \sum_{m=-\infty}^{\infty} \int_1^\infty \int_1^\infty \frac{dt_1 dt_2}{t_1 t_2} \int_0^\infty \int_0^\infty \exp\Bigg[\left(M_1 - \frac{jkt_1}{4z} \right) \rho_1^2 \\ + \left(M_1^* + \frac{jkt_1}{4z} \right) \rho_2^2 \Bigg] J_m(\xi_2 \rho \rho_1)\, J_m(\xi_2 \rho \rho_2)\, I_m(\xi_1 \rho_1 \rho_2)\, \rho_1 \rho_2 \, d\rho_1 d\rho_2 \, . \end{aligned} \tag{B.16}$$

We now focus on the integrals with respect to ρ_1 and ρ_2 in Eqn. (B.16). Let S represent these integrals:

$$\begin{aligned} S = \int_0^\infty \int_0^\infty \exp\Bigg[\left(M_1 - \frac{jk_0 t_1}{4z} \right) \rho_1^2 + \left(M_1^* + \frac{jk_0 t_1}{4z} \right) \rho_2^2 \Bigg] \\ \times J_m(\xi_2 \rho \rho_1)\, J_m(\xi_2 \rho \rho_2)\, I_m(\xi_1 \rho_1 \rho_2)\, \rho_1 \rho_2 \, d\rho_1 d\rho_2 \, . \end{aligned} \tag{B.17}$$

Equation (B.17) can be carried out using the Weber Integral Theorem:[76]

$$\int_0^\infty x \exp(-A_1 x^2) I_m(B_1 x) J_m(C_1 x) dx = \frac{1}{2A_1} \exp\left(\frac{{B_1}^2 - {C_1}^2}{4A_1} \right) J_m\left(\frac{B_1 C_1}{2A_1} \right) , \tag{B.18}$$

$$\int_0^\infty x \exp(-A_2 x^2) J_m(B_2 x) J_m(C_2 x) dx = \frac{1}{2A_2} \exp\left(-\frac{{B_2}^2 + {C_2}^2}{4A_2} \right) I_m\left(\frac{B_2 C_2}{2A_2} \right) , \tag{B.19}$$

where $A_{1,2}$, $B_{1,2}$ and $C_{1,2}$ are complex constants, with $\mathrm{Re}(\mathrm{A}_{1,2}) > 0$. It is straightforward to prove that $\mathrm{Re}(M_1) < 0$, so Eqn. (B.17) can be integrated with respect to ρ_1 first to obtain

$$\begin{aligned} S = \frac{\exp(-\xi_2^2 \rho^2 / 4Y_1)}{2Y_1} \int_0^\infty \exp\left[\left(\frac{\xi_1^2}{4Y_1} + m_1^* + \frac{jkt_2}{4z} \right) \rho_2^2 \right] \\ \times J_m\left(\frac{\xi_1 \xi_2 \rho \rho_2}{2Y_1} \right) J_m(\xi_2 \rho \rho_2) \rho_2 d\rho_2 \, , \end{aligned} \tag{B.20}$$

where $Y_1 = -M_1 + jkt_1/4z$. It can be shown that $\mathrm{Re}(\xi_1^2/4Y_1 + M_1^*) < 0$, so we use Eqn. (B.19) to obtain

$$S = \frac{-I_m(-\xi_1 \xi_2^2 \rho^2 / Y_2)}{Y_2} \exp\left\{ \frac{\xi_2^2 \rho^2 [-2\mathrm{Re}(M_1) + jk(t_1 - t_2)/(4z)]}{Y_2} \right\} , \tag{B.21}$$

$$Y_2 = \xi_1^2 + \left(2M_1^* + \frac{jkt_2}{2z} \right) \left(-2M_1 + \frac{jkt_1}{2z} \right) . \tag{B.22}$$

Substitution of Eqn. (B.21) into (B.16) yields

$$I_2^{\mathrm{sc}} = -S(r,z)\int_1^{\infty}\int_1^{\infty} \frac{\exp\{\xi_2^2\rho^2[-2\mathrm{Re}(M_1) + jk(t_1-t_2)/(4z)]/Y_2\}}{Y_2 t_1 t_2} \sum_{m=-\infty}^{\infty} I_m\left(-\frac{\xi_1\xi_2^2\rho^2}{Y_2}\right) dt_1 dt_2\,. \tag{B.23}$$

We now make use of the identity

$$\sum_{m=-\infty}^{\infty} I_m\left(-\frac{\xi_1\xi_2^2\rho^2}{Y_2}\right) = \exp\left(-\frac{\xi_1\xi_2^2\rho^2}{Y_2}\right)$$

to arrive at

$$I_2^{\mathrm{sc}} = -S(r,z)\int_1^{\infty}\int_1^{\infty}\frac{dt_1 dt_2}{Y_2 t_1 t_2}\exp\left\{\frac{\xi_2^2\rho^2[jk(t_1-t_2)/4z - \xi_1 - 2\mathrm{Re}(M_1)]}{Y_2}\right\}. \tag{B.24}$$

With ξ_1, ξ_2, M_1, Y_2 and $S(r,z)$ written in terms of A, B, θ, r and z, we finally obtain

$$\begin{aligned} I_2^{\mathrm{sc}} = {} & \frac{k^6\beta^2 p_0^4 a^8}{32\rho_0^3 c_0^5 z^2}\exp\left[-\frac{(Ak^2a^4/z^2)(r^2/a^2)}{A^2+(B-ka^2/2z)^2}\right] \\ & \times\int_1^{\infty}\int_1^{\infty}\frac{dt_1 dt_2}{t_1 t_2 \eta_1\eta_2 M(t_1,t_2)}\exp\left\{\frac{(\nu^2A^2k^2a^4/z^2)(r^2/a^2)}{M(t_1,t_2)\left[A^2+(B-ka^2/2z)^2\right]}\right\}, \end{aligned}$$

with

$$\begin{aligned} M(t_1,t_2) &= \left[A^2+\left(B-ka^2/2z\right)^2\right]\left[\frac{\nu^2}{2}\left(\frac{1}{\eta_1}+\frac{1}{\eta_2}\right)+1\right] + A\nu^2 \\ \eta_1 &= A - jB + \frac{jka^2t_1}{2z}\,, \quad \eta_2 = A + jB - \frac{jka^2t_2}{2z}\,, \end{aligned}$$

which have been given by Eqns. (4.26)–(4.28).

Appendix C

Evaluation of the integral $T(\rho_1, \rho_2)$

In this appendix we evaluate the integral in Eqn. (B.14), rewritten here:

$$T(\rho_1,\rho_2) = \int_0^{2\pi}\int_0^{2\pi} [\exp[\,\xi_1\rho_1\rho_2\,\cos(\theta_1-\theta_2)]\cos\{\xi_2\,[\rho\rho_1\cos(\theta-\theta_1)-\rho\rho_2\cos(\theta-\theta_2)]\,\} \\ +\exp[-\xi_1\rho_1\rho_2\cos(\theta_1-\theta_2)]\cos\{\xi_2\,[\rho\rho_1\cos(\theta-\theta_1)+\rho\rho_2\cos(\theta-\theta_2)]\,\}]\,d\theta_1 d\theta_2\,. \tag{C.1}$$

By making the substitutions $\theta_1' = \theta_1 - \theta$ and $\theta_2' = \theta_2 - \theta$ in Eqn. (C.1) we obtain

$$T = \int_{-\theta}^{2\pi-\theta}\int_{-\theta}^{2\pi-\theta} \{\exp[\xi_1\rho_1\rho_2\cos(\theta_1-\theta_2)]\cos[\xi_2(\rho\rho_1\cos\theta_1-\rho\rho_2\cos\theta_2)] \\ +\exp[-\xi_1\rho_1\rho_2\cos(\theta_1-\theta_2)]\cos[\xi_2(\rho\rho_1\cos\theta_1+\rho\rho_2\cos\theta_2)]\}\,d\theta_1 d\theta_2\,, \tag{C.2}$$

where the primes were dropped immediately following the substitutions. Since the expression inside the integral is a periodic function of both θ_1 and θ_2, and the integration regions are over one period, we have

$$T = \int_0^{2\pi}\int_0^{2\pi} \{\exp[\xi_1\rho_1\rho_2\cos(\theta_1-\theta_2)]\;\cos[\xi_2(\rho\rho_1\cos\theta_1-\rho\rho_2\cos\theta_2)] \\ +\exp[-\xi_1\rho_1\rho_2\cos(\theta_1-\theta_2)]\cos[\xi_2(\rho\rho_1\cos\theta_1+\rho\rho_2\cos\theta_2)]\}\,d\theta_1 d\theta_2. \tag{C.3}$$

Since both θ_1 and θ_2 appear as arguments of cosines in Eqn. (C.3), the integral over each of these quantities from 0 to 2π is simply twice the integral from 0 to π, such that

$$T = 4\int_0^{\pi}\int_0^{\pi} \exp[\xi_1\rho_1\rho_2\cos(\theta_1-\theta_2)]\;\cos[\xi_2(\rho\rho_1\cos\theta_1-\rho\rho_2\cos\theta_2)]d\theta_1 d\theta_2 \\ +4\int_0^{\pi}\int_0^{\pi} \exp[-\xi_1\rho_1\rho_2\cos(\theta_1-\theta_2)]\;\cos[\xi_2(\rho\rho_1\cos\theta_1+\rho\rho_2\cos\theta_2)]d\theta_1 d\theta_2\,. \tag{C.4}$$

With $\theta_1' = \theta_1 - \pi$, the second intgral can be written as

$$4\int_0^{\pi}\int_0^{\pi} \exp[-\xi_1\rho_1\rho_2\cos(\theta_1-\theta_2)]\;\cos[\xi_2(\rho\rho_1\cos\theta_1+\rho\rho_2\cos\theta_2)]d\theta_1 d\theta_2$$

$$= 4\int_{\theta_2=0}^{\pi}\int_{\theta_1=-\pi}^{0} \exp[\xi_1\rho_1\rho_2\cos(\theta_1-\theta_2)]\ \cos[\xi_2(\rho\rho_1\cos\theta_1-\rho\rho_2\cos\theta_2)]d\theta_1 d\theta_2\,, \tag{C.5}$$

where again the prime on θ_1 was dropped immediately following the change of variable. Note that the right-hand side is equivalent to the first pair of integrals in Eqn. (C.4), such that we now have

$$T = 4\int_{\theta_2=0}^{\pi}\int_{\theta_1=-\pi}^{\pi} \exp[\xi_1\rho_1\rho_2\cos(\theta_1-\theta_2)]\ \cos(\xi_2\rho\rho_1\cos\theta_1-\ \xi_2\rho\rho_2\cos\theta_2)d\theta_1 d\theta_2\,. \tag{C.6}$$

If we now make the substitutions:

$$r_1 = \sqrt{\xi_1}\,\rho_1\,, \qquad r_2 = \sqrt{\xi_1}\,\rho_2\,, \qquad r = \xi_2/2\sqrt{\xi_1}\,\rho\,,$$

Eqn. (C.6) becomes

$$T = 4\int_{\theta_2=0}^{\pi}\int_{\theta_1=-\pi}^{\pi} \exp[r_1r_2\cos(\theta_1-\theta_2)]\ \cos(2rr_1\cos\theta_1-\ 2rr_2\cos\theta_2)d\theta_1 d\theta_2\,. \tag{C.7}$$

First integrate Eqn. (C.7) with respect to θ_1. Let $\theta_1' = \theta_1 - \theta_2$ such that

$$\begin{aligned} T =&\ 4\int_{\theta_2=0}^{\pi}\int_{\theta_1'=-\pi-\theta_2}^{\pi-\theta_2} \exp(r_1r_2\cos\theta_1')\ \cos[2rr_1\cos(\theta_1'+\theta_2)-\ 2rr_2\cos\theta_2]d\theta_1' d\theta_2 \\ =&\ 4\int_{\theta_2=0}^{\pi}\int_{\theta_1'=-\pi}^{\pi} \exp(r_1r_2\cos\theta_1')\ \cos[2rr_1\cos(\theta_1'+\theta_2)-\ 2rr_2\cos\theta_2]d\theta_1' d\theta_2 \\ =&\ 4\int_{\theta_1'=-\pi}^{\pi} \exp(r_1r_2\cos\theta_1')\int_{\theta_2=0}^{\pi} \cos[2rr_1\cos(\theta_1'+\theta_2)-\ 2rr_2\cos\theta_2]d\theta_2 d\theta_1'\,. \end{aligned} \tag{C.8}$$

When we introduce

$$x_1 = 2rr_1\cos\theta_1' - 2rr_2\,, \qquad x_2 = 2rr_1\sin\theta_1'\,, \qquad \tan\beta = x_2/x_1\,,$$

Eqn. (C.8) can be written as

$$\begin{aligned} T =&\ 4\int_{\theta_1'=-\pi}^{\pi} \exp(r_1r_2\cos\theta_1')\int_{\theta_2=0}^{\pi} \cos[x_1\cos\theta_2 - x_2\sin\theta_2]d\theta_2 d\theta_1' \\ =&\ 4\int_{\theta_1'=-\pi}^{\pi} \exp(r_1r_2\cos\theta_1')\int_{\theta_2=0}^{\pi} \cos[\sqrt{x_1^2+x_2^2}\cos(\theta_2+\beta)]d\theta_2 d\theta_1'. \end{aligned} \tag{C.9}$$

Notice the integrand is a periodic function of θ_2, with period π, so we have

$$\begin{aligned}\int_0^\pi \cos\Big[\sqrt{x_1^2+x_2^2}\cos(\theta_2+\beta)\Big]\,d\theta_2 &= \int_0^\pi \cos\Big[\sqrt{x_1^2+x_2^2}\cos\theta_2\Big]\,d\theta_2 \\ &= \pi J_0\left(\sqrt{x_1^2+x_2^2}\right) \\ &= \pi J_0\left(\sqrt{(2rr_1)^2+(2rr_2)^2-8r_1r_2r^2\cos\theta_1'}\right) .\end{aligned}$$

Equation. (C.9) thus becomes

$$\begin{aligned}T &= 4\pi\int_{-\pi}^{\pi}\exp(r_1r_2\cos\theta_1')J_0\left(\sqrt{(2rr_1)^2+(2rr_2)^2-8r_1r_2r^2\cos\theta_1'}\right)d\theta_1' \\ &= 8\pi\int_0^{\pi}\exp(r_1r_2\cos\theta_1')J_0\left(\sqrt{(2rr_1)^2+(2rr_2)^2-8r_1r_2r^2\cos\theta_1'}\right)d\theta_1' .\end{aligned}$$

By using the identity[75]

$$J_0\left(\sqrt{y_1^2+y_2^2-2y_1y_2\cos\beta}\right) = \sum_{m=-\infty}^{\infty} J_m(y_1)J_m(y_2)\cos(m\beta) \tag{C.10}$$

we arrive at

$$\begin{aligned}T &= 8\pi\sum_{m=-\infty}^{\infty} J_m(2rr_1)J_m(2rr_2)\int_0^\pi \exp(r_1r_2\cos\theta_1')\cos(m\theta_1')d\theta_1' \\ &= 8\pi^2\sum_{m=-\infty}^{\infty} J_m(2rr_1)J_m(2rr_2)I_m(r_1r_2) \\ &= 8\pi^2\sum_{m=-\infty}^{\infty} J_m(\xi_2\rho\rho_1)J_m(\xi_2\rho\rho_2)I_m(\xi_1\rho_1\rho_2)\, ,\end{aligned} \tag{C.11}$$

which is Eqn. (B.14).

Appendix D

Statistical solutions for the second harmonic with screen at arbitary position

Explicit expressions for Eqn. (4.64) are presented here. Let $B_2 = b_2/d = (d - b_1)/d$ and $B_1 = b_1/d$. For I_{2l} we have

$$\begin{aligned} I_{2l} = {} & \frac{G^2 P_2^2 |\ln(B_2 - jB_1/G)|^2}{2\rho_0 c_0 (1+G^2)} \Big[(1-4\sigma^2)\exp(-4G^2\rho^2) \\ & + \frac{4\sigma^2}{1+\nu^2 B_2^2} \exp\left(-\frac{4G^2\rho^2}{1+\nu^2 B_2^2}\right)\Big] \, . \end{aligned} \tag{D.1}$$

For $b_1 \ll l$, it can be approximated by

$$I_{2l} \approx \frac{B_1^2 P_2^2}{2\rho_0 c_0} \left[(1-4\sigma^2)\exp\left(-4\tilde{G}^2\tilde{\rho}^2\right) + \frac{4\sigma^2}{1+\tilde{\nu}^2}\exp\left(-\frac{4\tilde{G}^2\tilde{\rho}^2}{1+\tilde{\nu}^2}\right)\right] \, , \tag{D.2}$$

with $\tilde{G}$, $\tilde{\nu}$ and $\tilde{\rho}$ defined in Eqns. (4.58).

The solution for I_{2ln} is

$$\begin{aligned} I_{2ln} = {} & \frac{1}{2\rho_0 c_0} \frac{G^2 P_2^2 \ln(B_2 + jB_1/G)}{(1+jG)(B_2 - jB_1/G)} \Big\{(1-3\sigma^2)\exp(-4G^2\rho^2) \\ & \times (B_2^2 + B_1^2/G^2) \frac{\ln[1/(B_1 + jB_2 G)]}{1 - j(B_2 G - B_1/G)} \\ & - \sigma^2 \exp(-4G^2\rho^2)(B_2^2 + B_1^2/G^2) \\ & \times \frac{\ln[1/(B_1 + jB_2 G) - 2j\nu^2 B_2/G]}{1 - j(B_2 G - B_1/G) + 2\nu^2(B_2^2 + B_1^2/G^2)} \\ & + 4\sigma^2 \exp(-4G^2\rho^2) \int_1^\infty \frac{\exp[4G^2\rho^2 B_2^2 \nu^2 M/V]}{tV} dt \Big\} + \text{c.c.} \, , \end{aligned} \tag{D.3}$$

where

$$M = \frac{jGt_1}{B_2} + \frac{1 - j(B_2 G - B_1/G)}{B_2^2 + B_1^2/G^2} \, , \tag{D.4}$$

$$V = \frac{\nu^2}{2} + (1 + \nu^2 B_2^2) M \, . \tag{D.5}$$

For $b_1 \ll l$, it can be approximated by

$$
\begin{aligned}
I_{2ln} \approx \frac{jB_1P_2^2}{2\rho_0 c_0}\Bigg\{ & \left[(1-3\sigma^2)\frac{\ln(-j/\tilde{G})}{(1-j\tilde{G})/\tilde{G}} - \sigma^2\frac{\ln[-j(1+2\tilde{\nu}^2)/\tilde{G}]}{(1-j\tilde{G}+2\tilde{\nu}^2)/\tilde{G}}\right] \\
& + \frac{4\sigma^2\tilde{G}}{\tilde{\nu}^2}\int_0^\infty \frac{\exp[4\tilde{G}^2\tilde{\rho}^2(1+j\tilde{G}t)/M_{ln})]}{(t+1)M_{ln}}\,dt\Bigg\}\exp(-4\tilde{G}^2\tilde{\rho}^2)+\text{c.c.}\,, \qquad \text{(D.6)}
\end{aligned}
$$

with

$$
M_{ln} = \frac{3}{2}+\frac{1}{\tilde{\nu}^2}+\frac{j\tilde{G}t(1+\tilde{\nu}^2)}{\tilde{\nu}^2}\,. \qquad \text{(D.7)}
$$

The solution for I_{2n} is

$$
\begin{aligned}
I_{2n} = \; & \frac{(1-2\sigma^2)P_2^2(B_2^2G^2+B_1^2)}{2\rho_0c_0[1+(B_2G-B_1/G)^2]}\left|\ln\left[\frac{B_1-jB_2G}{B_2^2G^2+B_1}\right]\right|^2\exp(-4G^2\rho^2) \\
& -2\sigma^2P_2^2(B_2^2G^2+B_1^2)\exp(-4G^2\rho^2)\times \\
& \operatorname{Re}\left\{\frac{\ln[1/(B_1+jB_2G)-j2\nu^2B_2/G)\;\ln[1/(B_1-jB_2G)]}{[2\nu^2(B_2^2+B_1^2/G^2)+1-j(B_2G-B_1/G)][1+j(B_2G-B_1/G)]}\right\} \\
& +\frac{\sigma^2 4G^2P_2^2}{\nu^4(B_2^2+B_1^2/G^2)}\exp(-4G^2\rho^2) \\
& \times\int_1^\infty\int_1^\infty \exp\left[\frac{4G^2\rho^2(1+\nu^2B_2^2)\nu^2B_2^2T}{(1+\nu^2B_2^2)M}\right]\frac{dt_1dt_2}{t_1t_2M}\,, \qquad \text{(D.8)}
\end{aligned}
$$

where

$$
\begin{aligned}
T &= \left[\frac{1+j(B_2G-B_1/G)}{\nu^2(B_2^2+B_1^2/G^2)}-\frac{jGt_2}{\nu^2B_2}\right]\left[\frac{1-j(B_2G-B_1/G)}{\nu^2(B_2^2+B_1^2/G^2)}+\frac{jGt_1}{\nu^2B_2}\right], \qquad \text{(D.9)} \\
M &= \frac{1}{\nu^2(B_2^2+B_1^2/G^2)}+\frac{jG(t_1-t_2)}{2\nu^2B_2}+\left(1+\nu^2B_2^2\right)T\,. \qquad \text{(D.10)}
\end{aligned}
$$

The approximation for $b_1 \ll d$ is given by Eqn. (4.65).

Bibliography

[1] H. Kuttruff, "Application of ultrasound in medical diagnostics," in *Ultrasonics Fundamentals and Applications* (Elsevier Applied Science, London, 1991), Chap. 11.

[2] B. Ward, A. C. Baker, and V. F. Humphrey, "Nonlinear propagation applied to the improvement of resolution in diagnostic medical ultrasound," *J. Acoust. Soc. Am.* **101,** 143–154 (1997).

[3] S. A. Goss, R. L. Johnston and F. Dunn, "Compilation of empirical ultrasonic properties of mammalian tissue," *J. Acoust. Soc. Am.* **68,** 93–108 (1980).

[4] M. E. Lyons and K. J. Parker, "Absorption and attenuation in soft tissue II: Experimental results," *IEEE Trans. Ultrason. Ferroelctr. Freq. Control* **35,** 511–521 (1988).

[5] T. D. Mast, L. M. Hinkelman, M. J. Orr, V. W. Sparrow, and R. C. Waag, "Simulation of ultrasonic pulse propagation through the abdominal wall," *J. Acoust. Soc. Am.* **102,** 1177–1190 (1997).

[6] P. T. Christopher, "Finite amplitude distortion-based inhomogeneous pulse echo ultrasonic imaging," *IEEE Trans. Ultrason. Ferroelctr. Freq. Control* **44,** 125–139 (1997).

[7] P. W. Ralls, "Tissue Harmonic Imaging," *http: // www.sonocredits.com /article.asp?TestID=9* (2000).

[8] E. L. Carstensen, W. K. Law, N. D. McKay and T. G. Muir, "Demonstration of nonlinear acoustic effects at biomedical frequencies and intensities," *Ultrasound Med. Biol.* **6,** 359–368 (1980).

[9] H. C. Starritt, M. A. Perkins, F. A. Duck, and V. F. Humphrey, "Evidence for ultrasonic finite-amplitude distortion in muscle using medical equipment," *J. Acoust. Soc. Am.* **77,** 302–306 (1985).

[10] H. C. Starritt, F. A. Duck, A. J. Hawkins, and V. F. Humphrey, "The development of harmonic distortion in pulsed finite-amplitude ultrasound passing through liver," *Phys. Med. Biol.* **31,** 1401–1409 (1986).

[11] M. A. Averkiou, D. N. Roundhill, and J. E. Powers, "A new imaging technique based on the nonlinear properties of tissues," *IEEE Ultrasonics Symposium* **2,** 1561–1566 (1997).

[12] P. N. Burns, D. H. Simpson and M. A. Averkiou, "Nonlinear imaging," *Ultrasound in Med. & Biol.* **26,** s19–s22 (2000).

[13] F. Tranquart, N. Grener, V. Eder, and L. Pourcelot, "Clinical use of ultrasoud tissue harmonic imaging," *Ultrasound in Med. & Biol.* **25,** 889–894 (1999).

[14] D. H. Simpson, C. T. Chin, and P. N. Burns, "Pulse inversion doppler: A new method for detecting nonlinear echoes from microbubble contrast agents," *IEEE Trans. Ultrason. Ferroelctr. Freq. Control* **46,** 372-382 (1999).

[15] P. C. Li, "Pulse compression for finite amplitude distortion based harmonic imaging using coded waveforms," *Ultrason. Imaging* **21,** 1–16 (1999).

[16] M. A. Averkiou, "Tissue harmonic imaging," *IEEE Ultrasonics Symposium* **2,** 1563–1572 (2000).

[17] M. A. Averkiou and M. F. Hamilton, "Nonlinear distortion of short pulses radiated by plane and focused circular pistons," *J. Acoust. Soc. Am.* **102,** 2539–2548 (1997).

[18] H. Becher, K. Tiemann, T. Schlosser, C. Pohi, N.Nanda, M. Averkiou, J. Powers, and B. Luderitz, "Improvement in endocardial border delineation using tissue harmonic imaging," *Echocardiography* **15,** 511–517 (1998).

[19] D. Zhang, X. Gong, and B. Zhang, "Second harmonic sound field after insertion of a biological tissue sample," *J. Acoust. Soc. Am.* **111,** 45–48 (2002).

[20] G. Wojcik, J. Mould, S. Ayter, and L. Carcione, "A study of second harmonic generation by focused medical transducer pulses," *IEEE Ultrasonics Symposium,* 1583–1588 (1998).

[21] P. T. Christopher, "Experimental investigation of finite amplitude distortion-based second harmonic pulse echo ultrasonic imaging," *IEEE Trans. Ultrason. Ferroelctr. Freq. Control* **45,** 158–162 (1998).

[22] L. M. Hinkelman, D.-L. Liu, L. A. Metlay, and R. C. Waag, "Measurements of ultrasonic pulse arrival time and energy level variations produced by propagation through abdominal wall," *J. Acoust. Soc. Am.* **95,** 530–541 (1994).

[23] S. W. Flax and M. O'Donnell, "Phase-aberration correction using signals from point reflectors and diffuse scatters: Measurements," *IEEE Trans. Ultrason. Ferroelctr. Freq. Control* **35,** 768–774 (1988).

[24] M. O'Donnell and S. W. Flax, "Phase aberration measurements in medical ultrasound: human studies," *Ultrasound Imaging* **10,** 1–11 (1988).

[25] P. Krammer and D. Hassler, "Measurement of spatial time-of-flight fluctuations of ultrasound pulses passing through inhomogeneous layers," *IEEE 1987 Ultrasonics Symposium Processings* **2,** 939–942 (1987).

[26] Y. Sumino and R. C. Waag, "Measurements of ultrasonic pulse arrival time difference produced by abdominal wall specimens," *J. Acoust. Soc. Am.* **90,** 2924–2930 (1991).

[27] D.-L. Liu and R. C. Waag, "Correction of ultrasonic wavefront distortion using backpropagation and a reference waveform method for time-shift compensation," *J. Acoust. Soc. Am.* **96,** 649–660 (1994).

[28] D.-L. Liu and R. C. Waag, "Estimation and correction of ultrasonic wavefront distortion using pulse-echo data received in a two-dimensional aperture," *IEEE Trans. Ultrason. Ferroelctr. Freq. Control* **45,** 473–490 (1998).

[29] D.-L. Liu and R. C. Waag, "Time-shift compensation of ultrasonic pulse focus degradation using least-mean-square error estimates of arrival time," *J. Acoust. Soc. Am.* **95,** 542–555 (1994).

[30] S. W. Flax and M. O'Donnell, "Phase-aberration correction using signals from point reflectors and diffuse scatters: Basic principle," *IEEE Trans. Ultrason. Ferroelctr. Freq. Control* **35,** 758–767 (1988).

[31] D.-H. Huang and J. Tsao, "Analysis and correction of ultrasonic wavefront distortion based on a multilayer phase-screen model," *IEEE Trans. Ultrason. Ferroelctr. Freq. Control* **49,** 1686–1703 (2002).

[32] M. A. Averkiou and V. A. Khokhlova, "Time-domain numerical solution of the KZK equation for modeling sound beams radiated by rectangular sources," *J. Acoust. Soc. Am.* **105,** 1208(A) (1999).

[33] E. A. Zabolotskaya and R. V. Khokhlov, "Quasi-plane waves in the nonlinear acoustics of confined beams," *Sov. Phys. Acoust.* **15,** 35–40 (1969).

[34] Y. Jing and R. Cleveland, "Effect of aberration on the acoustic field in tissue harmonic imaging (THI)," *J. Acoust. Soc. Am* **114,** 2436(A) (2003).

[35] M. Tabei, T. D. Mast, and R. C. Waag, "Simulation of ultrasonic focus aberration and correction through human tissue," *J. Acoust. Soc. Am.* **113,** 1166–1176 (2003).

[36] E. Soczkiewicz and R. C. Chivers, "Propagation of acoustic waves in random media using the parabolic equation and Greens function methods," *Acustica* **65,** 149–155 (1988).

[37] B. J. Uscinski, *The Elements of Wave Propagation in Random Media* (McGraw-Hill, New York, 1977).

[38] Yu. Kravtsov, *Geometrical Optics of Inhomogeneous Media* (Springer-Verlag, New York, 1990).

[39] P. G. Bergmann, "The wave equation in a medium with a variable index of refraction," *J. Acoust. Soc. Am.* **17,** 329–333 (1946).

[40] L. Chernov, *Wave Propagation in a Random Medium* (Dover, New York, 1960).

[41] L. A. Ostrovsky, "On the theory of waves in nonstationary compressible media," *Prikl. Matem.* **27,** 924–929 (English translation, 1412–1421) (1963).

[42] E. N. Pelinovskii and V. E. Fridman, "Equations of nonlinear geometrical acoustics," in *Nonlinear Deformation Waves*, edited by U. Nigel and Yu. K. Engel'brekht (Springer-Verlag, Berlin, 1982), pp. 143–148.

[43] O. V. Rudenko, A. K. Sukhorukova, and A. P. Sukhorukov, "Equations of high-frequency nonlinear acoustics for inhomogeneous media," *Acoust. Phys.* **40,** 264–268 (1994).

[44] O. V. Rudenko and A. K. Sukhorukova, "Nonlinear sawtooth waves in an inhomogeneous medium," *Sov. Phys. Acoust.* **37,** 392–395 (1991).

[45] P. Blanc-Benon, B. Lipkens, L. Dallois, M. F. Hamilton, and D. T. Blackstock, "Propagation of finite amplitude sound through turbulence: Modeling with geometrical acoustics and the parabolic approximation," *J. Acoust. Soc. Am.* **111,** 487–498 (2002).

[46] S. M. Rytov, Yu. A. Kravtsov, and V. I. Tatarskii, *Principles of Statistical Radiophysics* (Springer-Verlag, New York, 1987).

[47] R. A. Schmeltzer, "Means, variance and covariances for laser beam propagation through a random medium," *Quart. Appl. Math.* **24,** 339–354 (1967).

[48] J. Berntsen, J. Naze Tjøtta, and S. Tjøtta, "Nearfield of a large acoustic transducer. Part IV: Second harmonic and sum frequency radiation," *J. Acoust. Soc. Am.* **75,** 1383-1391 (1984).

[49] M. F. Hamilton, "Sound Beams," in *Nonlinear Acoustics*, edited by M. F. Hamilton and D. T. Blackstock (Academic Press, Boston, 1998), Chap. 8.

[50] M. F. Hamilton and C. L. Morfey, "Model Equations," in *Nonlinear Acoustics*, edited by M. F. Hamilton and D. T. Blackstock (Academic Press, Boston, 1998), Chap. 3.

[51] B. J. Landsberger, "Second harmonic generation in sound beams reflected and transmitted through immersed elastic solid," Ph.D. dissertation, The University of Texas at Austin (1997).

[52] V. P. Kuznetsov, "Equations of nonlinear acoustics," *Sov. Phys. Acoust.* **16,** 467–470 (1971).

[53] P. Alais and P. Y. Hennion, "A Fourier theory of the nonlinear interaction of acoustical beams in absorbing fluid. The spectral case of parametric emission," *Acustica* **43,** 1–11 (1979).

[54] B. J. Landsberger and M. F. Hamilton, "Second harmonic generation in sound beams reflected from, and transmitted through immersed elastic solid," *J. Acoust. Soc. Am* **109,** 488–500 (2001).

[55] R. J. Zemp, J. Tavakkoli and R. S. Cobbold, "Modeling of nonlinear ultrasound propagation in tissue from array transducers," *J. Acoust. Soc. Am.* **113,** 139–152 (2003).

[56] J. Naze Tjøtta and S. Tjøtta, "An analytical model for the nearfield of a baffled piston transducer," *J. Acoust. Soc. Am.* **68,** 334–339 (1980).

[57] A. C. Baker, A. M. Berg, A. Sahin, and J. Naze Tjøtta, "The nonlinear pressure field of plane, rectangular apertures: Experimental and theoretical results," *J. Acoust. Soc. Am.* **97,** 3510–3517 (1995).

[58] M. F. Hamilton, Yu. A. Ilinskii, and E. A. Zabolotskaya, "Dispersion," in *Nonlinear Acoustics*, edited by M. F. Hamilton and D. T. Blackstock (Academic Press, Boston, 1998), Chap. 5.

[59] G. S. Garrett, J. Naze Tjøtta and S. Tjøtta, "Near field of a large acoustic transducer: Part III: General results," *J. Acoust. Soc. Am.* **75,** 769–779 (1984).

[60] S. S. Kashcheeva, O. A. Sapozhnikov, V. A. Khokhlova, M. A. Averkiou, and L. A. Crum, "Nonlinear distortion and attenuation of intense acoustic waves in lossy media obeying a frequency power law," *Acoust. Phys.* **46,** 170–177 (2000).

[61] S. I. Aanonsen, T. Barkve, J. Naze Tjøtta and S. Tjøtta, "Distortion and harmonic generation in the nearfield of a finite amplitude sound beam," *J. Acoust. Soc. Am.* **75,** 749–768 (1984).

[62] Y.-S. Lee and M. F. Hamilton, "Time-domain modeling of pulsed finite amplitude sound beams," *J. Acoust. Soc. Am.* **97,** 906–917 (1995).

[63] P. T. Christopher and K. J. Parker, "New approches to nonlinear diffactive field propagation," *J. Acoust. Soc. Am.* **90,** 488–499 (1991).

[64] T. Kamakura, M. Tani, Y. Kumamoto and K. Ueda, "Harmonic generation in finite amplitude sound beam from a rectangular aperture source," *J. Acoust. Soc. Am.* **91,** 3144–3151 (1992).

[65] J. Naze Tjøtta and S. Tjøtta , "Interactions of sound waves. Part III: Two real beams," *J. Acoust. Soc. Am.* **83,** 487–495 (1988).

[66] J. W. Goodman, *Introduction to Fourier Optics* (McGraw-Hill, San Francisco, 1968).

[67] W. F. Ames, *Numerical Methods for Partial Differential Equations* (Academic Press, New York, 1977).

[68] J. J. McCoy and M. J. Beran, "Propagation of beamed signals through inhomogeneous media: A diffraction theory," *J. Acoust. Soc. Am.* **59,** 1142–1149 (1976).

[69] R. H. Clarke, "Analysis of laser beam propagation in a turbulent atmosphere," *ATT Technical Journal* **64,** 1585–1601 (1985).

[70] Y. Viniotis, "Processing of random processes," in *Probability and Random Processes for Electrical Engineers* (McGraw-Hill, Boston, 1998), Chap. 9.

[71] A. P. Berkhoff and J. M. Thijssen, "Correction of concentrated and distributed aberrators in medical ultrasound imaging," *IEEE Ultrasonics Symposium* 1405-1410 (1996).

[72] B. G. Lucas and T. G. Muir, "The field of a focusing source," *J. Acoust. Soc. Am.* **72,** 1289–1296 (1982).

[73] B. G. Lucas and T. G. Muir, "Field of finite amplitude focusing source," *J. Acoust. Soc. Am.* **74,** 1522–1528 (1983).

[74] D. T. Blackstock, *Fundamentals of Physical Acoustics* (Wiley, New York, 2000).

[75] M. Abramowitz and I. A. Stegun, *Handbook of Mathematical Functions, with Formulas, Graphs, and Mathematical Tables* (Dover, New York, 1965).

[76] I. S. Gradshteyn and I. M. Ryzhik, "Definite integrals of special functions," in *Table of Integrals, Series, and Products*, edited by A. Jeffrey and D. Zwillinger (Academic Press, San Diego, 2000), 6th ed., Chap. 6.

VITA

Xiang Yan was born on July 31, 1975 and raised in Jinan, Shandong, People's Republic of China, the daughter of Guo-liang Wu and Hua-fang Zhang. After graduating from Nanjing University in 1997 with a Bachelor's degree in Electrical Engineering, she went to the University of Massachusetts at Dartmouth. She graduated from the University of Massachusetts at Dartmouth in 2000 with a Master's degree in Electrical Engineering. She was admitted into the Graduate School of The University of Texas in the fall of 2000.

Permanent address:
1300 S. Pleasant Valley Road, Apt. 274, Austin, Texas, 78741

This dissertation was typeset[*] with LaTeX by the author.

---

[*] The LaTeX document preparation system was developed by Leslie Lamport as a special version of Donald Knuth's TeX program for computer typesetting. TeX is a trademark of the American Mathematical Society.